



**UNIVERSITY  
OF ICELAND**

**Ground deformation caused by  
viscoelastic relaxation and its role in  
the 2015-2021 post-eruptive period at the  
Bárðarbunga volcanic system, Iceland**

Siqi Li

2022

FACULTY OF EARTH SCIENCES



**Ground deformation caused by  
viscoelastic relaxation and its role in  
the 2015-2021 post-eruptive period at the  
Bárðarbunga volcanic system, Iceland**

Siqi Li

Dissertation submitted in partial fulfillment of a  
*Philosophiae Doctor degree in Geophysics*

Supervisor  
Freysteinn Sigmundsson

Doctoral Committee  
Freysteinn Sigmundsson  
Halldór Geirsson  
Andrew Hooper

Opponents  
Fred F. Pollitz  
Yang Liao

Faculty of Earth Sciences  
School of Engineering and Natural Sciences  
University of Iceland  
Reykjavik, December 2022

Ground deformation caused by viscoelastic relaxation and its role in the 2015-2021 post-eruptive period at the Bárðarbunga volcanic system, Iceland  
(Bárðarbunga post-eruptive ground deformation)

Dissertation submitted in partial fulfillment of a *Philosophiae Doctor* degree in Geophysics

Faculty of Earth Sciences  
School of Engineering and Natural Sciences  
University of Iceland  
Askja, Sturlugata 7  
102 Reykjavik  
Iceland

Telephone: 525-4000

Bibliographic information:

Siqi Li (2022) *Ground deformation caused by viscoelastic relaxation and its role in the 2015-2021 post-eruptive period at the Bárðarbunga volcanic system, Iceland*, PhD dissertation, Faculty of Earth Sciences, University of Iceland, 145 pp.

ISBN 978-9935-9555-7-9

Copyright © 2022 Siqi Li  
All rights reserved

Printing: Háskólaprent  
Reykjavik, Iceland, December 2022

# Abstract

Post-eruptive deformation following volcanic eruptions may originate from continued magma movements, or reflect delayed and continued Earth adjustment due to co-eruptive events, often referred to as viscoelastic relaxation. Post-eruptive deformation can continue for years, and it is challenging to reveal the details of the underlying processes. In this PhD project, the ground deformation in a post-eruptive period at the Bárðarbunga volcanic system is mapped using Global Navigation Satellite System (GNSS) geodesy and Interferometric analysis of Synthetic Aperture Radar satellite images (InSAR).

The Bárðarbunga volcanic system is a laboratory area for this study because of the large-scale magma transfer during an eruption in 2014-2015, lasting six months. Magma flowed laterally along a 48-km-long dike from a magma body below the Bárðarbunga caldera. An eruption occurred at the northern end of the dike. During this time, the Bárðarbunga caldera collapsed 65 m.

Data collected using GNSS and InSAR techniques provide information on the post-rifting ground deformation both in the area near the Bárðarbunga caldera and the northernmost segment of the Bárðarbunga-Holuhraun dike north of the Vatnajökull ice cap. The background deformation signal in the area includes plate spreading (18-19 mm/yr in the horizontal direction) and glacial isostatic adjustment (GIA, less than 7 mm/yr in the horizontal direction and up to 33 mm/yr in the vertical direction). Velocities from the plate spreading and GIA are subtracted from the observed deformation field, to isolate the movements caused by other processes, referred to as corrected average velocity.

The corrected average velocity field has horizontal movements away from the caldera and the dike in the post-eruptive period. The surface close to the caldera and near the dike uplifted. Around the caldera, the GNSS station closest to the caldera has maximum corrected uplift velocity of about 20 mm/yr and maximum corrected horizontal velocity away from the caldera of about 111 mm/yr between 2015 and 2018. Other stations show smaller average velocities. A GNSS station 16 km away from the caldera shows corrected subsidence up to about 12 mm/yr. Around the dike, the maximum corrected uplift rate between 2015-2020 measured by InSAR is  $\sim 12$  mm/yr. Two GNSS stations that are 20 km apart on different sides of the dike experience baseline lengthening at a corrected rate of  $\sim 19$  mm/yr in the direction perpendicular to the strike of the dike.

A two-layer model with an elastic layer on top of a viscoelastic half-space is used to model viscoelastic relaxation. Three possible explanations are explored for the corrected post-eruptive deformation around the Bárðarbunga caldera: viscoelastic relaxation, renewed magma inflow, or a combination of the processes. In the viscoelastic

---

relaxation model, the viscosity that best explains the displacements around the caldera is  $3 \times 10^{18}$  Pa s. Our study suggests that viscoelastic relaxation and/or renewed magma inflow can explain the observed deformation. It is hard to tell the difference between the processes by only comparing the average velocity field.

The post-eruptive deformation around the Bárðarbunga-Holuhraun dike is also modeled with the two-layer viscoelastic model. The best fitting model has a  $4 \times 10^{18}$  Pa s viscoelastic half-space below 18 km thick elastic layer. A comparable fit is found for a 2 km thick elastic layer, underlain by a viscoelastic half-space with viscosity  $12 \times 10^{18}$  Pa s.

The study of the deformation around the Bárðarbunga caldera suggests viscoelastic relaxation generates a similar average velocity field as magma inflow in the post-eruptive period. To better understand the difference between the two processes, it is explored if stress field and displacement time series differ. Modeling results suggest that the stress fields generated by these two processes are similar, and it is hard to distinguish them. The temporal variation of the horizontal surface displacement from the viscoelastic relaxation decays with time, comparable to exponential decay. The decay constant that describes the decay rate varies with distance from the source in the viscoelastic relaxation model. For magma inflow into a source of constant geometry, the rate of magma inflow may decay with time, causing time-dependent surface displacement. However, the decay constant is then the same over the study area. At the Bárðarbunga volcano, the continuous GNSS stations show decay of horizontal displacement. The decay constants differ somewhat at different locations but are all less than five years. A viscoelastic model with the viscosity  $1-6 \times 10^{18}$  Pa s has a decay constant larger than ten years. Using a model with different source geometry or a different type of viscoelastic relaxation model may better explain the post-eruptive deformation at the Bárðarbunga volcano.

# Útdráttur

Jarðskorpuhreyfingar á eldfjöllum eftir eldgos geta orsakast af mörgum ferlum, m.a. áframhaldandi kvikuhreyfingum, eða verið svörun jarðar við fyrri atburðum og kvikuhreyfingum í eldgosi, með taftíma. Slík síðbúin svörun jarðskorpunnar með taftíma getur orsakast af seigfjaðrandi efnishegðun jarðar. Jarðskorpuhreyfingar eftir eldgos geta varað árum saman og erfitt getur reynst að varpa skýru ljósi á ferlin sem stjórna slíkum hreyfingum. Í þessu doktorsverkefni eru jarðskorpuhreyfingar í eldstöðvakerfi Bárðarbungu eftir meiriháttar eldsumbrot metnar með GNSS (Global Navigation Satellite System) og InSAR (Interferometric analysis of Synthetic Aperture Radar satellite images) mælingum á jarðskorpuhreyfingum.

Eldstöðvakerfið er valið sem rannsóknasvæði vegna mikillar tilfærslu kviku í eldgosi 2014-2015, sem stóð í 6 mánuði. Kvika streymdi lárétt eftir um 48 km löngum kvikugangi úr kvikueiningu undir öskju Bárðarbungu, og eldgos varð við norðurenda gangansins. Bárðarbunguaskjan seig um 65 m.

Gögn sem safnað var með GNSS og InSAR mælingum veita upplýsingar um jarðskorpuhreyfingar á árabílinu eftir eldgos og kvikuinnskot, bæði á svæðinu næst Bárðarbunguöskjunni og eins við norðurenda kvikugangansins, norðan Vatnajökuls. Bakgrunnslarðskorpuhreyfingar á rannsóknarsvæðunum stafa af flekareki (18-19 mm/ári lárétt gliðnun) og vegna svörun jarðar við þynningu jökla (færslur minni en 7 mm/ári í lárétta stefnu, en allt að 33 mm/ári lóðrétt). Leiðrétt hraðasvið er metið því að draga frá færslur vegna þessara hreyfinga, til að meta jarðskorpuhreyfingar af öðrum ástæðum.

Leiðrétt meðal-hraðasvið sýnir láréttar færslu í átt frá Bárðarbunguöskjunni og kvikuganginum á árunum eftir gos. Svæði næst öskjunni og ganginum rísa. GNSS stöð sem liggur næst öskjunni hefur hæstan meðalrishaða, eða um 20 mm/ári, og hæstan láréttan færsluhraða, eða um 111 mm/ári, á árunum frá 2015 til 2018. Aðrar stöðvar sýna miklu lægri meðalhraða. GNSS stöð 16 km frá öskjunni sýnir leiðréttan sighthraða um 12 mm/ári. Í nágrenni kvikugangansins er leiðréttur meðalrishaði metin með InSAR um 12 mm/ári. Tvær GNSS stöðvar sitt hvoru megin við kvikuganginn sýna að leiðrétt fjarlægð milli þeirra lengist um 19 mm/ári.

Tvískipt jarðlagalíkan, með lárétu lagi af fjaðrandi efni ofan á seigfjaðrandi undirlagi er notað til að líkja eftir seigfjaðrandi hreyfingum. Þrjár mögulegar orsakir hreyfinga í kringum Bárðarbunguöskjuna eru metnar: seigfjaðrandi efnishegðun, kvikuinnstreymi eftir eldgos, eða samblanda þessara ferla. Ef hreyfisviðið er skýrt sem afleiðing af seigfjaðrandi svörun, þá passar seigjan  $3 \times 10^{18}$  Pa s best við niðurstöður. Líkanreikningar sýna að seigfjaðrandi svörun og/eða kvikuinnflæði getur útskýrt niðurstöðurnar, en erfitt er að greina á milli þessara ferla eingöngu með því að nota meðalhraða.

Jarðskorpuhreyfingar á tímabilinu eftir eldgos og kvikuinnskot í nágrenni við kvikuganginn voru notaðar til að skorða sambærilegt líkan fyrir það svæði. Það líkan sem

---

fellur best að mæligögnum þar er með  $4 \times 10^{18}$  Pa s seigju undir 18 km þykku lagi með fjaðrandi hegðun. Sambærilegt samræmi við mælingar fæst þó með líkani sem er með 2 km þykkt lag af fjaðrandi efni, með undirlagi með seigjuna  $12 \times 10^{18}$  Pa s.

Rannsóknin á aflögum jarðskorpunnar í kringum Bárðarbunguöskjuna sýnir að seigfjaðrandi svörun jarðskorpunnar býr til meðal-hraðasvið mjög líkt því sem getur orsakast af kvikuinnstreymi í rætur eldstöðvar á árum eftir gos. Til að meta frekar mismuninn á þessum ferlum, þá voru kannaðar spennubreytingar samfara þeim, sem og hvernig færslur á yfirborði jarðar breytast með tíma. Líkanreikningar sýna að spennusvið vegna þessara ferla geta verið mjög sambærileg og erfitt að greina á milli þeirra. Láréttar færslur á yfirborði vegna seigfjaðrandi svörunar dvína með tíma líkt og veldisfall, og þá er stuðullinn sem lýsir dvínuninni breytilegur með fjarlægð frá uppsprettunni. Fyrir kvikuinnflæði í kvikueiningu sem breytir ekki um geometríu, þá kann kvikuinnflæði einnig að dvína með tíma. Stuðull sem lýsir dvínandi jarðskorpuhreyfingum verður í því tilviki hins vegar sá sami í öllum fjarlægðum frá uppsprettunni. Samfelldar GNSS stöðvar næst Bárðarbungu sýna dvínun hreyfinga sem hægt er að fella að veldisfalli. Dvínunarstuðlarnir eru aðeins breytilegir eftir fjarlægð, en í öllum tilvikum lægri en 5 ár. Seigfjaðrandi líkan með seigju  $1-6 \times 10^{18}$  Pa s seigju hefur hinsvegar dvínunarstuðla hærri en 10 ár. Líkan með annari geometríu fyrir uppsprettu hreyfinganna eða önnur tegund af seigfjaðrandi líkani en hér könnuð getur e.t.v. úskýrt betur færslur jarðskorpunnar á árunum eftir eldgos.



# Contents

Abstract	iii
Útdráttur	v
Contents	vii
List of Figures	ix
List of Original Publications	xiii
Abbreviations	xv
Acknowledgments	xvii
<b>1 Introduction</b>	<b>1</b>
1.1 Space-geodetic measurements at volcanoes	1
1.1.1 GNSS	2
1.1.2 InSAR	6
1.2 Plate spreading and glacial isostatic adjustment (GIA)	9
1.3 Volcano deformation source models	9
1.3.1 Elastic models	12
1.3.2 Viscoelastic deformation models	13
1.3.3 Modeling strategy	15
1.4 The Bárðarbunga volcanic system and the 2014-2015 Bárðarbunga-Holuhraun eruption	16
1.5 Present work	19
<b>2 Paper I: Ground deformation after a caldera collapse: Contributions of magma inflow and viscoelastic response to the 2015-2018 deformation field around Bárðarbunga, Iceland</b>	<b>21</b>
2.1 Summary	21
2.2 Main results	24
<b>3 Paper II: Post-rifting relaxation during 2015-2020 following the Bárðarbunga - Holuhraun dike intrusion and eruption in Iceland</b>	<b>25</b>
3.1 Summary	25
3.2 Main results	28

<b>4</b>	<b>Paper III: Similarity of stress and ground displacement patterns caused by viscoelastic relaxation and magma inflow in a post-eruptive period: A case study at Bárðarbunga volcano, Iceland</b>	<b>29</b>
4.1	Summary . . . . .	29
4.2	Main results . . . . .	31
<b>5</b>	<b>General conclusions</b>	<b>33</b>
	<b>References</b>	<b>34</b>
	<b>Paper I</b>	<b>43</b>
	<b>Paper II</b>	<b>87</b>
	<b>Paper III</b>	<b>121</b>

# List of Figures

1.1	(a) Campaign and (b) continuous GNSS equipment set up in the field. For campaign GNSS (a), an antenna is installed on a tripod, above a benchmark, typically measured yearly or every few years. A receiver is connected to the antenna (inside the black box) to shelter it from bad weather. Continuous GNSS in Iceland (b) typically has an antenna installed on a quadropod. The receiver is in a box, connected to electricity. In Iceland, the continuous GNSS stations normally obtain electricity from a wind turbine and a solar panel. . . . .	4
1.2	Map view of the Bárðarbunga volcanic system and surroundings showing central volcanoes, calderas, and fissure swarms (for geological layers, see Sigmundsson et al. (2020a) and references there-in). White areas are the glaciers. Segments of the 2014-2015 dike path are indicated with red lines (Sigmundsson et al., 2015), and the 2014-2015 Holuhraun lava field is shown with dark gray shading. Blue and red triangles are campaign and continuous GNSS stations, respectively. The two rectangular boxes are the study areas in the first two papers of this thesis. . . . .	5
1.3	GNSS time series collected at GNSS station KISA (left, 2015-2022) and DYNC (right, 2008-2022) reference to the Eurasian plate. Displacements in the north (top), east (middle), and up (bottom) components are shown in mm, with an arbitrary shift for displaying purpose, so the middle of each displacement scale is at 0. The positions of the continuous GNSS stations are processed with GAMIT/GLOBK. The horizontal axis shows time in years. GNSS time series analysis from Sigrún Hreinsdóttir, translated to stable Eurasian plate reference and replotted. . . . .	6
1.4	Wrapped (upper) and unwrapped (lower) interferogram in the area in Figure 1.2 measured by InSAR. The time span of the interferogram (the acquisition times of the two SAR images used to form the interferogram) is from 09 July 2015 to 02 June 2022. Based on Sentinel-1 images from Track 9. The area with blurry fringes in the wrapped images is called incoherence, normally due to changes in the reflector on the ground. For wrapped interferogram calculated from Sentinel-1 images, one fringe ( $-\pi$ to $\pi$ ) corresponds to 2.83 cm. . . . .	8
1.5	East (a) and north (b) displacement rate of plate spreading model in the area shown in Figure 1.2. Model is from Drouin and Sigmundsson (2019). . . . .	10

1.6	Uplift (a), east (b) and north (c) rate of scaled GIA model in the area shown in Figure 1.2. The GIA model is a scaled version from Auriac (2014), with a scaling factor of 2.8 for horizontal and 1.5 for vertical components from Li et al. (2021). . . . .	11
1.7	Sketches of deformation source models discussed, in cross-sections. The elastic magma models are: a) pressure point source (Mogi model), b) Okada dislocation model, and c) penny-shaped crack sill model. The viscoelastic models are: d) a two-layer viscoelastic model, e) a viscoelastic shell around a spherical source, and f) a temperature-dependent viscoelastic model (panel f is modified from Del Negro et al. (2009)). In panel a-e, red indicates the magma body, light pink indicates elastic material, and orange is viscoelastic material. The two-layer viscoelastic model (panel d) considers an upper elastic layer and a lower viscoelastic half-space. Contour lines in panel f show different temperatures, and the viscosity is a function of that in temperature-dependent viscosity models. . . . .	13
1.8	Bárðarbunga volcanic system, including the two subglacial central volcanoes (Bárðarbunga and Hamarinn), the fissure swarm, and the lava flows from the volcano. Figure is from Larsen and Gudmundsson (2019). . . . .	17
2.1	Corrected GNSS and InSAR average velocities, in the period May 2015 - October 2018, compared with viscoelastic deformation model with optimal viscosity and magma withdrawal volume. The viscoelastic model considers a contraction volume of 0.4 km <sup>3</sup> at 10 km depth. Observed and modeled GNSS velocities in horizontal and vertical directions are shown in panels a and e. Black arrows in panel a show observations, and red arrows show the modeled velocities. The gray area in panel e is the distance range from the modeling center (-17.48°E, 64.63°N) to the caldera rim. The figure displays InSAR input data (b and f), modeling results (c and g), and residuals (d and h). The dot in the caldera in panel c shows the modeling center of the viscoelastic model. Corrected InSAR average velocities from ascending Track 118 and descending Track 9 are compared with the viscoelastic deformation model in panels b-d and f-h, respectively. . . . .	22
2.2	Corrected velocity fields compared with elastic modeling predictions considering a sill fixed at 10 km depth and fault slip on the caldera ring fault. The velocities are presented similarly in Figure 2.1. The input InSAR results are resampled to a grid, with dense point spacing close to the caldera and sparse points further away from the caldera. The grid within the caldera in panel c illustrates the location of the modeled sill. Panel i shows a three-dimensional view of the amount of slip on the caldera fault patches according to the model, and panel j shows the inferred sill opening similarly. . . . .	23

3.1	Corrected average velocity field in the horizontal (a) and vertical (e) directions during 2015-2020 from InSAR (color) and GNSS (black arrows). The modeled east and up velocity from the viscoelastic model with the optimal elastic layer thickness (18 km) and viscosity ( $4 \times 10^{18}$ Pa s) are shown in b and f. Panels c and g show the differences between corresponding observation (a and e) and model (b and f). Panels d and h show velocity profiles across the study area in the near-east (red line in a, b, and c) and near-up (red line in e, f, and g). . . . .	26
3.2	Root mean square residual between the corrected velocity fields (data) and predicted ground velocity fields from modeling. The data include near-east and near-up components from InSAR and north, east, and up components from GNSS. The weight of GNSS vs. InSAR is 1000:1. The weight of horizontal vs. vertical is 2:1. The x-axis is the elastic layer thickness (1-24 km with 1 km step), and the y-axis is the viscosity ( $3-36 \times 10^{18}$ Pa s with $1 \times 10^{18}$ Pa s step). The optimal viscosity for the velocities is at $4 \times 10^{18}$ Pa s, and the optimal elastic layer thickness is 18 km. . . . .	27
4.1	The spatial pattern of the stress change caused by viscoelastic relaxation (left) and magma inflow (middle) since $t=0^+$ . Panels to the right show the corresponding stress difference between the two models. The panels show cross-sections of four components of stress change in a plane parallel to the north-south direction in the initial 6.3 years. The left panels show the stress change in the viscoelastic relaxation caused by magma withdrawal from a $0.4 \text{ km}^3$ point source. The middle panels show stress change in a magma inflow model with a total inflow volume of $3.6 \times 10^8 \text{ m}^3$ . The four stress components are: $\sigma_{11}$ , $\sigma_{22}$ , $\sigma_{33}$ , $\sigma_{13}$ . The x-axis is the north-south direction, and the z-axis is the vertical direction. The crustal volume within a 2-km radius from the source center (white circle at the center of each panel) is masked to eliminate unrealistically high stress change predicted by the point source. . . . .	30
4.2	Amplitude (left) and decay constant (right) estimated from the horizontal surface displacement time series in a viscoelastic model, fit with an exponential function. The dots with error bars show the estimated amplitude and decay constant from viscoelastic models with different viscosities. The circles with error bars show the estimated amplitude and decay constant from the corrected GNSS time series. The x-axis is the distance from the source center in kilometers. . . . .	31



## List of Original Publications

- Paper I:** **Siqi Li**, Freysteinn Sigmundsson, Vincent Drouin, Michelle M. Parks, Benedikt G. Ófeigsson, Kristín Jónsdóttir, Ronni Grapenthin, Halldór Geirsson, Andrew Hooper, and Sigrún Hreinsdóttir, (2021). Ground deformation after a caldera collapse: Contributions of magma inflow and viscoelastic response to the 2015-2018 deformation field around Bárðarbunga, Iceland, *Journal of Geophysical Research: Solid Earth*, 126(3), p.e2020JB020157. <https://agupubs.onlinelibrary.wiley.com/doi/abs/10.1029/2020JB020157>
- Paper II:** **Siqi Li**, Ronni Grapenthin, Freysteinn Sigmundsson, Vincent Drouin, Sigrún Hreinsdóttir, and Benedikt G. Ófeigsson, (2022). Post-rifting relaxation during 2015-2020 following the Bárðarbunga-Holuhraun dike intrusion and eruption in Iceland, *Geophysical Research Letters*, 49(13), p.e2022GL098977. <https://agupubs.onlinelibrary.wiley.com/doi/abs/10.1029/2022GL098977>
- Paper III:** (in preparation) **Siqi Li**, Freysteinn Sigmundsson, Tadashi Yamasaki, Páll Einarsson, Kristín Jónsdóttir, Halldór Geirsson, and Andrew Hooper. Similarity of stress and ground displacement patterns caused by viscoelastic relaxation and magma inflow in a post-eruptive period: A case study at Bárðarbunga volcano, Iceland.





# Abbreviations

3D	Three dimension
a.s.l.	Above Sea Level
b.s.l.	Below Sea Level
GIA	Glacial Isostatic Adjustment
GNSS	Global Navigation Satellite System
GPS	Global Positioning System
IMO	Icelandic Meteorological Office
InSAR	Interferometric analysis of Synthetic Aperture Radar
ITRF2014	International Terrestrial Reference Frame 2014
LOS	Line-of-Sight
NSF	National Science Foundation
RANNÍS	Icelandic Centre for Research fund
RINEX	Receiver INdependent EXchange
SAR	Synthetic Aperture Radar
yr	year



## Acknowledgments

First of all, I would like to thank my supervisor, Freysteinn Sigmundsson, for accepting me as his PhD student, and always providing advice for my work. My PhD work is much better than I had imaged a PhD project would be, which I would like to contribute a lot to my supervisor. I highly appreciate all the time he devoted to my work, from suggesting my work plan, helping me with the data processing and modeling, and most but not least, reviewing and helping me with my writing.

To the rest of my PhD committee, working with you all has been a pleasure. Halldór, I still remember the first day we went on the GNSS fieldtrip when you taught me how to set up GNSS stations and change a car tire. Andy, it was great to meet you in Askja in the first year. Your fruitful comments always improve the content of the manuscripts and make me think deeper.

I am grateful that I have had such a wonderful team of co-authors, who are always responsive and supportive of my work in the past few years. Ronni, thank you for all the 7 AM discussions, which guided me in the second paper. Vincent, thank you for making all these convenient web pages, sharing your scripts and InSAR results with us, which made my coding life much easier. Michelle, there was never a delay from you sending me your results, even though you were busy. Sigrún, you really saved me from debugging GNSS data processing, and your comments on the manuscripts are always helpful. Benni and Kristín, it's wonderful to have you on the team, who supported me a lot on the seismicity data and plotting.

I'll miss the scientific environment and the people here in the Askja building at University of Iceland. The Wednesday meetings, Thursday remote sensing lectures, and Friday seminars taught me a lot in the past few years. It is my honor to meet everyone, especially Páll, Bryndis, Magnus, Gro, Ásta, Erik, Disa, Finnur, Guðfinna, Eyjólfur, Thora, and Þorsteinn, who are so nice and willing to help. Special thanks to Sveinbjörn, who I think is the best technician I have ever met! A field trip with you has always been so much fun. Thanks to Anna Jona, you are always so understanding.

It's a great pleasure to meet all my friends in both Askja and elsewhere, Cécile, Alberto, Chiara, Sonja, Vincent, Deirdre, Revathy, Erna, Barbara, Ed, Maja, Eemu, Tobias, Oliver, Mary, Talfan, Joaquin, Mylene, Mariel, Quinten, Hannah, Daniel Juncu, Daniel Ben-Yehoshua, Syd Ney, Louise, Nína, Maarit, Greta, Rob, Kate, Liz, Hanna, Félix, Zena, Martin, Sébastien, Sara, Cat, Maxwell, Jessica, Mark, Hugo, Iñigo, Becca, Yilin, Hanna, Ólafur, Josefa, and all the others. With you all, my Ph.D. life was so smooth and happy :D Also, I'd like to thank friends I met outside Askja, Hjördís, Kristlaug, Þór, María, and Ester. It's nice to meet you here in Iceland.

Thank you to the Chinese community in Iceland, who was there to help me with my homesickness. Thanks for the support from Jin Zhijian, Duan Junlong, Li Tong, Bu Jun,

Qi Huimin, Jia Yucheng, Zhou Lan, Yang Tao, and Cui Yang. Thanks for accompanying me in Iceland: Zheng Tingting, Anton, Yang Shu Yang, Miao Yu, Yi Zhiqian, Xiao Han, Meng Xue, Jiang Mengxu, Tian Yujie, Zhang Zichun, Yuetuan, Xu Maonian, Ji Xiang, Zhao Bin, Lu Yi, Wang Hang, Wei Yiran, Zhang Li, Geng Ming, Fu Lidan, Zheng Yiqun, Ge Fenfen, Wang Qiong, Song Huan, Zhou Lijing, Wu Yixiao, Li Mengyu, and all the others, thank you!

Last but not least, I would like to thank my family, for all their love, encouragement, care, and support. I'm really grateful that they stopped asking me about my PhD progress, and when I will finish my papers. I miss the amazing food made by everyone in my family: my parents, grandparents, uncles, and aunts.

This PhD project was funded by the Research Fund of University of Iceland, and the European Commission, through H2020 EUROVOLC project (Grant No. 731070).

# 1 Introduction

Crustal deformation studies can improve understanding of crustal layering and magma movements in the subsurface. In volcanic areas, crustal deformation signals arise, e.g., from earthquakes, magma accumulation, dike opening, rifting events, and geothermal production. Ground displacements due to these processes add to displacements generated by more regional ground deformation, that in Iceland primarily originates from plate boundary deformation processes and glacial isostatic adjustment (GIA). When interpreting observed ground deformation, a critical step is to separate the contribution of the different processes involved.

Post-eruptive deformation following volcanic eruptions may originate from renewed magma inflow, or Earth adjustment due to co-eruptive events. The latter is usually referred to as viscoelastic relaxation. The post-eruptive deformation signal is critical in forecasting the future of a volcano, as magma accumulation could be an indication for another eruption, such as in the Krafla Fires in 1975-1984, when a series of diking and eruption occurred. As magma accumulation may not be the only explanation for post-eruptive unrest at volcanoes, more study of processes such as viscoelastic relaxation is needed.

This project studies crustal deformation in Bárðarbunga volcanic system to improve understanding of the deformation observed there after the 2014-2015 Bárðarbunga-Holuhraun eruption. The study period is between March 2015 and August 2021. Before our study period, the Bárðarbunga-Holuhraun eruption terminated in February 2015, and after our study period, surface uplift began at the Askja volcano, suggesting magma inflow. This study uses two types of space geodesy techniques to measure ground deformation: Global Navigation Satellite Systems (GNSS) and Interferometric analysis of Synthetic Aperture Radar satellite images (InSAR).

The following sub-chapters briefly introduce the measurement techniques (GNSS and InSAR) and the models used in the study. This is followed by introducing the Bárðarbunga volcanic system and the 2014-2015 eruption. The last section of the Introduction gives an overview of the work carried out. Chapters 2-4 present summaries of three papers, which form the basis for this PhD thesis. Chapter 5 concludes the thesis.

## 1.1 Space-geodetic measurements at volcanoes

Geodesy is a science that focuses on understanding the Earth's geometric shape and size, movements on the Earth, and the gravity field (e.g., Vanicek and Krakiwsky, 2015). Geodesy is capable of monitoring the Earth at various scales, from the tides of the Earth and plate movements, to events such as the movement of a single building. Geodesy is

widely used to monitor the surface movement around a volcano, to improve understanding of processes such as movements of the magma in the subsurface (e.g., Biggs et al., 2010; Euillades et al., 2017), or to monitor the post-emplacement contraction of lava (e.g., Stevens et al., 2001; Wittmann et al., 2017).

There are a variety of geodetic measurement techniques that are applied in volcano monitoring (Dzurisin, 2006), including:

- Electronic distance measurements (EDM), which measures the distance between two benchmarks installed on the ground.
- Leveling, which measures the height difference between benchmarks along a leveling line.
- Tilt observations, which can continuously record ground inclination of the Earth's surface.
- Strainmeters, which measure changes in the strain of the subsurface, sometimes done by measuring the relative displacements between two separate points.
- GNSS, which measures the three-dimensional position of a benchmark continuously or intermittently.
- InSAR, which measures the displacement field change between the measuring times in the line-of-sight (LOS) direction, from ground to satellite, over an area.

The following gives an introduction to two satellite-based geodesy techniques: GNSS and InSAR.

### 1.1.1 GNSS

Global Navigation Satellite Systems (GNSS) use satellites to position points on the ground where specific instruments are located. The satellites transmit electromagnetic signals that travel at the speed of light. GNSS receivers measure the signal travel time from the satellite to the receiver, enabling the calculation of the distance between the satellites and the ground instrument. A satellite constellation with satellites in different orbits makes it possible to determine the position of the ground instrument in three dimensions (3D) (e.g., Seeber, 2008; Dzurisin, 2006). Ground displacements are inferred by calculating station positions at different times (Dzurisin, 2006). GNSS constellations include the Global Positioning System (GPS, owned by the United States), GLONASS (Russian), Galileo (European Union), and Beidou (China; Hofmann-Wellenhof et al., 2007).

GNSS ground instruments need an antenna, that receives the satellite signal, and a receiver, which collects the data (Figure 1.1). GNSS measurements are divided into continuous and campaign measurements. Both are commonly used to measure displacements in volcanic areas. A continuous GNSS station has equipment placed at a site that continuously collects data over the years. The first continuous station in the study area of this thesis was installed in 2002 (Figure 1.2; Geirsson et al., 2010). For campaign GNSS stations, a benchmark is installed on-site as a reference and visited intermittently. Equipment is set up temporarily, typically only for a few days. The

station is revisited later, and the measurement is repeated (Figure 1.2; Árnadóttir et al., 2009). Campaign measurements were carried out at GNSS stations around the Bárðarbunga volcano in 1997, 2002, 2006, 2010, and 2014, before the 2014-2015 Bárðarbunga-Holuhraun eruption (Li et al., 2021). After that, field measurements were carried out yearly between 2014 and 2020, in expeditions from the University of Iceland.

Data collected by the GNSS receivers are referred to as raw data. The raw data can be converted into Receiver INdependent EXchange (RINEX) format data, a data interchange format for GNSS data processing. Some receivers record the received satellite signal directly into RINEX format.

GAMIT/GLOBK is one of the available software for precise GNSS data processing (Herring et al., 2010; Hreinsdóttir et al., 2009). The derived coordinates of a GNSS station are inferred at different times to form time series. Linear fitting the GNSS time series provides the average velocity of the station measured. GNSS coordinates in this thesis are derived by analyses with the GAMIT/GLOBK software, and the data are referenced to the International Terrestrial Reference Frame 2014 (ITRF2014; Altamimi et al., 2012). Coordinates in the ITRF2014 reference frame can be transformed into a reference frame fixed to a stable plate interior, such as the Eurasian reference frame (Altamimi et al., 2012).

Some GNSS time series from continuous and campaign GNSS sites in the Bárðarbunga area span more than ten years (Figure 1.3). Continuous GNSS station KISA is the closest to the Bárðarbunga caldera (see Figure 1.2 for location) installed during the 2014-2015 eruption. Time series from this station show well post-eruptive displacements, suggesting northwestward displacement and uplift in 2015-2022. DYNC continuous station has a long history since 2008, revealing pre-, co-, and post-eruptive deformation. At DYNC, the 2014-2015 Bárðarbunga-Holuhraun eruption causes northwestward displacement during the diking period, southwestward displacement during the eruption northwestward displacement after the eruption. The vertical component shows subsidence in the co-eruptive period, while no significant velocity change is observed in the post-eruptive period compared to the pre-eruptive period.

The GNSS measurements and data analysis in Iceland is based on an extensive collaboration of a number of institutes. Installation of continuous GNSS receivers has received funding from various institutes and universities, e.g., the Icelandic Research Fund (IRF) handled by the Icelandic Centre for Research (RANNÍS) and the National Science Foundation (NSF) in the USA. The Icelandic Meteorological Office (IMO) operates the continuous stations, while researchers at University of Iceland visit the campaign sites. I led the campaign measurements from 2017 to 2020 in the study area of this thesis with technician Sveinbjörn Steinþórsson at the Institute of Earth Sciences, University of Iceland. The GNSS processing facility at the University of Iceland is named Strokur, maintained by Halldór Geirsson and Sigrún Hreinsdóttir (GNS Science, New Zealand). Halldór's automatic GNSS processing uses GIPSY ([https://notendur.hi.is/hgeirs/iceland\\_gps/icel\\_100p.html](https://notendur.hi.is/hgeirs/iceland_gps/icel_100p.html)). Sigrún also runs GAMIT processing for the continuous stations (<https://strokur.raunvis.hi.is/gps/#CHIL>). IMO runs automatic data processing from continuous GNSS stations (led by Benedikt G. Ófeigsson), with results available at <https://hraun.vedur.is/gps/>. I analyzed the campaign GNSS measurements within the framework of this PhD study with the GAMIT/GLOBK software. The time series from continuous GNSS shown in this thesis are from the data



*Figure 1.1. (a) Campaign and (b) continuous GNSS equipment set up in the field. For campaign GNSS (a), an antenna is installed on a tripod, above a benchmark, typically measured yearly or every few years. A receiver is connected to the antenna (inside the black box) to shelter it from bad weather. Continuous GNSS in Iceland (b) typically has an antenna installed on a quadropod. The receiver is in a box, connected to electricity. In Iceland, the continuous GNSS stations normally obtain electricity from a wind turbine and a solar panel.*



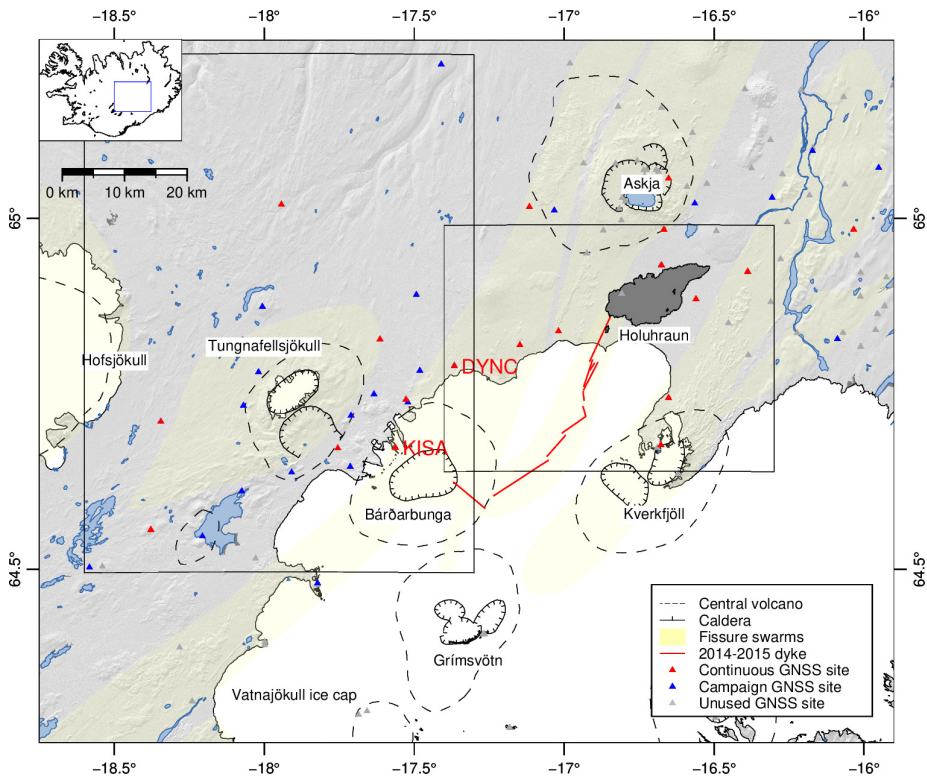
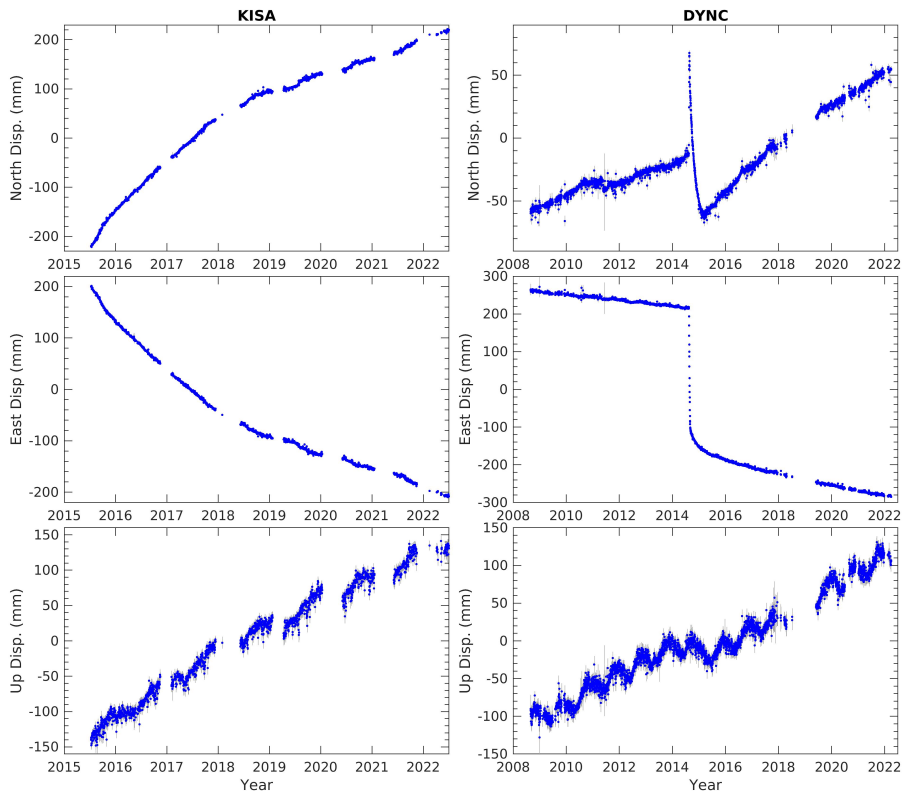


Figure 1.2. Map view of the Bárðarbunga volcanic system and surroundings showing central volcanoes, calderas, and fissure swarms (for geological layers, see Sigmundsson et al. (2020a) and references there-in). White areas are the glaciers. Segments of the 2014-2015 dike path are indicated with red lines (Sigmundsson et al., 2015), and the 2014-2015 Holuhraun lava field is shown with dark gray shading. Blue and red triangles are campaign and continuous GNSS stations, respectively. The two rectangular boxes are the study areas in the first two papers of this thesis.

analysis by Sigrún Hreinsdóttir.



*Figure 1.3. GNSS time series collected at GNSS station KISA (left, 2015-2022) and DYNC (right, 2008-2022) reference to the Eurasian plate. Displacements in the north (top), east (middle), and up (bottom) components are shown in mm, with an arbitrary shift for displaying purpose, so the middle of each displacement scale is at 0. The positions of the continuous GNSS stations are processed with GAMIT/GLOBK. The horizontal axis shows time in years. GNSS time series analysis from Sigrún Hreinsdóttir, translated to stable Eurasian plate reference and replotted.*

### 1.1.2 InSAR

Satellites with Synthetic Aperture Radar (SAR) form the basis for an active remote sensing data collection technique. SAR satellites transmit electromagnetic signals that are reflected off the ground, and received back by the SAR satellites. The frequencies selected for SAR are lower than light, enabling the signals to penetrate clouds, providing "visibility" in bad weather conditions and darkness (e.g., Dzurisin, 2006). Three frequency bands are commonly used for ground deformation monitoring: X band (8-12

GHz), C band (4-8 GHz), and L band (1-2 GHz) (Lu and Dzurisin, 2014).

After initial processing, the reflected signals are saved as SAR images, including the amplitude and phase of the reflected signal at each pixel location. The phase depends on records the distance between the satellite and the ground. Satellites repeat their orbit and acquire images over the same area of the Earth at different times. With two images taken from the same track, one can calculate the phase difference between the two acquisition times for each pixel on the ground, which is influenced by the displacement of the ground in the intervening time. This difference image is called an interferogram, and the technique is referred to as Interferometric analysis of Synthetic Aperture Radar (InSAR) satellite images. Interferograms show changes in length from the ground to satellite, or in other words, the displacement in the LOS direction, in addition to several sources of noise (e.g., Dzurisin, 2006).

LOS displacements have different look directions, depending on whether the images are collected from an ascending satellite track (satellite moving from south to north; towards the north pole), or descending track (satellite moving from north to south). Different look angles enable decomposition of the LOS displacement into the displacement in the east and up directions, when imaging is available in both descending and ascending satellite orbits. LOS displacements have inherent very little sensitivity to ground displacements in the north direction. The decomposed displacements can provide approximate estimates of east and up components of displacements and can be referred to as near-east and near-up components (Drouin and Sigmundsson, 2019).

A number of satellites and satellite constellations have been launched for SAR imaging, including ERS-1/2, JERS-1, ENVISAT-ASAR, RADARSAT-1/2, ALOS-1/2, Cosmo-SkyMed, TerraSAR-X, TanDEM-X, RISAT-1, Sentinel-1, and Gaofen-3 (Hamazaki, 1999; Misra et al., 2006; Musa et al., 2015; Zhang and Liu, 2019). This PhD study uses mainly data from the Sentinel-1A and -1B satellites for InSAR analyses. At the beginning of this PhD, I processed both Sentinel-1 and TerraSAR-X interferograms. The InSAR time series and average velocity fields used in the publications are from Vincent Drouin at the IMO.

The Sentinel-1 satellites are part of the Copernicus Programme of the European Space Agency. The Sentinel-1 mission consists of two polar-orbiting satellites, which provide free-available, open-access SAR images for land monitoring (Torres et al., 2012). Four tracks cover the area around the Bárðarbunga volcano (Figure 1.2), two ascending and two descending tracks. Tracks 9 and 111 are descending tracks, and tracks 118 and 147 are ascending tracks.

The Sentinel-1 SAR images have been processed with the InSAR Scientific Computing Environment (ISCE) software (Rosen et al., 2012). The phase difference calculated from the two SAR images creates a wrapped interferogram (Figure 1.4a). Each fringe, i.e., one full-color cycle from red to purple and then back to red, corresponds to half the wavelength of the electromagnetic signal transmitted by the satellite (since it relates to the two-way travel time from the satellite to the ground). For the Sentinel-1 satellites, one fringe corresponds to 2.83 cm LOS displacement. An interferogram can be "unwrapped," giving cumulative range change from a reference point (e.g., in meters) instead of fringes. The product is referred to as an unwrapped interferogram (Figure 1.4b).

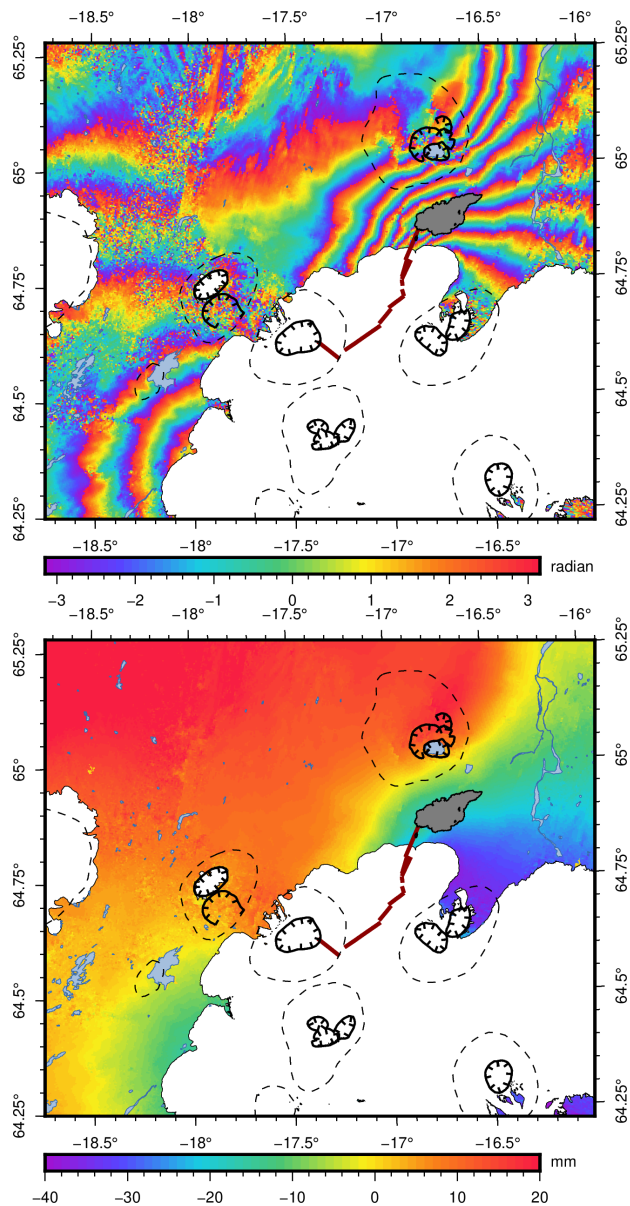


Figure 1.4. Wrapped (upper) and unwrapped (lower) interferogram in the area in Figure 1.2 measured by InSAR. The time span of the interferogram (the acquisition times of the two SAR images used to form the interferogram) is from 09 July 2015 to 02 June 2022. Based on Sentinel-1 images from Track 9. The area with blurry fringes in the wrapped images is called incoherence, normally due to changes in the reflector on the ground. For wrapped interferogram calculated from Sentinel-1 images, one fringe ( $-\pi$  to  $\pi$ ) corresponds to 2.83 cm.

## 1.2 Plate spreading and glacial isostatic adjustment (GIA)

Before interpreting the observed ground displacements in terms of magmatic processes, it is necessary to correct background displacements. Around the Bárðarbunga volcanic system, the main background signals are caused by plate spreading and glacial isostatic adjustment (GIA).

Iceland is located at the divergent plate boundary between the North American Plate and the Eurasian Plate. The plates are moving apart in the direction of  $N(100-105)^{\circ}E$  (Sigmundsson et al., 2020a). Drouin and Sigmundsson (2019) studied the average velocity field over Iceland with InSAR and derived a plate spreading model with a spreading rate of 18-19 mm/yr in the Bárðarbunga area (Figure 1.5).

The GIA process has been well documented around the world, from studies of ongoing ground uplift in areas formerly glaciated during the Pleistocene (e.g., Peltier et al., 2015). A common assumption in many GIA studies is that the Earth's behavior can be described by a Maxwell material (Peltier, 1974). During the Weichselian glaciation, Iceland was covered by glacier with a size larger than current Iceland. The post-glacial rebound at the end of the Weichselian deglaciation has been estimated to be completed in about 1000 years, constraining viscosity below an elastic layer to be  $1 \times 10^{19}$  Pa s or less (e.g., Sigmundsson, 1991).

The retreat of glaciers after the "Little Ice Age" in Iceland, since 1890 generates a clear GIA signal, with uplift and horizontal displacement away from glaciers observed by GNSS and InSAR (e.g., Árnadóttir et al., 2009; Auriac et al., 2013; Auriac, 2014; Drouin and Sigmundsson, 2019). A GIA model fitted to GNSS and InSAR data by Auriac (2014) suggests the GIA signal had a maximum uplift rate of 22 mm/yr and maximum horizontal velocity of 2 mm/yr in 2008-2010 in the area shown in Figure 1.2. When predicted ground displacements according to this model are compared to more recent GNSS and InSAR observations, it is evident that observed ground velocities are higher than observed. GIA velocities have been fluctuating in recent years, including accelerating but also some slowing down (e.g., Belart et al., 2020; Compton et al., 2015; von Hippel and Harig, 2019). A simple estimation of the GIA signal in our study period is to scale the GIA model from Auriac (2014) with a scaling factor (Figure 1.6).

## 1.3 Volcano deformation source models

Geodetic models are used to simulate the deformation field caused by magma movements in volcano roots, providing essential information when interpreting observed crustal deformation. Volcano deformation models are often based on a number of assumptions to simplify the calculation, such as the assumption of homogeneous isotropic material in the Earth layers (e.g., Battaglia et al., 2013). Inversion of geodetic data to infer the deformation source gives an estimate of the parameters of the magma source, such as the source depth and magma inflow volume, which is crucial for volcano monitoring and disaster prediction.

A selection of volcano deformation models is presented in the following, which

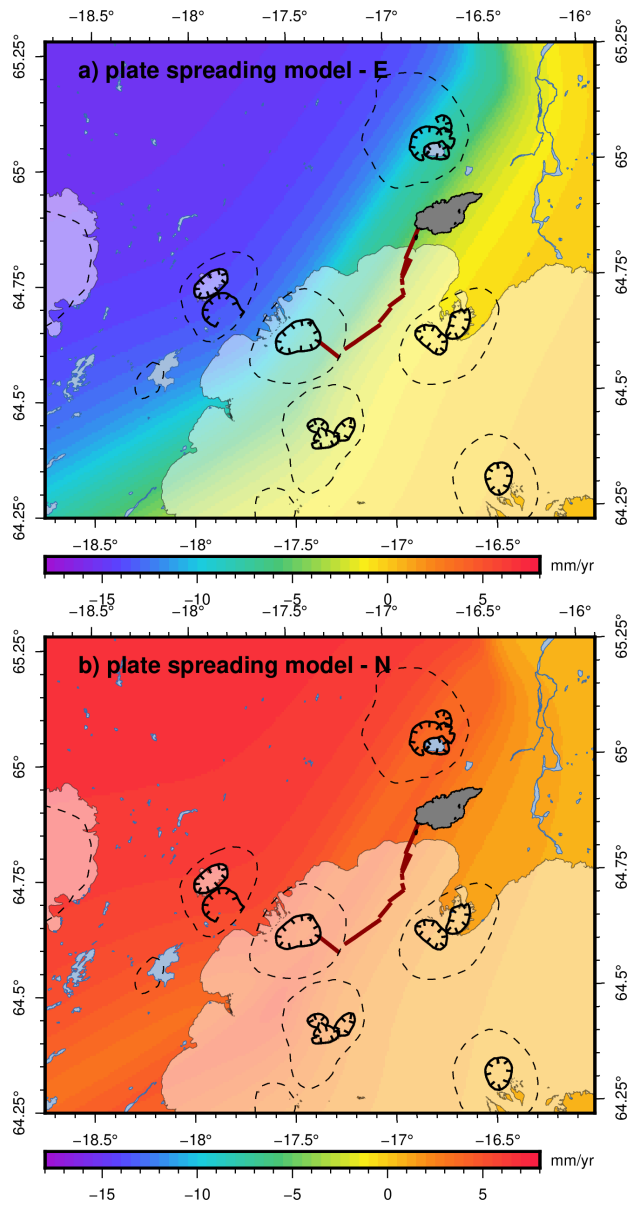


Figure 1.5. East (a) and north (b) displacement rate of plate spreading model in the area shown in Figure 1.2. Model is from Drouin and Sigmundsson (2019).

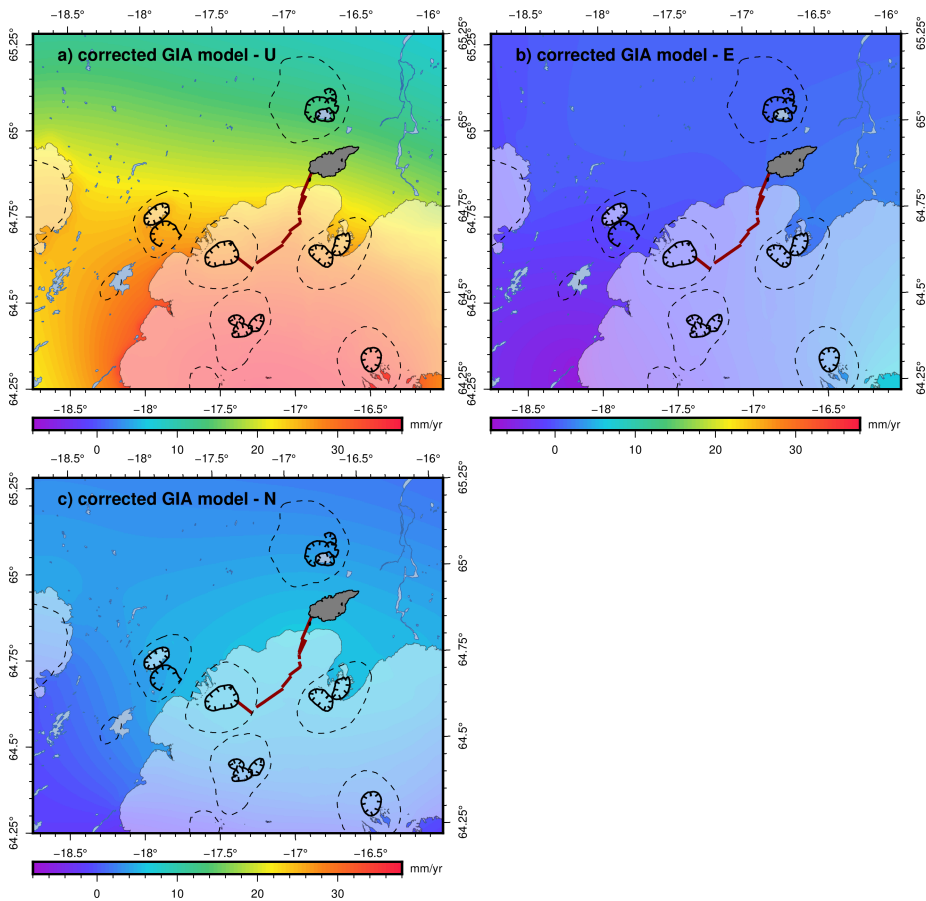


Figure 1.6. Uplift (a), east (b) and north (c) rate of scaled GIA model in the area shown in Figure 1.2. The GIA model is a scaled version from Auriac (2014), with a scaling factor of 2.8 for horizontal and 1.5 for vertical components from Li et al. (2021).

have been utilized in this PhD work. The models divide into two categories: elastic and viscoelastic deformation. Elastic models refer to models under the assumption of elastic host rock material, which deforms immediately in response to magma movement. Three elastic deformation models are introduced considering three different geometries for the deformation source, the so-called Mogi, Okada, and penny-shaped crack model. Viscoelastic deformation models refer to models that are at least partly with a viscoelastic material. The viscoelastic deformation processes last long, e.g., significant viscoelastic relaxation to an eruption can last for years or decades after an eruption ends.

### 1.3.1 Elastic models

Elastic models here refer to deformation models where a deformation source is located within an otherwise linearly homogeneous isotropic flat half-space, neglecting complications in subsurface structure and surface topography. These basic models are able to explain many geodetic observations, even though they are based on many simplifications. Three elastic models discussed here have different shapes of the deformation source, which can, e.g., describe the effects of a pressure change in magma bodies with different geometries (e.g., Battaglia et al., 2013).

A model referred to as the Mogi model was proposed by Mogi (1958) to simulate deformation resulting from a point pressure source (Figure 1.7a). When the source radius is significantly smaller than the depth of the source, it can be treated as a point source. McTigue (1987) provides a more comprehensive analytical solution, which also includes the situation when the source is close to the surface.

The equations to calculate the surface displacement for the Mogi model can be written as (e.g. Lisowski, 2007)

$$\begin{pmatrix} u \\ v \\ w \end{pmatrix} = a^3 \Delta P \frac{1-\nu}{G} \frac{1}{R^3} \begin{pmatrix} x \\ y \\ d \end{pmatrix}. \quad (1)$$

Here  $\nu$  is Poisson's ratio,  $G$  is the shear modulus,  $a$  is the radius of the source, and  $\Delta P$  is the pressure change in the cavity. The source center is at  $(0, 0, -d)$  where  $d$  is the source depth. The observation point is at  $(x, y, 0)$ .  $R$  is the distance from the source center to the observation point,  $R = \sqrt{x^2 + y^2 + d^2}$ .  $(u, v, w)$  is the surface displacement in the  $x$ ,  $y$ , and  $z$  directions. The volume contraction of the spherical deformation source  $\Delta V$  is

$$\Delta V \cong \frac{\Delta P}{G} \pi a^3 \quad (2)$$

when the source radius is significantly smaller than the source depth. Equation 1 can also be written as

$$\begin{pmatrix} u \\ v \\ w \end{pmatrix} \cong \Delta V \frac{1-\nu}{\pi} \frac{1}{R^3} \begin{pmatrix} x \\ y \\ d \end{pmatrix}. \quad (3)$$

A point source is the simplest geodetic model to describe an inflation/deflation source. Except for the elastic parameters that are needed to define the strength of the subsurface, a minimum of four independent parameters are needed to define the source: three



parameters to define the source location ( $x$ ,  $y$  and  $d$ ), and one parameter for the source strength.

Okada (1985) introduced a suite of analytical solutions to explain deformation caused by fault movements, rectangular dike intrusion, or sill inflation (Figure 1.7b). The model assumes the dike/sill opens uniformly on a rectangular dislocation plane. The model requires ten source parameters: source location ( $x$ ,  $y$ , and  $d$ ), dike/sill length, width, opening, strike, strike-slip, dip-slip, movement, and opening. If only opening is allowed on the dislocation plane, there are eight parameters.

Fialko et al. (2001) presented a horizontal penny-shaped crack model to describe magma inflow/outflow to/from a horizontal sill (Figure 1.7c). The pressure is uniformly distributed on the boundary of the penny-shaped crack. Constructing the magma body requires five parameters: source location ( $x$ ,  $y$  and  $d$ ), radius ( $a$ ), and volume change of the sill ( $\Delta V$ ).

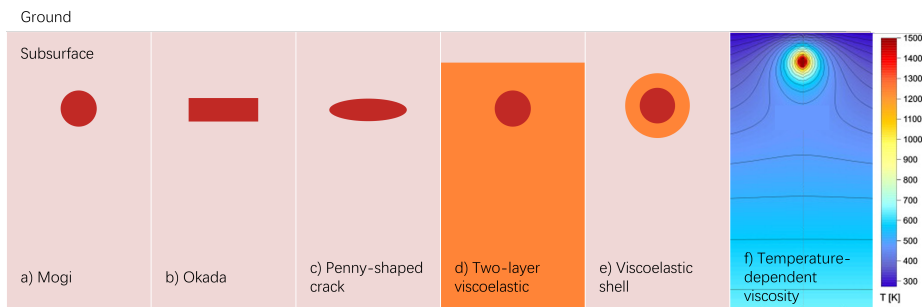


Figure 1.7. Sketches of deformation source models discussed, in cross-sections. The elastic magma models are: a) pressure point source (Mogi model), b) Okada dislocation model, and c) penny-shaped crack sill model. The viscoelastic models are: d) a two-layer viscoelastic model, e) a viscoelastic shell around a spherical source, and f) a temperature-dependent viscoelastic model (panel f is modified from Del Negro et al. (2009)). In panel a-e, red indicates the magma body, light pink indicates elastic material, and orange is viscoelastic material. The two-layer viscoelastic model (panel d) considers an upper elastic layer and a lower viscoelastic half-space. Contour lines in panel f show different temperatures, and the viscosity is a function of that in temperature-dependent viscosity models.

### 1.3.2 Viscoelastic deformation models

Viscoelastic material exhibits both elastic and viscous characteristics. Elastic material deforms as a spring, with an instantaneous response to the applied force. Viscous material deforms as a dashpot, where the applied force is resisted by viscous friction, causing gradual response of the dashpot (over time) to the applied force. Viscoelastic material is a combination of both elastic and viscous material. Viscoelastic response of the Earth is considered in geoscience in many situations, such as describing GIA (e.g., Auriac et al., 2013; Barnhoorn et al., 2011; Pagli et al., 2007a), analyzing post-seismic ground deformation (e.g., Nur and Mavko, 1974; Puskas et al., 2007), and

describing the Earth structure, in particular the brittle-ductile boundary (e.g., Ellis and Stöckhert, 2004; Lavallée and Kendrick, 2021; Lavier et al., 2013). Viscoelastic behavior may be particularly important to consider at volcanoes, as relatively shallow depth of the brittle-ductile boundary, the high temperature around a magma body, or the temperature-dependent subsurface may lead to significant viscoelastic responses at volcanoes, e.g., due to magma movements. Maxwell viscoelastic material is used here. The mechanical analog of the material is a spring and dashpot connected in series. It has both instantaneous response dependent on elastic parameters, and long term response influenced by the viscosity of the material.

Viscoelastic volcano modeling mainly uses three types of models: 1) a layered viscoelastic model with an elastic layer on top of one or more viscoelastic layers (Figure 1.7d), 2) a uniform viscoelastic shell around a magma body (Figure 1.7e), and 3) temperature-dependent viscoelastic subsurface structure (Figure 1.7f). Some studies use more complex geometries, such as by Carbotte et al. (2020), considering a melted mush below a magma reservoir.

Some studies use a layered subsurface model to simulate the different properties at depth, similar to that used in the GIA studies (e.g., Auriac et al., 2013; Barnhoorn et al., 2011; Pagli et al., 2007a). The layered viscoelastic model normally considers a 2-3 layer structure consisting of a homogeneous material in each layer, based on the idea that the hot lower crust and mantle behave viscoelastically due to their temperature. The models typically consider an elastic layer on top of one or two viscoelastic layers, where the elastic layer represents the upper crust above the brittle-ductile boundary, and the lower layers represent the lower crust as well as the upper mantle (e.g., Foulger et al., 1992; Hamling et al., 2014; Yamasaki et al., 2020). For explaining the 1987-1992 post-eruptive deformation at the Krafla volcanic system, Iceland, Hofton and Foulger (1996) suggest the best fit model consisting of two layers: a 10 km thick elastic layer on top of a  $1.1 \times 10^{18}$  Pa s viscoelastic half-space. Hamling et al. (2014) monitored the surface displacement after the 2005 intrusion episode around the Dabbahu rift in Afar. Their two-layered, semi-analytical, elastic-viscoelastic model is insufficient to reproduce horizontal and vertical deformation fields. They conclude that both viscoelastic relaxation and magma movement are needed to explain their observations. Yamasaki et al. (2020) use a two-layer model to study uplift before and after the 1914 eruption of Sakurajima volcano. The viscoelastic model suggests a lower post-eruptive inflation rate than an elastic model.

Models considering a viscoelastic shell around the magma body within an otherwise elastic half-space are also used, to simulate a thermal metamorphic shell surrounding a magma chamber (e.g. Bonafede et al., 1986; Dragoni and Magnanensi, 1989; Segall, 2010, 2016). The study by Novoa et al. (2019) finds a viscoelastic model can explain up to 50% of the accumulated surface displacement during the 2007-2017 surface uplift at Laguna del Maule, Chile. To study the 1997 inflation at the Long Valley Caldera, USA, Newman et al. (2006) uses a prolate spheroid geometry source with a viscoelastic shell model to explain the inflation episode. The viscoelastic model requires a maximum pressure change of 14.3 MPa, which is smaller than an elastic model, which requires pressure change of 45 MPa.

Some studies construct a thermal-mechanical model to represent the temperature-dependent viscoelasticity of the subsurface (e.g., Scandura et al., 2007; Gregg et al.,

2013; Hickey and Gottsmann, 2014). For the 1993-1997 inflation at the Etna volcano in Italy, Del Negro et al. (2009) used a 3D temperature-dependent viscoelastic model. The authors conclude that a viscoelastic model requires a 200 MPa pressure increase to explain the uplift, while an elastic model requires a 300 MPa pressure increase. To explain the same inflation-like displacement, a viscoelastic relaxation model requires less pressure increase than an elastic model. In the study by Masterlark et al. (2010), it is concluded that an elastic subsurface has difficulty in explaining the 1997 co-eruptive subsidence at Okmok volcano, USA, as it requires a deflation source that exceeds the lithostatic pressure constraint. A magma body with the mass flux rate of  $4.2 \times 10^9$  kg/d with a viscoelastic rind best predicts the InSAR displacements. Morales Rivera et al. (2019) explain the 2010-2011 unrest deformation at Taal volcano using a temperature-dependent spatially varied viscoelastic model. Their best-fitting viscoelastic model has a shallow magmatic source overlain by an extensive hydrothermal system, which provides a better explanation than a simple elastic model.

### 1.3.3 Modeling strategy

GIA studies indicate that viscoelastic show that ice retreat since 1890 is causing large deformation in our study area. Therefore, it is appropriate to consider if magma movements may similarly lead to viscoelastic response to the Earth. The role of viscoelastic relaxation of stresses around magma bodies where accumulation of magma takes gradually place in a pre-eruptive period has been studied by (Sigmundsson et al., 2020b). We here explore if simple viscoelastic models of response to co-eruptive large-scale magma transfer can explain observed deformation in a post-eruptive period. Alternative models, relating post-eruptive ground movements to elastic response to magma inflow or a combination of magma inflow and viscoelastic response, are also explored. Purely elastic response to magma inflow or purely viscoelastic response to co-eruptive magma movements can be considered two end-member type of models to explain deformation in a post-eruptive period.

Most GIA studies in Iceland used a two- or three-layer viscoelastic structure, with an elastic layer lies on top of a viscoelastic half-space, or on top of two viscoelastic layers (e.g. Auriac et al., 2013; Pagli et al., 2007a). The depth extent of tectonic earthquakes also indicates brittle-ductile transition in the crust. Therefore, the viscoelastic relaxation modeling in this PhD project considers a similar structure as the GIA studies. The two-layer model has an elastic layer on top of a Maxwell viscoelastic half-space, with a linearly homogeneous isotropic material in each layer. Post-eruptive volcano deformation models utilizing such rheological layering to explain localized volcano deformation have for example been evaluated by Yamasaki et al. (2020, 2022).

The open-source three-dimensional semi-analytical software RELAX (Barbot, 2014; Barbot and Fialko, 2010a,b) is used to infer the viscoelastic response to deformation sources, such as pressure point source, opening, and dislocation planes, in a two-layer structure as explained above. The software utilizes that displacements in an elastic material due to slip and opening on dislocation planes, or radial displacements on a point source, can equally be modeled as response to a set of force moments and tractions at the sources (Barbot, 2014; Aki and Richards, 2002). This equivalent body-force representation of deformation processes (Barbot et al., 2009) is used in RELAX. The

software evaluates the displacement and stress throughout Earth layers as a function of time. The numerical calculation is based in the Fourier-domain using Green's function. A number of studies have used RELAX to calculate co- and post-seismic deformation (e.g., Barbot et al., 2009; Qiu et al., 2019; Tian et al., 2020).

## 1.4 The Bárðarbunga volcanic system and the 2014-2015 Bárðarbunga-Holuhraun eruption

The Bárðarbunga volcanic system is located in the Eastern and Northern Volcanic Zones of Iceland, with a considerable part of the system under the northwestern part of the Vatnajökull ice cap (Sigmundsson et al., 2020a; Thordarson and Höskuldsson, 2008). The volcanic system (Figure 1.8) has two central volcanoes, Bárðarbunga (2000 m a.s.l.) and Hamarinn, and a fissure swarm, 190 km long and 25 km wide (Larsen and Gudmundsson, 2019). It extends 55 km in the NNE direction and 115 km to the SW away from the Bárðarbunga central volcano (Larsen and Gudmundsson, 2019). The caldera is ellipsoidal ( $11 \times 8$  km), 500-700 meters deep, and covered by 700-800 m thick ice Gudmundsson et al. (2016). Lava from the volcanic system has flowed far out of the fissure swarm, all the way to the south and the north coasts of Iceland (Halldorsson et al., 2008).

Tephra stratigraphy study, together with historical records and analysis of ash layers in soil and ice cores, suggest  $\sim 350$  eruptions have occurred in the system during the last  $\sim 7600$  years (Björnsson and Einarsson, 1990; Óladóttir et al., 2011), with an average of  $\sim 5$  eruptions each century. The inferred eruption frequency has varied, from 16 eruptions per 1000 years in the period 8000-7000 years ago to 80 eruptions every 1000 years in the period 2000-1000 years ago (Óladóttir et al., 2011). There were at least 26 eruptions in the last 11 centuries, including explosive and effusive eruptions (Thordarson and Larsen, 2007; Larsen and Gudmundsson, 2019). Most of the erupted material is basaltic.

A petrological study on temporally diverse eruptive units from the Bárðarbunga volcano reveals the occurrence of a multi-level plumbing system in which magma are processed at variable depths within the crust. In particular, they found temporally-invariant magma storage reservoirs at about  $7.3 \pm 2.7$  km depth (Caracciolo et al., 2020). This is consistent with depth estimates calculated for the 2014-15 Holuhraun eruption (Hartley et al., 2018). Lower crustal storage zones, located at about 17.5 km depth, are exclusively recorded in subglacial and middle Holocene samples, possibly because of a larger contribution of deep-seated reservoirs during this time, due to glacial isostatic effects (Caracciolo et al., 2020).

The Bárðarbunga central volcano is close to other volcanic systems, including the Tungnafellsjökull volcano and Grímsvötn volcano. Some studies have explored the interaction between the systems. Parks et al. (2017) suggests the 2014-2015 Bárðarbunga-Holuhraun eruption changed the stress field at the Tungnafellsjökull volcano (25 km away), causing significant earthquake activity there. Bato et al. (2018) study GPS time series at Grímsvötn and Bárðarbunga before the Bárðarbunga-Holuhraun eruption. They find a displacement rate change at Grímsvötn volcano ten months before the 2014-2015

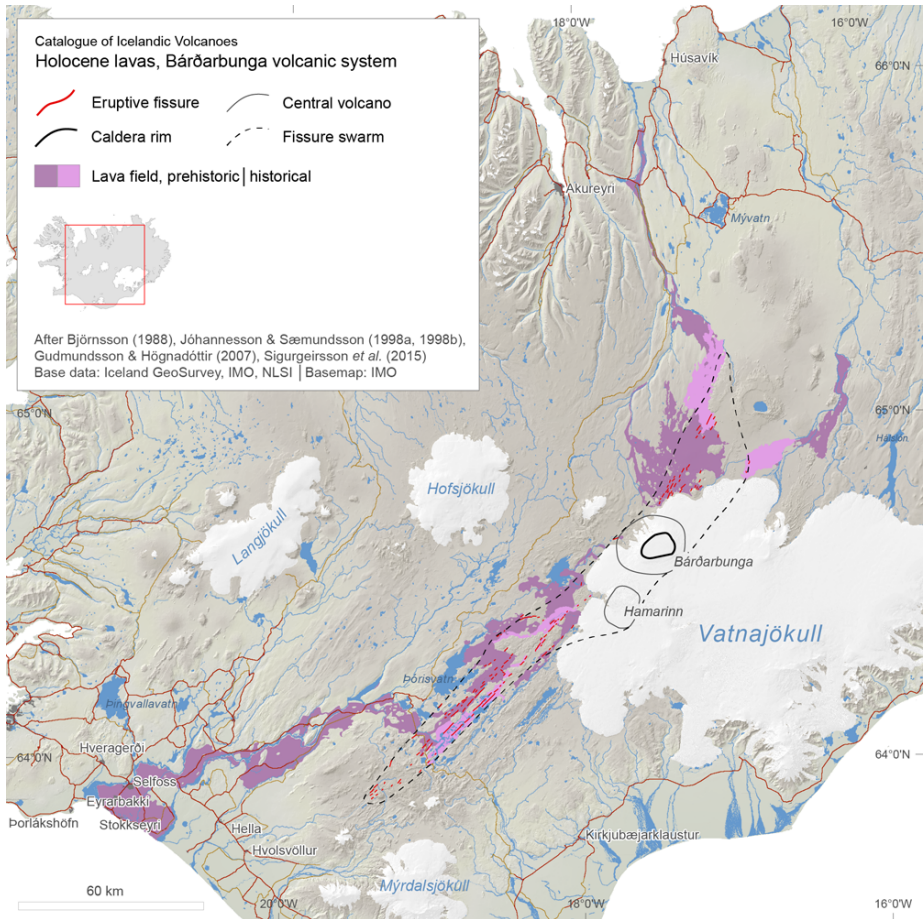


Figure 1.8. Bárðarbunga volcanic system, including the two subglacial central volcanoes (Bárðarbunga and Hamarinn), the fissure swarm, and the lava flows from the volcano. Figure is from Larsen and Gudmundsson (2019).

Bárðarbunga-Holuhraun eruption. They suggest that the magma that flows into the Bárðarbunga and Grímsvötn volcanic systems may have a connection at depth. A study for the 1996 Gjálp subglacial eruption suggests a pressure connection between the Gjálp eruptive fissure and the Bárðarbunga volcano (Pagli et al., 2007b).

Dike intrusion before the most recent Bárðarbunga-Holuhraun eruption began on 16 August 2014 with an intense seismic swarm. Seismicity started below the caldera, propagated  $\sim 7$  km towards the southeast on the first day, and then turned northeast for another  $\sim 41$  km (Sigmundsson et al., 2015). The dike propagation was mostly under the Vatnajökull ice cap, but the northernmost dike segment is north of the Vatnajökull ice cap in the Holuhraun area. On 29 August, a minor fissure eruption lasted 4 hours at the northern end of the dike (Sigmundsson et al., 2015). A major eruption began on 31 August and ended on 27 February 2015, creating a new  $84 \text{ km}^2$  Holuhraun lava field (Gudmundsson et al., 2016; Pedersen et al., 2017). GPS observation and InSAR show deformation interpreted as deflation of the caldera and dike propagation (Riel et al., 2015; Sigmundsson et al., 2015; Gudmundsson et al., 2016). The estimated total volume of magma involved in the diking and eruption is  $1.9 \pm 0.3 \text{ km}^3$ , including  $\sim 1.4 \text{ km}^3$  Holuhraun lava and  $\sim 0.5 \text{ km}^3$  magma in the dike (Sigmundsson et al., 2015; Gudmundsson et al., 2016; Pedersen et al., 2017). Three ice cauldrons formed during the eruption (Reynolds et al., 2019).

Earthquake activity in the Bárðarbunga area is monitored by IMO using the Icelandic national seismic network (Böðvarsson et al., 1999) and by temporary seismic network installations, including the collaborative operation of seismic stations by the University of Cambridge and the University of Iceland. Sigmundsson et al. (2015) interpreted the seismicity in the Bárðarbunga volcanic system between 16 August and 6 September 2014 to infer the path and the speed of dike propagation. Gudmundsson et al. (2016) studied the seismicity during the six-month-long eruption period and the relationship between seismicity and caldera collapse. A detailed study of Bárðarbunga seismicity from January 2014 to August 2015 was carried out by Ágústsdóttir et al. (2019), focusing on the seismicity at the caldera and along the dike. The depths of earthquakes within the caldera are shallower than 7.5 km b.s.l. The long-term brittle-ductile transition is interpreted to be at 4–6 km b.s.l. based on the seismic study by Ágústsdóttir et al. (2016, 2019). Jónsdóttir et al. (2019) and Rodríguez-Cardozo et al. (2021) investigate the waveforms of earthquakes in the co- and post-eruptive period. They found that the waveforms had changed polarity already two months after the eruption ceased when compared to earthquakes during the eruption, from being consistent with downward (deflation) to up (inflation) movement of the central block of the caldera. Sigmundsson et al. (2020b) argue the trigger for this eruption was accumulation of buoyant magma in viscoelastic crust over long-term, as the pre-eruptive inflation is minor compared with the erupted magma volume.

The Bárðarbunga caldera collapsed  $65 \pm 3$  m during the eruption, as inferred from a combination of radio-echo sounding, GNSS, and aerial altimeter survey (Gudmundsson et al., 2016). One-day CSK interferograms initially formed by Riel et al. (2015) constrain subsidence within the caldera and show that it was on the order of 50 cm/day at the beginning of the eruption. Using the data from moderate resolution imaging spectroradiometer (MODIS) and GPS, Coppola et al. (2017) and Gudmundsson et al. (2016) find that the temporal evolution of the caldera subsidence rate is very similar to

the temporal evolution of the effusive eruption rate. A gravity-driven inelastic magma withdrawal explains well the observed exponential decay in subsidence and eruption rates. A seismic study from Rodríguez-Cardozo et al. (2021) classified earthquakes with  $M_w$  between 3.7 and 5.5 into five event families. Three of them agree with the hypothesis that slip occurred on curved faults, one agrees with the asymmetric collapse of Bárðarbunga, and the last family may indicate a temporally stuck plug in the plumbing system or viscoelastic relaxation to the caldera collapse. Riel et al. (2015) proposed a model consistent with the InSAR, GPS, and seismic observations, suggesting that most subsidence occurs aseismically. Sigmundsson (2019) compares the characteristics of the 2014-2015 Bárðarbunga and 2018 Kīlauea caldera collapse, suggesting a dynamic relationship between the caldera collapse and rifting eruption in both cases.

Post-eruptive earthquake activity indicates a significant role slip on the caldera ring fault. Compared to the co-eruptive period, flipped polarity of focal mechanisms of earthquakes along the caldera ring fault suggests the central block within the caldera (piston) has been moving upwards in the post-eruptive period (Jónsdóttir et al., 2019; Rodríguez-Cardozo et al., 2021). Gravity surveys by Gudmundsson et al. (2020) provide additional constraints. The results can be interpreted as raising the caldera floor by several meters. Reynolds et al. (2019) modeled the fluid flow and heat transport in the uppermost 1 km of the crust, and suggested that the observed increase in geothermal activity could be reproduced by renewed magma inflow and high permeability pathways.

## 1.5 Present work

Following an eruption, a volcano may show unrest signals again, such as after the 2014-2015 Bárðarbunga-Holuhraun eruption. Measuring and modeling ground deformation in a post-eruptive period can thus improve understanding of the behavior of a volcano after an eruption. Magma inflow and viscoelastic relaxation are two possible causes of unrest. Understanding post-eruptive unrest is critical for understanding a volcano and for hazard management.

The 2014-2015 Bárðarbunga-Holuhraun eruption provides a unique opportunity to study post-eruptive deformation both at a central volcano and in the vicinity of a newly formed major dike, in particular viscoelastic relaxation and magma movements.

Data collected in the post-eruptive period can be compared with detailed observations from the co-eruptive period. The eruption progress was well monitored with multiple techniques. Tracking magma movement with seismic and geodetic observations provides constraints on geodetic models for the caldera collapse, magma withdrawal, and dike propagation.

The research carried out in this PhD project focuses on understanding the post-eruptive unrest at the Bárðarbunga central volcano and in the surroundings of the dike formed in 2014. The main research questions are:

1. How did the Bárðarbunga volcanic system deform in the post-eruptive period after its 2014-2015 eruption?
2. What is the best approach to correct observed deformation signals for GIA and plate spreading to infer deformation caused by other processes?

3. Can viscoelastic relaxation explain the post-eruptive deformation around the Bárðarbunga caldera and the dike?
4. Is it possible to distinguish between deformation caused by viscoelastic relaxation and renewed magma inflow?

The first paper, presented in section two, maps surface displacements with GNSS and InSAR to find an explanation for the post-eruptive unrest at Bárðarbunga. The post-eruptive average velocity field from GNSS and InSAR are first corrected for the background deformation processes: GIA and plate spreading. To explain the 2015-2018 velocity field, both the viscoelastic relaxation and magma inflow models are considered.

Paper two presented in section three maps the post-eruptive deformation signal along the Bárðarbunga-Holuhraun dike and uses a two-layer viscoelastic relaxation model to explain the observed deformation. The dataset includes InSAR average velocity from three Sentinel-1 tracks and GNSS average velocity from eight continuous stations. These observations are used to constrain the viscosity and elastic layer thickness in the dike area.

The third paper, presented in section four, focuses on attempts to distinguish the two processes that may be the main cause of deformation in a post-eruptive period: viscoelastic relaxation and magma inflow. The viscoelastic relaxation model has an elastic layer above a viscoelastic half-space. The magma inflow model is in an elastic half-space. The stress field and the temporal variation of the surface displacement are considered in this paper to help distinguish the two processes.

Section five gives a short summary of the work presented in this thesis.



## **2 Paper I: Ground deformation after a caldera collapse: Contributions of magma inflow and viscoelastic response to the 2015-2018 deformation field around Bárðarbunga, Iceland**

### **2.1 Summary**

The 2015-2018 deformation field around Bárðarbunga is mapped using GNSS and InSAR to explore the post-eruptive deformation field. The average velocity of the area shows horizontal displacement away from the caldera and surface uplift in 2015-2018. This study evaluated the role of viscoelastic relaxation and renewed magma inflow in the post-eruptive period.

The deformation signal caused by local volcanic processes is initially isolated from the observations by correcting for GIA and plate spreading. Auriac (2014) modeled GIA deformation signal in 2008-2010 around the Vatnajökull ice cap. A scaled version of the GIA deformation field derived by Auriac (2014) is used to correct the GIA signal in our study period. For the plate spreading deformation signal, the model by Drouin and Sigmundsson (2019) is used. After correcting these signals, the remaining deformation signal from both GNSS and InSAR suggests horizontal displacement away from the caldera. The highest deformation rate observed is at KISA GNSS station located 2.7 km away from the caldera rim. The 2015-2018 horizontal average velocity at this station is about 127 mm/yr away from the caldera, and uplift is at an average rate of about 46 mm/yr. A GNSS station 6.6 km away from the caldera shows an average horizontal velocity of about 28 mm/yr and 31 mm/yr vertically.

Two deformation processes are considered to explain the observed deformation field: 1) viscoelastic relaxation caused by co-eruptive magma withdrawal and caldera collapse, and 2) renewed magma inflow into a magma body. When modeling deformation due to these processes, homogeneous isotropic material is considered in Earth layers, with the shear modulus of 30 GPa and Poisson's ratio of 0.25.

When modeling deformation due to viscoelastic relaxation, the response to magma withdrawal and caldera collapse in a two-layer model with a 7 km elastic layer on top of a viscoelastic half-space is considered. Magma withdrawal from a point source 10 km deep below the caldera, together with the caldera collapse is modeled. By systematically varying the viscosity of the viscoelastic half-space and the volume contraction of the source, it is found that viscosity of  $3 \times 10^{18}$  Pa s and a contraction volume of  $0.4 \text{ km}^3$

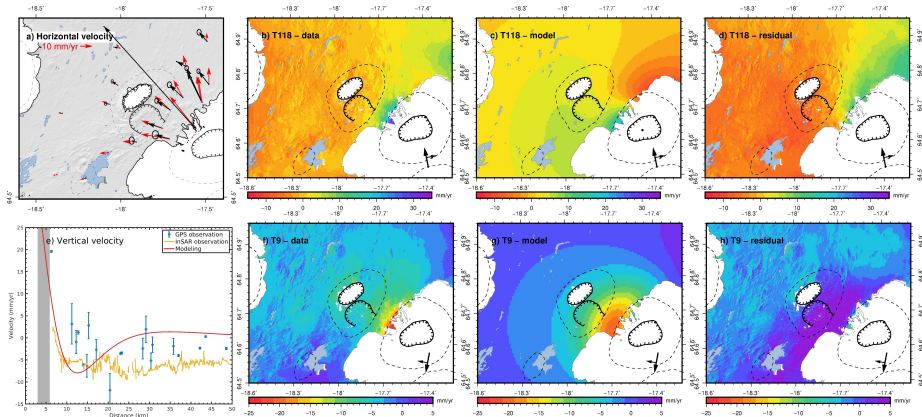


Figure 2.1. Corrected GNSS and InSAR average velocities, in the period May 2015 - October 2018, compared with viscoelastic deformation model with optimal viscosity and magma withdrawal volume. The viscoelastic model considers a contraction volume of  $0.4 \text{ km}^3$  at 10 km depth. Observed and modeled GNSS velocities in horizontal and vertical directions are shown in panels a and e. Black arrows in panel a show observations, and red arrows show the modeled velocities. The gray area in panel e is the distance range from the modeling center ( $-17.48^\circ \text{ E}$ ,  $64.63^\circ \text{ N}$ ) to the caldera rim. The figure displays InSAR input data (b and f), modeling results (c and g), and residuals (d and h). The dot in the caldera in panel c shows the modeling center of the viscoelastic model. Corrected InSAR average velocities from ascending Track 118 and descending Track 9 are compared with the viscoelastic deformation model in panels b-d and f-h, respectively.

best explains the observed deformation field (Figure 2.1). The total magma drainage volume from beneath Bárðarbunga relates only partly to this contraction volume, with an inferred larger contribution due to piston-like collapse of a block within a caldera ring fault system in relation to the caldera collapse.

For magma inflow, two possibilities are considered. One scenario considers magma inflow only. The other considers the magma inflow into the magma body under the Bárðarbunga caldera that fed the 2014-2015 eruption (at 10 km depth), together with slip-on caldera faults in such a manner that the piston inside the caldera moves upwards, i.e., the reverse process of what happened during the 2014-2015 caldera collapse and eruption. If only magma inflow is considered, a point source at 0.7 km depth below the model surface with the average inflow rate of  $0.011 \text{ km}^3/\text{yr}$  broadly fits the observations. This model with such a shallow source is not considered realistic. The other model uses the co-eruptive fault and sill patch geometries inferred by Parks et al. (2017) and inverts for the fault slip and sill openings to explain the 2015-2018 average velocity field (Figure 2.2i and j). The modeling results suggests an inflow rate of  $0.032 \text{ km}^3/\text{yr}$  at 10 km depth (Figure 2.2).

The magma inflow model is then combined with the viscoelastic relaxation model. Such a joint model can also explain the observations well.

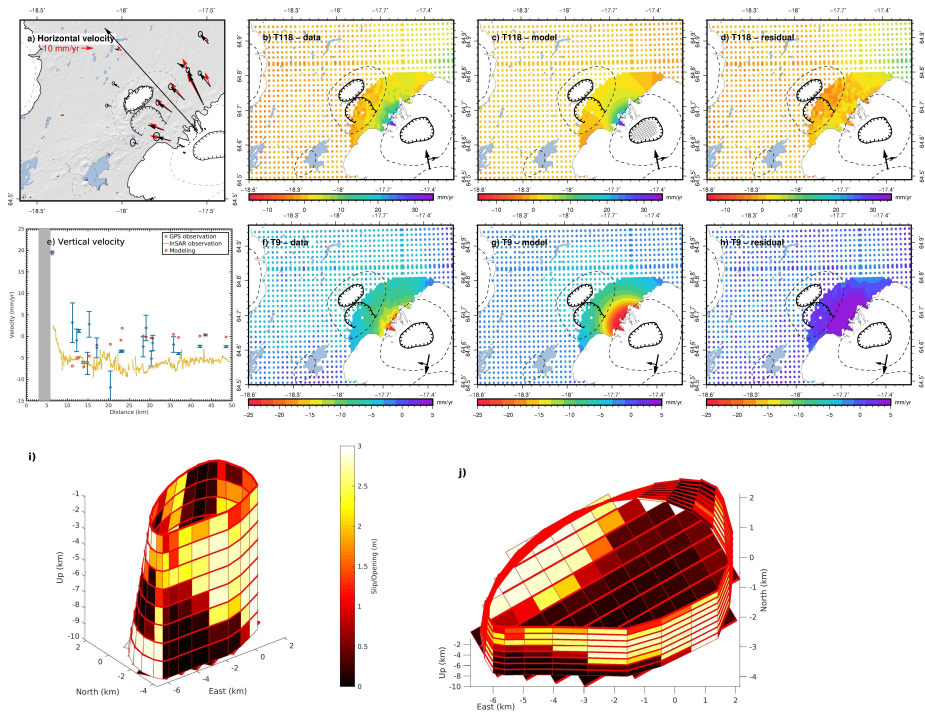


Figure 2.2. Corrected velocity fields compared with elastic modeling predictions considering a sill fixed at 10 km depth and fault slip on the caldera ring fault. The velocities are presented similarly in Figure 2.1. The input InSAR results are resampled to a grid, with dense point spacing close to the caldera and sparse points further away from the caldera. The grid within the caldera in panel c illustrates the location of the modeled sill. Panel i shows a three-dimensional view of the amount of slip on the caldera fault patches according to the model, and panel j shows the inferred sill opening similarly.

## 2.2 Main results

- GIA causes surface uplift in the vicinity of the Bárðarbunga caldera outside the ice cap. Estimated GIA uplift from a scaled model by Auriac (2014) has a maximum vertical displacement of 33 mm/yr outside the ice cap in 2015-2018 near Bárðarbunga. Plate spreading generates 18-19 mm/yr of horizontal displacements.
- After correcting for GIA and plate spreading processes, the remaining deformation around the Bárðarbunga caldera shows horizontal displacement away from the caldera and uplift. The 2015-2018 maximum average horizontal displacement measured by a GNSS station closest to the caldera (KISA) is about 111 mm/yr, and uplift is about 20 mm/yr.
- Post-eruptive inflation-like volcano deformation signal can result from viscoelastic relaxation in response to major magma drainage (with no magma inflow in the post-eruptive period). Viscoelastic relaxation model with a viscosity of  $3 \times 10^{18}$  Pa s and a co-eruptive point source contraction volume of  $0.4 \text{ km}^3$  best explains the observations, but has difficulty in explaining the localized large horizontal deformation signal.
- Deep magma inflow coupled with a reversed slip on caldera faults can also explain the post-eruptive deformation field around the Bárðarbunga caldera. The best-fitting magma inflow rate for the deep magma inflow model is  $0.032 \text{ km}^3/\text{yr}$ .
- Viscoelastic relaxation, renewed magma inflow, or a combination of both processes may contribute to the Bárðarbunga post-eruptive deformation field.

# 3 Paper II: Post-rifting relaxation during 2015-2020 following the Bárðarbunga - Holuhraun dike intrusion and eruption in Iceland

## 3.1 Summary

Following the 2014-2015 Bárðarbunga-Holuhraun eruption, ground deformation continued in the affected area north of the Vatnajökull ice cap. The 2015-2020 average velocity field is estimated from data collected in three Sentinel-1 InSAR tracks and eight continuous GNSS stations. The InSAR LOS average velocity field is decomposed into approximately east (near-east) and north (near-up) directions. The InSAR near-east velocity field and GNSS average horizontal velocities describe the horizontal movement. The InSAR near-up velocity field and GNSS vertical velocities describe the vertical displacement field. GIA and plate spreading deformation signals are corrected to isolate the post-eruptive deformation signal, providing a corrected velocity field.

The corrected velocity field from InSAR and GNSS shows uplift and horizontal movement away from the dike. Two GNSS stations 20 km away on different sides of the dike move apart, showing about 9 mm/yr and 10 mm/yr horizontal displacement in the direction perpendicular to the dike, respectively. The near-east corrected velocity field (Figure 3.1a) shows horizontal displacements away from the dike, with a higher rate on the west side of the dike than on the east side. In the vertical, the study area is mainly uplifting. The maximum uplift rate occurs along the edge of the ice cap (Figure 3.1e). An uplift rate higher than 10 mm/yr occupies a smaller area on the west side than on the east side of the dike.

A two-layer viscoelastic relaxation model is applied. The top layer consists of homogeneous elastic material, while the lower half-space is a homogeneous Maxwell viscoelastic material. The dike model applied is from Sigmundsson et al. (2015), which divides the dike into 120 patches from the surface to 10 km depth along the 48 km long dike. We run a series of models with different elastic layer thicknesses and viscosities to explore their effect on surface displacement in the post-eruptive period due to the diking event. The viscosities range from  $3\text{-}36 \times 10^{18}$  Pa s, and the elastic layer thicknesses range between 1-24 km.

The RMS residuals between the models and observations suggest an 18 km thick elastic layer on top of a viscoelastic half-space with the viscosity  $4 \times 10^{18}$  Pa s best explains the 3D velocity field (including north, east, and up velocity field from GNSS and near-east, near-up velocity field from InSAR; Figure 3.2). The model misfit space

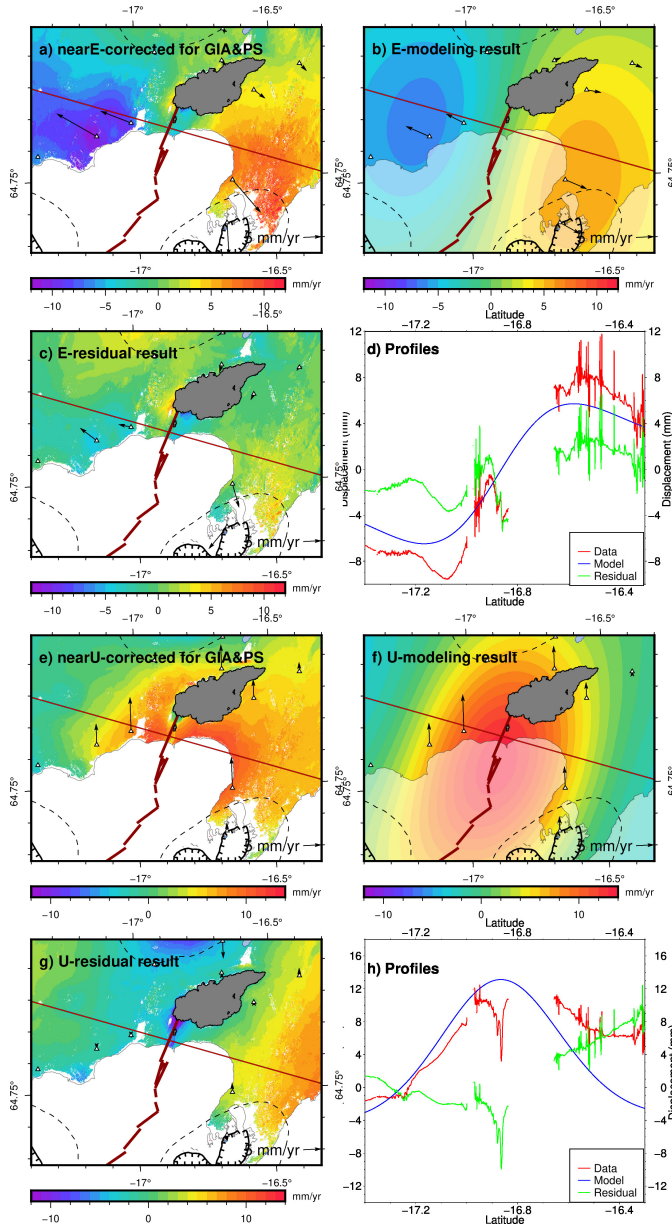


Figure 3.1. Corrected average velocity field in the horizontal (a) and vertical (e) directions during 2015-2020 from InSAR (color) and GNSS (black arrows). The modeled east and up velocity from the viscoelastic model with the optimal elastic layer thickness (18 km) and viscosity ( $4 \times 10^{18}$  Pa s) are shown in b and f. Panels c and g show the differences between corresponding observation (a and e) and model (b and f). Panels d and h show velocity profiles across the study area in the near-east (red line in a, b, and c) and near-up (red line in e, f, and g).

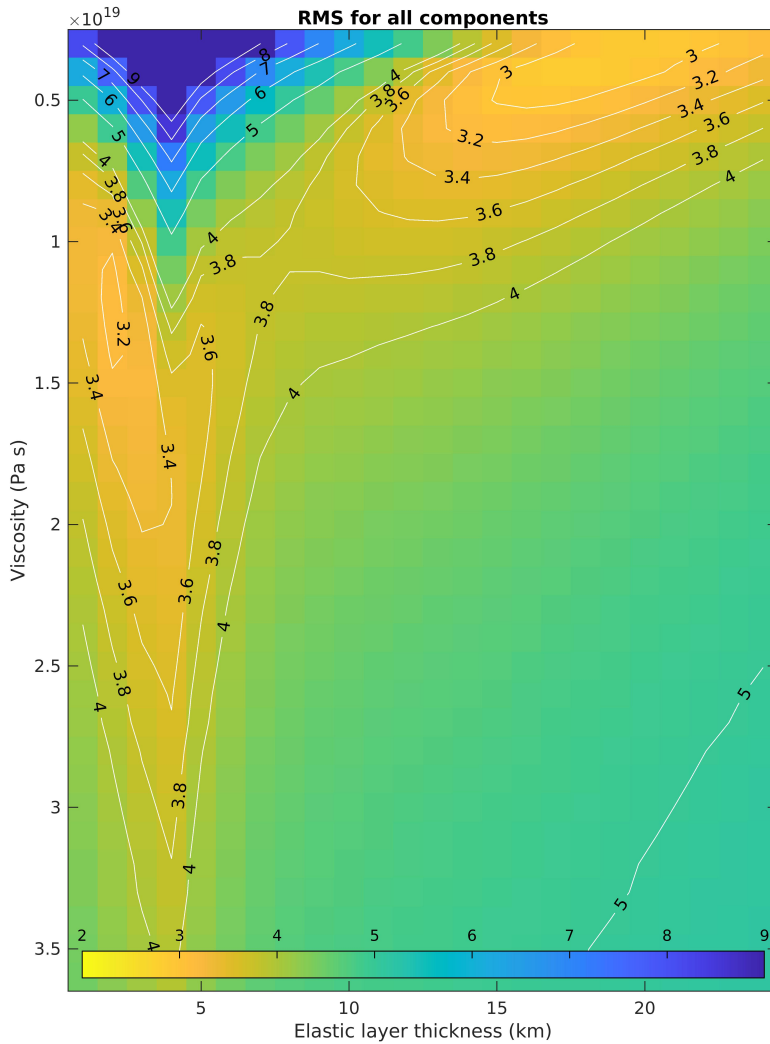


Figure 3.2. Root mean square residual between the corrected velocity fields (data) and predicted ground velocity fields from modeling. The data include near-east and near-up components from InSAR and north, east, and up components from GNSS. The weight of GNSS vs. InSAR is 1000:1. The weight of horizontal vs. vertical is 2:1. The x-axis is the elastic layer thickness (1-24 km with 1 km step), and the y-axis is the viscosity ( $3\text{-}36 \times 10^{18}$  Pa s with  $1 \times 10^{18}$  Pa s step). The optimal viscosity for the velocities is at  $4 \times 10^{18}$  Pa s, and the optimal elastic layer thickness is 18 km.

shows the second regime of a good fit with  $12 \times 10^{18}$  Pa s and 2 km elastic layer thickness, likely driven by deformation near the dike that may, however, result from other un-modeled processes such as cooling compaction of the emplaced dike (Figure 3.2). The horizontal and vertical velocities give different preferences for a best-fit model. The horizontal velocity field prefers a combination of a 3 km thick elastic layer and  $15 \times 10^{18}$  Pa s viscosity. In comparison, the vertical velocity field finds the optimal model with  $4 \times 10^{18}$  Pa s viscosity and 24 km thick elastic layer, which is the deepest elastic layer tested in the model.

## 3.2 Main results

- After correcting for the GIA and plate spreading signal, InSAR and GNSS velocities indicate  $\sim 19$  mm/yr widening across a dike after its formation, which is interpreted as post-rifting viscoelastic relaxation.
- A two-layer viscoelastic model with the  $4 \times 10^{18}$  Pa s viscoelastic half-space below an 18 km thick elastic layer best explains corrected GNSS and InSAR average velocities.
- A comparable fit is with an elastic layer of  $\sim 2$  km and a viscosity of  $12 \times 10^{18}$  Pa s, but un-modeled processes may have an influence, such as cooling compaction of the emplaced dike.
- Horizontal average velocity field prefers a model with a thinner elastic layer (3 km) and viscosity of  $15 \times 10^{18}$  Pa s. In comparison, the vertical average velocity field prefers the thickest tested elastic layer (24 km) with  $4 \times 10^{18}$  Pa s viscosity.



## **4 Paper III: Similarity of stress and ground displacement patterns caused by viscoelastic relaxation and magma inflow in a post-eruptive period: A case study at Bárðarbunga volcano, Iceland**

### **4.1 Summary**

Earlier studies suggest that viscoelastic relaxation can produce a similar average velocity field as renewed magma inflow in a post-eruptive period. This study explores the possibility of distinguishing the two processes using the following approaches: 1) stress fields reflected in seismicity patterns, and 2) the time series of the surface displacements.

Predictions from viscoelastic relaxation and magma inflow models in the initial 6.3 years after an eruption are compared. Both use linearly homogeneous material in each Earth layer, and have a magma body at 10 km depth. For the viscoelastic relaxation model, we consider a two-layer model with a 7-km thick elastic layer that lies on top of a Maxwell viscoelastic half-space with viscosity  $3 \times 10^{18}$  Pa s. A  $0.40 \text{ km}^3$  contraction volume is imposed at the magma body at  $t=0$ , approximating the effect of an eruption. Stress and time series of ground displacement are evaluated as a function of time in the following period. The magma inflow model has a purely elastic material, with the inflow rate varying with time.

The magma inflow volume is scaled to find a magma inflow stress field most comparable to the stress field produced by the viscoelastic model. In the study period, a total of  $0.36 \text{ km}^3$  magma inflow creates a similar stress field as that generated by the viscoelastic relaxation model (Figure 4.1). A time-dependent magma inflow model can broadly reproduce spatial and temporal patterns of stress changes caused by viscoelastic relaxation. Therefore, stress fields cannot easily help to distinguish between viscoelastic relaxation and the magma inflow process.

The temporal variation of the surface displacement field caused by viscoelastic relaxation and magma inflow is also compared. Depending on magma inflow rates, the velocity field due to magma inflow is time-dependent. At each particular location, the horizontal displacement from the viscoelastic model fits an exponential decay, with the decay constant varying with distance from the source (Figure 4.2). On the contrary, magma inflow into a magma source of constant geometry (not evolving with time), with a magma inflow rate that decays exponentially with time, has the same decay constant at all distances. Therefore, detailed observations and interpretations of time-dependent

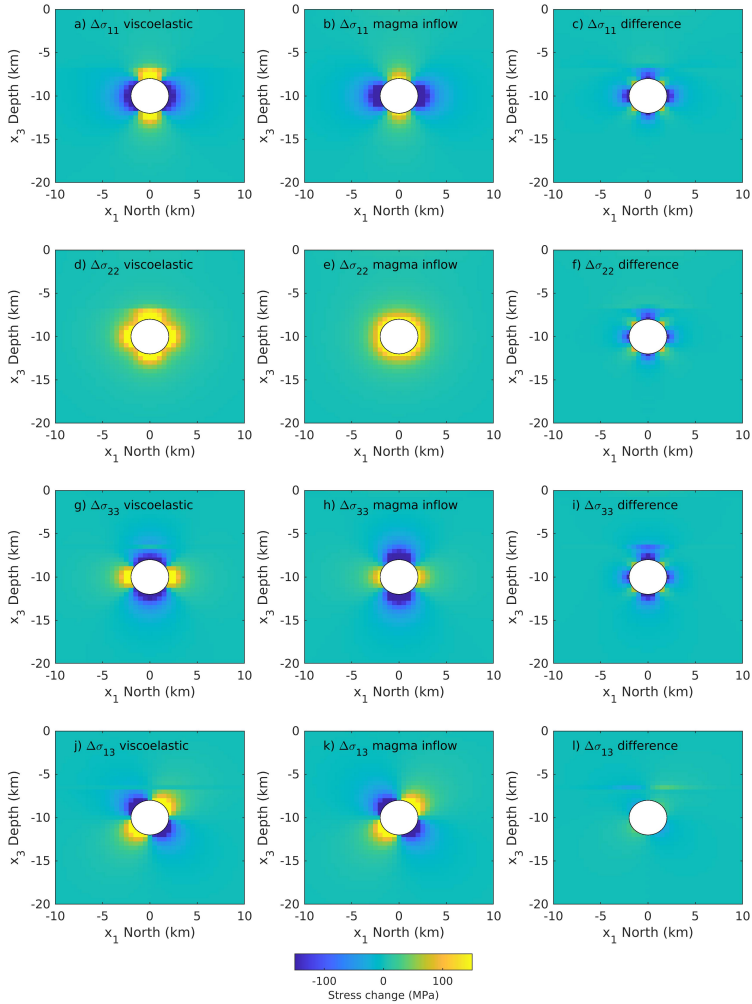


Figure 4.1. The spatial pattern of the stress change caused by viscoelastic relaxation (left) and magma inflow (middle) since  $t=0^+$ . Panels to the right show the corresponding stress difference between the two models. The panels show cross-sections of four components of stress change in a plane parallel to the north-south direction in the initial 6.3 years. The left panels show the stress change in the viscoelastic relaxation caused by magma withdrawal from a  $0.4 \text{ km}^3$  point source. The middle panels show stress change in a magma inflow model with a total inflow volume of  $3.6 \times 10^8 \text{ m}^3$ . The four stress components are:  $\sigma_{11}$ ,  $\sigma_{22}$ ,  $\sigma_{33}$ ,  $\sigma_{13}$ . The  $x$ -axis is the north-south direction, and the  $z$ -axis is the vertical direction. The crustal volume within a 2-km radius from the source center (white circle at the center of each panel) is masked to eliminate unrealistically high stress change predicted by the point source.

surface displacement rates could be a tool to distinguish the two processes.

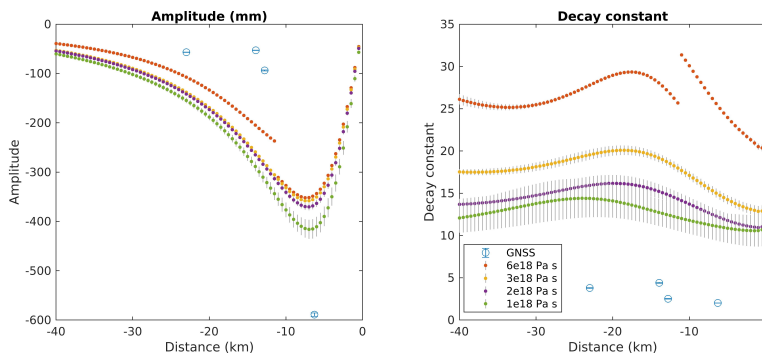


Figure 4.2. Amplitude (left) and decay constant (right) estimated from the horizontal surface displacement time series in a viscoelastic model, fit with an exponential function. The dots with error bars show the estimated amplitude and decay constant from viscoelastic models with different viscosities. The circles with error bars show the estimated amplitude and decay constant from the corrected GNSS time series. The x-axis is the distance from the source center in kilometers.

Data from the post-eruptive period following the 2014–2015 Bárðarbunga–Holuhraun eruption can be compared to these modeling results. Preliminary evaluation suggests that seismicity patterns in the post-eruptive period can relate to stress changes caused either by viscoelastic relaxation or magma inflow. Four continuous GNSS stations around the Bárðarbunga caldera measure the ground displacement. The observed horizontal displacements of the stations show an exponential decay rate with time, with a decay constant between 2–5 years. A viscoelastic relaxation model with a viscosity between  $1\text{--}6 \times 10^{18}$  Pa s has a decay constant longer than ten years for all the stations.

## 4.2 Main results

- Post-eruptive stress field generated by a two-layer viscoelastic model is comparable to that caused by magma inflow. Both processes tend to decrease co-eruptive stresses formed during the modeled eruption.
- Time-dependent magma inflow model can create a time-dependent stress field similar to that caused by viscoelastic relaxation following sudden magma drainage.
- The horizontal displacement caused by viscoelastic relaxation of magma drainage shows exponential decay over time.
- The decay constant for horizontal displacements varies with the distance from the source. In contrast, the magma inflow model has the same decay constant everywhere if the geometry of the deformation source is constant (source shape

not changing with time). The decay constant of ground displacements due to magma inflow at a decaying rate is the same as that of the magma inflow.

- At the Bárðarbunga volcano, the decay constant for the observed GNSS time series is between 2-5 years, while our modeling results with the viscosity of  $1-6 \times 10^{18}$  Pa s suggest a decay constant of more than ten years.

## 5 General conclusions

Post-eruptive ground deformation studies are important to fully understand volcano behavior, especially if volcanic unrest continues after an eruption. The post-eruptive period following the 2014-2015 Bárðarbunga-Holuhraun eruption provides a good study case, because of the large-scale magma transfer that occurred during the eruption and the associated dike event, and good monitoring with multiple techniques in the co- and post-eruptive period.

Campaign and continuous GNSS stations in the Bárðarbunga-Holuhraun eruption area provide long-term deformation trends in the pre-, co-, and post-eruptive periods. InSAR interferograms from Sentinel-1 satellites map the average velocity field in the area in the post-eruptive period. GIA and plate spreading correction are needed when studying ground deformation at the Bárðarbunga volcanic system, as these processes significantly influence the deformation field in this area (velocities corrected for GIA and plate spreading are referred to as corrected velocities).

The GNSS and InSAR average velocity fields show consistency in the displacement direction and rate. The 2015-2018 corrected average velocity field around the Bárðarbunga caldera horizontal displacement away from the caldera and uplift near the caldera. Further away, there is minor subsidence at around 20 km distance from the Bárðarbunga caldera center. Modeling by Li et al. (2021) concludes that magma inflow, viscoelastic relaxation, or a combination of the processes contributes to the post-eruptive deformation field in the vicinity of the Bárðarbunga caldera.

The 2015-2020 corrected average velocity field along the Bárðarbunga-Holuhraun dike is presented by Li et al. (2022) shows horizontal displacements move away from the dike, and uplift on both sides of it. The best-fitting model suggests an elastic layer thickness of 18 km and viscosity of the lower viscoelastic half-space of  $4 \times 10^{18}$  Pa s. A comparable fit is with an elastic layer of  $\sim 2$  km and a viscosity of  $12 \times 10^{18}$  Pa s. The comparable fits of these two models may be due to influence of unmodeled processes, such as cooling compaction of the emplaced dike. Overall, the modeling results suggest viscoelastic relaxation can explain the major part of the corrected ground velocities in the dike area.

As Li et al. (2021) suggests a similarity of the deformation field caused by the viscoelastic relaxation and magma inflow, a question arises: can we distinguish the two processes? To answer this question, stresses and temporal evolution ground displacements are studied by Li et al. (prep). It is found that the stress field caused by the viscoelastic relaxation and magma inflow can be similar. Temporal variation of the surface displacements can be different, but intensive monitoring is needed to identify such differences.

There are still several unanswered questions. In the Bárðarbunga area, a more

detailed study of temporal variation of the surface displacement may tell more features on the post-eruptive magmatic movements, as time series at KISA GNSS station suggests slowing down after our study period. Alternative viscoelastic models, such as a three-horizontally layered model, magma body with a viscoelastic shell, a temperature-dependent viscoelastic model, or a localized low viscosity zone under the Bárðarbunga could be considered. Models with different source geometry are also worth to explore. Other processes, such as accelerated GIA or a change in plate spreading rate, could contribute to the displacement field. Our study suggests viscoelastic relaxation and magma inflow may both contribute to the post-eruptive deformation field, however, the relative contribution from each process is hard to evaluate. Although spatial patterns and temporal variation of surface displacements can be a tool to distinguish between viscoelastic relaxation and magma inflow, geodetic observations at the Bárðarbunga volcano are not spatially dense for that purpose due to ice cover and major topographic relief. Such an approach can be tested at other volcanoes where better temporal and spatial coverage of the surface displacement monitoring network is available, ideally following a major magma drainage event.

## References

- Ágústsdóttir, T., Winder, T., Woods, J., White, R. S., Greenfield, T., and Brandsdóttir, B. (2019). Intense Seismicity During the 2014-2015 Bárðarbunga-Holuhraun Rifting Event, Iceland, Reveals the Nature of Dike-Induced Earthquakes and Caldera Collapse Mechanisms. *Journal of Geophysical Research: Solid Earth*, 124.
- Ágústsdóttir, T., Woods, J., Greenfield, T., Green, R. G., White, R. S., Winder, T., Brandsdóttir, B., Steinthorsson, S., and Soosalu, H. (2016). Episodic Propagation of the 2014 Bárðarbunga-Holuhraun Dike Intrusion, Central Iceland. *Geophysical Research Letters*, submitted:1495–1503.
- Aki, K. and Richards, P. G. (2002). *Quantitative seismology*.
- Altamimi, Z., Métivier, L., and Collilieux, X. (2012). ITRF2008 plate motion model. *Journal of Geophysical Research: Solid Earth*, 117(7):1–14.
- Árnadóttir, T., Lund, B., Jiang, W., Geirsson, H., Björnsson, H., Einarsson, P., and Sigurdsson, T. (2009). Glacial rebound and plate spreading: results from the first countrywide GPS observations in Iceland. *Geophysical Journal International*, 177(2):691–716.
- Auriac, A. (2014). *Solid Earth response to ice retreat and glacial surges in Iceland inferred from satellite radar interferometry and finite element modelling*. PhD thesis, Faculty of Earth Sciences, University of Iceland.
- Auriac, A., Spaans, K. H., Sigmundsson, F., Hooper, A., Schmidt, P., and Lund, B. (2013). Iceland rising: Solid Earth response to ice retreat inferred from satellite radar interferometry and viscoelastic modeling. *Journal of Geophysical Research: Solid Earth*, 118(4):1331–1344.
- Barbot, S. (2014). RELAX v1.0.7 [software], Computational Infrastructure for Geodynamics.
- Barbot, S. and Fialko, Y. (2010a). A unified continuum representation of post-seismic relaxation mechanisms: semi-analytic models of afterslip, poroelastic rebound and viscoelastic flow: Semi-analytic models of postseismic transient. *Geophysical Journal International*, 182(3):1124–1140.
- Barbot, S. and Fialko, Y. (2010b). Fourier-domain Green’s function for an elastic semi-infinite solid under gravity, with applications to earthquake and volcano deformation: Fourier-domain elastic solutions. *Geophysical Journal International*, 182(2):568–582.
- Barbot, S., Fialko, Y., and Bock, Y. (2009). Postseismic deformation due to the Mw 6.0 2004 Parkfield earthquake: Stress-driven creep on a fault with spatially variable rate-and-state friction parameters. *Journal of Geophysical Research: Solid Earth*, 114(B7).
- Barnhoorn, A., van der Wal, W., and Drury, M. R. (2011). Upper mantle viscosity and

- lithospheric thickness under Iceland. *Journal of Geodynamics*, 52(3-4):260–270.
- Bato, M. G., Pinel, V., Yan, Y., Jouanne, F., and Vandemeulebrouck, J. (2018). Possible deep connection between volcanic systems evidenced by sequential assimilation of geodetic data. *Scientific reports*, 8(1):1–13.
- Battaglia, M., Cervelli, P. F., and Murray, J. R. (2013). Modeling crustal deformation near active faults and volcanic centers: a catalog of deformation models and modeling approaches. Technical report, US Geological Survey.
- Belart, J. M., Magnússon, E., Berthier, E., Gunnlaugsson, Á., Pálsson, F., Aðalgeirsdóttir, G., Jóhannesson, T., Thorsteinsson, T., and Björnsson, H. (2020). Mass Balance of 14 Icelandic Glaciers, 1945–2017: Spatial Variations and Links With Climate. *Frontiers in Earth Science*, 8(June):1–15.
- Biggs, J., Mothes, P., Ruiz, M., Amelung, F., Dixon, T. H., Baker, S., and Hong, S.-H. (2010). Stratovolcano growth by co-eruptive intrusion: The 2008 eruption of Tungurahua Ecuador. *Geophysical Research Letters*, 37(21).
- Björnsson, H. and Einarsson, P. (1990). Volcanoes beneath Vatnajökull, Iceland: Evidence from radio echo-sounding, earthquakes and jökulhlaups. *Jökull*, 40:147–168.
- Bonafede, M., Dragoni, M., and Quarenì, F. (1986). Displacement and stress fields produced by a centre of dilation and by a pressure source in a viscoelastic half-space: application to the study of ground deformation and seismic activity at Campi Flegrei, Italy. *Geophysical Journal of the Royal Astronomical Society*, 87(2):455–485.
- Böðvarsson, R., Rögnvaldsson, S. T., Slunga, R., and Kjartansson, E. (1999). The SIL data acquisition system-at present and beyond year 2000. *Physics of the Earth and Planetary Interiors*, 113(1-4):89–101.
- Caracciolo, A., Bali, E., Guðfinnsson, G. H., Kahl, M., Halldórsson, S. A., Hartley, M. E., and Gunnarsson, H. (2020). Temporal evolution of magma and crystal mush storage conditions in the Bárðarbunga-Veiðivötn volcanic system, Iceland. *Lithos*, 352:105234.
- Carbotte, S. M., Arnulf, A., Spiegelman, M., Lee, M., Harding, A., Kent, G., Canales, J. P., and Nedimović, M. (2020). Stacked sills forming a deep melt-mush feeder conduit beneath Axial Seamount. *Geology*, 48(7):693–697.
- Compton, K., Bennett, R. A., and Hreinsdóttir, S. (2015). Climate-driven vertical acceleration of Icelandic crust measured by continuous GPS geodesy. *Geophysical Research Letters*, 42(3):743–750.
- Coppola, D., Ripepe, M., Laiolo, M., and Cigolini, C. (2017). Modelling satellite-derived magma discharge to explain caldera collapse. *Geology*, 45(6):523–526.
- Del Negro, C., Currenti, G., and Scandura, D. (2009). Temperature-dependent viscoelastic modeling of ground deformation: Application to Etna volcano during the 1993-1997 inflation period. *Physics of the Earth and Planetary Interiors*, 172(3-4):299–309.
- Dragoni, M. and Magnanensi, C. (1989). Displacement and stress produced by a pressurized, spherical magma chamber, surrounded by a viscoelastic shell. *Physics of the Earth and Planetary Interiors*, 56(3):316–328.
- Drouin, V. and Sigmundsson, F. (2019). Countrywide Observations of Plate Spreading and Glacial Isostatic Adjustment in Iceland Inferred by Sentinel-1 Radar Interferometry, 2015 – 2018. *Geophysical Research Letters*, 46:8046–8055.
- Dzurisin, D. (2006). *Volcano deformation: new geodetic monitoring techniques*.



- Springer Science & Business Media.
- Ellis, S. and Stöckhert, B. (2004). Elevated stresses and creep rates beneath the brittle-ductile transition caused by seismic faulting in the upper crust. *Journal of Geophysical Research: Solid Earth*, 109(B5).
- Euillades, P. A., Euillades, L. D., Blanco, M. H., Velez, M. L., Grosse, P., and Sosa, G. J. (2017). Co-eruptive subsidence and post-eruptive uplift associated with the 2011–2012 eruption of Puyehue-Cordón Caulle, Chile, revealed by DInSAR. *Journal of Volcanology and Geothermal Research*, 344:257–269.
- Fialko, Y., Khazan, Y., and Simons, M. (2001). Deformation due to a pressurized horizontal circular crack in an elastic half-space, with applications to volcano geodesy. *Geophysical Journal International*, 146(1):181–190.
- Foulger, G. R., Jahn, C.-H., Seeber, G., Einarsson, P., Julian, B. R., and Heki, K. (1992). Post-rifting stress relaxation at the divergent plate boundary in Northeast Iceland. *Nature*, 358(6386):488–490.
- Geirsson, H., Árnadóttir, T., Hreinsdóttir, S., Decriem, J., LaFemina, P. C., Jónsson, S., Bennett, R. A., Metzger, S., Holland, A., Sturkell, E., et al. (2010). Overview of results from continuous GPS observations in Iceland from 1995 to 2010. *Jökull*, 60:3–22.
- Gregg, P., De Silva, S., and Grosfils, E. (2013). Thermomechanics of shallow magma chamber pressurization: Implications for the assessment of ground deformation data at active volcanoes. *Earth and Planetary Science Letters*, 384:100–108.
- Gudmundsson, M. T., Högnadóttir, T., Sigmundsson, F., and Geirsson, H. (2020). Rapid resurgence of the subglacial Bárðarbunga caldera following collapse in 2014–2015, quantified with repeated Bouguer gravity surveys. In *EGU General Assembly Conference Abstracts*, number June 2015, page 18744.
- Gudmundsson, M. T., Jónsdóttir, K., Hooper, A., Holohan, E. P., Halldórsson, S. A., Ófeigsson, B. G., Cesca, S., Vogfjörð, K. S., Sigmundsson, F., Högnadóttir, T., Einarsson, P., Sigmarsson, O., Jarosch, A. H., Jónasson, K., Magnússon, E., Hreinsdóttir, S., Bagnardi, M., Parks, M. M., Hjörleifsdóttir, V., Pálsson, F., Walter, T. R., Schöpfer, M. P. J., Heimann, S., Reynolds, H. I., Dumont, S., Bali, E., Gudfinnsson, G. H., Dahm, T., Roberts, M. J., Hensch, M., Belart, J. M. C., Spaans, K., Jakobsson, S., Gudmundsson, G. B., Fridriksdóttir, H. M., Drouin, V., Dürig, T., Adalgeirsdóttir, G., Riishuus, M. S., Pedersen, G. B. M., Van Boeckel, T., Oddsson, B., Pfeffer, M. A., Barsotti, S., Bergsson, B., Donovan, A., Burton, M. R., Aiuppa, A., Aðalgeirsdóttir, G., Riishuus, M. S., Pedersen, G. B. M., Van Boeckel, T., Oddsson, B., Pfeffer, M. A., Barsotti, S., Bergsson, B., Donovan, A., Burton, M. R., and Aiuppa, A. (2016). Gradual caldera collapse at Bárðarbunga volcano, Iceland, regulated by lateral magma outflow. *Science*, 353(6296):aaf8988.
- Halldórsson, S. A., Oskarsson, N., Gronvold, K., Sigurdsson, G., Sverrisdóttir, G., and Steinthorsson, S. (2008). Isotopic-heterogeneity of the Thjorsa lava—implications for mantle sources and crustal processes within the Eastern Rift Zone, Iceland. *Chemical Geology*, 255(3–4):305–316.
- Hamazaki, T. (1999). Overview of the Advanced Land Observing Satellite (ALOS): Its mission requirements, sensors, and a satellite system. In *Proceedings of the ISPRS Joint Workshop—Sensors and Mapping from Space, Hannover, Germany*, pages 27–30. Citeseer.

- Hamling, I. J., Wright, T. J., Calais, E., Lewi, E., and Fukahata, Y. (2014). InSAR observations of post-rifting deformation around the Dabbahu rift segment, Afar, Ethiopia. *Geophysical Journal International*, 197(1):33–49.
- Hartley, M. E., Bali, E., Maclennan, J., Neave, D. A., and Halldórsson, S. A. (2018). Melt inclusion constraints on petrogenesis of the 2014–2015 Holuhraun eruption, Iceland. *Contributions to Mineralogy and Petrology*, 173(2).
- Herring, T., King, R., and McClusky, S. (2010). Introduction to GAMIT/GLOBK. *Massachusetts Institute of Technology, Cambridge, Massachusetts*.
- Hickey, J. and Gottsmann, J. (2014). Benchmarking and developing numerical Finite Element models of volcanic deformation. *Journal of Volcanology and Geothermal Research*, 280:126–130.
- Hofmann-Wellenhof, B., Lichtenegger, H., and Wasle, E. (2007). *GNSS—global navigation satellite systems: GPS, GLONASS, Galileo, and more*. Springer Science & Business Media.
- Hofton, M. and Foulger, G. (1996). Post-rifting anelastic deformation around the spreading plate boundary, north Iceland: 1. Modeling of the 1987–1992 deformation field using a viscoelastic Earth structure. *Journal of Geophysical Research: Solid Earth*, 101(B11):25403–25421.
- Hreinsdóttir, S., Árnadóttir, T., Decriem, J., Geirsson, H., Tryggvason, A., Bennett, R. A., and LaFemina, P. (2009). A complex earthquake sequence captured by the continuous GPS network in SW Iceland. *Geophysical Research Letters*, 36(12).
- Jónsdóttir, K., Rodríguez, F. R., Hjørleifsdóttir, V., Jónsdóttir, K., Rodríguez, F. R., and Hjørleifsdóttir, V. (2019). Using repeating earthquakes to reveal temporal behavior of caldera faults. *Abstract EGU2019-2690 presented at 2019 EGU General Assembly, Vienna, 7-12 April.*, page 2690.
- Larsen, G. and Gudmundsson, M. T. (2019). The Bárðarbunga volcanic system. *Catalogue of Icelandic Volcanoes, IMO, UI and CPD-NCIP*. Accessed: 2020-03-28.
- Lavallée, Y. and Kendrick, J. E. (2021). Chapter 5 - A review of the physical and mechanical properties of volcanic rocks and magmas in the brittle and ductile regimes. In Papale, P., editor, *Forecasting and Planning for Volcanic Hazards, Risks, and Disasters*, volume 2 of *Hazards and Disasters Series*, pages 153–238. Elsevier.
- Lavier, L. L., Bennett, R. A., and Duddu, R. (2013). Creep events at the brittle ductile transition. *Geochemistry, Geophysics, Geosystems*, 14(9):3334–3351.
- Li, S., Grapenthin, R., Sigmundsson, F., Drouin, V., Hreinsdóttir, S., and Ófeigsson, B. G. (2022). Post-rifting relaxation during 2015–2020 following the Bárðarbunga-Holuhraun dike intrusion and eruption in Iceland. *Geophysical Research Letters*, page e2022GL098977.
- Li, S., Sigmundsson, F., Drouin, V., Parks, M. M., Ófeigsson, B. G., Jónsdóttir, K., Grapenthin, R., Geirsson, H., Hooper, A., and Hreinsdóttir, S. (2021). Ground Deformation After a Caldera Collapse: Contributions of Magma Inflow and Viscoelastic Response to the 2015–2018 Deformation Field Around Bárðarbunga, Iceland. *Journal of Geophysical Research: Solid Earth*, 126(3):e2020JB020157.
- Li, S., Sigmundsson, F., Yamasaki, T., Einarsson, P., Jónsdóttir, K., Geirsson, H., and Hooper, A. (prep). Improving understanding of post-eruptive viscoelastic relaxation and magma inflow by studies of stress and surface displacement: A case study at Bárðarbunga volcano, Iceland. unpublished.

- Lisowski, M. (2007). Analytical volcano deformation source models. In *Volcano deformation*, pages 279–304. Springer.
- Lu, Z. and Dzurisin, D. (2014). Introduction to interferometric synthetic aperture radar. In *InSAR Imaging of Aleutian Volcanoes*, pages 1–23. Springer.
- Masterlark, T., Haney, M., Dickinson, H., Fournier, T., and Searcy, C. (2010). Rheologic and structural controls on the deformation of Okmok volcano, Alaska: FEMs, InSAR, and ambient noise tomography. *Journal of Geophysical Research: Solid Earth*, 115(B2).
- McTigue, D. F. (1987). Elastic stress and deformation near a finite spherical magma body: Resolution of the point source paradox. *Journal of Geophysical Research: Solid Earth*, 92(B12):12931–12940.
- Misra, T., Rana, S., Tyagi, R., and Thyagarajan, K. (2006). RISAT: first planned SAR mission of ISRO. In *GEOSS and Next-Generation Sensors and Missions*, volume 6407, pages 111–118. SPIE.
- Mogi, K. (1958). Relations between the eruptions of various volcanoes and the deformations of the ground surfaces around them. *Bulletin of the Earthquake Research Institute*, 36:99–134.
- Morales Rivera, A. M., Amelung, F., Albino, F., and Gregg, P. M. (2019). Impact of Crustal Rheology on Temperature-Dependent Viscoelastic Models of Volcano Deformation: Application to Taal Volcano, Philippines. *Journal of Geophysical Research: Solid Earth*, 124:978–994.
- Musa, Z. N., Popescu, I., and Mynett, A. (2015). A review of applications of satellite SAR, optical, altimetry and DEM data for surface water modelling, mapping and parameter estimation. *Hydrology and Earth System Sciences*, 19(9):3755–3769.
- Newman, A. V., Dixon, T. H., and Gourmelen, N. (2006). A four-dimensional viscoelastic deformation model for Long Valley Caldera, California, between 1995 and 2000. *Journal of Volcanology and Geothermal Research*, 150(1-3):244–269.
- Novoa, C., Remy, D., Gerbault, M., Baez, J. C., Tassara, A., Cordova, L., Cardona, C., Granger, M., Bonvalot, S., and Delgado, F. (2019). Viscoelastic relaxation: A mechanism to explain the decennial large surface displacements at the Laguna del Maule silicic volcanic complex. *Earth and Planetary Science Letters*, 521:46–59.
- Nur, A. and Mavko, G. (1974). Postseismic viscoelastic rebound. *Science*, 183(4121):204–206.
- Okada, Y. (1985). Surface deformation due to shear and tensile faults in a half-space. *Bulletin of the Seismological Society of America*, 75(4):1135–1154.
- Óladóttir, B. A., Larsen, G., and Sigmarsson, O. (2011). Holocene volcanic activity at Grímsvötn, Bárðarbunga and Kverkfjöll subglacial centres beneath Vatnajökull, Iceland. *Bulletin of Volcanology*, 73(9):1187–1208.
- Pagli, C., Sigmundsson, F., Lund, B., Sturkell, E., Geirsson, H., Einarsson, P., Árnadóttir, T., and Hreinsdóttir, S. (2007a). Glacio-isostatic deformation around the Vatnajökull ice cap, Iceland, induced by recent climate warming: GPS observations and finite element modeling. *Journal of Geophysical Research: Solid Earth*, 112(8):1–12.
- Pagli, C., Sigmundsson, F., Pedersen, R., Einarsson, P., Árnadóttir, T., and Feigl, K. L. (2007b). Crustal deformation associated with the 1996 Gjálp subglacial eruption, Iceland: InSAR studies in affected areas adjacent to the Vatnajökull ice cap. *Earth and Planetary Science Letters*, 259(1-2):24–33.

- Parks, M. M., Heimisson, E. R., Sigmundsson, F., Hooper, A., Vogfjörð, K. S., Árnadóttir, T., Ófeigsson, B., Hreinsdóttir, S., Hjartardóttir, Á. R., Einarsson, P., Gudmundsson, M. T., Högnadóttir, T., Jónsdóttir, K., Hensch, M., Bagnardi, M., Dumont, S., Drouin, V., Spaans, K., and Ólafsdóttir, R. (2017). Evolution of deformation and stress changes during the caldera collapse and dyking at Bárðarbunga, 2014–2015: Implication for triggering of seismicity at nearby Tungnafellsjökull volcano. *Earth and Planetary Science Letters*, 462:212–223.
- Pedersen, G., Höskuldsson, A., Dürig, T., Thordarson, T., Jónsdóttir, I., Riishuus, M., Óskarsson, B., Dumont, S., Magnússon, E., Gudmundsson, M., Sigmundsson, F., Drouin, V., Gallagher, C., Askew, R., Guðnason, J., Moreland, W., Nikkola, P., Reynolds, H., and Schmith, J. (2017). Lava field evolution and emplacement dynamics of the 2014–2015 basaltic fissure eruption at Holuhraun, Iceland. *Journal of Volcanology and Geothermal Research*, 340:155–169.
- Peltier, W. (1974). The impulse response of a Maxwell Earth. *Reviews of Geophysics*, 12(4):649–669.
- Peltier, W. R., Argus, D., and Drummond, R. (2015). Space geodesy constrains ice age terminal deglaciation: The global ice-6g\_c (vm5a) model. *Journal of Geophysical Research: Solid Earth*, 120(1):450–487.
- Puskas, C. M., Smith, R. B., Meertens, C. M., and Chang, W. L. (2007). Crustal deformation of the Yellowstone–Snake River Plain volcano-tectonic system: Campaign and continuous GPS observations, 1987–2004. *Journal of Geophysical Research: Solid Earth*, 112(B3).
- Qiu, Q., Feng, L., Hermawan, I., and Hill, E. M. (2019). Coseismic and postseismic slip of the 2005 Mw 8.6 Nias-Simeulue earthquake: Spatial overlap and localized viscoelastic flow. *Journal of Geophysical Research: Solid Earth*, 124(7):7445–7460.
- Reynolds, H. I., Gudmundsson, M. T., Högnadóttir, T., and Axelsson, G. (2019). Changes in Geothermal Activity at Bárðarbunga, Iceland, Following the 2014–2015 Caldera Collapse, Investigated Using Geothermal System Modeling. *Journal of Geophysical Research: Solid Earth*, 124(8):8187–8204.
- Riel, B., Milillo, P., Simons, M., Lundgren, P., Kanamori, H., and Samsonov, S. (2015). The collapse of Bárðarbunga caldera, Iceland. *Geophysical Journal International*, 202:446–453.
- Rodríguez-Cardozo, F., Hjörleifsdóttir, V., Jónsdóttir, K., Iglesias, A., Franco, S. I., Geirsson, H., Trujillo-Castrillón, N., and Hensch, M. (2021). The 2014–2015 complex collapse of the Bárðarbunga caldera, Iceland, revealed by seismic moment tensors. *Journal of Volcanology and Geothermal Research*, 416:107275.
- Rosen, P. A., Gurrola, E., Sacco, G. F., and Zebker, H. (2012). The InSAR scientific computing environment. In *EUSAR 2012; 9th European Conference on Synthetic Aperture Radar*, pages 730–733, Nuremberg, Germany: VDE.
- Scandura, D., Currenti, G., and Del Negro, C. (2007). 3D Finite Element Models of Ground Deformation and Stress Field in a Viscoelastic Medium. *Proceedings of the COMSOL Users Conference 2007 Grenoble*.
- Seeber, G. (2008). Satellite geodesy. In *Satellite Geodesy*. de Gruyter.
- Segall, P. (2010). Earthquake and volcano deformation. In *Earthquake and Volcano Deformation*. Princeton University Press.
- Segall, P. (2016). Repressurization following eruption from a magma chamber with a

- viscoelastic aureole. *Journal of Geophysical Research : Solid Earth*, pages 8501–8522.
- Sigmundsson, F. (1991). Post-glacial rebound and asthenosphere viscosity in Iceland. *Geophysical Research Letters*, 18(6):1131–1134.
- Sigmundsson, F. (2019). Calderas collapse as magma flows into rifts. *Science*, 366(6470):1200–1201.
- Sigmundsson, F., Einarsson, P., Ásta Rut Hjartardóttir, Drouin, V., Jónsdóttir, K., Árnadóttir, T., Geirsson, H., Hreinsdóttir, S., Li, S., and Ófeigsson, B. G. (2020a). Geodynamics of Iceland and the signatures of plate spreading. *Journal of Volcanology and Geothermal Research*, 391:106436.
- Sigmundsson, F., Hooper, A., Hreinsdóttir, S., Vogfjörð, K. S., Ófeigsson, B. G., Heimisson, E. R., Dumont, S., Parks, M., Spaans, K., Gudmundsson, G. B., Drouin, V., Árnadóttir, T., Jónsdóttir, K., Gudmundsson, M. T., Högnadóttir, T., Fridriksdóttir, H. M., Hensch, M., Einarsson, P., Magnússon, E., Samsonov, S., Brandsdóttir, B., White, R. S., Ágústsdóttir, T., Greenfield, T., Green, R. G., Hjartardóttir, Á. R., Pedersen, R., Bennett, R. A., Geirsson, H., la Femina, P. C., Björnsson, H., Pálsson, F., Sturkell, E., Bean, C. J., Möllhoff, M., Braiden, A. K., and Eibl, E. P. (2015). Segmented lateral dyke growth in a rifting event at Bárðarbunga volcanic system, Iceland. *Nature*, 517(7533):191–195.
- Sigmundsson, F., Pinel, V., Grapenthin, R., Hooper, A., Halldórsson, S. A., Einarsson, P., Ófeigsson, B. G., Heimisson, E. R., Jónsdóttir, K., Gudmundsson, M. T., Vogfjörð, K., Parks, M., Li, S., Drouin, V., Geirsson, H., Dumont, S., Fridriksdóttir, H. M., Gudmundsson, G. B., Wright, T. J., and Yamasaki, T. (2020b). Unexpected large eruptions from buoyant magma bodies within viscoelastic crust. *Nature Communications*, 11(1):2403.
- Stevens, N., Wadge, G., Williams, C., Morley, J., Muller, J.-P., Murray, J., and Upton, M. (2001). Surface movements of emplaced lava flows measured by synthetic aperture radar interferometry. *Journal of Geophysical Research: Solid Earth*, 106(B6):11293–11313.
- Thordarson, T. and Höskuldsson, Á. (2008). Postglacial volcanism in Iceland. *Jökull*, 58(198):e228.
- Thordarson, T. and Larsen, G. (2007). Volcanism in Iceland in historical time : Volcano types , eruption styles and eruptive history. *Journal of Geodynamics*, 43(1):118–152.
- Tian, Z., Freymueller, J. T., and Yang, Z. (2020). Spatio-temporal variations of afterslip and viscoelastic relaxation following the Mw 7.8 Gorkha (Nepal) earthquake. *Earth and Planetary Science Letters*, 532:116031.
- Torres, R., Snoeij, P., Geudtner, D., Bibby, D., Davidson, M., Attema, E., Potin, P., Rommen, B. Ö., Floury, N., Brown, M., Traver, I. N., Deghaye, P., Duesmann, B., Rosich, B., Miranda, N., Bruno, C., L'Abbate, M., Croci, R., Pietropaolo, A., Huchler, M., and Rostan, F. (2012). GMES Sentinel-1 mission. *Remote Sensing of Environment*, 120:9–24.
- Vanicek, P. and Krakiwsky, E. J. (2015). *Geodesy: the concepts*. Elsevier.
- von Hippel, M. and Harig, C. (2019). Long-Term and Inter-annual Mass Changes in the Iceland Ice Cap Determined From GRACE Gravity Using Slepian Functions. *Frontiers in Earth Science*, 7:171.
- Wittmann, W., Sigmundsson, F., Dumont, S., and Lavallée, Y. (2017). Post-emplacment

- cooling and contraction of lava flows: InSAR observations and a thermal model for lava fields at Hekla volcano, Iceland. *Journal of Geophysical Research: Solid Earth*, 122(2):946–965.
- Yamasaki, T., Sigmundsson, F., and Iguchi, M. (2020). Viscoelastic crustal response to magma supply and discharge in the upper crust: Implications for the uplift of the Aira caldera before and after the 1914 eruption of the Sakurajima volcano. *Earth and Planetary Science Letters*, 531:115981.
- Yamasaki, T., Sigmundsson, F., and Iguchi, M. (2022). Variable inflation rate of a magmatic deformation source beneath Aira caldera after the 1914 eruption of Sakurajima volcano: Inferences from a linear Maxwell viscoelastic model constrained by geodetic data. *Journal of Volcanology and Geothermal Research*, 421:107446.
- Zhang, Q. and Liu, Y. (2019). Overview of Chinese first C band multi-polarization SAR satellite GF-3. *AEROSPACE CHINA*, 18(3):22–31.

# Paper I

## **Ground deformation after a caldera collapse: Contributions of magma inflow and viscoelastic response to the 2015-2018 deformation field around Bárðarbunga, Iceland**

Siqi Li, Freysteinn Sigmundsson, Vincent Drouin, Michelle M. Parks, Benedikt G. Ofeigsson, Kristín Jónsdóttir, Ronni Grapenthin, Halldór Geirsson, Andrew Hooper, and Sigrún Hreinsdóttir, 2021

Journal of Geophysical Research: Solid Earth, 10.1029/2020JB020157

<https://agupubs.onlinelibrary.wiley.com/doi/abs/10.1029/2020JB020157>





# JGR Solid Earth

## RESEARCH ARTICLE

10.1029/2020JB020157

### Key Points:

- Post-eruptive inflation-like volcano deformation signal can result from viscoelastic relaxation in response to eruptive events
- Deep magma inflow coupled with reversed slip on caldera faults can create deformation signal similar to that caused by shallow magma inflow
- Bárðarbunga post-eruptive deformation field may be influenced by viscoelastic relaxation, renewed magma inflow or a combination of both

### Supporting Information:

- Supporting Information S1

### Correspondence to:

S. Li,  
[sil10@hi.is](mailto:sil10@hi.is)

### Citation:

Li, S., Sigmundsson, F., Drouin, V., Parks, M. M., Ófeigsson, B. G., Jónsdóttir, K., et al. (2021). Ground deformation after a caldera collapse: Contributions of magma inflow and viscoelastic response to the 2015–2018 deformation field around Bárðarbunga, Iceland. *Journal of Geophysical Research: Solid Earth*, 126, e2020JB020157. <https://doi.org/10.1029/2020JB020157>

Received 15 MAY 2020  
 Accepted 28 JAN 2021

© 2021. American Geophysical Union.  
 All Rights Reserved.

## Ground Deformation After a Caldera Collapse: Contributions of Magma Inflow and Viscoelastic Response to the 2015–2018 Deformation Field Around Bárðarbunga, Iceland

Siqi Li<sup>1</sup>, Freysteinn Sigmundsson<sup>1</sup>, Vincent Drouin<sup>2</sup>, Michelle M. Parks<sup>3</sup>, Benedikt G. Ófeigsson<sup>3</sup>, Kristín Jónsdóttir<sup>3</sup>, Ronni Grapenthin<sup>4</sup>, Halldór Geirsson<sup>1</sup>, Andrew Hooper<sup>5</sup>, and Sigrún Hreinsdóttir<sup>6</sup>

<sup>1</sup>Nordic Volcanological Center, Institute of Earth Sciences, University of Iceland, Reykjavik, Iceland, <sup>2</sup>Iceland Geosurvey ISOR, Reykjavik, Iceland, <sup>3</sup>Icelandic Meteorological Office, Reykjavik, Iceland, <sup>4</sup>Geophysical Institute and Dept. of Geosciences, University of Alaska Fairbanks, Fairbanks, AK, USA, <sup>5</sup>School of Earth and Environment, COMET, University of Leeds, England, UK, <sup>6</sup>GNS Science, Lower Hutt, New Zealand

**Abstract** Improvement of our understanding of the role of ground deformation due to viscoelastic relaxation following eruptions is important, as the generated signals can resemble renewed magma inflow. We study post-eruptive unrest at the subglacial Bárðarbunga volcano, Iceland, after a caldera collapse and major magma drainage in 2014–2015. Elevated seismicity began about 6 months after the eruption ended, including nine  $M_w > 4.5$  earthquakes. Global Navigation Satellite System and Sentinel-1 Interferometric Synthetic Aperture Radar geodesy are applied to evaluate post-eruptive ground deformation from 2015 to 2018. Horizontal velocities locally exceed 10 cm/year and rapidly decay with distance away from the caldera. We explore two end-member models and their combination to explain the post-eruptive deformation field: 1) viscoelastic relaxation caused by the co-eruptive caldera collapse and magma withdrawal, and 2) renewed magma inflow. We find parameter combinations for each model that explain the observed ground deformation. The purely viscoelastic relaxation model, consisting of a half-space composed of a 7-km thick elastic layer on top of a viscoelastic layer with a viscosity of  $3.0 \times 10^{18}$  Pa s reproduces broadly the observations. A simple magma inflow model consisting of a single point source with an inflow rate of  $1 \times 10^7$  m<sup>3</sup>/year at 0.7 km depth broadly fits the observations, but may be unrealistic. A more elaborate model of magma inflow into a 10-km deep sill combined with slip on the caldera ring fault explains the observations well. Our results suggest that the co-eruptive deformation field is likely influenced by viscoelastic relaxation, renewed magma inflow, or a combination of both processes.

## 1. Introduction

Ground deformation indicating volcano inflation, increase in seismic activity, changes in volcanic gas release, and thermal anomalies within a volcanic system are generally recognized as the indicators of volcanic unrest (e.g., Phillipson et al., 2013; Sigmundsson et al., 2010, 2018), which often precedes eruptions. A total of 1.9 km<sup>3</sup> magma left the magma body beneath the Bárðarbunga caldera during 2014–2015 Holuhraun eruption, causing 65 m caldera floor subsidence (Gudmundsson et al., 2016). After the eruption, the volcano continued to show signs of unrest. The unrest signals include elevated seismic activity, uplift and horizontal displacements away from the caldera, suggesting inflation of the volcano. In the post-eruptive period, ice cauldrons that formed during the co-eruptive period have grown and new ice-cauldrons have formed (Reynolds et al., 2019). Given the size and duration of this caldera reactivation eruption, we address the following question: can the post-eruptive unrest signal be explained by viscoelastic relaxation following major magma drainage and caldera collapse, or has there been renewed magma inflow into the system?

Magma inflow is one common explanation for volcanic unrest. In Iceland, elevated seismicity and inflation were observed, for example, prior to the Eyjafjallajökull eruptions in 2010 (Sigmundsson et al., 2010). Volcano inflation after an eruption can also represent magma inflow, as observed, e.g., in the Krafla rifting episode 1975–1984. A total of about twenty rifting-deflation events, including nine eruptions with lava flow, occurred during the period (e.g., Árnadóttir et al., 1998; Björnsson, 1985; Wright et al., 2012). Between the

eruptions and diking events at Krafla, continuous inflation of the volcano was interpreted to result from magma inflow.

Viscoelastic relaxation is a gradual stress recovery process in ductile regions of the lithosphere and asthenosphere. Due to elevated crustal temperature in volcano roots, viscoelastic relaxation may be pronounced in relation to large-volume magma transfer events. Multiple studies have focused on viscoelastic deformation related to rifting events and volcanic eruptions, for example, following dyking events during the 2005–2010 Dabbahu rifting episode at Afar (Hamling et al., 2014), at the Kutcharo caldera, Japan (Yamasaki et al., 2018), at Taal volcano (Morales Rivera et al., 2019) and Laguna del Maule volcano in Chile (Novoa et al., 2019). During the 2005–2010 Dabbahu rifting episode, continuous displacements were observed by Interferometric Synthetic Aperture Radar (InSAR) and Global Navigation Satellite System (GNSS). There, the observations suggest the post-rifting deformation reflects a combination of magma inflow and post-rifting viscoelastic response (Hamling et al., 2014). Yamasaki et al. (2018) explains uplift (1993–1995) and following subsidence (1995–1998) at Kutcharo caldera in Japan with a syn-inflation uplift due to magma emplacement and subsequent post-inflation subsidence signal due to viscoelastic response. Morales Rivera et al. (2019) explain the 2010–2011 unrest deformation at Taal volcano using a temperature-dependent spatially varied viscoelastic model. Novoa et al. (2019) studied Laguna del Maule volcano in Chile during an inflation period between 2007 and 2017 using a model of a viscoelastic shell surrounding a magma body. They find that the observed uplift can be explained by this model with magma inflow in the initial 4–6 years followed by viscoelastic relaxation. If the same data set is interpreted with a fully elastic model, magma accumulation over the full 10 year study interval is inferred. The magma source volume change for the viscoelastic model is 50% lower than that in the elastic model.

At Bárðarbunga, viscoelastic relaxation in relation to the caldera collapse should be considered as a potential explanation for the observed post-eruptive unrest, considering the result referred to above. Furthermore, Sigmundsson et al. (2020) show that the behavior of Bárðarbunga volcano in the pre-eruptive period and during the 2014–2015 eruption is well explained in terms of a model with magma inflow/outflow to/from a buoyant magma body within viscoelastic crust. When considering the post-eruptive period, surface unloading caused by co-eruptive caldera collapse due to major magma withdrawal can be expected to cause similar effects as the response of the Earth to retreating glaciers causing glacial isostatic adjustment (GIA), as both involve mass removal from the surface, albeit at very different spatial scales. The retreat of Icelandic glaciers since 1890, for instance, causes a viscoelastic ground deformation response as observed and modeled, e.g. by Auriac, (2014). The deposition of the Holuhraun lava field and the dyke propagation causes also viscoelastic ground deformation, which is observed by both GNSS and InSAR in the post-eruptive period (Grapenthin et al., 2017).

Our study focuses on the near-field ground deformation around the Bárðarbunga caldera after its 2014–2015 eruption. Specifically, our study period is the post-eruptive phase between May 2015 and October 2018. We first explore the roles of viscoelastic response to the co-eruptive events, and then consider alternative choices, such as renewed magma inflow. To understand the processes at work, we compare geodetic data sets from GNSS and InSAR geodesy with modeling results from: (a) viscoelastic response to surface unloading during caldera collapse in the co-eruptive period, (b) viscoelastic response due to magma withdrawal during the co-eruptive period, (c) renewed magma inflow during the post-eruptive period, and d) a combination of these processes.

## 2. Background

### 2.1. Bárðarbunga

The Bárðarbunga volcanic system in central Iceland lies at the divergent plate boundary between the North American and the Eurasian plates, partly covered by the Vatnajökull glacier. It is composed of the Bárðarbunga central volcano, with an  $8 \times 11$  km elliptical caldera, and fissure swarms extending 115 km southwest and 55 km north-northeast (Figure 1). The caldera is 500–700 m deep, with 700–800 m thick ice filling the caldera (Gudmundsson et al., 2016; Larsen & Gudmundsson, 2019). At least 23 eruptions are attributed to the Bárðarbunga volcanic system in historical time in Iceland. The majority of these eruptions have taken place underneath the ice-covered part of the volcanic system (Larsen, 2002; Thordarson & Lars-

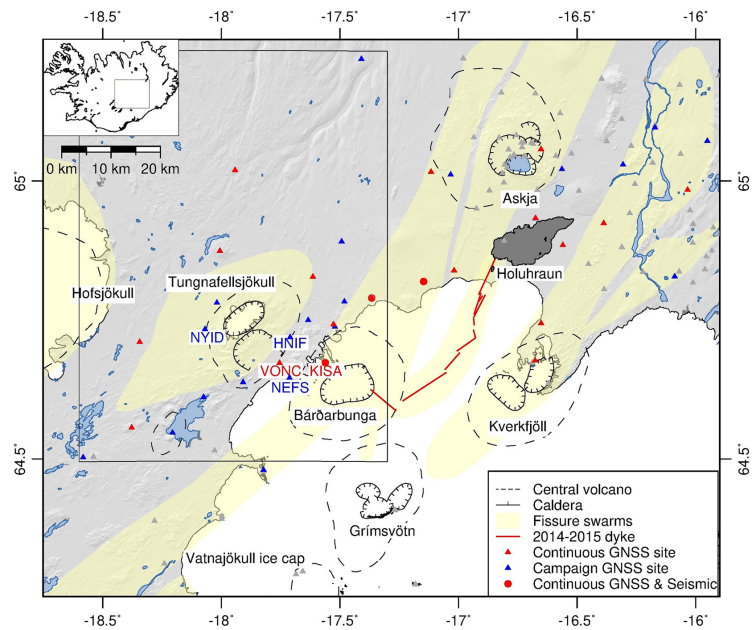


**Figure 1.** Map view of the Bárðarbunga volcano and surroundings showing central volcanoes, calderas, and fissure swarms (for geological layers, see Sigmundsson, Einarsson et al. (2020) and references there-in). Glaciers are shown in white. Segments of the 2014–2015 dyke path are indicated with red lines (Sigmundsson et al., 2015), and the new Hólhauur lava field is shown with dark gray shading. Blue and red triangles are the locations of campaign and continuous GNSS stations, respectively. Gray triangles are GNSS stations not used in this study. The names of five GNSS stations mentioned in the text are labeled: KISA, HNIF, VONC, NEFS, and NYID. Three seismic stations closest to the Bárðarbunga caldera are located close to continuous GNSS stations (red dots). Observations within the rectangular box are used for further analysis.

en, 2007). The most recent eruptive activity occurred from August 2014 to February 2015 (Gudmundsson et al., 2016; Pedersen et al., 2017). A 48 km-long dyke propagated laterally away from the Bárðarbunga caldera over a period of 2 weeks and then initiated a fissure eruption on the Hólhauur plain, north of the Vatnajökull ice cap, at the far end of the dyke (Figure 1). A 6-months-long effusive eruption drained a magma body located at about  $10 \pm 2$  km depth below the caldera (Gudmundsson et al., 2016; Hartley et al., 2018). The caldera floor subsided  $65 \pm 3$  m during the eruption as measured by GNSS and altimeter aircraft data. The caldera floor subsidence stopped at the time when the eruption terminated. The total volume of the caldera collapse was about  $1.8 \pm 0.2$  km<sup>3</sup> (Gudmundsson et al., 2016). The erupted lava volume is around  $1.4 \pm 0.2$  km<sup>3</sup> (Gudmundsson et al., 2016; Pedersen et al., 2017) and the total inferred volume intruded into the dyke is  $0.7 \pm 0.04$  km<sup>3</sup> (Parks et al., 2017). A total contraction of  $1.9 \pm 0.3$  km<sup>3</sup> of a magma body underneath Bárðarbunga caldera is inferred (Gudmundsson et al., 2016; Parks et al., 2017), about the same as the caldera collapse volume and the combined dyke and lava volume.

The caldera collapse and the formation of the Hólhauur lava field during the eruption were well monitored (e.g. Dumont et al., 2018; Gudmundsson et al., 2016; Pedersen et al., 2017; Riel et al., 2015; Sigmundsson et al., 2015). A continuous GNSS station installed in the center of the caldera on the ice surface, repeated radar altimeter survey, and maps from optical satellite images revealed the temporal evolution of subsidence within the caldera (Gudmundsson et al., 2016). The caldera bedrock subsidence rate was inferred to be

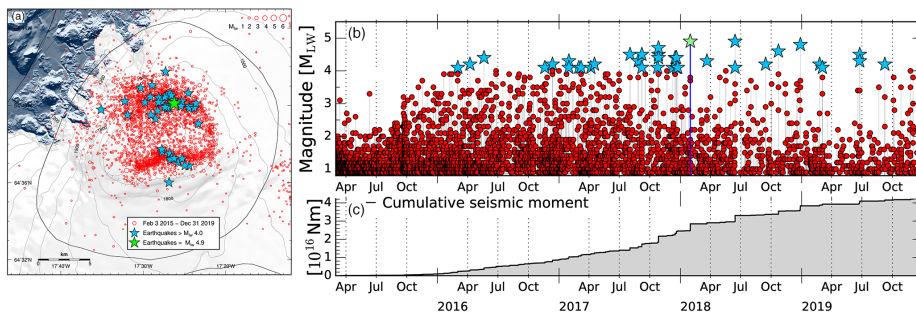


**Figure 2.** Seismicity  $M_{LW} > 0.8$  at the Bárðarbunga central volcano (within the area shown) from March 1, 2015 until December 31, 2019, as recorded and reported by the Icelandic Meteorological Office. (a) Locations of earthquakes, (b) earthquake magnitude, and (c) cumulative seismic moment. The background map (in panel a) shows the outline of the central volcano (oval shape), and outline of the caldera boundary (line with tick markers). Earthquakes focus on the Bárðarbunga caldera, with large earthquakes occurring along the caldera ring fault. Red circles are the earthquake locations and the size of circles depends on the magnitude of the earthquake. Stars indicate earthquakes  $M_{LW} > 4.0$  (largest earthquake is  $M_{LW} = 4.9$  marked by the green star).

around 1 m/day at the beginning and decayed near exponentially over time during the eruption, taking into consideration a correction for ice-flow (Gudmundsson et al., 2016).

## 2.2. Seismicity

Seismicity is an important indicator for volcanic unrest, which also provides information about the structure of volcanoes and evolution of the eruptions. Sigmundsson et al. (2015) interpreted the seismicity in the Bárðarbunga volcanic system between August 16 and September 6, 2014 to infer the path and the speed of dyke propagation. Gudmundsson et al. (2016) studied the seismicity during the six-months-long eruption period and the relationship between seismicity and caldera collapse. A detailed study of Bárðarbunga seismicity from January 2014 to August 2015 was carried out by Ágústsdóttir et al. (2019), focusing on the seismicity both at the caldera and along the dyke. The depths of earthquakes within the caldera are shallower than 7.5 km b.s.l. The long-term brittle-ductile transition is interpreted to be at 4–6 km b.s.l. based on the seismic study by Ágústsdóttir et al. (2019).

Earthquake activity in the Bárðarbunga area is monitored by the Icelandic Meteorological Office (IMO) using the Icelandic national seismic network (Böðvarsson et al., 1999). The seismicity in the initial 6 months after the eruption was low, but since September 2015, seismicity within the caldera has been elevated. Locations of earthquakes  $M_{LW} > 0.8$  detected after the eruption, between March 1, 2015 and December 31, 2019, cluster mainly at the caldera along the caldera ring faults, while some are along the dyke formed in 2014 (Figure 2a). More earthquakes are observed beneath the northern caldera rim than the southern rim, which is consistent with the pattern during the eruption period (Ágústsdóttir et al., 2019). Figures 2b and 2c show the earthquake magnitude and cumulative seismic moment release over the same period. Seismicity was low following the eruption until around September 2015, with only two  $M_{LW} > 3$  in that period. The frequency and magnitude of earthquakes increase afterward, with the largest earthquake of magnitude  $M_{LW} 4.9$  on 30 January 2018.

Jónsdóttir et al. (2019) investigated the waveforms of earthquakes in the post-eruptive period and compared earthquakes located at similar locations in the co-eruptive period. They found that the waveforms had changed polarity already two months after the eruption seized when compared to earthquakes during the eruption, from being consistent with downward (deflation) to up (inflation) movement of the central block of the caldera. The reversal is confirmed by moment tensor analysis of earthquakes with  $M_{LW} > 4.5$ , which shows that solutions were reversed after the unrest, or between February 19, 2015 and March 2, 2016 (in other words, solutions from this time interval show opposite mechanisms). Since then, the polarity of earthquakes has always been reversed compared with that observed during the eruption (Cardozo et al., 2019).

These observations suggest that general fault movements have remained reversed since two months after the eruption ended, when compared to fault movement during the caldera collapse.

### 2.3. Regional Deformation

In addition to magmatic processes, the Bárðarbunga area is affected by two long-term regional deformation processes: plate spreading and GIA. Plate spreading is caused by the divergence of the Eurasian and the North American plates. The plates are moving apart in direction N(100–105)°E at a full plate spreading rate of about 18–19 mm/year (Sigmundsson, Einarsson et al., 2020, and references therein). GIA is caused by mass loss of Icelandic glaciers, causing uplift and horizontal displacement away from Vatnajökull ice cap (e.g. Árnadóttir et al., 2009; Auriac, 2014; Drouin & Sigmundsson, 2019). Within our main study area (box in Figure 1), Drouin and Sigmundsson (2019) find GIA uplift rates ranging from 7 to 21 mm/year, and horizontal GIA displacements up to 1 mm/year during 2015–2018.

## 3. Geodetic Data and Processing

We use GNSS and InSAR to measure crustal deformation between May 2015 and October 2018 focusing on processes taking place in the vicinity of the Bárðarbunga caldera after the 2014–2015 eruption. Deformation south of Bárðarbunga is influenced by unrest of the Grímsvötn volcano, and the area to the northeast is influenced by viscoelastic response to the dyke intrusion (Grapenthin et al., 2017). We therefore exclude data from these areas in our modeling. The model input includes campaign and continuous GNSS data, and C-band Sentinel-1 interferograms. Models are applied to take plate spreading and GIA into account, in order to isolate the deformation caused by processes at the Bárðarbunga central volcano.

### 3.1. GNSS

We use data from a total of 22 GNSS stations located in the box in Figure 1, which includes 13 campaign and 9 continuous stations. GNSS campaign observations in the study area began in 1997 (Hreinsdóttir et al., 1998), but only at a few sites. Measurements were carried out in 1997, 2002, 2006, and again in 2014 at all sites, one month before the eruption started. We have carried out yearly campaign measurements after the eruption, beginning in 2015. The VONC continuous station (see Figure 1 for location) was installed in August 2013, 12 months prior to the beginning of the eruption, 9.5 km west of the caldera rim. In addition, five continuous stations were installed in the vicinity of Bárðarbunga during or after the eruption, three of which are within our study area (Sigmundsson et al., 2015). The continuous GNSS station closest to the caldera is the KISA station, 2.7 km northwest of the rim of the Bárðarbunga caldera, installed four months after the eruption ended.

We carried out GNSS campaign measurements every August in 2015, 2016, 2017, and 2018. The continuous and campaign GNSS data were analyzed using the GAMIT/GLOBK software version 10.6 (Herring et al., 2010; Hreinsdóttir et al., 2009) in the ITRF2008 (Altamimi et al., 2012) reference frame. Daily site positions and mean velocities were derived from the measurements. The average velocities are then transformed from the ITRF2008 reference frame to a stable Eurasian plate reference frame using GLOBK.

The majority of the GNSS timeseries show mostly steady horizontal displacement before and after the eruption until summer 2018 (Figure 3). Some deviation from a linear trend is, however, observed at the KISA continuous GNSS site. After the station was installed, the horizontal velocity was initially faster for a few months, but thereafter the station moves at a relatively constant rate until it slows down in 2018 (Figure 3). After removing the effects of plate spreading and GIA from the velocity timeseries, we find that the velocity at KISA station before August 2015 is twice the velocity compared to after August 2015. This period spans 4 months, roughly 10% of our study period (2015–2018). Vertical displacements are influenced by seasonal loading, mostly caused by snow accumulation during the winter and snow/ice melting during the summer (e.g., Drouin et al., 2017; Grapenthin et al., 2006). As GNSS campaigns in the area were carried out in August each year and our observation period starts and finishes at similar times of the year, the effects of annual variations are assumed to have minimal influence on the derived velocities at campaign and continuous sites inferred from linear fitting of the temporal evolution of the station coordinates. Observed average

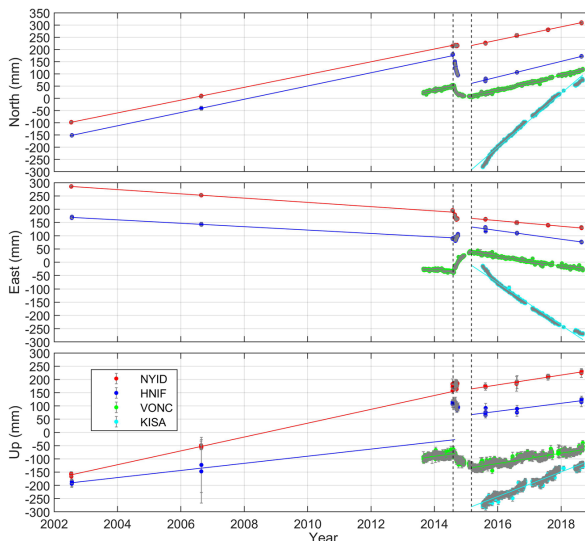


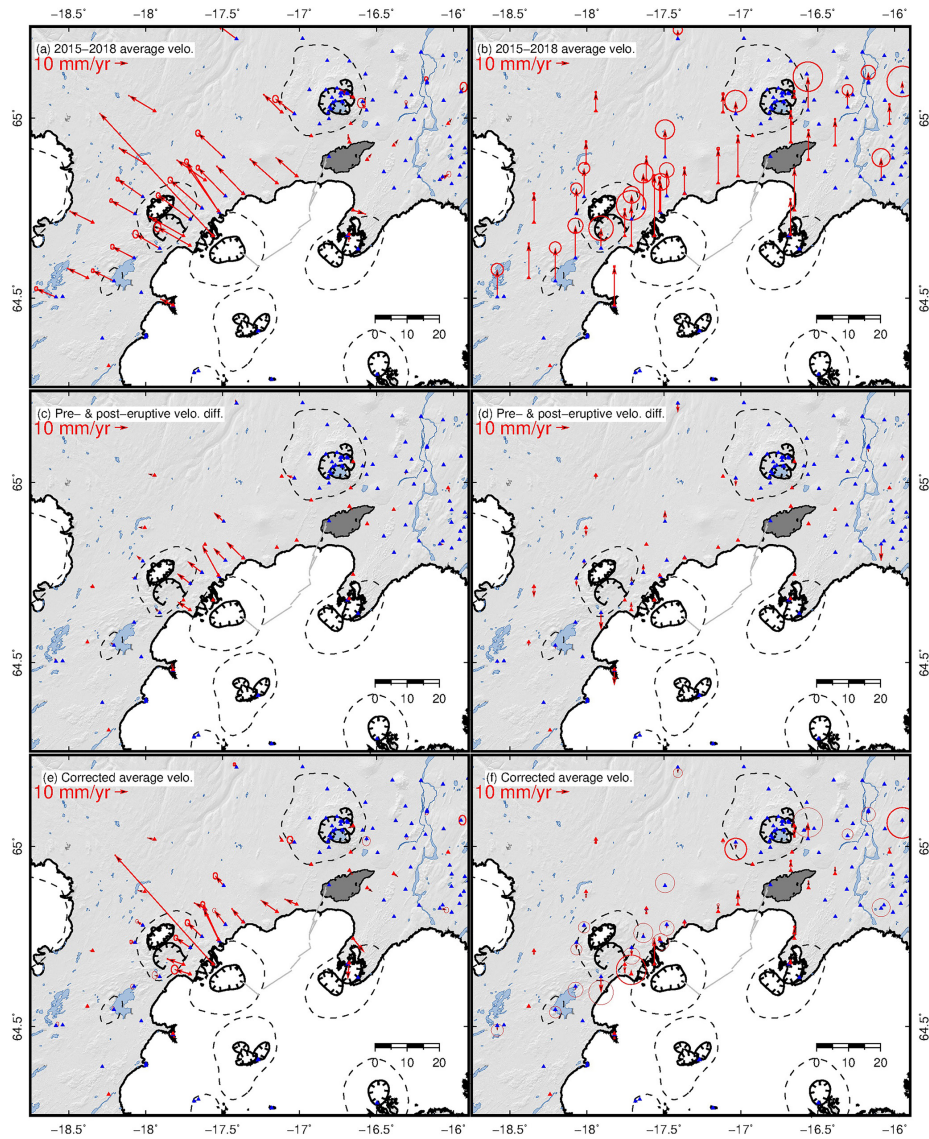
**Figure 3.** Examples of GNSS timeseries at selected campaign GNSS sites (NYID, HNFIF) and continuous GNSS sites (VONC and KISA) in the area northwest of Bárðarbunga caldera in the ITRF08 reference frame. Site locations are shown in Figure 1. The north, east and up components of displacements are displayed. The timeseries are shifted for presentation purpose. Seasonal variation is evident in the vertical component timeseries of the continuous stations, but are minor in the horizontal component. The dots show measured displacement, with error bars shown in gray. Lines show linear least squares fit to observations. Vertical dashed lines delimit the period of the 2014–2015 eruption.

horizontal and vertical GNSS 2015–2018 velocities are shown in Figures 4a and 4b (values are in Table S1). The velocities show consistent northwestward displacement and uplift. The maximum horizontal average velocity of  $126.6 \pm 0.1$  mm/year in N43°W direction is observed at the KISA station with an average uplift velocity of  $46.0 \pm 0.2$  mm/year. The average horizontal velocity at NEFS station (6.6 km from the caldera; see Figure 1 for location) is  $28.2 \pm 1.7$  mm/year, and the average vertical velocity is  $30.5 \pm 4.6$  mm/year. VONC station is 9.5 km from the caldera rim, with average horizontal and vertical velocity of  $29.5 \pm 0.1$  mm/year and  $20.2 \pm 0.3$  mm/year, respectively, relative to a stable Eurasian plate.

### 3.2. InSAR

InSAR, Interferometric Synthetic Aperture Radar, uses two or more SAR images to generate interferograms, showing the change in line-of-sight (LOS) distance from ground to satellite in the time period between the acquisitions of two images. We use SAR images from Sentinel-1A and 1B satellites, launched by the European Space Agency in 2014 and 2016, respectively (Torres et al., 2012). The two satellite orbits are 180° apart and provide SAR images every 12 days (prior to 2017) or 6 days (after 2017) along the same track, covering the same area. These C-band SAR images are collected regardless of daylight, but there is reduced interferogram coherence during the snow months and there is no long-term coherence on Iceland’s ice caps.

Interferograms were generated and unwrapped using the InSAR Scientific Computing Environment (ISCE) software (Rosen et al., 2012). Images from four Sentinel tracks are used in this study: Track 9 (descending), 111 (descending), 118 (ascending) and 147 (ascending). Timeseries analysis of the interferograms improves information about the time-history of the deformation and reduces noise. For each satellite track, we create average velocity maps covering the 2015–2018 period from interferograms with the same master image



using coherent pixels, after discarding images with significant atmospheric contaminations (Figures 5a and 5b, S1, and 6a–6d). The inferred average velocity maps are referenced to the velocities of continuous GNSS stations in Iceland, projected into the satellite line-of-sight (LOS), with the GNSS velocities referenced to the Eurasian plate. With this referencing, the GNSS and InSAR velocities are fully compatible. The angle between azimuth directions of the ascending and descending tracks is small and GNSS measurements indicate the north component of velocities in the area is of the same magnitude as in the east and up directions. In such a situation, the north component is expected to have minor influence on the LOS signal, so the average LOS velocity maps can be decomposed into an approximate east component (near-East, Figures 5c and 6e) and an approximate vertical (near-Up, Figures 5d and 6f) component. For a more detailed description of the InSAR data processing and decomposing into near-East and near-Up components, see Drouin and Sigmundsson (2019).

Inferred InSAR LOS velocity fields in the same area as shown in Figure 1 are shown in Figures 5a, 5b and S1. Figures 6a–6d are a zoomed-in deformation field focusing on the area around the Bárðarbunga caldera from all the tracks. A comparison of LOS and GNSS velocities is included in Figures 6 and S3. Ground deformation in our study area is caused by a combination of processes (Figure 5). Plate spreading is evident in Figure 5ca as a velocity gradient from west to east in the near-East direction. GIA is seen in Figure 5d as the gradient away from the ice cap to the area further away in the near-Up direction. The localized deformation signal around Bárðarbunga caldera indicates westward and upward motion in the area on the west side of Bárðarbunga caldera, suggesting inflation and displacement away from the caldera.

### 3.3. Corrections for GIA and Plate Spreading

GIA, plate spreading and volcanic activity are the main sources causing ground deformation in the Bárðarbunga area. The respective velocities are  $v_{GIA}$ ,  $v_{PS}$ , and  $v_{volcano}$ . The observed average velocity field,  $v_{observed}$ , can then be expressed as

$$v_{observed} = v_{GIA} + v_{PS} + v_{volcano} + v_{noise} \quad (1)$$

Here,  $v_{volcano}$  includes the deformation caused by magma movements and viscoelastic response due to previous volcanic activities.  $v_{noise}$  is the noise in the observation data as well as unmodeled deformation. We correct our observations for GIA and plate spreading to derive the ground deformation signal caused by volcanic processes alone. GIA is corrected using a scaled model from Auriac (2014) and the plate spreading correction uses a model by Drouin and Sigmundsson (2019).

The model of Auriac (2014) gives horizontal and vertical velocities caused by GIA for all Iceland for the period between 2008 and 2010. We assume the spatial pattern of the 2015–2018 deformation is the same as in the model of Auriac (2014) and apply scaling factors to the horizontal and vertical model velocities, as explained below, corrects the observed deformation field for GIA in our study period.

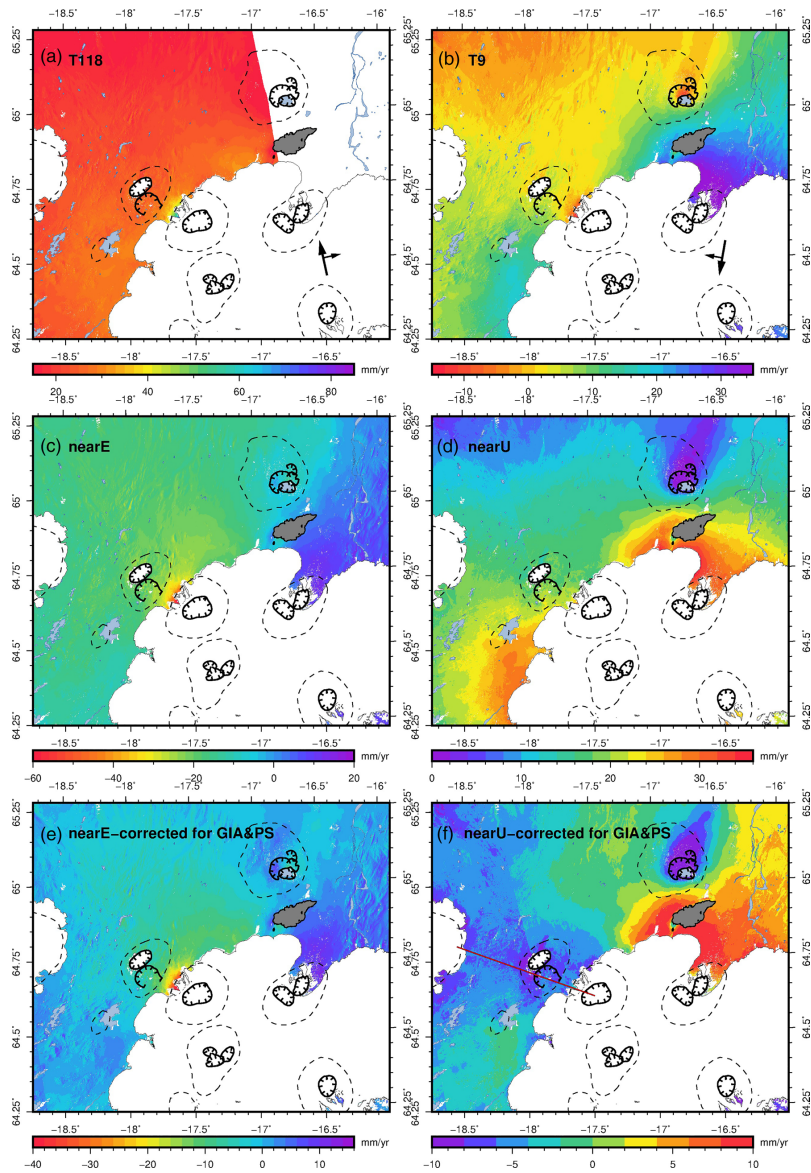
There are two approaches that may be applied to derive the post-eruptive volcano deformation signal: 1) compare velocity fields before and after the eruption, and 2) correct the post-eruptive velocity field for the effects of GIA and plate spreading signal. Approach 1 ( $v_1$ ) can be applied to a number of GNSS sites in the area as indicated in Figure 1, where there are measurements in both pre- (2002–2013,  $v_{observed}^{pre-eruptive}$ ) and post-eruptive (2015–2018,  $v_{observed}^{post-eruptive}$ ) periods. This can be expressed as

$$v_1 = v_{observed}^{post-eruptive} - v_{observed}^{pre-eruptive} = \delta_{GIA} + \delta_{PS} + \delta_{volcano} + \delta_{noise} \quad (2)$$

The result of approach 1 is shown in Figures 4c and 4d.  $\delta_{GIA}$  and  $\delta_{PS}$  are the differences in GIA and plate spreading (PS) velocities between the pre- and post-eruptive period. We assume the GIA and plate spreading signals are the same in both periods, and then  $\delta_{GIA} = \delta_{PS} = 0$ .  $\delta_{volcano}$  is the velocity difference between the

**Figure 4.** Average velocity field from GNSS measurements covering the period 2015–2018. The panels on the left/right are horizontal/vertical velocities, respectively. Uppermost panels (a and b) show inferred average velocity relative to a stable Eurasian plate. The middle panels (c and d) are the velocity differences between the pre- and post-eruptive periods at available sites. Bottom panels (e and f) show the average velocities after correcting for the effects of GIA and plate spreading with models (see Section 3.3). Ellipses at the end of the arrows indicate 95% confidence intervals.





post- and pre-eruptive period caused by volcanic activity, such as post-eruptive viscoelastic response due to magma withdrawal and dyke opening in our case. Assuming no volcano deformation in the pre-eruptive period, then the post-eruptive volcano deformation is  $v_1 = v_{volcano}^{post-eruptive} + \delta_{noise}$ . The noise,  $\delta_{noise}$ , is due to the combined effects of observation error and unmodeled effects, in both the pre-eruptive and post-eruptive periods.

The velocity field derived by approach 2 ( $v_2$ ) corrects the post-eruptive velocity field ( $v_{post-eruptive}$ ) for a GIA signal from a scaled version of a model ( $v_{GIA,model}$ ) by Auriac (2014) and the plate spreading with a model ( $v_{PS,model}$ ) by Drouin and Sigmundsson (2019), such that

$$v_2 = v_{post-eruptive} - \alpha v_{GIA,model} - v_{PS,model} = v_{volcano} + \delta_{noise} \quad (3)$$

There is need to adjust the GIA model for larger crustal response than accounted for in the model used, in relation to larger influence of glacial retreat in recent years (e.g., Compton et al., 2015). Therefore a scaling factor  $\alpha$  is applied to the GIA model, so the estimated GIA signal is  $\alpha v_{GIA,model}$ . The velocities after correction include velocities caused by volcanic processes ( $v_{volcano}$ ), as well as noise in the measurements ( $\delta_{noise}$ ). This approach can be applied to both InSAR and all GNSS velocities, as we do not need corresponding pre-eruptive observations. However, the GIA scaling factor  $\alpha$  is unknown and needs to be inferred. The model uncertainties should be considered as well.

We assume that the optimal GIA scaling factor has the result that the velocities from the two approaches are similar, that is  $v_1 \approx v_2$ . Therefore, we can use GNSS data, for which pre- and post-eruptive velocities exist, to determine the value of the scaling factor. By changing the scaling factor  $\alpha$  and comparing the horizontal and vertical velocities inferred by approaches 1 and 2, the  $\alpha$  which minimizes the residuals of  $v_1 - v_2$  from all sites is the optimal scaling factor. We calculated the horizontal and vertical velocities corrected from the GIA model with a scaling factor ranging from 1.0 to 5.0 with the steps of 0.1. By calculating the root mean square, we find the optimal scaling factors for horizontal and vertical are 2.8 and 1.5, respectively (Figure 7).

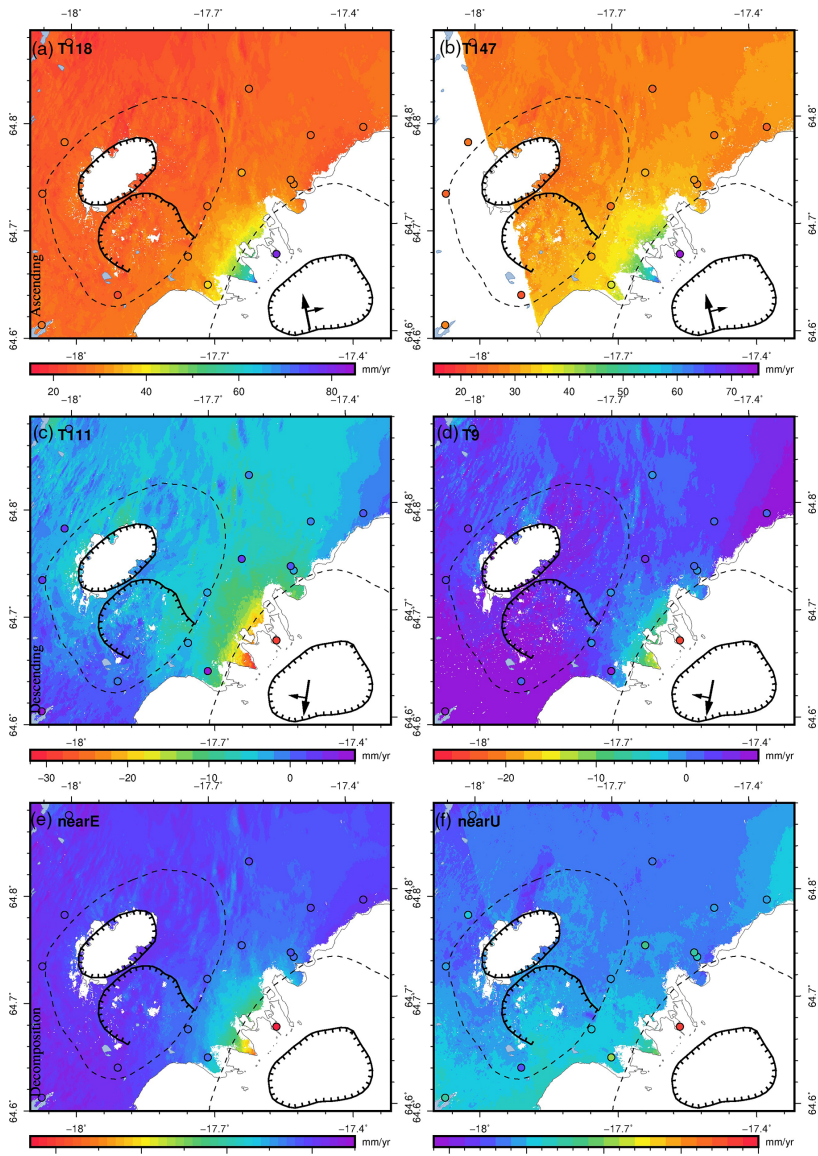
With the optimal scaling factor, approach 2 is applied to all velocities from both GNSS (results shown in Figures 4e and 4f, Table S1) and InSAR (results shown in Figures 5e, 5f and S2) measurements. Localized deformation around the Bárðarbunga caldera is clear in both GNSS and InSAR velocity fields after the correction. The post-eruptive deformation associated with the dyke is evident in Figure 5f, eventually due to a viscoelastic response. After correcting the GIA and plate spreading signals, the largest GNSS-observed horizontal and vertical uplift signal is at KISA GNSS station. The corrected average velocity at KISA is  $110.7 \pm 0.1$  mm/year in the horizontal direction and  $19.6 \pm 0.2$  mm/year in the vertical direction. The maximum corrected rate of subsidence is  $11.9 \pm 3.8$  mm/year. The result from approach 2 is the model input for the following sections.

#### 4. Modeling and Results

In this section we examine models to explain the observed localized deformation near Bárðarbunga central volcano, considering both viscoelastic response and magma inflow. Our goal, in particular, is to find a model that explains the horizontal displacement away from Bárðarbunga, the large spatial gradient in horizontal velocity near the caldera, the uplift in the vicinity of Bárðarbunga caldera and the minor subsidence further away, as shown in Figures 4e, 4f, 5e, and 5f. We compare the model results to GNSS and InSAR observations corrected for GIA and plate spreading to determine models that best explain the observations.

Our Earth models have layers consisting of homogeneous and isotropic material, with Poisson's ratio  $\nu = 0.25$  and shear modulus  $\mu = 30$  GPa (Grapenthin et al., 2006). As the elevation of the GNSS measuring points is in the range 684–1,632 m a.s.l.,  $z = 0$  in our models corresponds to 1,000 m a.s.l., which is around

**Figure 5.** InSAR average velocity fields from 2015–2018. LOS velocities from Sentinel-1 Track 118 (a) and 9 (b) (LOS velocities from Track 147 and 111 are in Figure S1). InSAR velocities are decomposed into near-East (c) and near-Up (d) components. After correcting for GIA and plate spreading, the remaining decomposed velocities in near-East and near-Up components are shown in (e) and (f). Velocities extracted from pixels along the red line in panel f are compared with the modeling results in Figures 12e, 13e and S7e.



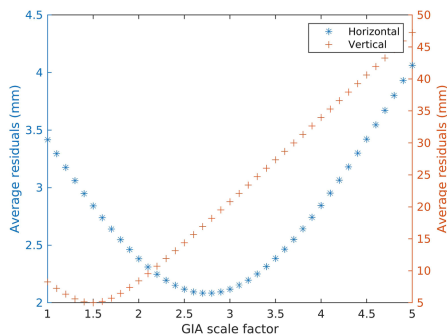


**Figure 7.** Derivation of optimal GIA scaling factors for GIA signal correction for horizontal and vertical velocities with the approach described in the text. The x-axis displays the value of the scaling factor for the GIA model, while y-axes show the root mean square residual in mm/year. Minimum values occur when scaling factors are 2.8 and 1.5 for the horizontal and vertical components, respectively.

the average elevation in the study area. Effects from topography and the glacier on top of the Bárðarbunga volcano are not considered specifically.

To understand the volcanic processes that cause the observed deformation, we model the following processes: (a) viscoelastic response to co-eruptive events, including the caldera collapse and magma withdrawal, (b) renewed magma inflow into the magmatic system after the eruption, and (c) combination of these processes. The modeling of the viscoelastic response to co-eruptive events considers the effects of the surface topography change associated with the collapse through a surface unloading model, and the effects of the magma withdrawal beneath the caldera using a point source of pressure change. After exploring features of viscoelastic ground deformation caused separately by surface unloading and pressure drop at depth, we combine the two models to evaluate the joint viscoelastic response. We then explore the possibility to explain the observed deformation signal with viscoelastic relaxation only, by varying the viscosity and volume contraction of the point source. To model the renewed magma inflow into the magmatic system in the post-eruptive period, we apply two different approaches. In the first approach, we model a single inflating magmatic source considering several possible source geometries separately. In the second approach, we consider a geodetically-inferred model previously used to explain the caldera collapse (Parks et al., 2017), with pressure variations in a sill under the caldera together with slip on caldera ring faults. Finally, we apply both approaches to derive combined models.

#### 4.1. Viscoelastic Response to Co-eruptive Events

The viscoelastic modeling is aimed at estimating the viscoelastic response caused by the large co-eruptive magma withdrawal and the surface unloading associated with caldera collapse. We expect a viscoelastic response given the strong observed GIA response in our study area as presented earlier. We use a three-dimensional (3D) semi-analytical software, RELAX (Barbot, 2014; Barbot & Fialko, 2010a, 2010b), to infer the viscoelastic response to the deformation sources. The model space is a Cartesian coordinate system. We use a model domain with horizontal dimensions of 256 km (North axis)  $\times$  256 km (East axis), and a thickness of 128 km. The grid size (pixel size used when running the software) is set to 0.5 km. The model has two rheological layers: an elastic layer on top of a viscoelastic layer characterized by linear Maxwell rheology. Figure 8a shows a zoomed-in section of the model. The coordinate of the center of the coordinate system is set to  $-17.48^\circ\text{E}$ ,  $64.63^\circ\text{N}$ , roughly at the surface projection of the center of a deflating sill under the Bárðarbunga caldera, responsible for the collapse, as in the model of Parks et al. (2017). We test models with the center at other geographical locations within the caldera to evaluate the influence of the exact location of the viscoelastic source center. The influence of source location is not large, but if the source center at  $-17.45^\circ\text{E}$ ,  $64.64^\circ\text{N}$  (corresponding to the BARC GNSS station (Gudmundsson et al., 2016), 1.81 km NE of the original point), the misfit is about 5% better than the original center.

As introduced above, seismic studies suggest the long-term brittle-ductile transition zone at Bárðarbunga is at 4–6 km b.s.l. (5–7 km depth in our model). For modeling purposes, we initially use a reference Earth model with the boundary between elastic and viscoelastic layer set at 7 km depth and viscosity  $\eta = 5 \times 10^{18}$  Pa s in the viscoelastic layer. This viscosity is similar to that inferred for the GIA model by Auriac et al. (2013). These model parameters are used in the following to demonstrate the behavior of the model.

The temporal scale of relaxation in our viscoelastic models relates to the Maxwell time, given by

**Figure 6.** A comparison between observed InSAR LOS average velocity field and GNSS velocities in 2015–2018 from Track 118 (a), 147 (b), 111 (c), and 9 (d). The InSAR LOS velocities are decomposed into near-East (e) and near-Up (f) components. The circles are 2015–2018 average velocities from GNSS measurements projected onto the LOS direction (a)–(d) or in the near-East (e) and near-Up (f) directions, with the same color scale as the InSAR velocities.

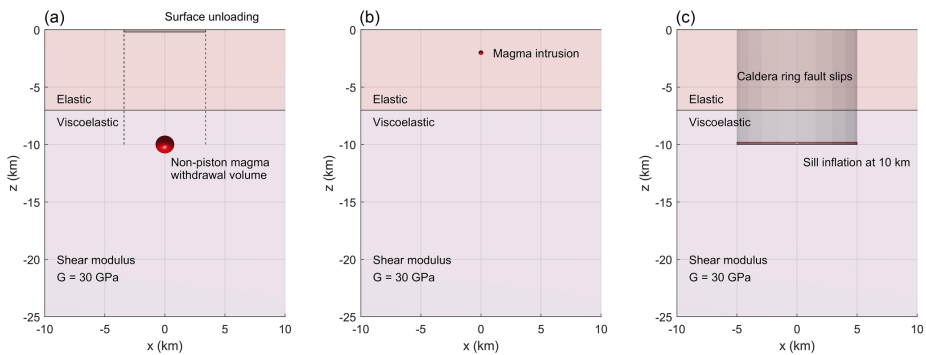


**Figure 8.** Zoomed cross-sections of models used in this study: (a) viscoelastic model driven by co-eruptive surface unloading and magma withdrawal at 10 km depth, (b) post-eruptive magma inflow modeled as a point source, (c) post-eruptive sill inflation and fault slip. The figures only show the central part of the model. Panel a shows vertical caldera ring faults as hatched lines. A central block within the caldera subsides and creates surface unloading. The viscoelastic response to the creation of this surface topography (the horizontal gray area at  $z = 0$  shown in panel a) is modeled. The effects of magma withdrawal under the caldera is modeled by a contracting point source at 10 km depth. We also search for possible deformation sources associated with renewed magma inflow in the post-eruptive period. Panel b shows a simple magma inflow into a point source with unknown depth and volume. Panel c shows the set up of an alternative magma inflow model, with a sill at 10 km depth that deflated during the eruption, inflating again, and simultaneous slip on caldera ring faults, as the central block of the caldera moves upwards.

$$\tau = \frac{\eta}{\mu} \quad (4)$$

where  $\mu$  is the shear modulus,  $\eta$  is the viscosity and  $\tau$  is the Maxwell time. For the reference Earth model with  $\mu = 30$  GPa, and  $\eta = 5 \times 10^{18}$  Pa s, the corresponding Maxwell time ( $\tau$ ) is 5.3 years. For modeling purposes, we assume that the caldera collapse and magma withdrawal occurred instantaneously as a step function, at time  $t = 0$ . We consider this to be the time when half of the magma withdrawal and caldera collapse had occurred. We accordingly set  $t = 0$  to October 15, 2014. The observational period in this study with GNSS and InSAR measurements ranges from May 2015 to October 2018, i.e., from 0.6 to 4 years since  $t = 0$  ( $\sim 0.6\tau$  of the reference Earth model). The eruption lasted for 6 months ( $\sim 0.1\tau$  of the reference Earth model). We explored the sensitivity of the model to the choice of  $t = 0$  by also setting  $t = 0$  to August 16, 2014, when the seismicity started within the Bárðarbunga caldera, but this has limited influence on the results.

We use a simplified viscoelastic model that broadly agrees with the understanding of what happened in the 2014–2015 eruption (including magma withdrawal from a source under the Bárðarbunga caldera and caldera collapse with slip on caldera ring fault system). Prior to the onset of the caldera collapse, it has been estimated that about  $0.3 \text{ km}^3$  of magma had already flowed into the lateral dyke (Sigmundsson, Pínel, et al., 2020). As more magma flowed out and the pressure dropped further in the underlying magma body, slip on caldera faults and downward movement of the piston within the caldera occurred, creating topographic change (Sigmundsson, Pínel, et al., 2020). Most of the magma volume drained from depth in the system was replaced by a subsiding piston (Gudmundsson et al., 2016; Parks et al., 2017). The pressure drop is implemented in the model as a certain volume contraction of the source, that we here refer to as non-piston magma withdrawal volume. This naming convention is chosen as a large part of the magma expelled from the source is replaced by a piston collapse into the source, and the non-piston magma withdrawal volume change is only a fraction of the eruption volume. In our modeling, the non-piston magma withdrawal volume is considered as a free parameter, but it turns out the modeling presented below finds an optimal value corresponding closely to the value of magma drained from the magma body prior to the caldera collapse (i.e.,  $\sim 0.3 \text{ km}^3$ ). The pressure source is under the caldera, at the approximate center of the modeled center of sill by Parks et al. (2017). The depth of the source is at 10 km, comparable to the results

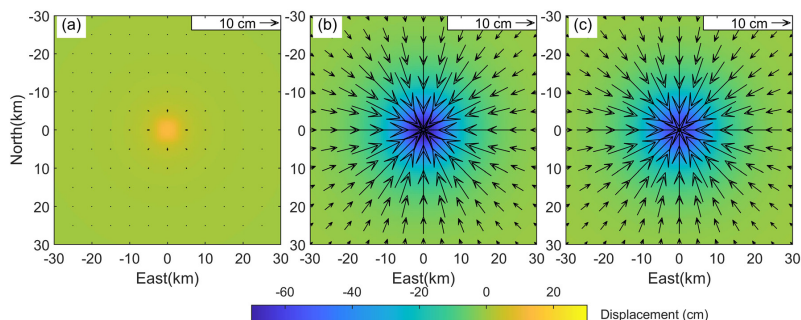


**Figure 9.** Surface displacement at  $t = 0^+$  in viscoelastic models (same as elastic response) of (a) surface unloading, which causes uplift and displacement away from the center at  $t = 0^+$ . (b) point source of volume decrease at 10 km depth, which causes subsidence and displacement toward center at  $t = 0^+$  of much larger amplitude. (c) joint model at  $t = 0^+$ , which is dominated by the effects the pressure decrease at 10 km depth at  $t = 0^+$ . See text for model parameters. Arrows show horizontal displacements and color represents vertical movement. Displacements are in cm.

of Parks et al. (2017); Gudmundsson et al. (2016) and Hartley et al. (2018). We consider also the additional unloading effect due to reduction of pressure head at the base of the underlying magma body and the creation of surface topography during the period when the caldera faults were moving. We implement this as unloading at the surface, corresponding to the topographic change, as it is simple to implement. In reality, this unloading effect may have rather been partly or fully applied at depth at the base of the magma body under the caldera, depending on how freely the subsiding piston within the caldera was slipping and the density contrast between magma and piston.

#### 4.1.1. Viscoelastic Response to Caldera Collapse

Caldera collapse was observed by multiple techniques during the Bárðarbunga eruption (e.g., Ágústsdóttir et al., 2019; Gudmundsson et al., 2016). The total volume of the collapse was  $1.8 \pm 0.2 \text{ km}^3$  (Gudmundsson et al., 2016). A surface unloading model is calculated in RELAX to understand the viscoelastic response to the caldera collapse process. Surface unloading is implemented in the model by applying negative pressure over a  $5.3 \text{ km} \times 5.3 \text{ km}$  square area corresponding to the removal of 65 m thick layer of rock with density of  $3 \times 10^3 \text{ kg/m}^3$ . The square area with 5.3 km on each side is calculated based on the total volume and the subsidence depth of the caldera floor. This corresponds to the collapsed volume of  $1.8 \text{ km}^3$ . The effect of the surface unloading is thus implemented in the RELAX software by evaluating the effect of reducing normal stress on the surface by  $1.91 \times 10^6 \text{ Pa}$ . The commands used to parameterize and run the RELAX models are given in Text S1.

The displacement at  $t = 0^+$  (shown in Figure 9a) represents the displacement immediately after the surface unloading occurred, which is the same as the purely elastic response. This immediate elastic response shows maximum uplift at the center of the footprint of the removed surface load. Horizontal displacement is away from the caldera. The average velocities during our study period are summarized in Figures 10a and 10d. The average velocities are about constant in the 4-year period, with uplift at the center and horizontal movement away from the center. The maximum uplift of the elastic response at  $t = 0^+$  is 13.2 cm at the center and the average maximum vertical velocity during the study period (0.6–4 years) is 9 mm/year. The maximum horizontal displacement is 2.0 cm at 3 km away from the center at  $t = 0^+$ . The maximum horizontal velocity is 1.4 mm/year during our study period.

#### 4.1.2. Viscoelastic Response to Magma Withdrawal

A total of about  $1.9 \text{ km}^3$  magma is inferred to have intruded and erupted during the eruption, over the same period as the caldera collapse (Gudmundsson et al., 2016). The viscoelastic contraction volume should, however, be only a fraction of this, because most of the magma expelled from the source is replaced by piston collapse into the source. In an initial reference model, we use  $0.3 \text{ km}^3$  as the modeled non-piston

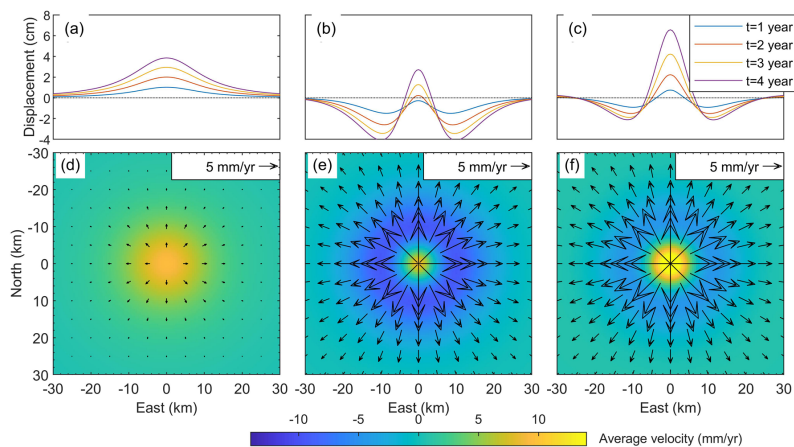


**Figure 10.** Displacements and average velocities since  $t = 0^+$  from viscoelastic models of surface unloading (a and d), a point source of volume decrease at 10 km depth (b and e), and joint model (c and f). Surface unloading and pressure decrease occurred at  $t = 0$  instantaneously. The deformation after  $t = 0$  are caused by the time delayed response of the viscoelastic material. The upper panels show the cumulative vertical displacement at  $y = 0$  since  $t = 0^+$  at  $t = 1, 2, 3,$  and  $4$  years. The lower panels show the horizontal (arrows) and vertical (colors) components of average velocities in our study period (0.6–4 years). Average velocities are in mm/year. Surface unloading causes uplift increasing approximately linearly with time and displacement away from center during our study period. Magma withdrawal causes horizontal movement away from the center. There is uplift at the center, and subsidence at the adjacent area.

magma withdrawal volume, which is the estimated volume of magma that flowed into the dyke prior to the caldera collapse (Sigmundsson, Pinel, et al., 2020). We use a point source approximation for the non-piston magma source, as it requires the minimum number of parameters to describe the source geometry. A point source of  $0.3 \text{ km}^3$  is removed instantaneously at  $t = 0$  at 10 km depth, the same source depth as modeled in Parks et al. (2017). The commands used to parameterize and run the RELAX models are given in Text S2.

The magma withdrawal causes contraction toward the center in horizontal direction and subsidence in vertical direction at  $t = 0^+$  (Figure 9b). The viscoelastic relaxation causes the surface to uplift at the center and subside in the adjacent area during our study period (0.6–4 years, Figure 10e). The horizontal velocity is approximately steady in time, with movement away from the center.

For  $t > 0$ , all areas initially subside. The subsidence rate at the center gradually reduces to 0 at  $t = 0.8$  years ( $0.2\tau$  of the reference Earth model), and then uplift begins (Figure 10b). Surrounding areas show similar trends with the vertical deformation changing from subsidence to uplift, but the time of reversal from subsidence to uplift increases with increasing distance from the center. At 10 km distance from the center, we observe the maximum rate of subsidence of 9 mm/year during our study period. The average velocity in the vertical direction at the center is 8 mm/year of uplift during our study period. Horizontal velocities are all radially away from the center after  $t = 0^+$ .

#### 4.1.3. Joint Viscoelastic Model

Combining the result of the two viscoelastic models, i.e. surface unloading and magma withdrawal, gives the joint viscoelastic response. The rheology assumed is linear, so the modeled effects can be added together to derive a joint model considering all the processes simultaneously. Figure 9c shows the displacement at  $t = 0^+$ . Figures 10c and 10f show the displacement at  $t = 1, 2, 3,$  and  $4$  years ( $0.2\tau, 0.4\tau, 0.6\tau,$  and  $0.8\tau$  of the reference Earth model) and the average velocity in the study period. The combined average velocity fields show horizontal movement away from the center, uplift at the center and subsidence in the adjacent area around the center in the vertical direction.

#### 4.1.4. Optimal Viscosity and Non-piston Magma Withdrawal Volume

We explore further the influence of two parameters in the viscoelastic model: the viscosity of the viscoelastic layer below 7 km depth and the non-piston magma withdrawal volume. For both elastic and Maxwell viscoelastic material, there is a linear relationship between the non-piston magma withdrawal volume and the corresponding displacement (Bonafede et al., 1986; Mogi, 1958). A single model output from RELAX can thus be used to generate a series of models with different non-piston magma withdrawal volumes, by scaling the model output. According to Equation 4, the Maxwell time and relaxation in the model scale linearly with the viscosity. Displacement rates predicted by the model scale inversely with the viscosity. For example, if the viscosity is  $5 \times 10^{18}$  Pa s and the shear modulus is 30 GPa, the Maxwell relaxation time is 5.3 years. If we change the viscosity to  $2.5 \times 10^{18}$  Pa s and keep the shear modulus the same, the relaxation time will be 2.6 years. Therefore, if viscosity is lowered by a factor of 2, the same deformation stage is reached twice as fast. Therefore, one can also use a single model to generate a series of models for different viscosities by appropriate scaling.

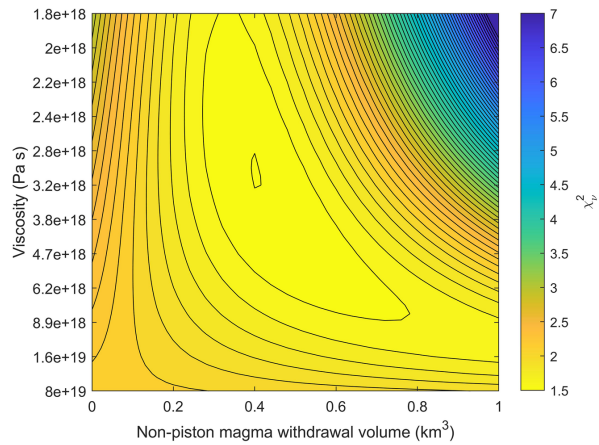
In practice, we derive the predicted deformation of different viscosity models from a single model by extracting the displacement difference between different timespans. We infer the surface velocities for a series of models with different non-piston magma withdrawal volume and different viscosities using the approach explained above (appropriate scaling of output from one RELAX model with viscosity of  $8 \times 10^{19}$  Pa s and non-piston magma withdrawal volume of  $1.0 \text{ km}^3$ ). The series of models are then compared to the observed average InSAR velocities from four satellite tracks. For each model, corresponding velocity residuals are evaluated by comparing the InSAR observed velocities and modeling velocities. The velocity residual is calculated using the reduced chi-squared statistic,  $\chi_v^2$ , as

$$\chi_v^2 = \sum_i \frac{1}{\nu} \frac{(O_i - C_i)^2}{\sigma_i^2} \quad (5)$$

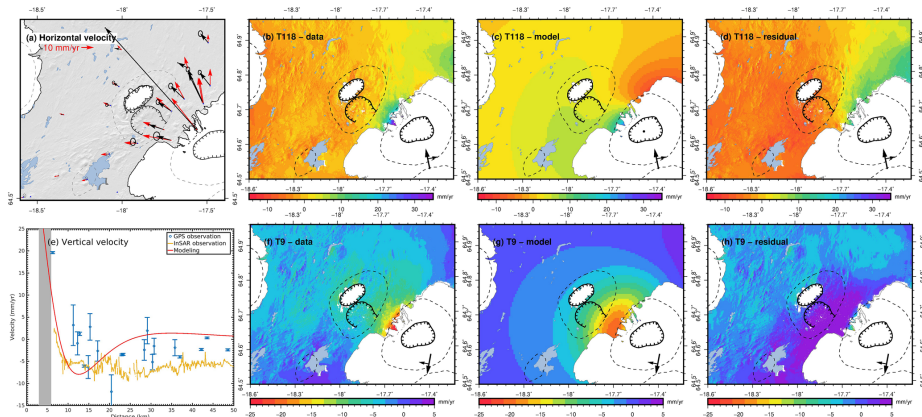
where  $O_i$  is the observed data at point  $i$  and  $C_i$  is the model output in the same grid geometry as the observations projected to LOS directions.  $\nu$  is here the degrees of freedom, equal to the number of observations minus the number of model parameters.  $\sigma_i^2$  is the data variance, found by adding together the InSAR velocity variance and the variance due to GIA and plate spreading correction, assuming zero covariance. The average InSAR velocity variance in each pixel is calculated during the creation of the average velocity maps. The variance in LOS direction is less than 3 mm/year in the majority of the area, except closest to the caldera, where the variance is up to 5 mm/year. We take 2 mm/year as the standard deviation of the GIA and plate spreading correction.  $\chi_v^2$  equal to 1 would indicate the model fully explains the observations considering the value of the variance. We explore models with non-piston magma withdrawal volume ranging between 0 and  $1.0 \text{ km}^3$  with  $0.04 \text{ km}^3$  steps and viscosity from  $1.8 \times 10^{18}$  Pa s to  $8 \times 10^{19}$  Pa s. The viscosity values tested are such that  $n_{\text{th}}$  viscosity =  $8 \times 10^{19}$  Pa s/ $n$ , where  $n$  is from 1 to 45.

Figure 11 shows the reduced chi-square statistic inferred with the procedure explained above. The lower the value of the reduced chi-square statistic, the better the model fits the observations. The minimal value is achieved with a viscosity of  $3.0 \times 10^{18}$  Pa s and a non-piston magma withdrawal volume of  $0.4 \text{ km}^3$ . The results indicate some trade-off between the parameters considered, such that a model with higher viscosity needs more non-piston magma withdrawal volume to fit the observations. Figures 12 and S4 show the GNSS and InSAR observations compared with the model with the optimal viscosity and non-piston magma withdrawal volume. The model reproduces the horizontal displacement outward from the caldera and subsidence measured by some GNSS stations (Figures 12a and 12e). The deformation pattern observed by both ascending and descending InSAR tracks can be broadly explained, especially the rapid velocity change in the area closest to the Bárðarbunga caldera in vertical direction (Figures 12b–12d, 12f–12h and S4). Nevertheless, some residuals still remain, including the fast horizontal velocity observed at KISA GNSS station and some LOS residuals (Figure 12 and S4).





**Figure 11.** Reduced chi-squared statistic for the InSAR observations and viscoelastic models. Colors indicate the reduced chi-squared statistic considering all the four InSAR tracks. The optimal (lowest value) is found when viscosity is  $3.0 \times 10^{18}$  Pa s and the non-piston magma withdrawal volume is  $0.4 \text{ km}^3$ . The contour line spacing is 0.1.



**Figure 12.** Corrected GNSS and InSAR average velocities compared with joint viscoelastic deformation model with optimal viscosity and non-piston magma withdrawal volume. The GNSS velocities in horizontal and vertical directions from model and observation are shown in panels a and e. Black arrows in panel a show observations and red arrows show the modeled velocities. Decomposed InSAR vertical displacement shown in panel e is taken along the profile indicated by the red line in Figure S4. Gray area in panel e is the distance range from the modeling center to the caldera rim. The figure displays InSAR input data (b) and (f), modeling result (c) and (g) and residuals (d) and (h). The dot in the caldera in panel c shows the modeling center of the joint viscoelastic model. Corrected InSAR average velocity from ascending Track 118 and descending Track 9 compared with joint viscoelastic deformation model in panels b–d and f–h, respectively (results from other two tracks are shown in Figure S4 in the supporting information). The observation period for average velocity is May 2015–October 2018.

#### 4.2. Renewed Magma Inflow Models

We consider another end-member series of models, that explore whether all the observed deformation can be explained by magma inflow during the post-eruptive period. Such a process is typically modeled considering fully elastic host rock behavior. Considering the viscoelastic modeling above, it is, however, also important to evaluate whether viscoelastic relaxation in response to magma inflow is significant. To evaluate that effect, we first apply an elastic magma inflow model (fitting the observations), and then consider how large potential viscoelastic effects would be for the reference Earth model. Over the considered time frame we find that the final viscoelastic response to steady magma inflow is less than 5% of the elastic signal in the vertical direction. Since this effect is so small, we did not consider it further. Due to the large volume of magma involved, the viscoelastic response to co-eruptive events, on the other hand, is significant during the post-eruptive period.

The input data (the same as for the viscoelastic model) include average LOS velocities from all four InSAR tracks, as well as average GNSS velocities. We assume a constant rate of magma inflow, modeling the first-order linear behavior observed by the GNSS timeseries in our observation period. Such a model, however, can't explain the velocity variations observed at the KISA station, in particular the higher velocity in the initial months after the eruption ended when compared to the main part of our study period. We use the Geodetic Bayesian Inversion Software (GBIS) by Bagnardi and Hooper (2018) to invert for the best-fitting model for magma inflow. We give the InSAR and GNSS data the same weight. We test two magma inflow models: 1) a single source with a center within a rectangular search area covering the caldera at any depth below the caldera, 2) a sill source at fixed 10 km depth combined with slip on a caldera ring fault. For the latter we consider the same sill and fault geometry as used by Parks et al. (2017), with reversed processes compared to what happened during the 2014–2015 eruption.

##### 4.2.1. Single Magma Inflow Source

We test different model geometries: A point source (Mogi, 1958), a sill (Okada, 1985), and a penny-shaped crack (Fialko et al., 2001). They differ in the number of parameters to describe them and the surface displacements they induce (e.g., Sigmundsson et al., 2018). First, we run the inversions with the GBIS software to obtain the optimal parameters for inflow source considering different geometries. The InSAR grid is subsampled using a quadtree partition in the software. We search for a source with a center within a rectangular area with northeast and southwest coordinates of (64.86°N, −17.13°E) and (64.50°N, −17.75°E), covering the caldera. The search intervals for the depth is constrained to be between 0 and 15 km, and for the inflow rate between 100 and 10<sup>9</sup> m<sup>3</sup>/year. No good sill models were found as the models did not converge, which may relate to the fact that we only have observation data limited to the northwest of the caldera.

The result suggests a most probable pressure increase as a point source at a depth of 0.7 km, with a yearly inflow rate corresponding to  $1.1 \times 10^7$  m<sup>3</sup>/year (Figures 13 and S5). The calculated maximum surface uplift above the point source is 4.9 m/year. The modeled interferograms fit the rapid velocity decay with distance away from the Bárðarbunga caldera, and the horizontal velocities measured by GNSS sites can be broadly explained by this shallow magma inflow model. The shallowness of the source and very fast uplift rate make this source unlikely, although the fit to the data is reasonable. Pressure increase at this depth could though relate to the formation of a magma intrusion rather than magma inflow into a long-lived magma body (temperature gradients would be extremely high), but no particular local seismicity is known within the caldera corresponding to such process. Alternatively, it could be a pressure source under the influence of interaction of a heat source and ground water, but this may also be unrealistic.

In order to evaluate the effect of data from the KISA station for the inversion results, we carried out an inversion without data from the KISA station (including all the other GNSS velocities and InSAR velocities), but did not get any realistic result. This test suggests that KISA station plays an essential role in controlling the optimal solution reached by the inversion for this model, as our observations are limited due to the glacier coverage on top of the caldera.

##### 4.2.2. Magma Inflow and Caldera Fault Slip

Another possible model for the observed deformation is that additional melt is being supplied to the same magma body that was tapped during the 2014–2015 eruption (at about 10 km depth). This process results

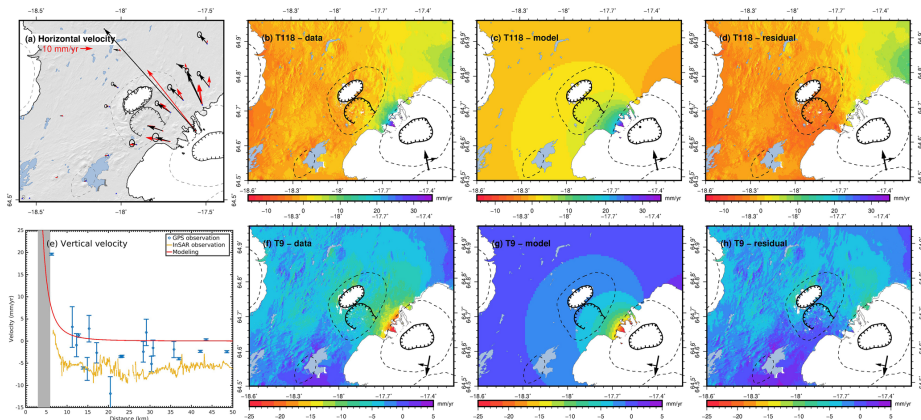


**Figure 13.** Corrected GNSS and InSAR average velocities compared with the optimal single magma inflow point source model. Data are presented in the same way as in Figure 12. Corrected InSAR average velocity from ascending Track 118 and descending Track 9 are compared with the magma inflow model (results from other two tracks are shown in Figure S5 in the supporting information). The point within the caldera in panel c shows the inferred location of the source center of the magma inflow model.

in inflation and slip on the caldera ring faults in such a manner that the piston inside the caldera moves upward: the reverse of the process that occurred during the caldera collapse. We use the model geometry and the approach of Parks et al. (2017) to simulate this process. A fixed geometry is used for the caldera ring fault and the sill under the caldera. A Bayesian inversion approach is applied to invert the joint GNSS and InSAR geodetic observations. The modeled sill is divided into 85 patches and the caldera ring fault into 192 patches. The geographical coordinates and shape of the sill patches and caldera ring fault patches are fixed, and the Bayesian approach derives values for the opening on the sill patches and slip on the fault patches within pre-set bounds. Thus the model searches for a distribution of opening and slip on the patches, rather than searching for traction applied to the patches. In the Bayesian approach we derived one million models fitting the observations, and from these the posterior probability functions for slip/opening on each patch were derived (Bagnardi & Hooper, 2018). The models presented show the derived mean slip/opening. This approach eliminates the need for a smoothness constraint, as the posterior probability functions identify the spread and trade-offs between the inferred model parameter values. For instance, if high slip on either of two adjacent patches will fit the data almost equally well, some solutions will have high slip on one, and some will have high slip on the other. The full posterior probability solution will identify this trade-off, and the mean slip for both patches will give approximately equal values, producing a smooth result (as seen in Figure 14). The maximum allowed sill opening and fault slip on each patch is set to 3 m during the inversion. In this modeling approach, the input InSAR results were resampled to a grid consisting of denser points close to the caldera and sparse points further away from the caldera (e.g. Figures 14b and 14f).

The predicted surface deformation by this model is shown in Figures 14 and S6. The largest sill opening is located in the northwest of the caldera (Figure 14). The yearly inflow rate is  $31.6 \pm 6.0$  million  $\text{m}^3/\text{year}$  and the surface uplift in the center of the caldera is 1.7 m/year. This joint model has the ability to fit the deformation gradient close to the caldera and it explains well the high horizontal velocity measured at the KISA GNSS point, closest to Bárðarbunga caldera. This model overestimates the InSAR signal closest to the caldera, so there are some residuals outside the ice cap. The observations from the KISA GNSS station play a minor role in these analysis. Inversion carried out excluding data from the KISA station (but otherwise the same) result in a model similar to that presented in Figure 14.

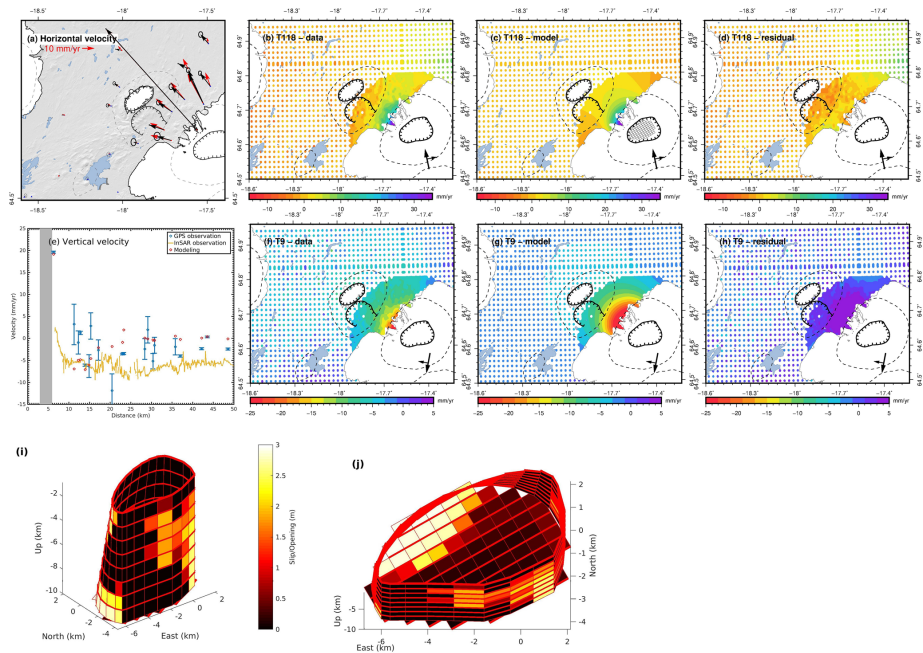


**Figure 14.** Corrected InSAR LOS velocities and GNSS horizontal velocities compared with the model predictions considering the response from a model with a sill fixed at 10 km depth and fault slip on the caldera ring fault. Data are presented in a similar way as in Figure 12. The input InSAR results were resampled to a grid consisting of denser points close to the caldera and sparse points further away from the caldera. The grid within the caldera in panel c illustrates the location of the modeled sill. Results from other two tracks are shown in Figure S6 in the supporting information. Panel i shows a three-dimensional view of amount of slip on the caldera fault patches according to the model, and panel j shows similarly the inferred sill opening.

### 4.3. Combination of Viscoelastic Relaxation and Magma Inflow Model

We evaluate two end-member cases in the previous two sections: 1) only viscoelastic relaxation, 2) only magma inflow. We find that an optimal model from both approaches can explain majority of the signals we observed. However, neither model alone fully explains the observations. The viscoelastic relaxation cannot explain some of the rapid velocity decay closest to the Bárðarbunga caldera, while the magma inflow model cannot explain observed subsidence in some nearby areas after correcting for a GIA model. A model combining viscoelastic relaxation and magma inflow may therefore best explain the observations. Here, we present examples of combined viscoelastic relaxation and renewed magma inflow models.

We initially considered to use the optimal viscoelastic model, which can explain the majority of the observed deformation field, and use residuals from this model as an input to a magma inflow model. However, the residuals are too insignificant to constrain a magma inflow model well. Here, we use our reference Earth model as an example of a joint model. We set the viscosity in our reference model as  $5 \times 10^{18}$  Pa s and use a non-piston magma withdrawal volume of  $0.4 \text{ km}^3$ . The viscosity is similar to that inferred for the GIA model by Auriac et al. (2013) and the volume is the same as found in Section 4.1.4. We consider the viscoelastic relaxation in the same manner as before. We test two combinations: 1) viscoelastic response to co-eruptive events and the renewed magma inflow in a single point source (Figures 8a and 8b), and 2) viscoelastic

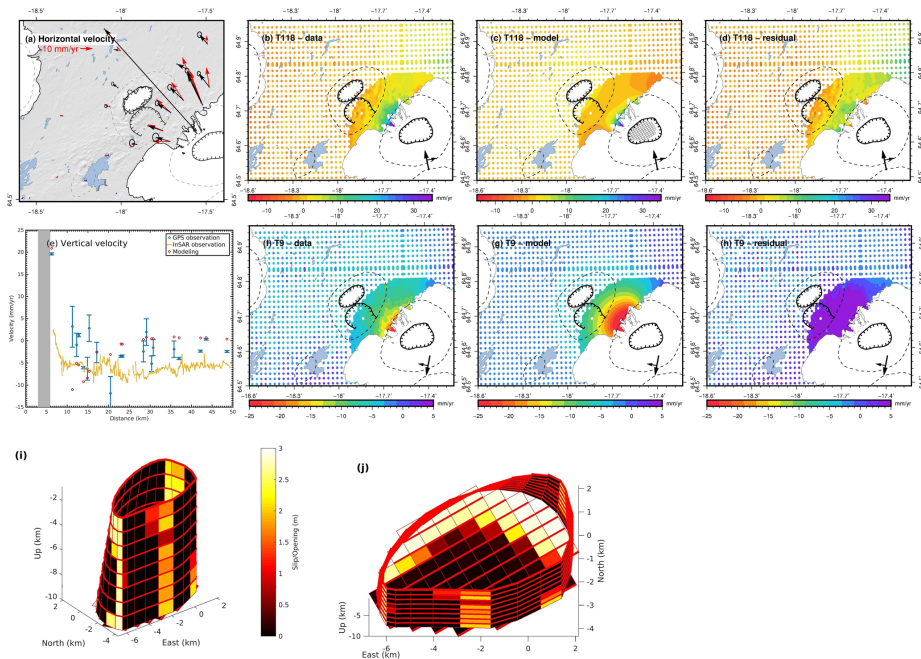


**Figure 15.** Corrected InSAR LOS velocities and GNSS horizontal velocities compared with the model predictions considering the response from viscoelastic relaxation of co-eruptive magma withdrawal and caldera collapse, as well as renewed magma inflow at 10 km together with caldera ring fault slip. Data and modeling results are presented in a similar way as in Figure 14. Results from the other two tracks are shown in Figure S8.

response to co-eruptive events together with fault slip on the caldera ring fault and sill inflation at 10 km depth (Figures 8a and 8c).

When combining the viscoelastic relaxation with a single inflation source (described in Text S3 and Figure S7), the result suggests a shallow source at 0.5 km depth with a yearly inflow rate of 2.4 million  $\text{m}^3/\text{year}$ , which may be unlikely. To find the result from the second combination, we combine the viscoelastic relaxation signal with sill inflation at a fixed 10 km depth together with slip on caldera ring fault (Figures 8a and 8c). After correcting for the co-eruptive viscoelastic relaxation model, the data are processed in the same way as in Section 4.2.2 with maximum allowed slip on the ring fault and opening of the sill set to 3 m. The inflation rate is  $39.3 \pm 4.8$  million  $\text{m}^3/\text{year}$ , with maximum opening occurring at the northern rim of the caldera (Figure 15 and Figure S8). The surface uplift at the center of the caldera caused by the sill and ring fault is 0.9 m/year. This joint model provides a good fit to the input data close to the caldera and can also explain the high horizontal velocity measured by the GNSS point KISA.

## 5. Discussion

The two independent and complementary geodetic techniques (InSAR and GNSS) are important for measuring the ground deformation at Bárðarbunga. A relatively large localized deformation signal was observed at the GNSS station closest to the caldera and is confirmed by the InSAR observations that show a rapid decay of LOS velocities with distance from the caldera at the same magnitude as the GNSS velocities. The

GNSS and InSAR observations can be compared in two ways. The three-dimensional GNSS velocities can be projected onto the InSAR satellite LOS direction for direct comparison with InSAR derived LOS velocities (Figures 6a–6d, and S3), or alternatively InSAR LOS velocities from different satellite tracks can be decomposed into near-East and near-Up velocities and these can be compared with the respective components of the GNSS velocities (Figures 6e and 6f). In our case, both approaches show good agreement between the GNSS and InSAR average velocities.

The volcanic deformation signal at Bárðarbunga is of a similar magnitude or smaller than the background deformation signal throughout a large part of the study area in both horizontal and vertical directions. The GNSS observed ground deformation velocities are in the range of 16–127 mm/year in the horizontal and 7–46 mm/year in the vertical direction. The average velocities are 30 mm/year and 22 mm/year in horizontal and vertical components, respectively. The average standard deviation of the average InSAR velocities are 2 mm/year. We corrected for two deformation processes prior to modeling the deformation: the GIA and plate spreading signals. GIA signal has a large influence on the vertical deformation field. The GIA model by Auriac et al. (2014) has a maximum vertical velocity of 22 mm/year from 2008 to 2010 in our study region but the GIA velocities are fluctuating in recent years, including accelerating and slowing down (Belart et al., 2020; Compton et al., 2015; Geirsson et al., 2020; von Hippel & Harig, 2019; Zemp et al., 2019). Therefore, we apply a scaling factor constrained from GNSS data to reduce the uncertainty caused by the GIA correction, although there may also be spatial variations different from that in the model used. The scaling factors found in our study are 2.8 for horizontal and 1.5 for vertical, comparable to the values found by Drouin et al. (2017) (3.2 for horizontal and 1.8 for vertical).

The correction process for GIA and plate spreading contains uncertainties. The plate spreading model we applied (Drouin & Sigmundsson, 2019) is composed of multiple back slip segments to find the best-fitting central axis of the plate boundary in Iceland. In our area, the modeled divergent plate boundary axis locates under the Vatnajökull ice cap passing through the Bárðarbunga caldera. Uncertainties in the plate spreading model may translate into uncertainties of up to a few mm/year within our study area. Regarding the GIA modeling approach, although we applied two approaches to get a better understanding of the current GIA signal, we still cannot reach millimeter-scale accuracy for GIA correction, because of eventual fluctuations in the GIA velocities, that may be influenced by an elastic response to irregular annual variations in mass balance of Iceland's ice caps. The different scaling factor we infer for the horizontal and vertical displacement components warrants an explanation. Their difference may relate to the GIA model approach. In a similar context, Spaans et al. (2015) consider that FEM models of the GIA process may systematically underpredict horizontal displacements, and therefore different scaling factors for vertical and horizontal components are needed. This takes into consideration both observed systematic difference in misfit in vertical and horizontal components of observed and predicted GIA velocities in a series of studies (e.g. Árnadóttir et al., 2009), and that previous studies (e.g. Latychev et al., 2005; Schmidt et al., 2012; Whitehouse et al., 2006) have shown that the horizontal component of the surface deformation is generally more sensitive to three-dimensional Earth structure than the vertical component. If we change the GIA scaling factor by 0.1, it leads to up to 0.2 mm/year horizontal velocity change or 2.2 mm/year vertical velocity change. Since the inferred volcano deformation signal is sensitive to the GIA and plate spreading corrections, our inferred deformation processes occurring beneath Bárðarbunga volcano are dependent on successful correction for the effects of GIA and plate spreading.

Viscoelastic models have been applied to different volcanic settings to explain observed post-eruptive inflation signals, and deflation signals following magma inflow. For example, Yamasaki et al. (2018, 2020) use a three-layer model at the Kutcharo caldera and a two-layer model at the Aira caldera in Japan to explain deformation, including an elastic top layer and viscoelastic layers below. Similar to these studies, our model structure assumes homogeneous material within each layer. Other studies apply spatially varying viscosity models, such as Morales Rivera et al. (2019) used for the 2010–2011 Taal volcano unrest and Del Negro et al. (2009) used for the 1993–1997 Etna volcano inflation. These authors apply temperature dependent models to explain the volcano deformation. Compared to our model, the temperature dependent spatially varying viscoelastic model is more complex. Compared to such models, the value of our model is to test in a relatively simple manner the role of viscosity of whole crustal sections, as known from GIA studies in Iceland, and evaluate the importance of the response of such structures for volcano behavior.

The viscoelastic response and the renewed magma inflow models suggest similar deformation pattern in the area outside of the ice cap. However, due to the spatial distribution of the available geodetic data, finding the contribution of each of the processes involved is difficult. This is because there is a trade-off between 1) viscosity and non-piston magma withdrawal volume (Figure 11), and 2) viscoelastic relaxation and renewed magma inflow. As presented in Figure 11, we can fit our observations equally well with higher non-piston magma withdrawal volume or lower viscosity. Since the deformation velocity in the far field outside the ice cap has similar patterns due to different processes, finding the optimal trade-off between viscoelastic relaxation and renewed magma inflow result is difficult with the available data.

The influence of a caldera ring fault slip needs to be considered when studying ground deformation at calderas, as slip at caldera faults may lead to localized deformation pattern. Liu et al. (2019) studied the influence of caldera fault slip with sill inflation at depth using experiments and boundary element modeling, and suggested that a localized geodetic signal is not necessarily caused by shallow intrusion. In our case, both the shallow magma inflow and a model with a sill inflation fixed at 10 km depth combined with fault slip can fit the rapid deformation signal closest to the Bárðarbunga caldera. The latter model has a sill volume increase around three times of the volume rate increase of the single shallow source model when considering the renewed magma inflow only. For the renewed magma inflow model, the accumulated magma volume of the 10-km sill source is 31.6 million km<sup>3</sup> during our study period, equivalent to 2% of the magma volume involved in the 2014–2015 eruption.

When considering a viscoelastic response to the co-eruptive events at the Bárðarbunga caldera, we need to consider the role of movements on the caldera faults. In particular, the caldera ring fault inclination can have a significant effect on deformation fields (Segall et al., 2019). The dip of the Bárðarbunga caldera ring fault is somewhat uncertain as different studies offer different conclusions. Parks et al. (2017) suggest near-vertical dipping. Gudmundsson et al. (2016) suggest outward dipping in the northern cluster and near vertical/vertical dip on the south side. Ágústsdóttir et al. (2019) find subvertical arrays of normal faults, with fault planes dipping inwards at  $\sim 60^\circ \pm 9^\circ$ . We decide to use vertical dipping faults in our simplified viscoelastic model.

Both the viscoelastic and renewed magma inflow models have their advantages and disadvantages. Viscoelastic relaxation explains the subsidence signal at some GNSS stations and in general we expect that viscoelastic material needs to be considered in this area because of ongoing GIA. Our viscoelastic relaxation model shows slight horizontal velocity variation in our study period, which is less than the temporal variation in the timeseries at the KISA GNSS station. A renewed magma inflow model with variable rate of inflow may be more appropriate to explain this temporal variation. The formation of seven ice cauldrons at Bárðarbunga after the eruption suggests the possibility of new heat sources at shallow depth, in favor of renewed magma inflow. Reynolds et al. (2019) modeled the fluid flow and heat transport in the uppermost 1 km of the crust, and suggested that the observed increase in geothermal activity could be reproduced by renewed magma inflow and high permeability pathways. However, as the study focused on modeling the geothermal activity within 1 km below the caldera bedrock, it is hard to use it to help us distinguish a preferred magma inflow model. Gravity surveys by Gudmundsson et al. (2020) can provide an additional constraint. The results can be interpreted in terms of rise of the caldera floor by several meters. Earthquake activity in the post-eruptive indicates a significant role of the caldera ring fault. The flipped polarity of focal mechanisms of earthquakes along the caldera ring fault in the post-eruptive period when compared to the co-eruptive period suggests the central block within the caldera (piston) has been moving upwards in the post-eruptive period (Cardozo et al., 2019; Jónsdóttir et al., 2019). Both viscoelastic relaxation and renewed magma inflow create uplift in our study period.

We compare the predictions of the different models of maximum uplift rate, the root mean square (RMS) residuals and the reduced chi-squared statistic between observations and models over a focused area (Table S2). The lowest RMS and reduced chi-squared statistics are for a model considering only fault slip and sill inflation at 10 km depth. Even if the magmatic recharge model provides mathematically the best fit with the approach presented here, the fact that it does not account for the effect of viscoelasticity is unsatisfying. One limitation of the model combining magma inflow and caldera fault slip is the large number of model parameters (85 sill patches and 192 caldera ring fault patches), which poses a risk of overfitting the data. A combination of this magma inflow and viscoelastic response has slightly higher RMS but may be more

satisfying in the sense that a viscoelastic rheology is likely more appropriate than a purely elastic rheology as previous work has demonstrated strong GIA effects in this area. The model considering only the viscoelastic relaxation has higher RMS misfit and produces a much smaller surface uplift at the source center. One thing to notice is that our viscoelastic relaxation modeling result strongly depends on the rheological structure of the area and we are only using one simplified model here. An improved viscoelastic model, considering different rheological structure or different source geometry and caldera collapse model, could provide a better fit to the data.

Our study suggests that viscoelastic response needs to be considered in general for large volume eruptions (e.g. the 2018 Kilauea eruption Neal et al., 2019), as the magnitude of post-eruptive ground deformation induced by viscoelastic deformation due to co-eruptive changes can be of a similar magnitude as deformation due to the post-eruptive magma inflow. The deformation field observed around Bárðarbunga outside the ice cap can either be explained by viscoelastic relaxation, renewed magma inflow, or a combination of both. The deformation fields generated by the two processes are hard to distinguish in the far field in our study period. Magma inflation at depth, together with the caldera ring fault slip, creates localized deformation similar to deformation caused by magma inflation at a shallower depth. Future work to improve our understanding of ground deformation at Bárðarbunga in the post-eruptive period could consider more complex source models in viscoelastic material, such as a sill model or more complex source geometries, as suggested for the co-eruptive period (Parks et al., 2017). More complex models for Earth and host rock rheology can be considered, as well as improved GIA and plate spreading corrections. We explored trade-offs between two viscoelastic model parameters (viscosity and non-piston magma withdrawal volume), but more exploration of other model parameters is also warranted in future studies. Investigating the stress changes caused by the viscoelastic relaxation and their influence on the magma inflow can also be considered. Analyzing the stress changes caused by viscoelastic relaxation and renewed magma inflow will deepen our understanding of the processes in the post-eruptive period and may improve our understanding of the processes involved.

## 6. Conclusion

Following caldera collapse and major magma drainage at the ice-covered Bárðarbunga caldera in 2014–2015, InSAR and GNSS data reveal post-eruptive inflation at the volcano in 2015–2018. After correcting for the effects of GIA and plate spreading, the remaining deformation signal around Bárðarbunga caldera in our study period (May 2015–October 2018) includes average horizontal displacement away from the caldera at maximum observed rate of  $\sim 111$  mm/year, with velocities decaying quickly with distance away from the caldera. The corrected vertical displacement has maximum uplift of  $\sim 20$  mm/year and maximum subsidence of  $\sim 12$  mm/year.

The corrected deformation signal can be broadly reproduced by a model incorporating viscoelastic relaxation due to co-eruptive processes (magma withdrawal under Bárðarbunga volcano and changes to surface topography due to caldera collapse), and/or continuous magma inflow in the post-eruptive period. When considering viscoelastic relaxation in a two layers Earth model driven by co-eruptive events as the only source for ground deformation, we derive optimal viscosity of  $3.0 \times 10^{18}$  Pa s. This model cannot reproduce the localized high horizontal velocity close to the Bárðarbunga caldera. When considering renewed magma inflow as the only source for ground deformation, the same corrected velocity field can be well explained by a sill inflation at  $\sim 10$  km depth expanding  $\sim 3.2 \times 10^7$  m<sup>3</sup>/year together with fault slip on a caldera ring fault. Viscoelastic relaxation alone, renewed magma inflow alone, or a combination of both processes can broadly explain the corrected deformation field. Our study therefore suggests that after a major eruption with a large volume of magma involved, viscoelastic relaxation needs to be considered when evaluating post-eruptive deformation as the resulting deformation may be of similar magnitude as that due to renewed magma inflow.

## Data Availability Statement

The authors thank the European Space Agency (ESA) for providing free-accessible Sentinel-1 satellite SAR data. MATLAB (2020) is used for calculation and figure plotting, and some figures are plotted by The Generic Mapping Tools (GMT) (Wessel et al., 2013). Parts of the campaign GNSS data were collected using



#### Acknowledgments

The authors thank staff at the Institute of Earth Sciences at University of Iceland and the Icelandic Meteorological Office, in particular Páll Einarsson, Gro Birkefeldt Møller Pedersen, and Ásta Rut Hjartardóttir, as well as Vala Hjörleifsdóttir from Reykjavík Energy, for extensive discussions with us about the research presented here. The authors thank Sveinbjörn Steinþórsson who provided important technical help for the campaign GNSS fieldwork and Cécile Adélie Ducrocq for advice on GNSS data processing. The authors thank Amandine Auriac who provided the Glacial Isostatic Adjustment model grid (Auriac, 2014). The authors thank the Research Fund of University of Iceland for funding for the Ph.D. work of the first author (S. Li), which this research is a part of. Partial financial support from the H2020 project EUROVOLC funded by the European Commission is acknowledged (grant number 731070). R.G. acknowledges partial support for this work through NSF grant EAR-1464546. The authors thank the reviewers for comments that helped us to greatly improve the manuscript.

#### References

- Ágústsdóttir, T., Winder, T., Woods, J., White, R. S., Greenfield, T., & Brandsdóttir, B. (2019). Intense seismicity during the 2014–2015 Bárðarbunga–Holuhraun rifting event, Iceland, reveals the nature of dike-induced earthquakes and caldera collapse mechanisms. *Journal of Geophysical Research: Solid Earth*, *124*, 8331–8357. <https://doi.org/10.1029/2018jb016010>
- Altamimi, Z., Métivier, L., & Collilieux, X. (2012). ITRF2008 plate motion model. *Journal of Geophysical Research*, *117*(7), 1–14. <https://doi.org/10.1029/2011JB008930>
- Árnadóttir, T., Lund, B., Jiang, W., Geirsson, H., Björnsson, H., Einarsson, P., & Sigurdsson, T. (2009). Glacial rebound and plate spreading: Results from the first countrywide GPS observations in Iceland. *Geophysical Journal International*, *177*(2), 691–716. <https://doi.org/10.1111/j.1365-246X.2008.04059.x>
- Árnadóttir, T., Sigurdsson, F., & Delaney, P. (1998). Sources of crustal deformation associated with the Krafla, Iceland, eruption of September 1984. *Geophysical Research Letters*, *25*(7), 1043–1046. <https://doi.org/10.1029/98GL50655>
- Auriac, A. (2014). *Solid Earth response to ice retreat and glacial surges in Iceland inferred from satellite radar interferometry and finite element modelling*. Ph.D. thesis. Faculty of Earth Sciences, University of Iceland.
- Auriac, A., Sigurdsson, F., Hooper, A., Spaans, K. H., Björnsson, H., Pálsson, F., et al. (2014). InSAR observations and models of crustal deformation due to a glacial surge in Iceland. *Geophysical Journal International*, *198*(3), 1329–1341. <https://doi.org/10.1093/gji/ggu205>
- Auriac, A., Spaans, K. H., Sigurdsson, F., Hooper, A., Schmidt, P., & Lund, B. (2013). Iceland rising: Solid Earth response to ice retreat inferred from satellite radar interferometry and viscoelastic modeling. *Journal of Geophysical Research: Solid Earth*, *118*(4), 1331–1344. <https://doi.org/10.1002/jgrb.50082>
- Bagnardi, M., & Hooper, A. (2018). Inversion of surface deformation data for rapid estimates of source parameters and uncertainties: A Bayesian approach. *Geochemistry, Geophysics, Geosystems*, *19*(7), 2194–2211. <https://doi.org/10.1029/2018GC007585>
- Barbot, S. (2014). *Relax v1.0.7 [software]*. Computational Infrastructure for Geodynamics (CIG). <https://geodynamics.org/cig/software/relax/>
- Barbot, S., & Fialko, Y. (2010). A unified continuum representation of post-seismic relaxation mechanisms: Semi-analytic models of afterslip, poroelastic rebound and viscoelastic flow: Semi-analytic models of postseismic transient. *Geophysical Journal International*, *182*(3), 1124–1140. <https://doi.org/10.1111/j.1365-246X.2010.04678.x>
- Barbot, S., & Fialko, Y. (2010). Fourier-domain green's function for an elastic semi-infinite solid under gravity, with applications to earthquake and volcano deformation: Fourier-domain elastic solutions. *Geophysical Journal International*, *182*(2), 568–582. <https://doi.org/10.1111/j.1365-246X.2010.04655.x>
- Belart, J. M., Magnússon, E., Berthier, E., Gunnlaugsson, Á., Pálsson, F., Aðalgeirsdóttir, G., et al. (2020). Mass balance of 14 Icelandic Glaciers, 1945–2017: Spatial variations and links with climate. *Frontiers of Earth Science*, *8*, 1–15. <https://doi.org/10.1029/2018GC007585>
- Björnsson, A. (1985). Dynamics of crustal rifting in NE Iceland. *Journal of Geophysical Research*, *90*(B12), 10151–10162. <https://doi.org/10.1029/JB090B12p10151>
- Bonafede, M., Dragoni, M., & Quarení, F. (1986). Displacement and stress fields produced by a centre of dilatation and by a pressure source in a viscoelastic half-space: Application to the study of ground deformation and seismic activity at Campi Flegrei, Italy. *Geophysical Journal of the Royal Astronomical Society*, *87*(2), 455–485. <https://doi.org/10.1111/j.1365-246X.1986.tb06632.x>
- Böðvarsson, R., Rögnvaldsson, S. T., Slunga, R., & Kjartansson, E. (1999). The SIL data acquisition system-at present and beyond year 2000. *Physics of the Earth and Planetary Interiors*, *113*(1–4), 89–101. [https://doi.org/10.1016/S0031-9201\(99\)00032-1](https://doi.org/10.1016/S0031-9201(99)00032-1)
- Cardozo, F. R. R., Hjörleifsdóttir, V., Jónsdóttir, K., Geirsson, H., Iglesias, A., & Franco-Sánchez, S. I. (2019). *A timeline of the Bárðarbunga 2014–2015 caldera collapse and fissure eruption, based on a full waveform moment tensor catalog*. San Francisco, CA: AGU Fall Meeting Abstracts.
- Compton, K., Bennett, R. A., & Hreinsdóttir, S. (2015). Climate-driven vertical acceleration of Icelandic crust measured by continuous GPS geodesy. *Geophysical Research Letters*, *42*(3), 743–750. <https://doi.org/10.1002/2014GL062446>
- Del Negro, C., Currenti, G., & Scandura, D. (2009). Temperature-dependent viscoelastic modeling of ground deformation: Application to Etna volcano during the 1993–1997 inflation period. *Physics of the Earth and Planetary Interiors*, *172*(3–4), 299–309. <https://doi.org/10.1016/j.pepi.2008.10.019>
- Drouin, V., & Sigurdsson, F. (2019). Countrywide observations of plate spreading and glacial isostatic adjustment in Iceland inferred by sentinel-1 radar interferometry, 2015–2018. *Geophysical Research Letters*, *46*, 8046–8055. <https://doi.org/10.1029/2019GL082629>
- Drouin, V., Sigurdsson, F., Ófeigsson, B. G., Hreinsdóttir, S., Sturkell, E., & Einarsson, P. (2017). Deformation in the Northern Volcanic Zone of Iceland 2008–2014: An interplay of tectonic, magmatic, and glacial isostatic deformation. *Journal of Geophysical Research: Solid Earth*, *122*(4), 3158–3178. <https://doi.org/10.1002/2016JB013206>
- Dumont, S., Sigurdsson, F., Parks, M. M., Drouin, V. J. P., Pedersen, G. B. M., Jónsdóttir, I., et al. (2018). Integration of SAR data into monitoring of the 2014–2015 Holuhraun eruption, Iceland: Contribution of the Icelandic volcanoes super site and the FutureVolc projects. *Frontiers in Earth Science*, *6*, 231. <https://doi.org/10.3389/feart.2018.00231>
- Fialko, Y., Khazan, Y., & Simons, M. (2001). Deformation due to a pressurized horizontal circular crack in an elastic half-space, with applications to volcano geodesy. *Geophysical Journal International*, *146*(1), 181–190. <https://doi.org/10.1046/j.1365-246X.2001.00452.x>
- Geirsson, H., Valsson, G., Ófeigsson, B. G., Sturkell, E., Árnadóttir, T., Lafemina, P. C., et al. (2020). *Significant temporal changes in glacio isostatic adjustment in Iceland during the 1950s to present*. Paper presented at EGU General Assembly Conference Abstracts (pp. 17390).
- Grapenthin, R., S. Li, B. Ófeigsson, F. Sigurdsson, V. Drouin, S. Hreinsdóttir, et al. (2017). *Post-eruptive deformation following the 2014 Holuhraun rift, Iceland*. In AGU Fall Meeting Abstracts.
- Grapenthin, R., Sigurdsson, F., Geirsson, H., Árnadóttir, T., & Pínel, V. (2006). Icelandic rhythmicity: Annual modulation of land elevation and plate spreading by snow load. *Geophysical Research Letters*, *33*(24), L24305. <https://doi.org/10.1029/2006GL028081>

- Gudmundsson, M. T., Högnadóttir, T., Sigmundsson, F., & Geirsson, H. (2020). *Rapid resurgence of the subglacial Bárðarbunga caldera following collapse in 2014–2015, quantified with repeated Bouguer gravity surveys*. Paper presented at EGU General Assembly Conference Abstracts (pp. 18744).
- Gudmundsson, M. T., Jónsdóttir, K., Hooper, A., Holohan, E. P., Halldórsson, S. A., Ófeigsson, B. G., et al. (2016). Gradual caldera collapse at Bárðarbunga volcano, Iceland, regulated by lateral magma outflow. *Science*, 353(6296), aaf8988. <https://doi.org/10.1126/science.aaf8988>
- Hamling, I. J., Wright, T. J., Calais, E., Lewi, E., & Fukahata, Y. (2014). InSAR observations of post-rifting deformation around the Dabbahu rift segment, Afar, Ethiopia. *Geophysical Journal International*, 197(1), 33–49. <https://doi.org/10.1093/gji/ggu003>
- Hartley, M. E., Bali, E., Maclennan, J., Neave, D. A., & Halldórsson, S. A. (2018). Melt inclusion constraints on petrogenesis of the 2014–2015 Holuhraun eruption, Iceland. *Contributions to Mineralogy and Petrology*, 173(2), 1–23. <https://doi.org/10.1007/s00410-017-1435-0>
- Herring, T., King, R., & McClusky, S. (2010). *Introduction to gamit/globk*. Cambridge, MA: Massachusetts Institute of Technology.
- Heinsdóttir, S., Árnadóttir, T., Deciem, J., Geirsson, H., Tryggvason, A., Bennett, R. A., & LaFemina, P. (2009). A complex earthquake sequence captured by the continuous gps network in Swiceland. *Geophysical Research Letters*, 36(12), L12309. <https://doi.org/10.1029/2009GL038391>
- Heinsdóttir, S., Einarsson, P., Jónsson, S., & Sigmundsson, F. (1998). *GPS geodetic measurements around Bárðarbunga volcano, central Iceland 1997*. Science Institute.
- Jónsdóttir, K., Rodriguez, F. R., Hjørleifsdóttir, V., Jónsdóttir, K., Rodriguez, F. R., & Hjørleifsdóttir, V. (2019). *Using repeating earthquakes to reveal temporal behavior of caldera faults*. Paper presented at EGU General Assembly Conference Abstract EGU2019-2690.
- Larsen, G. (2002). A brief overview of eruptions from ice-covered and ice-capped volcanic systems in Iceland during the past 11 centuries: Frequency, periodicity and implications. *Geological Society, London, Special Publications*, 202(1), 81–90. <https://doi.org/10.1144/gsl.sp.2002.202.01.05>
- Larsen, G., & Gudmundsson, M. T. (2019). *The Bárðarbunga volcanic system, Catalogue of Icelandic Volcanoes*. Icelandic Meteorological Office, the Institute of Earth Sciences at the University of Iceland, and the Civil Protection Department of the National Commissioner of the Iceland Police. Retrieved from <https://icelandicvolcanoes.is/?volcano=BAR#>
- Latychev, K., Mitrovica, J. X., Tamisiea, M. E., Tromp, J., & Moucha, R. (2005). Influence of lithospheric thickness variations on 3-D crustal velocities due to glacial isostatic adjustment. *Geophysical Research Letters*, 32(1), 1–4. <https://doi.org/10.1029/2004GL021454>
- Liu, Y.-K., Ruch, J., Vasyura-Bathke, H., & Jónsson, S. (2019). Influence of ring faulting in localizing surface deformation at subsiding calderas. *Earth and Planetary Science Letters*, 526(115), 784. <https://doi.org/10.1016/j.epsl.2019.115784>
- MATLAB (2020). *Version 9.8.0.1323502 (R2020a)*. Natick, MA: The MathWorks Inc.
- Mogi, K. (1958). Relations between the eruptions of various volcanoes and the deformations of the ground surfaces around them. *Bulletin of the Earthquake Research Institute*, 36, 99–134. <https://doi.org/10.1016/j.epsl.2004.04.016>
- Morales Rivera, A. M., Amelung, F., Albino, F., & Gregg, P. M. (2019). Impact of crustal rheology on temperature-dependent viscoelastic models of volcano deformation: Application to Taal volcano, Philippines. *Journal of Geophysical Research: Solid Earth*, 124, 978–994. <https://doi.org/10.1029/2018JB016054>
- Neal, C. A., Brantley, S. R., Antolik, L., Babb, J. L., Burgess, M., Calles, K., et al. (2019). The 2018 rift eruption and summit collapse of Kilauea volcano. *Science*, 363(6425), 367–374. <https://doi.org/10.1126/science.aav7046>
- Novoa, C., Remy, D., Gerbault, M., Baez, J. C., Tassara, A., Cordova, L., et al. (2019). Viscoelastic relaxation: A mechanism to explain the decennial large surface displacements at the Laguna del Maule silicic volcanic complex. *Earth and Planetary Science Letters*, 521, 46–59. <https://doi.org/10.1016/j.epsl.2019.06.005>
- Okada, Y. (1985). Surface deformation due to shear and tensile faults in a half-space. *Bulletin of the Seismological Society of America*, 75(4), 1135–1154. [https://doi.org/10.1016/0148-9062\(86\)90674-1](https://doi.org/10.1016/0148-9062(86)90674-1)
- Parks, M. M., Heimisson, E. R., Sigmundsson, F., Hooper, A., Vogfjörð, K. S., Árnadóttir, T., et al. (2017). Evolution of deformation and stress changes during the caldera collapse and dyking at Bárðarbunga, 2014–2015: Implication for triggering of seismicity at nearby Tungnafellsjökull volcano. *Earth and Planetary Science Letters*, 462, 212–223. <https://doi.org/10.1016/j.epsl.2017.01.020>
- Pedersen, G., Höskuldsson, A., Dürig, T., Thordarson, T., Jónsdóttir, I., Riisshuus, M., et al. (2017). Lava field evolution and emplacement dynamics of the 2014–2015 basaltic fissure eruption at Holuhraun, Iceland. *Journal of Volcanology and Geothermal Research*, 340, 155–169. <https://doi.org/10.1016/j.jvolgeores.2017.02.027>
- Phillipson, G., Sobradelo, R., & Gottsmann, J. (2013). Global volcanic unrest in the 21st century: An analysis of the first decade. *Journal of Volcanology and Geothermal Research*, 264, 183–196. <https://doi.org/10.1016/j.jvolgeores.2013.08.004>
- Reynolds, H. I., Gudmundsson, M. T., Högnadóttir, T., & Axelsson, G. (2019). Changes in geothermal activity at Bárðarbunga, Iceland, Following the 2014–2015 caldera collapse. Investigated using geothermal system modeling. *Journal of Geophysical Research: Solid Earth*, 124(8), 8187–8204. <https://doi.org/10.1029/2018JB017290>
- Riel, B., Millilo, P., Simons, M., Lundgren, P., Kanamori, H., & Samsonov, S. (2015). The collapse of Bárðarbunga caldera, Iceland. *Geophysical Journal International*, 202, 446–453. <https://doi.org/10.1093/gji/ggv157>
- Rosen, P. A., Gurrula, E., Sacco, G. F., & Zebker, H. (2012). *The InSAR scientific computing environment*. Paper presented at EUSAR 2012; 9th European conference on synthetic aperture radar (pp. 730–733). Nuremberg, Germany: VDE.
- Schmidt, P., Lund, B., Árnadóttir, T., & Schmeling, H. (2012). Glacial isostatic adjustment constrains dehydration stiffening beneath Iceland. *Earth and Planetary Science Letters*, 359–360, 152–161. <https://doi.org/10.1016/j.epsl.2012.10.015>
- Segall, P., Anderson, K. R., Johanson, I., & Miklius, A. (2019). Mechanics of inflationary deformation during caldera collapse: Evidence from the 2018 Kilauea eruption. *Geophysical Research Letters*, 46(21), 11782–11789. <https://doi.org/10.1029/2019GL084689>
- Sigmundsson, F., Einarsson, P., Hjartardóttir, Á. R., Drouin, V., Jónsdóttir, K., Árnadóttir, T., et al. (2020). Geodynamics of Iceland and the signatures of plate spreading. *Journal of Volcanology and Geothermal Research*, 391(106), 436. <https://doi.org/10.1016/j.jvolgeores.2018.08.014>
- Sigmundsson, F., Hooper, A., Heinsdóttir, S., Vogfjörð, K. S., Ófeigsson, B. G., Heimisson, E. R., et al. (2015). Segmented lateral dyke growth in a rifting event at Bárðarbunga volcanic system, Iceland. *Nature*, 517(7533), 191–195. <https://doi.org/10.1038/nature14111>
- Sigmundsson, F., Heinsdóttir, S., Hooper, A., Árnadóttir, T., Pedersen, R., Roberts, M. J., et al. (2010). Intrusion triggering of the 2010 Eyjafjallajökull explosive eruption. *Nature*, 468(7322), 426–430. <https://doi.org/10.1038/nature09558>
- Sigmundsson, F., Parks, M., Pedersen, R., Jónsdóttir, K., Ófeigsson, B. G., Grapenthin, R., et al. (2018). *Magma movements in volcanic plumbing systems and their associated ground deformation and seismic patterns*. Volcanic and igneous plumbing systems (pp. 285–322). Elsevier. <https://doi.org/10.1016/b978-0-12-809749-6.00011-x>
- Sigmundsson, F., Pinel, V., Grapenthin, R., Hooper, A., Halldórsson, S. A., Einarsson, P., et al. (2020). Unexpected large eruptions from buoyant magma bodies within viscoelastic crust. *Nature Communications*, 11(1), 2403. <https://doi.org/10.1038/s41467-020-16054-6>

- Spaans, K., Hreinsdóttir, S., Hooper, A., & Ófeigsson, B. G. (2015). Crustal movements due to Iceland's shrinking ice caps mimic magma inflow signal at Katla volcano. *Scientific Reports*, 5, 1–8. <https://doi.org/10.1038/srep10285>
- Thordarson, T., & Larsen, G. (2007). Volcanism in Iceland in historical time: Volcano types, eruption styles and eruptive history. *Journal of Geodynamics*, 43(1), 118–152. <https://doi.org/10.1016/j.jog.2006.09.005>
- Torres, R., Snoeij, P., Geudtner, D., Bibby, D., Davidson, M., Attema, E., et al. (2012). GMES Sentinel-1 mission. *Remote Sensing of Environment*, 120, 9–24. <https://doi.org/10.1016/j.rse.2011.05.028>
- von Hippel, M., & Harig, C. (2019). Long-term and inter-annual mass changes in the Iceland ice cap determined from grace gravity using slepian functions. *Frontiers in Earth Science*, 7, 171. <https://doi.org/10.3389/feart.2019.00171>
- Wessel, P., Smith, W. H. F., Scharroo, R., Luis, J., & Wobbe, F. (2013). Generic mapping tools: Improved version released. *Eos, Transactions - American Geophysical Union*, 94(45), 409–410. <https://doi.org/10.1002/2013EO450001>
- Whitehouse, P., Latychev, K., Milne, G. A., Mitrovica, J. X., & Kendall, R. (2006). Impact of 3-D Earth structure on Fennoscandian glacial isostatic adjustment: Implications for space-geodetic estimates of present-day crustal deformations. *Geophysical Research Letters*, 33(13), L13302. <https://doi.org/10.1029/2006GL026568>
- Wright, T. J., Sigmundsson, F., Pagli, C., Belachew, M., Hamling, I. J., Brandsdóttir, B., et al. (2012). Geophysical constraints on the dynamics of spreading centres from rifting episodes on land. *Nature Geoscience*, 5(4), 242–250. <https://doi.org/10.1038/ngeo1428>
- Yamasaki, T., Kobayashi, T., Wright, T. J., & Fukahata, Y. (2018). Viscoelastic crustal deformation by magmatic intrusion: A case study in the Kutcharo caldera, eastern Hokkaido, Japan. *Journal of Volcanology and Geothermal Research*, 349, 128–145. <https://doi.org/10.1016/j.jvolgeores.2017.10.011>
- Yamasaki, T., Sigmundsson, F., & Iguchi, M. (2020). Viscoelastic crustal response to magma supply and discharge in the upper crust: Implications for the uplift of the Aira caldera before and after the 1914 eruption of the Sakurajima volcano. *Earth and Planetary Science Letters*, 531, 115981. <https://doi.org/10.1016/j.epsl.2019.115981>
- Zemp, M., Huss, M., Thibert, E., Eckert, N., McNabb, R., Huber, J., et al. (2019). Global glacier mass changes and their contributions to sea-level rise from 1961 to 2016. *Nature*, 568(7752), 382–386. <https://doi.org/10.1038/s41586-019-1071-0>



*JGR – Solid Earth*

Supporting Information for

**Ground deformation after a caldera collapse: Contributions of magma inflow and viscoelastic response to the 2015-2018 deformation field around Bárðarbunga, Iceland**

Siqi Li<sup>1</sup>, Freysteinn Sigmundsson<sup>1</sup>, Vincent Drouin<sup>2</sup>, Michelle M. Parks<sup>3</sup>, Benedikt G. Ofeigsson<sup>3</sup>, Kristín Jónsdóttir<sup>3</sup>, Ronni Grapenthin<sup>4</sup>, Halldór Geirsson<sup>1</sup>, Andrew Hooper<sup>5</sup> and Sigrún Hreinsdóttir<sup>6</sup>

<sup>1</sup>Nordic Volcanological Center, Institute of Earth Sciences, University of Iceland, Iceland

<sup>2</sup>Iceland GeoSurvey ÍSOR, Reykjavik, Iceland

<sup>3</sup>Icelandic Meteorological Office, Reykjavik, Iceland

<sup>4</sup>Geophysical Institute and Dept. Geosciences, University of Alaska Fairbanks, USA

<sup>5</sup>COMET, School of Earth and Environment, University of Leeds, UK

<sup>6</sup>GNS Science, New Zealand

**Contents of this file**

Texts S1 to S3  
Figures S1 to S8  
Table S1 to S2  
References

**Introduction**

Texts S1 and S2 give the input commands for viscoelastic modeling using RELAX software version 1.0.7 [Barbot 2014; Barbot and Fialko 2010a, 2010b], for both surface unloading model and the point source model with volume decrease at depth. Text S3 explains the modeling procedures for a combined model considering both the viscoelastic relaxation and renewed magma inflow into a point source, with results presented in Figure S7. Figure S1 shows the 2015-2018 LOS velocity fields for Sentinel-1 Track 147 and Track 111. Figure S2 shows LOS velocities after correcting for Glacial Isostatic Adjustment (GIA) and plate spreading signals for all the four satellite tracks used. Figure S3 shows the comparison between the GNSS and InSAR velocities in the LOS direction. The modeling results from the two satellite tracks (Track 147 and 111) for all the models are presented in Figure S4, S5, S6, and S8 (complementing information for the other two tracks in the main text). The GNSS station velocities are listed in Table S1. A comparison between the different models is presented in Table S2.

**Text S1.**

Commands used for viscoelastic modeling using RELAX software for surface unloading model. The units all correspond to SI units. The elastic layer is 7 km thick and the viscoelastic material has a viscosity of  $5 \times 10^{18}$  Pa s. The surface unloading is in a squared area with each side of 5.3 km. The pressure decrease at the surface is  $1.91 \times 10^6$  Pa.

grid size (sx1,sx2,sx3)	# n depth gammadot0 cohesion
512 512 512	1 7000 1.89216e-1 0
# sampling size & smoothing	# number of linear weak zones
(dx1,dx2,dx3,beta) & nyquist	0
500 500 500 0.2 1	# number of powerlaw viscous interfaces
# origin position and rotation	0
0 0 0	# number of friction faults
# observation depth (displacement and	0
stress)	# number of inter-seismic strike-slip
0 0.5	segments
# output directory	0
surfeload.53	# number of inter-seismic tensile segments
# elastic parameters (lambda,mu) and gravity	0
effect	# number of coseismic events
30e9 30e9 8.33e-7	1
# integration time and time step	# number of shear dislocations
100 0.1	0
# number of observation planes	# index slip x1 x2 x3 length width strike dip
0	rake
# number of observation points	0
0	# number of dilatation point sources
# number of stress observation segments	0
0	# number of surface loads
# number of prestress interfaces	1
0	# n xs ys length width t3 T phi
# number of linear viscous interfaces	1 0 0 5262 5262 -1.91e6 0 0
1	

**Text S2.**

Commands used for viscoelastic modeling using RELAX software for the point source with volume decrease at depth model. The units all correspond to SI units. The elastic layer is 7 km thick and the viscoelastic material has a viscosity of  $5 \times 10^{18}$  Pa s. The point source is at 10 km depth with a volume decrease of  $0.3 \text{ km}^3$ .

# grid size (sx1,sx2,sx3)	1
512 512 512	# n depth gammadot0 cohesion
# sampling size & smoothing	1 7000 1.89216e-1 0
(dx1,dx2,dx3,beta) & nyquist	# number of linear weak zones
500 500 500 0.2 1	0
# origin position and rotation	# number of powerlaw viscous interfaces
0 0 0	0
# observation depth (displacement and stress)	# number of friction faults
0 0.5	0
# output directory	# number of inter-seismic strike-slip segments
spherical_visco	0
# elastic parameters (lambda,mu) and gravity effect	# number of inter-seismic tensile segments
30e9 30e9 8.33e-7	0
# integration time and time step	# number of coseismic events
100 0.1	1
# number of observation planes	# number of shear dislocations
0	0
# number of observation points	# number of tensile cracks
0	0
# number of stress observation segments	# number of dilatation point sources
0	1
# number of prestress interfaces	# no dilatation xs ys zs
0	1 -5.283e8 0 0 10000
# number of linear viscous interfaces	# number of surface loads
0	

**Text S3.**

We combine the viscoelastic relaxation and renewed magma inflow as a point source in section 4.3 as an example considering both processes. The rheology assumed is linear, so the modeled effects can be added together to derive a joint model. For the viscoelastic relaxation model, we use our reference Earth model as an example of a joint model. We accordingly set the viscosity in our reference model as  $5 \times 10^{18}$  Pa s and use a non-piston magma withdrawal volume of  $0.4 \text{ km}^3$ . The viscosity is similar to that inferred for the GIA model (Auriac et al., 2013) and the volume is the same as we found in section 4.1. We consider the viscoelastic relaxation in the same manner as before, and present here viscoelastic response to co-eruptive events and the renewed magma inflow in a single point source (Figure 8a and b).

Firstly, we run RELAX to calculate the average velocity for the viscoelastic response to the surface unloading and magma withdrawal. We subtract this result from the observations corrected for GIA and plate spreading signals. Then these residual GNSS and InSAR velocities are used to evaluate the optimal magma inflow model with a single magma inflow source or a sill source together with caldera fault slip. Thus, we consider both viscoelastic relaxation and renewed magma inflow in this approach.

With this approach, the GBIS inversion suggests a single inflation source at a depth of 0.5 km and a yearly inflow rate of 2.4 million  $\text{m}^3/\text{yr}$ . The calculated maximum uplift of the point source is 2.6 m/yr, at the surface projection of the source center. Figure S7 shows the combined model result including the viscoelastic response and magma inflow. The modeled interferograms fit the rapid velocity decay with distance away from the Bárðarbunga caldera. The velocities of the majority of the GNSS points are also explained by such a shallow magmatic inflow source when combined with a viscoelastic relaxation signal, except the velocity of the KISA station, especially in the horizontal direction.

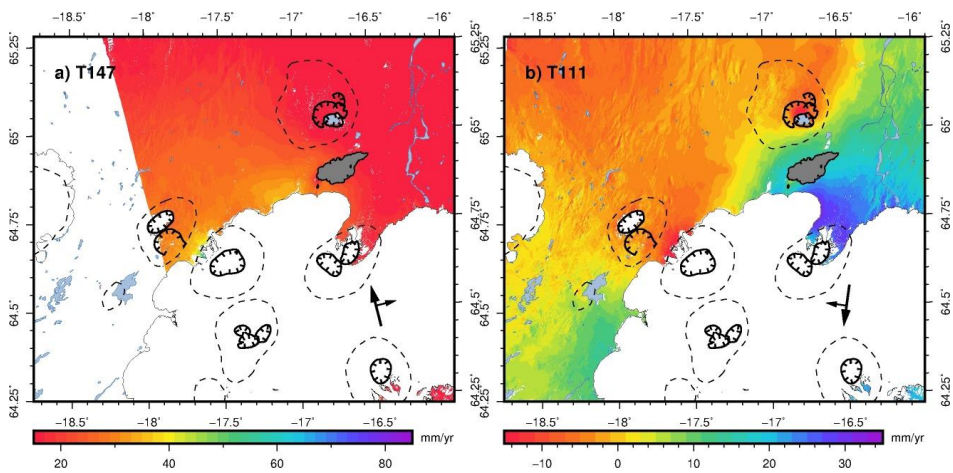


**Figure S1.** InSAR average velocity fields 2015-2018. LOS velocities from Sentinel-1 Track 147 (a) and Track 111 (b) from Drouin and Sigmundsson [2019]. Arrows show the Sentinel-1 satellite heading (large arrow) and look angle (small arrow).



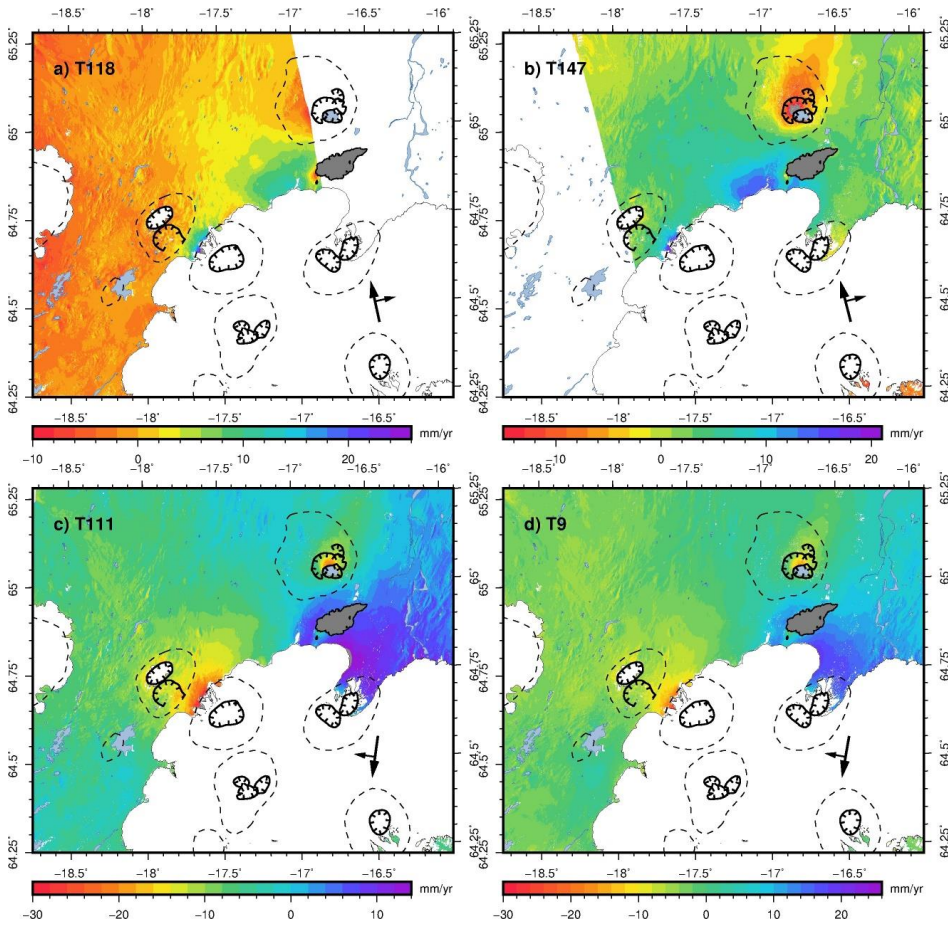


**Figure S2.** InSAR average velocity fields 2015-2018 corrected for Glacial Isostatic Adjustment (GIA) and plate spreading. Corrected LOS velocities from Sentinel-1 Track 118 (a), 147 (b), 111 (c) and 9 (d). Arrows show the Sentinel-1 satellite heading (large arrow) and look angle (small arrow).

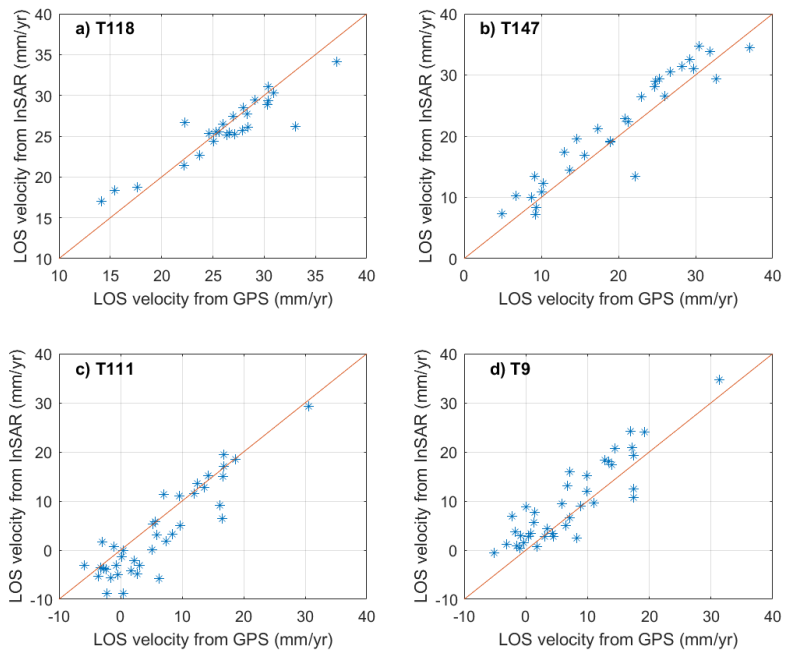


**Figure S3.** Comparison between InSAR velocities and GNSS velocities projected to LOS direction at the same location. The red lines show a one-to-one correlation.

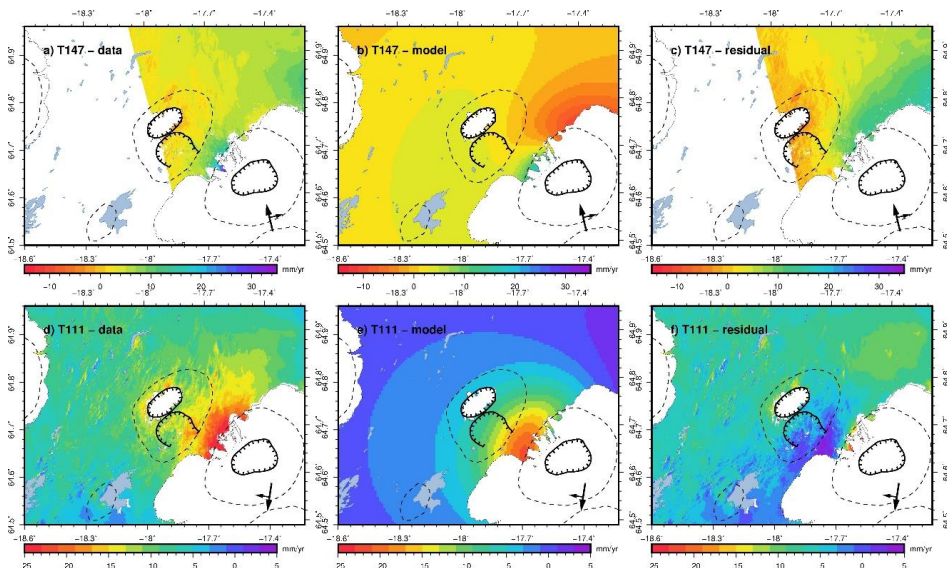


**Figure S4.** Corrected InSAR average velocities compared with joint viscoelastic deformation model with optimal viscosity and optimal non-piston magma withdrawal volume (and no magma inflow). Corrected InSAR average velocity from ascending Track 147 and descending Track 111 are compared with model predictions in panels a-c and d-f, respectively. The observation period for average velocity is May 2015 - October 2018. Panels display InSAR input data (a and d), modeling result (b and e) and residuals (c and f).

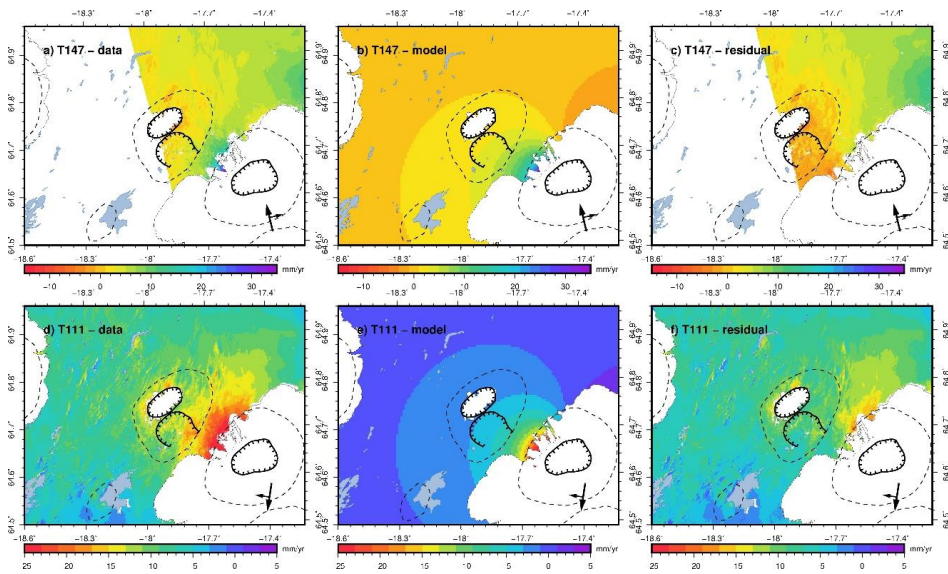


**Figure S5.** Corrected InSAR average velocities compared with the optimal single magma inflow source model. The optimal magma inflow rate from inversion results is from the GBIS software [Bagnardi and Hooper, 2018]. Corrected InSAR average velocity from ascending Track 147 and descending Track 111 compared with model predictions are in panels a-c and d-f, respectively. Panels display InSAR input data (a and d), modeling result (b and e) and residuals (c and f).

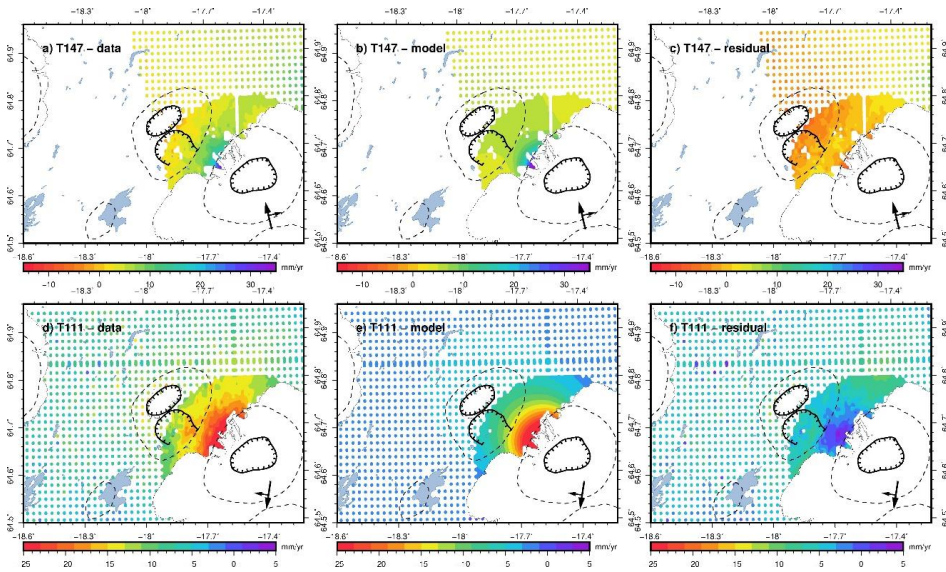


**Figure S6.** InSAR LOS velocities compared with the model considering the response from a model with a sill fixed at 10 km depth and fault slip on the caldera ring fault. The input InSAR results were resampled to a grid consisting of denser points close to the caldera and sparse points further away from the caldera. Corrected InSAR average velocity from ascending Track 147 and descending Track 111 compared with model predictions are in panels a-c and d-f, respectively. Panels display InSAR input data (a and d), modeling result (b and e) and residuals (c and f).

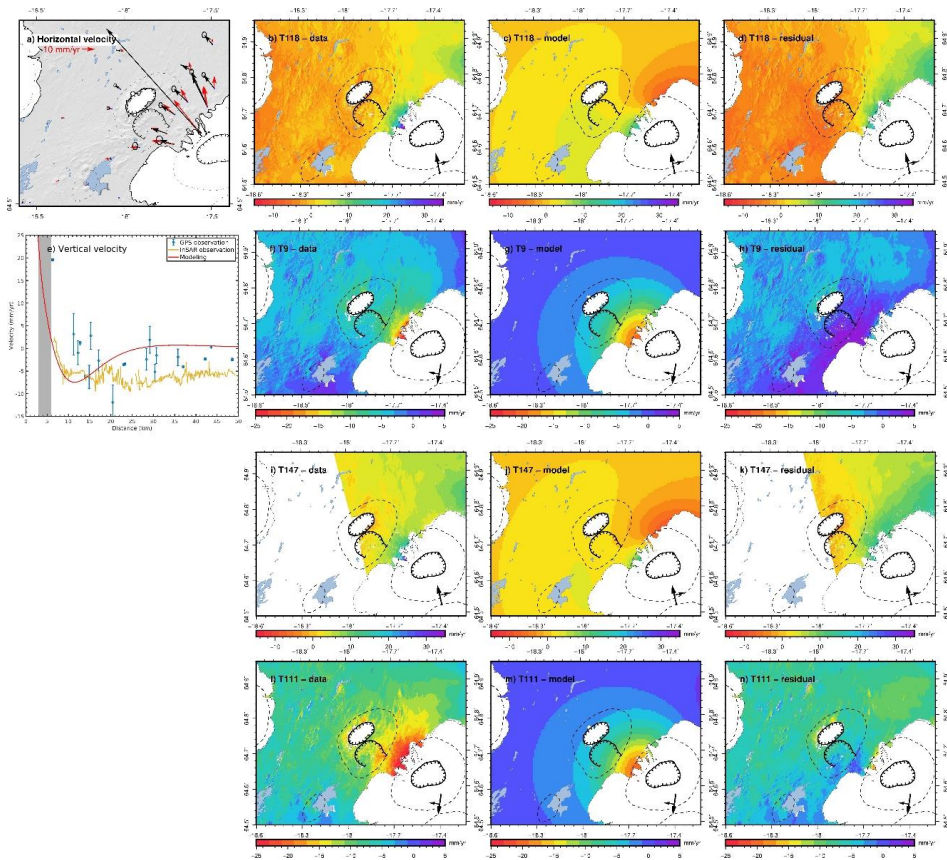


**Figure S7.** Corrected InSAR average velocities compared with the combination of viscoelastic relaxation and a single inflating source model. The data in the upper two lines are presented in the same way as in Figure 12. GNSS data and model in horizontal and vertical directions are in panels a and e, respectively. Panels display InSAR input data (b, f, i and l), modeling result (c, g, j and m) and residuals (d, h, k and n).

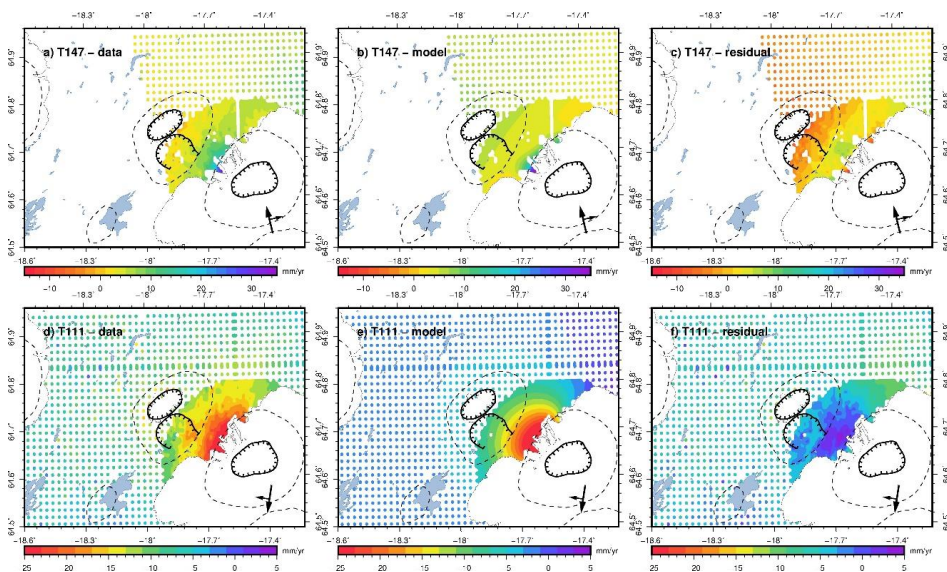


**Figure S8.** Corrected InSAR LOS velocities compared with the model predictions considering both viscoelastic response and renewed magma inflow at 10 km depth together with caldera ring fault slip. The input InSAR results were resampled to a grid consisting of denser points close to the caldera and sparse points further away from the caldera. Corrected InSAR average velocity from ascending Track 147 and descending Track 111 compared with model predictions are in panels a-c and d-f, respectively. Panels display InSAR input data (a and d), modeling result (b and e) and residuals (c and f).

GNSS station name	Longitude	Latitude	Observed velocity (mm/yr)			Corrected velocity (mm/yr)		
			East	North	Up	East	North	Up
DYNC	-17.366	64.791	-19.90	20.80	19.74	-8.57	10.23	-2.60
ISHO	-17.410	65.216	-15.57	11.60	6.84	-1.59	2.24	-4.26
GAEH	-17.481	64.784	-20.95	21.57	19.83	-8.50	10.73	-2.67
SURT	-17.493	64.892	-19.61	18.32	21.11	-6.41	7.44	1.96
RJUB	-17.521	64.739	-24.93	38.61	23.19	-12.63	27.86	-0.94
RJUC	-17.527	64.743	-23.77	33.96	25.17	-11.36	23.18	1.23
KISA	-17.562	64.674	-85.92	92.95	46.00	-74.33	82.72	19.61
GJAC	-17.614	64.829	-21.40	15.15	17.75	-7.99	4.15	-3.55
TIND	-17.634	64.751	-24.19	21.33	26.55	-11.07	10.49	2.81
HNIF	-17.710	64.720	-24.38	18.08	18.58	-10.97	7.41	-6.30
NEFS	-17.713	64.647	-24.56	13.85	30.52	-11.61	3.37	3.19
VONC	-17.754	64.674	-25.71	14.54	20.21	-12.20	4.13	-6.07
SHOF	-17.909	64.639	-18.37	10.83	15.27	-3.83	1.23	-11.86
KIDC	-17.942	65.019	-19.46	11.61	14.24	-5.30	1.19	-2.39
FJOC	-18.006	64.875	-19.26	11.49	16.59	-4.95	0.92	-3.99
TOMA	-18.019	64.782	-19.16	13.48	21.76	-4.34	3.08	-1.55
NYID	-18.069	64.734	-18.16	10.20	19.35	-2.93	0.48	-5.17
HSKE	-18.075	64.612	-16.54	8.51	24.59	-1.32	-0.04	-2.41
SHAG	-18.206	64.548	-16.08	7.90	25.40	-0.62	0.80	-1.90
HAUC	-18.345	64.711	-17.19	8.39	22.03	-1.97	0.01	-2.32
SKRO	-18.378	64.557	-15.24	7.18	26.19	0.66	0.62	0.31
SVAA	-18.583	64.503	-15.05	6.34	20.96	1.05	1.18	-3.58

**Table S1.** GNSS stations used within our study area. Columns show 4-character station identification code, station coordinates, their observed velocities and their velocities corrected for Glacial Isostatic Adjustment (GIA) and plate spreading. The observed velocities are plotted in Figure 4a,b and the corrected velocities are shown in Figure 4e,f.



Section	Data description	Surface uplift rate (m/yr)	Magma inflow rate (million m <sup>3</sup> /yr)	Root mean square* (mm/yr)	Reduced chi-squared** (mm/yr)
3.3	Observation data corrected for GIA and plate spreading processes, which is the corrected data used as an input for all the modeling	-	-	9.8	
4.1.4	Only viscoelastic relaxation	0.05	-	5.7	3.8
4.2.1	Only renewed magma inflow as a point source	4.9	10.7±0.01	6.3	5.0
Text S3 & Figure S7	Combined model considering both viscoelastic relaxation and point source magma inflow	2.6	2.4±0.05	5.7	3.7
4.2.2	Only renewed magma inflow considering both the sill opening at 10 km depth and fault slip	1.7	31.6±6.0	3.9	1.9
4.3	Combined model considering both viscoelastic relaxation and magma inflow include sill opening and fault slip	0.9	39.3±4.8	4.4	2.5

**Table S2.** Summary of models and estimates of model misfits using RMS (root mean square) of residuals and reduced chi-square estimate. Column 3 gives the surface uplift rate above the center of the source, and column 4 gives the magma inflow rate (for relevant models). Column 5 gives the RMS of residuals of the combined InSAR and GNSS data and column 6 gives the reduced chi-squared values.

\* To calculate the root mean squares (RMS) residuals, we consider all GNSS velocities within the black square box area in Figure 1, and InSAR residuals for all tracks within a box outlined by (18.00 W, 64.50 N) and (17.30 W, 64.80 N). This subarea is selected to give a clearer picture of how the modeled deformation fits the observation in the near-field, where the main deformation signal is. Resulting InSAR grids are formatted into the same format as in Figure 14 and 15, to keep the consistency between the models. To calculate the RMS for each model, we use the equation

$$x_{RMS} = \sqrt{\frac{1}{n} \left( \sum_{i=1}^n x_i^2 \right)}$$

Here,  $x_i$  is the residual of each pixel in the InSAR observations or on each displacement component at a GNSS station, and  $n$  is the number of total observations. For the observations considered,  $n$  equals  $4.8 \times 10^6$  (thereof 66 for 22 GNSS sites).

\*\* The reduced chi-squared is calculated using equation 5 in the main text. For the number of model parameters, we use 2 for the viscoelastic relaxation model (source volume and viscosity), and 4 for a point source (X, Y, Z and depth). There are 85 sill patches and 192 fault patches in the model considering both sill inflation at 10 km depth and caldera ring fault slip, so we use  $85+192=277$  as the number of free modeling parameters.

**References**

- Auriac, A., Spaans, K. H., Sigmundsson, F., Hooper, A., Schmidt, P., & Lund, B. (2013). Iceland rising: Solid Earth response to ice retreat inferred from satellite radar interferometry and viscoelastic modeling. *Journal of Geophysical Research: Solid Earth*, *118*(4), 1331–1344. <https://doi.org/10.1002/jgrb.50082>
- Bagnardi, M., & Hooper, A. (2018). Inversion of Surface Deformation Data for Rapid Estimates of Source Parameters and Uncertainties: A Bayesian Approach. *Geochemistry, Geophysics, Geosystems*, *19*(7), 2194–2211. <https://doi.org/10.1029/2018GC007585>
- Barbot, S. (2014). RELAX v1.0.7 [software], Computational Infrastructure for Geodynamics. Retrieved from <https://geodynamics.org/cig/software/relax/>
- Barbot, S., & Fialko, Y. (2010a). A unified continuum representation of post-seismic relaxation mechanisms: Semi-analytic models of afterslip, poroelastic rebound and viscoelastic flow. *Geophysical Journal International*, *182*(3), 1124–1140. <https://doi.org/10.1111/j.1365-246X.2010.04678.x>
- Barbot, S., & Fialko, Y. (2010b). Fourier-domain Green's function for an elastic semi-infinite solid under gravity, with applications to earthquake and volcano deformation. *Geophysical Journal International*, *182*(2), 568–582. <https://doi.org/10.1111/j.1365-246X.2010.04655.x>
- Drouin, V., & Sigmundsson, F. (2019). Countrywide Observations of Plate Spreading and Glacial Isostatic Adjustment in Iceland Inferred by Sentinel-1 Radar Interferometry, 2015 – 2018. *Geophysical Research Letters*, *46*, 8046–8055. <https://doi.org/10.1029/2019GL082629>

## Paper II

### **Post-Rifting Relaxation During 2015–2020 Following the Bárðarbunga-Holuhraun Dike Intrusion and Eruption in Iceland**

Siqi Li, Ronni Grapenthin, Freysteinn Sigmundsson, Vincent Drouin, Sigrún Hreinsdóttir, Benedikt G. Ófeigsson, 2022

Geophysical Research Letters, 10.1029/2022GL098977

<https://agupubs.onlinelibrary.wiley.com/doi/10.1029/2022GL098977>



# Geophysical Research Letters

## RESEARCH LETTER

10.1029/2022GL098977

### Key Points:

- Interferometric Synthetic Aperture Radar (InSAR) & Global Navigation Satellite System (GNSS) velocities indicate  $\sim 19$  mm/yr widening across a dike after its formation interpreted as post-rifting viscoelastic relaxation
- A two-layer viscoelastic model with  $0.4 \times 10^{19}$  Pa s viscoelastic half-space below 18 km depth best explains the GNSS and InSAR observations
- Elastic thickness of  $\sim 18$  km provides best fit, but a comparable fit is at  $\sim 2$  km, most likely due to unmodeled processes

### Supporting Information:

Supporting Information may be found in the online version of this article.

### Correspondence to:

S. Li.  
sli10@hi.is






### Citation:

Li, S., Grapenthin, R., Sigmundsson, F., Drouin, V., Hreinsdóttir, S., & Ófeigsson, B. G. (2022). Post-rifting relaxation during 2015–2020 following the Bárðarbunga–Holuhraun dike intrusion and eruption in Iceland. *Geophysical Research Letters*, 49, e2022GL098977. <https://doi.org/10.1029/2022GL098977>

Received 8 APR 2022  
Accepted 20 JUN 2022

© 2022. American Geophysical Union.  
All Rights Reserved.

## Post-Rifting Relaxation During 2015–2020 Following the Bárðarbunga–Holuhraun Dike Intrusion and Eruption in Iceland

Siqi Li<sup>1</sup> , Ronni Grapenthin<sup>2</sup> , Freysteinn Sigmundsson<sup>1</sup> , Vincent Drouin<sup>3</sup> , Sigrún Hreinsdóttir<sup>4</sup> , and Benedikt G. Ófeigsson<sup>3</sup>

<sup>1</sup>Nordic Volcanological Center, Institute of Earth Sciences, University of Iceland, Reykjavík, Iceland, <sup>2</sup>Geophysical Institute, Department of Geosciences, University of Alaska Fairbanks, Fairbanks, AK, USA, <sup>3</sup>Icelandic Meteorological Office, Reykjavík, Iceland, <sup>4</sup>GNS Science, Lower Hutt, New Zealand

**Abstract** Post-rifting ground deformation may be driven by viscoelastic relaxation of stresses generated by dike intrusions. The single-dike intrusion of the 2014–2015 Bárðarbunga eruption in Iceland presents an opportunity for a detailed study of this process. We use continuous Global Navigation Satellite System (GNSS) and Interferometric Synthetic Aperture Radar (InSAR) velocity fields to analyze the 2015–2020 post-rifting deformation, showing uplift on both sides of the dike and horizontal displacement away from the dike after correcting for background deformation. Two GNSS stations experience baseline lengthening at a rate of 19 mm/yr in the direction perpendicular to the strike of the dike. A two-layer viscoelastic model with a  $0.4 \times 10^{19}$  Pa s viscoelastic half-space overlain by an 18 km thick elastic layer best explains the observed horizontal and vertical InSAR and GNSS displacements. The model misfit space shows a second regime of good fit, likely driven by deformation near the dike that may result from cooling compaction of the emplaced dike.

**Plain Language Summary** Surface displacement can continue for years after a fissure eruption ends. This has been found at some volcanoes, such as in Afar (Ethiopia) and Krafla (Iceland). The 2014–2015 Bárðarbunga eruption in Iceland created a 48 km long dike, that led to an eruption to the northeast of the Bárðarbunga caldera outside the Vatnajökull ice cap. Here, we focus on exploring an explanation for the surface movement in the dike area after the eruption. Other non-volcanic processes cause surface movements in the area, including glacial isostatic adjustment caused by the ice retreat and plate spreading due to the divergence of the Eurasian plate and North American plate. We first correct for deformation due to these processes. The remaining deformation signal shows uplift on both sides of the dike and horizontal displacement away from the dike. We test if a two-layer model consisting of an elastic layer on top of a viscoelastic half-space can explain our observations. Our results suggest that material properties similar to other nearby areas explain the observations well. Systematic difference between observed and modeled deformation near the dike feeding the eruption is likely due to its cooling.

### 1. Introduction

The Bárðarbunga volcanic system is located in central Iceland at the divergent plate boundary between the North American and Eurasian plates, with a caldera, central volcano, and part of its fissure swarm lying under the Vatnajökull ice cap (Figure 1). In August 2014, a dike propagated away from the caldera, leading to a 6-month-long Holuhraun eruption at the far end of the dike until February 2015, which resulted in a collapse of the Bárðarbunga caldera (Gudmundsson et al., 2016; Pedersen et al., 2017). The track of the 48 km long segmented dike was well constrained by the analysis of seismicity and deformation data (e.g., Ágústsdóttir et al., 2016, 2019; Sigmundsson et al., 2015; Woods et al., 2018). Observations at two continuous Global Navigation Satellite System (GNSS) stations, located 25 km apart on each side of the dike, recorded 1.3 m lengthening between the stations during the activity (Sigmundsson et al., 2015).

Excessive surface displacement has been observed following the 2014–2015 Bárðarbunga–Holuhraun eruption. Li et al. (2021) infer that the post-rifting deformation to the northwest of the Bárðarbunga caldera may be caused by either post-eruption inflation, viscoelastic relaxation in response to magma withdrawal from beneath the caldera, or a combination of both processes. They considered a two-layer rheological crustal structure: a 7 km thick elastic layer on top of a viscoelastic halfspace (Maxwell rheology). If the viscoelastic relaxation process is

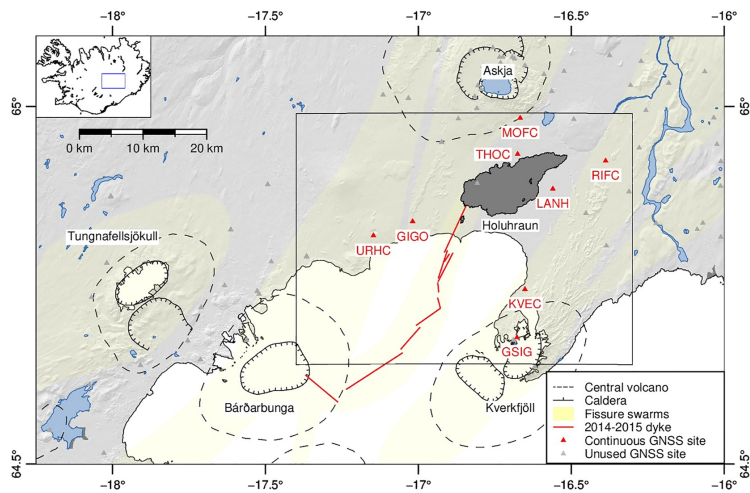


**Figure 1.** Map view of the Bárðarbunga central volcano, the Bárðarbunga-Holuhraun dike, and surroundings (red lines showing dike segments inferred by Sigmundsson et al. (2015)). The rectangle area marked with black boundary is our study area. The Holuhraun lava field is shown in dark gray. Yellow transparent layers show locations of fissure swarms (for geological layers, see Sigmundsson et al. (2020) and references therein). Glaciers are shown in white. Red triangles are continuous Global Navigation Satellite System (GNSS) sites used in this study. Gray triangles show GNSS stations not used.

the only explanation, the viscosity that best explains the observations is  $0.3 \times 10^{19}$  Pa s assuming a shear modulus of 30 GPa.

As our study area is adjacent to the Vatnajökull ice cap, studies of glacial isostatic adjustment (GIA) can provide important information on the subsurface viscoelastic properties. GIA studies in Iceland have mainly used GNSS data (Árnadóttir et al., 2009; Fleming et al., 2007; Pagli et al., 2007), sometimes in combination with other techniques, such as Interferometric Synthetic Aperture Radar (InSAR; Auriac, 2014), and gravity (Jacoby et al., 2009). These studies find models with a 10–40 km thick uppermost elastic layer, underlain by viscoelastic material with a viscosity in the range of  $0.01$ – $1 \times 10^{19}$  Pa s.

Several studies have addressed viscoelastic relaxation in response to emplacement of large dikes during rifting episodes, such as the 1978 Ghoubbet-Asal rifting episode in Djibouti, Africa (Cattin et al., 2005), the Dabbahu 2005–2010 rifting episode in Afar (Hamling et al., 2014; Nooner et al., 2009; Wright et al., 2012), and the 1975–1984 Krafla rifting episode in north Iceland (Ali et al., 2014; Foulger et al., 1992; Pollitz & Sacks, 1996). For the Ghoubbet-Asal seismovolcanic crisis, Cattin et al. (2005) suggest dike inflation and fault creep as the main sources for post-rifting deformation, although part of the rifting could be the result of viscoelastic relaxation. The Dabbahu rifting episode consisted of 14 dike intrusions. Viscoelastic modeling indicates a 12–30 km thick elastic layer on top of a viscoelastic material with a viscosity of  $0.1$ – $1 \times 10^{19}$  Pa s (Hamling et al., 2014; Nooner et al., 2009). The Krafla rifting episode includes around 20 diking events, nine of them ending in an eruption. Modeling of deformation data, spanning more than 20 years in the post-eruptive period, is consistent with deformation driven by the viscoelastic response to diking events (e.g., Foulger et al., 1992; Pollitz & Sacks, 1996). The most recent study suggests an elastic layer thickness of 8.0–9.5 km for the Krafla region, underlain by viscoelastic lower crust with a viscosity in the range of  $1.9$ – $4.9 \times 10^{19}$  Pa s (Ali et al., 2014).

We analyze and model the post-rifting deformation associated with the 2014–2015 Bárðarbunga-Holuhraun dike. Given the dike volume of about  $0.6 \text{ km}^3$  with an average opening of 1.0 m (Gudmundsson et al., 2016; Parks et al., 2017), we expect appreciable post-rifting relaxation as previously observed from the events referenced

above. We analyze InSAR and GNSS data to examine ground deformation. We limit our study area (Figure 1) to a region where the influence of the post-eruptive deformation around the Bárðarbunga caldera and the long-term subsidence at Askja volcano (see location in Figure 1) are not significant. Our study period is selected to be the relatively quiet period from March 2015 to December 2020, after the cessation of the 2014–2015 Bárðarbunga eruption and before the onset of measurable Askja inflation in August 2021. We consider a two-layer viscoelastic model for post-rifting relaxation surface displacement. By varying the thickness of the top elastic layer and the viscosity of the lower viscoelastic half-space, we explore if such a rheological model explains our observations. The Bárðarbunga rifting event overlaps with GIA processes, which allows us to sample the rheologic properties at different spatial and temporal periods. Importantly, this rifting event involves only one dike intrusion, which provides us the opportunity to better understand the role of viscoelastic relaxation in the post-rifting deformation field, and guides future studies of post-rifting deformation in general.

## 2. Observations

### 2.1. GNSS

We use data from 8 continuous GNSS stations north of the Vatnajökull ice cap, on both sides of the dike (Figure 1). The data are analyzed with the GAMIT/GLOBK 10.7 software (Herring et al., 2010; Hreinsdóttir et al., 2009) in the ITRF2014 (Altamimi et al., 2016) reference frame. We present our solutions relative to the stable Eurasian plate (Argus et al., 2010). Daily site positions are derived from the data to form timeseries of three-dimensional displacements.

We estimate seasonal variations in each displacement component using the equation

$$disp = A\cos(\omega t) + B\sin(\omega t) + C\cos(\omega 2t) + D\sin(\omega 2t) + vt \quad (1)$$

modified from Grapenthin et al. (2006), where  $t$  represents the time over which the station data are observed,  $v$  represents the estimated average velocity, and  $disp$  is a vector containing the observed east, north, and up GNSS timeseries. The angular frequency  $\omega$  is  $\frac{2\pi}{365}$  to span the period of 1 year. We estimate annual and semiannual coefficients  $A$ ,  $B$ ,  $C$ ,  $D$  for the three displacement directions separately through least squares inversion. These estimates of seasonal variations are then removed from the observed GNSS timeseries (Figures S1–S8 in Supporting Information S1).

We correct the timeseries for the background deformation processes, including plate spreading and GIA caused by ice retreat, which also causes ground deformation in our study area. GIA generates surface uplift and displacement toward the north, as suggested by the model from Auriac (2014). Li et al. (2021) applied a scaling factor to the GIA model from Auriac (2014) to correct for the GIA displacement during the period 2015–2018. We assume the GIA signal does not change from 2015 to 2020 and apply the same scaling factor to correct for the GIA signal as done by Li et al. (2021). Plate spreading in our study area is caused by the divergent plate movements as the Eurasian and North American plates move apart. The divergent plate boundary is striking in an approximately north-south direction in our area. We apply the plate spreading model by Drouin and Sigmundsson (2019) to remove this signal.

The average velocities in the north, east, and up components are estimated using a linear inverse function, which are referred to as corrected velocity in the following text. The GIGO and KVEC stations (Figure 1) are closest to the dike on each side of it, spaced about 20 km apart, 6 and 13 km from the dike, respectively. Their horizontal velocities can be rotated into velocity components parallel and perpendicular to the dike, yielding 9.0 mm/yr and 10.2 mm/yr dike-perpendicular average velocities at GIGO and KVEC, respectively (Figure 2). The vertical velocity at GIGO is 9.3 mm/yr, similar to 8.5 mm/yr estimated at KVEC.

KVEC shows a temporal variation in the horizontal component from 2015 to 2020 (Figures 2 and S3 in Supporting Information S1). If this temporal variation of surface displacement were caused by viscoelastic relaxation, we would expect exponential decay of the displacement. Therefore, we also fit the following equation to the observed displacement:

$$disp = Ae^{-\frac{1}{\tau}t} \quad (2)$$

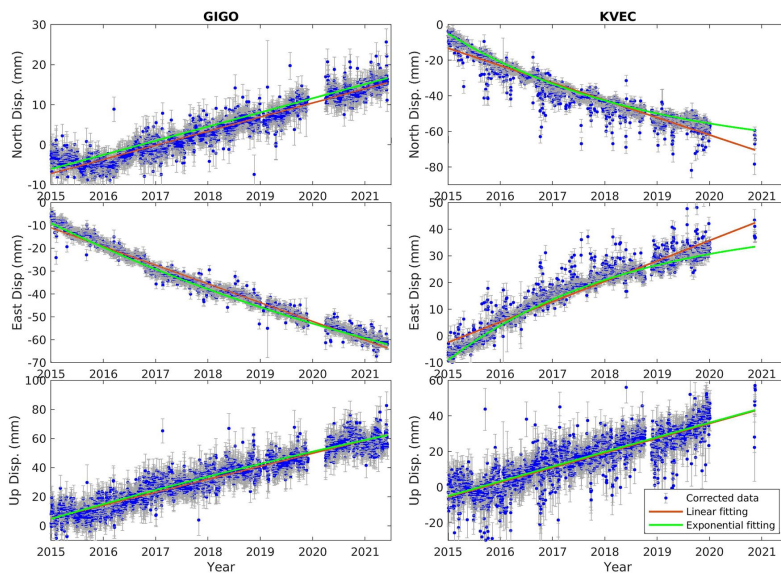


**Figure 2.** Corrected Global Navigation Satellite System timeseries at GIGO (left) and KVEC (right) stations. Timeseries are referenced to the Eurasian plate and then corrected for seasonal variation (annual and semi-annual cycle), glacial isostatic adjustment, and plate spreading (see the data before correction in Figures S1–S8 in Supporting Information S1). The timeseries are then both fit for linear displacement (red) and exponential decay (green). From top to bottom, the panels show north, east, and up displacements in mm.

where  $t$  is the time in years and  $disp$  is the displacement over time.  $A$  and  $T$  are the amplitude of the displacement and the relaxation time. For KVEC, we find a relaxation time of 3 years in the horizontal direction. Station GIGO also shows a smaller temporal variation, with a relaxation time of 10 years. Both stations show almost insignificant temporal variation in the vertical direction. The same analysis is carried out for all the GNSS stations (Table S1 in Supporting Information S1). The majority of the stations show a slight temporal variation in the horizontal direction, but none of them show significant temporal variation in the vertical (Figures S1–S8 in Supporting Information S1).

## 2.2. InSAR

We analyze SAR data collected from Sentinel-1 satellites every June–October 2015–2020 using the InSAR Scientific Computing Environment (ISCE) software (Rosen et al., 2012). Average line-of-sight (LOS) velocity fields are produced using the small baseline method. The average LOS velocities from Track 9 (descending), 111 (descending), and 147 (ascending) are then converted into approximate velocity fields in the east and up displacement components, which we refer to as near-east and near-up velocity fields (Figure S9 in Supporting Information S1; Drouin & Sigmundsson, 2019). The near-east velocity field is relative to a fixed Eurasian plate. Both the near-east and near-up velocity fields are in good agreement with GNSS velocities (Figure S10 in Supporting Information S1).

The near-east velocity field (Figure S9d in Supporting Information S1) suggests a transition from westward movement to eastward movement when going from the west to the east. Plate spreading in the area produces 18–19 mm/yr displacement in this region in the N(100–105)°E direction, which is the main reason for the horizontal divergent movement in the near-east velocity field. The vertical decomposed InSAR velocity field (Figure



S9e in Supporting Information S1) shows uplift in the whole study area, which is under the influence of GIA. These extra deformation processes are corrected in the average velocity fields using the same procedure as for the GNSS data.

### 2.3. Velocities Corrected for GIA and Plate Spreading

After removal of models for GIA and plate spreading from the observations, the remaining GNSS and InSAR velocity field (Figures 3a and 3e), which we refer to as corrected velocities, show spatially coherent motion centered on the dike. The near-east corrected velocity field (Figure 3a) shows displacements away from the dike, slightly higher on the west side of the dike than on the east side. The horizontal movement is largest about 11 km away from the dike. In the vertical direction, the area is uplifting, with the maximum uplift observed at the edge of the ice cap (Figure 3e). An uplift rate higher than 10 mm/yr occupies a larger area on the east side than on the west side of the dike. The profile across the dike suggests both broad long-wavelength deformation and focused, near-dike, short-wavelength deformation along the dike (Figures 3d and 3h). An InSAR near-east displacement profile of selected points near the dike suggests temporal variation in the near-field of the dike (Figure S11 in Supporting Information S1). Both the horizontal and vertical velocity fields have localized signals in the area directly above the dike and where the eruption occurred.

## 3. Modeling and Results

To test the hypothesis that viscoelastic relaxation is the main source of the post-rifting deformation signal, we employ a suite of viscoelastic models by varying elastic plate thickness and viscosity parameters, in order to simulate post-rifting relaxation induced surface displacement following the Bárðarbunga-Holuhraun dike intrusion.

We use the semi-analytical software RELAX (Barbot & Fialko, 2010a, 2010b) to calculate post-rifting displacement fields in response to the formation of a dike. We start with a two-layer Maxwell viscoelastic model, where a 7 km thick elastic layer lies on top of a  $0.3 \times 10^{19}$  Pa s viscoelastic half-space, as described by Li et al. (2021). Both layers consist of homogeneous isotropic material, with Poisson's ratio  $\nu = 0.25$  and shear modulus  $\mu = 16$  GPa (Grapenthin et al., 2006). The dike model is inferred from co-eruptive deformation by Sigmundsson et al. (2015). The injected dike is divided into 120 patches down to 10 km depth. Each patch is 2 km deep, with the opening in the range of 0.09–8.87 m. The average opening of the patches is 1.0 m, with the majority of the opening occurring above 6 km depth.

We determine the RMS of the model residuals and expect that the parameter combinations that yield the smallest RMS fit our observation best (Figures 4 and S12 in Supporting Information S1). By giving different weights to GNSS and InSAR average velocity fields, as well as horizontal and vertical components, we can combine all average displacement fields to determine the model that best explains our observations. GNSS and InSAR average velocities are used with a relative weight of 1000:1 (See details in Figure S13 in Supporting Information S1). As the horizontal velocities are less influenced by seasonal variations than the vertical components (e.g., Figure 2), the horizontal velocity is given twice the weight of the vertical velocity.

The difference between observed velocities and those predicted by the starting model yields residuals with a larger RMS (9.0 mm/yr) than if a zero model is applied (4.1 mm/yr). Therefore, we consider a range of different elastic layer thicknesses and viscosities to explain the corrected velocities. We explore elastic layer thickness ranging from 1 to 24 km in steps of 1 km. As the displacement rate predicted by the viscoelastic model scales inversely with viscosity, we derive the result of different viscosities by scaling the displacement rate of the initial model, as done by Li et al. (2021). We test viscosities in  $0.1 \times 10^{19}$  Pa s steps from  $0.3$ – $3.6 \times 10^{19}$  Pa s.

Our residual analysis produces an RMS misfit space that contains two areas of good fit (Figure 4), one centered at a 2 km thick elastic layer and  $1.2 \times 10^{19}$  Pa s, while the other is at 18 km and  $0.4 \times 10^{19}$  Pa s. This nonconvex misfit space represents model sensitivities to near-dike, short-wavelength deformation (2 km thick and  $1.2 \times 10^{19}$  Pa s) and broad long-wavelength deformation (18 km,  $0.4 \times 10^{19}$  Pa s) as captured in horizontal and vertical velocity fields (Figures S12 and S14 in Supporting Information S1). As post-eruptive deformation is generally a broad signal, we select 18 km and  $0.4 \times 10^{19}$  Pa s as the optimal model, which is also supported by the slightly lower

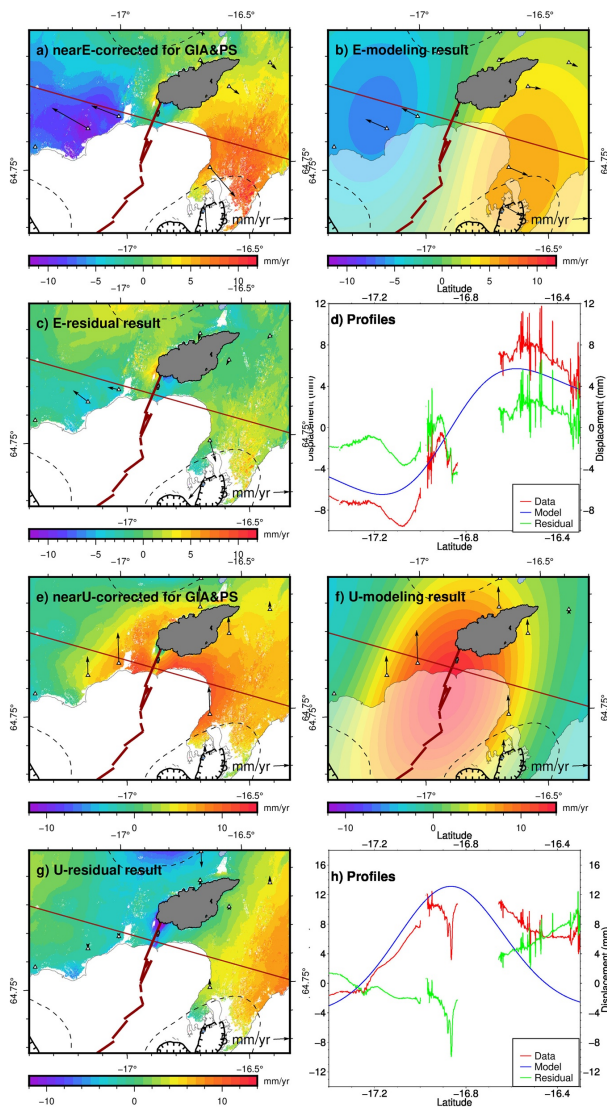


**Figure 3.** Corrected average velocity field in the (a–d) horizontal and (e–h) vertical directions during 2015–2020 from Interferometric Synthetic Aperture Radar (InSAR; color) and Global Navigation Satellite System (black arrows). The decomposed near-east and near-up InSAR average velocities after correcting glacial isostatic adjustment and plate spreading signals are in panels (a and e). The modeled east and up velocity from the viscoelastic model with the optimal elastic layer thickness (18 km) and viscosity ( $0.4 \times 10^{19}$  Pa s) are in panels (b and f). Panels (c and g) are the differences between corresponding observations (a and e) and model (b and f). Panels (d and h) are the near-east (red line in panels (a, b, and c)) and near-up (red line in panels (e, f, and g)) velocity profiles across the study area.

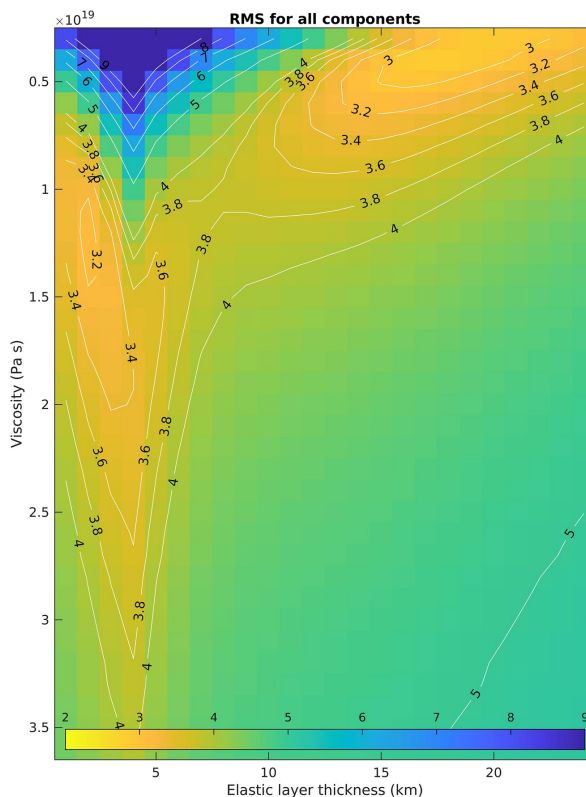


**Figure 4.** Root mean square residual between the corrected velocity fields (data) and modeling results. The data include near-east and near-up components from Interferometric Synthetic Aperture Radar (InSAR) and north, east, and up components from Global Navigation Satellite System (GNSS). The weight of GNSS versus InSAR is 1000:1. The weight of horizontal versus vertical is 2:1. The  $x$ -axis is the elastic layer thickness (1–24 km with 1 km step) and the  $y$ -axis is the viscosity ( $0.3$ – $3.6 \times 10^{19}$  Pa s with  $0.1 \times 10^{19}$  Pa s step). The optimal viscosity for the velocities is found at  $0.4 \times 10^{19}$  Pa s and the optimal elastic layer thickness is 18 km.

RMS residuals in that region of the parameter space. For the optimal model, the overall weighted RMS residual is improved from 4.1 for no model to 2.8 mm/yr. The RMS of the corrected velocity without a model is 5.5 and 5.2 mm/yr for InSAR near-east and near-up components, which improved to 1.8 and 3.9 mm/yr after removing the optimal viscoelastic model. The GNSS velocities are also improved from 5.6 (east), 5.5 (north), and 5.9 (up) mm/yr for no model to 2.8, 3.5, and 2.2 mm/yr, respectively.

Predicted displacements according to the model are compared to the corrected velocities from InSAR and GNSS in Figure 3. The near-east displacement rate on the west side of the dike is higher than on the east side of the dike (Figure 3b). The majority of the misfit in both the near-east and near-up velocity fields are in the close vicinity of the dike (Figures 3c and 3g). The near-up velocity field also shows misfit on the east side of the dike.

#### 4. Discussion

The misfit space in Figure 4 shows two regimes that provide a good fit to our corrected velocity field based on the weighted RMS residual, one with an 18 km thick elastic layer and a viscosity of  $0.4 \times 10^{19}$  Pa s, the other with the localized minimum with elastic layer thickness at 2 km and viscosity at  $1.2 \times 10^{19}$  Pa s (Figure S15 in Supporting Information S1). These two regimes correspond well to the different preferred models by the horizontal and vertical velocity fields (Figure S14 in Supporting Information S1). The horizontal velocity field prefers a model with a thinner elastic layer (3 km) and higher viscosity ( $1.5 \times 10^{19}$  Pa s, Figure S16 in Supporting Information S1), while the vertical velocity field prefers a model with a thicker elastic layer (24 km) and lower viscosity ( $0.4 \times 10^{19}$  Pa s, Figure S17 in Supporting Information S1). Nevertheless, all models suggest the viscosity in the region is in the range of  $0.4\text{--}1.5 \times 10^{19}$  Pa s.

To explain the different preferred elastic layer thicknesses for the horizontal and vertical velocity fields, we propose possibilities such as inappropriate GIA modeling, higher ice mass-loss rate in the area, or renewed magma inflow. Our test suggests that applying a different GIA scaling factor to the model by Auriac (2014) can not explain the excess uplift (Figure S18 in Supporting Information S1). The higher ice mass-loss rate in recent years at Vatnajökull (Compton et al., 2015) might explain the excess uplift. However, more detailed ice loss data is needed to quantify the produced deformation field. The trend change in the east component of KVEC timeseries in 2017 (Figure 2) might suggest magma injected into the dike, as observed at Ghoubbet-Asal (Cattin et al., 2005). A similar mismatch between horizontal and vertical viscoelastic post-rifting model fit is found by Nooner et al. (2009) in Afar.

We select our preferred model, 18 km and  $0.4 \times 10^{19}$  Pa s, based on an overall lower misfit and the reasoning that viscoelastic processes are generally of longer spatial wavelength. However, this model does not explain the localized deformation residual directly above the dike in the corrected InSAR average velocity fields (Figures 3a and 3e). The horizontal motion toward the dike and subsidence above the dike could be a result of non-linear displacement in this area, as suggested by the InSAR timeseries (Figure S11 in Supporting Information S1). The co-eruptive model has the largest dike opening, 8.87 m, in this area. The cooling of the dike, resulting in localized contraction, could be the explanation for this localized signal. Non-homogeneous subsurface structure close to the dike, or an over-estimation of the opening from the co-eruptive model could provide alternate explanations.

Compared with previous GIA studies at Vatnajökull, which suggest an elastic crustal thickness in the range of 10–40 km and the viscosity of the shallow mantle at  $0.1\text{--}1 \times 10^{19}$  Pa s (Auriac, 2014; Árnadóttir et al., 2009; Fleming et al., 2007; Pagli et al., 2007), our model suggests a comparable elastic layer thickness and viscosity. The viscosity underneath Bárðarbunga caldera, around 30 km away from our study area, was estimated to be  $0.3 \times 10^{19}$  Pa s (Li et al., 2021), which is comparable to the value found here.

The approximately  $1.4 \text{ km}^3$  Holuhraun lava field formed in 2014–2015 over an  $84 \text{ km}^2$  area (Pedersen et al., 2017). To understand whether the response to loading by the lava field influences our deformation field, we run a forward model considering the lava load in a  $7 \times 17$  km rectangular area with uniform lava thickness of 17 m and density of  $2300 \text{ kg/m}^3$ , using the same subsurface structure as in our optimal model. This yields an insignificant viscoelastic response at the edges of the Holuhraun lava field of less than 1 mm/yr in the horizontal component and less than 4 mm/yr in the vertical direction during our study period.

Our study considers a two-layer viscoelastic model with homogeneous isotropic Maxwell material to explain average velocities and the spatial pattern of deformation. We pay less attention to the temporal variation measured at GNSS stations in the area, which could be further explored in future studies. More complex model geometries, such as the model with three or more layers, with non-linear rheology, or considering lateral variation in layer thickness and viscosity, could be considered in future studies, to better understand the subsurface structure of our area.

#### 5. Conclusion

We analyze the post-rifting ground deformation field around the Bárðarbunga-Holuhraun dike. After correcting for the background deformation field (GIA and plate spreading signal), the remaining signal shows horizontal displacement away from the dike and uplift. Our modeling result suggests that a two-layer viscoelastic model considering an elastic layer on top of a viscoelastic half-space can explain both the horizontal and vertical

deformation signal. The optimal model that best explains the displacement fields has  $0.4 \times 10^{19}$  Pa s viscoelastic material below an 18 km thick elastic layer. Another alternate parameter combination consists of an elastic layer thickness of 2 km and viscosity of  $1.2 \times 10^{19}$  Pa s, which is likely due to unmodeled short wavelength signals in the vicinity of the dike. Our study suggests that viscoelastic relaxation is an important process to consider after a rifting event. Alternate modeling approaches to that considered here or other processes such as cooling of the dike, ongoing dike inflation, and - in the case of Iceland - time-varying GIA, heterogeneous viscosity and elastic layer thickness may have to be invoked to fully explain the deformation field.

### Data Availability Statement

Interferometric Synthetic Aperture Radar average velocity field is available at <https://doi.org/10.17605/OSF.IO/3B2GF>. SAR images from Sentinel-1 satellites are retrieved from Copernicus Open Access Hub (<https://scihub.copernicus.eu/dhus/#/home>) provided by European Space Agency. Rinex data for calculating the GNSS timeseries are available at UNAVCO Inc. uploaded by Grapenthin (2016a, 2016b, 2016c, 2016d, 2016e) (<https://doi.org/10.7283/WKZ3-NW79>, <https://doi.org/10.7283/QSTY-N037>, <https://doi.org/10.7283/PDN2-N051>, <https://doi.org/10.7283/N65C-JN46>, <https://doi.org/10.7283/XN8V-RZ54>). RELAX software used for viscoelastic deformation modeling is available at <https://github.com/geodynamics/relax>. The dike model is published by Sigmundsson et al. (2015). Details of the Iceland map is provided by Sigmundsson et al. (2020). Holuhraun lava field contour is described in Pedersen et al. (2017). MATLAB (2020) is used for calculation and figure plotting, and some figures are plotted by the Generic Mapping Tools (Wessel et al., 2013).

### Acknowledgments

We thank the Research Fund of the University of Iceland for funding for the Ph.D. work of the first author (S. Li), of which this research is a part of. Partial financial support from the H2020 project EUROVOLC funded by the European Commission is acknowledged (Grant No. 731070). R. Grapenthin acknowledges partial support for this work through NSF grant EAR-1464546. We thank Chiara Lanzani for helping to benchmark the dike model. We thank the fruitful discussion with Halldór Geirsson and Andrew Hooper. We thank the reviewer for the constructive comments, which helped strengthen our manuscript. We thank the editor and editor's assistant for their time in helping us with this article.

### References

- Ágústsdóttir, T., Winder, T., Woods, J., White, R. S., Greenfield, T., & Brandsdóttir, B. (2019). Intense seismicity during the 2014–2015 Bárðarbunga-Holuhraun rifting event, Iceland, reveals the nature of dike-induced earthquakes and caldera collapse mechanisms. *Journal of Geophysical Research: Solid Earth*, *124*(8), 8331–8357. <https://doi.org/10.1029/2018JB016010>
- Ágústsdóttir, T., Woods, J., Greenfield, T., Green, R. G., White, R. S., Winder, T., et al. (2016). Strike-slip faulting during the 2014 Bárðarbunga-Holuhraun dike intrusion, central Iceland. *Geophysical Research Letters*, *43*(4), 1495–1503. <https://doi.org/10.1002/2015GL067423>
- Árnadóttir, T., Lund, B., Jiang, W., Geirsson, H., Björnsson, H., Einarsson, P., & Sigurdsson, T. (2009). Glacial rebound and plate spreading: Results from the first countrywide GPS observations in Iceland. *Geophysical Journal International*, *177*(2), 691–716. <https://doi.org/10.1111/j.1365-246X.2008.04059.x>
- Ali, S. T., Feigl, K. L., Carr, B. B., Masterlark, T., & Sigmundsson, F. (2014). Geodetic measurements and numerical models of rifting in Northern Iceland for 1993–2008. *Geophysical Journal International*, *196*(3), 1267–1280. <https://doi.org/10.1093/gji/ggt462>
- Altamimi, Z., Rebischung, P., Métivier, L., & Collilioux, X. (2016). ITRF2014: A new release of the International Terrestrial Reference Frame modeling nonlinear station motions. *Journal of Geophysical Research: Solid Earth*, *121*(8), 6109–6131. <https://doi.org/10.1002/2016JB013098>
- Argus, D. F., Gordon, R. G., Heflin, M. B., Ma, C., Eanes, R. J., Willis, P., et al. (2010). The angular velocities of the plates and the velocity of Earth's centre from space geodesy. *Geophysical Journal International*, *180*(3), 913–960. <https://doi.org/10.1111/j.1365-246X.2009.04463.x>
- Auriac, A. (2014). *Solid earth response to ice retreat and glacial surges in Iceland inferred from satellite radar interferometry and finite element modelling*. Doctoral dissertation, Faculty of Earth Sciences, University of Iceland.
- Barbot, S., & Fialko, Y. (2010a). Fourier-domain green's function for an elastic semi-infinite solid under gravity, with applications to earthquake and volcano deformation: Fourier-domain elastic solutions. *Geophysical Journal International*, *182*(2), 568–582. <https://doi.org/10.1111/j.1365-246X.2010.04655.x>
- Barbot, S., & Fialko, Y. (2010b). A unified continuum representation of post-seismic relaxation mechanisms: Semi-analytic models of after-slip, poroelastic rebound and viscoelastic flow: Semi-analytic models of postseismic transient. *Geophysical Journal International*, *182*(3), 1124–1140. <https://doi.org/10.1111/j.1365-246X.2010.04678.x>
- Cattin, R., Doubre, C., De Chabalier, J.-B., King, G., Vigny, C., Avouac, J.-P., & Ruegg, J.-C. (2005). Numerical modelling of quaternary deformation and post-rifting displacement in the Asal-Ghoubbet rift (Djibouti, Africa). *Earth and Planetary Science Letters*, *239*(3–4), 352–367. <https://doi.org/10.1016/j.epsl.2005.07.028>
- Compton, K., Bennett, R. A., & Hreinsdóttir, S. (2015). Climate-driven vertical acceleration of Icelandic crust measured by continuous GPS geodesy. *Geophysical Research Letters*, *42*(3), 743–750. <https://doi.org/10.1002/2014GL062446>
- Drouin, V., & Sigmundsson, F. (2019). Countrywide observations of plate spreading and glacial isostatic adjustment in Iceland inferred by Sentinel-1 radar interferometry, 2015–2018. *Geophysical Research Letters*, *46*(14), 8046–8055. <https://doi.org/10.1029/2019GL082629>
- Fleming, K., Martinec, Z., & Wolf, D. (2007). Glacial-isostatic adjustment and the viscosity structure underlying the Vatnajökull Ice Cap, Iceland. *Pure and Applied Geophysics*, *164*(4), 751–768. <https://doi.org/10.1007/s00024-007-0187-6>
- Foulger, G. R., Jahn, C.-H., Seeber, G., Einarsson, P., Julian, B. R., & Heki, K. (1992). Post-rifting stress relaxation at the divergent plate boundary in Northeast Iceland. *Nature*, *358*(6386), 488–490. <https://doi.org/10.1038/358488a0>
- Grapenthin, R. (2016a). Hopnet GPS network - GIGO-gigoldur p.s., the gage facility operated by UNAVCO, Inc., GPS/GNSS observations dataset [dataset]. UNAVCO, Inc. <https://doi.org/10.7283/WKZ3-NW79>
- Grapenthin, R. (2016b). Hopnet GPS network - KVEC-Kverkfjöll p.s., the gage facility operated by UNAVCO, Inc., GPS/GNSS observations dataset [dataset]. UNAVCO, Inc. <https://doi.org/10.7283/xn8v-rz54>
- Grapenthin, R. (2016c). Hopnet GPS network - LANH-Langahli p.s., the gage facility operated by UNAVCO, Inc., GPS/GNSS observations dataset [dataset]. UNAVCO, Inc. <https://doi.org/10.7283/N65C-JN46>
- Grapenthin, R. (2016d). Hopnet GPS network - MOFC-Moflatir p.s., the gage facility operated by UNAVCO, Inc., GPS/GNSS observations dataset [dataset]. UNAVCO, Inc. <https://doi.org/10.7283/PDN2-N051>

- Grapenthin, R. (2016e). Hopenet GPS network - RIFC-Rifnihnjukur, the gage facility operated by UNAVCO, Inc., GPS/GNSS observations dataset [dataset]. UNAVCO, Inc. <https://doi.org/10.7283/QSTY-N037>
- Grapenthin, R., Sigmundsson, F., Geirsson, H., Árnadóttir, T., & Pínel, V. (2006). Icelandic rhythmic: Annual modulation of land elevation and plate spreading by snow load. *Geophysical Research Letters*, *33*(24), L24305. <https://doi.org/10.1029/2006GL028081>
- Gudmundsson, M. T., Jónsdóttir, K., Hooper, A., Holohan, E. P., Halldórsson, S. A., Ófeigsson, B. G., et al. (2016). Gradual caldera collapse at Bárðarbunga volcano, Iceland, regulated by lateral magma outflow. *Science*, *353*(6296), aaf8988. <https://doi.org/10.1126/science.aaf8988>
- Hamling, I. J., Wright, T. J., Calais, E., Lewi, E., & Fukahata, Y. (2014). InSAR observations of post-rifting deformation around the Dabbahu rift segment, Afar, Ethiopia. *Geophysical Journal International*, *197*(1), 33–49. <https://doi.org/10.1093/gji/ggu003>
- Herring, T., King, R., & McClusky, S. (2010). *Introduction to GAMIT/GLOBK*. Massachusetts Institute of Technology.
- Hreinsdóttir, S., Árnadóttir, T., Decriem, J., Geirsson, H., Tryggvason, A., Bennett, R. A., & LaFemina, P. (2009). A complex earthquake sequence captured by the continuous GPS network in SW Iceland. *Geophysical Research Letters*, *36*(12), L12309. <https://doi.org/10.1029/2009GL038391>
- Jacoby, W. R., Hartmann, O., Wallner, H., Smilde, P. L., Buerger, S., Sjöberg, L. E., et al. (2009). Temporal gravity variations near shrinking Vatnajökull ice cap, Iceland. *Pure and Applied Geophysics*, *166*(8), 1283–1302. <https://doi.org/10.1007/s00024-009-0499-9>
- Li, S., Sigmundsson, F., Drouin, V., Parks, M. M., Ófeigsson, B. G., Jónsdóttir, K., et al. (2021). Ground deformation after a caldera collapse: Contributions of magma inflow and viscoelastic response to the 2015–2018 deformation field around Bárðarbunga, Iceland. *Journal of Geophysical Research: Solid Earth*, *126*(3), e2020JB020157. <https://doi.org/10.1029/2020JB020157>
- MATLAB. (2020). *Version 9.8.0.1323502 (r2020a)*. The MathWorks Inc. Retrieved from <https://www.mathworks.com/products/matlab.html>
- Nooner, S. L., Bennati, L., Calais, E., Buck, W. R., Hamling, I. J., Wright, T. J., & Lewi, E. (2009). Post-rifting relaxation in the Afar region, Ethiopia. *Geophysical Research Letters*, *36*(21), L21308. <https://doi.org/10.1029/2009GL040502>
- Pagli, C., Sigmundsson, F., Lund, B., Sturkell, E., Geirsson, H., Einarsson, P., et al. (2007). Glacio-isostatic deformation around the Vatnajökull ice cap, Iceland, induced by recent climate warming: GPS observations and finite element modeling. *Journal of Geophysical Research*, *112*(8), 1–12. <https://doi.org/10.1029/2006JB004421>
- Parks, M. M., Heimgsson, E. R., Sigmundsson, F., Hooper, A., Vogfjörð, K. S., Árnadóttir, T., et al. (2017). Evolution of deformation and stress changes during the caldera collapse and dyking at Bárðarbunga, 2014–2015: Implication for triggering of seismicity at nearby Tungnafellsjökull volcano. *Earth and Planetary Science Letters*, *462*, 212–223. <https://doi.org/10.1016/j.epsl.2017.01.020>
- Pedersen, G., Höskuldsson, A., Dürig, T., Thordarson, T., Jónsdóttir, I., Riishuus, M., et al. (2017). Lava field evolution and emplacement dynamics of the 2014–2015 basaltic fissure eruption at Holuhraun, Iceland. *Journal of Volcanology and Geothermal Research*, *340*, 155–169. <https://doi.org/10.1016/j.jvolgeores.2017.02.027>
- Pollitz, F. F., & Sacks, I. S. (1996). Viscosity structure beneath northeast Iceland. *Journal of Geophysical Research*, *101*(B8), 17771–17793. <https://doi.org/10.1029/96JB01074>
- Rosen, P. A., Currolo, E., Sacco, G. F., & Zebker, H. (2012). The InSAR scientific computing environment. In *Eusar 2012; 9th european conference on synthetic aperture radar* (pp. 730–733). VDE.
- Sigmundsson, F., Einarsson, P., Hjartardóttir, Á. R., Drouin, V., Jónsdóttir, K., Árnadóttir, T., et al. (2020). Geodynamics of Iceland and the signatures of plate spreading. *Journal of Volcanology and Geothermal Research*, *391*, 106436. <https://doi.org/10.1016/j.jvolgeores.2018.08.014>
- Sigmundsson, F., Hooper, A., Hreinsdóttir, S., Vogfjörð, K. S., Ófeigsson, B. G., Heimgsson, E. R., et al. (2015). Segmented lateral dyke growth in a rifting event at Bárðarbunga volcanic system, Iceland. *Nature*, *517*(7533), 191–195. <https://doi.org/10.1038/nature14111>
- Wessel, P., Smith, W. H. F., Scharroo, R., Luis, J., & Wobbe, F. (2013). Generic mapping tools: Improved version released. *Eos, Transactions American Geophysical Union*, *94*(45), 409–410. <https://doi.org/10.1002/2013EO450001>
- Woods, J., Donaldson, C., White, R. S., Caudron, C., Brandsdóttir, B., Hudson, T. S., & Ágústsdóttir, T. (2018). Long-period seismicity reveals magma pathways above a laterally propagating dyke during the 2014–15 Bárðarbunga rifting event, Iceland. *Earth and Planetary Science Letters*, *490*, 216–229. <https://doi.org/10.1016/j.epsl.2018.03.020>
- Wright, T. J., Sigmundsson, F., Pagli, C., Belachew, M., Hamling, I. J., Brandsdóttir, B., et al. (2012). Geophysical constraints on the dynamics of spreading centres from rifting episodes on land. *Nature Geoscience*, *5*(4), 242–250. <https://doi.org/10.1038/ngeo1428>

# Supporting Information for "Post-rifting relaxation during 2015-2020 following the Bárðarbunga-Holuhraun dike intrusion and eruption in Iceland"

Siqi Li<sup>1</sup>\*, Ronni Grapenthin<sup>2</sup>, Freysteinn Sigmundsson<sup>1</sup>, Vincent Drouin<sup>3</sup>,

Sigrún Hreinsdóttir<sup>4</sup> and Benedikt G. Ófeigsson<sup>3</sup>

<sup>1</sup>Nordic Volcanological Center, Institute of Earth Sciences, University of Iceland, Iceland

<sup>2</sup>Geophysical Institute and Dept. of Geosciences, University of Alaska Fairbanks, USA

<sup>3</sup>Icelandic Meteorological Office, Reykjavík, Iceland

<sup>4</sup>GNS Science, New Zealand

## Contents of this file

1. Figures S1 to S18
2. Tables S1

## Introduction

We present the GNSS timeseries from 8 continuous stations in Figures S1-S8. The corrected velocities from these stations are in Table S1. Figure S9 is the observed Sentinel-1 InSAR average velocity field in both Line-of-

---

\*Nordic Volcanological Center, Institute of Earth Science, University of Iceland, Iceland

Sight directions and decomposed approximately into east and up directions. Figure S10 is the comparison between corrected GNSS and InSAR velocities in the east and up directions at the GNSS stations. The timeseries of six selected points close to the dike from the decomposed approximately east direction are shown in Figure S11. Figure S12 shows a grid search for finding the optimal modeling parameters from different components from GNSS and InSAR velocities. Figure S13 shows how the GNSS weight influences our best-fitting model parameters and RMS residuals calculated from GNSS and InSAR. Figure S14 shows a grid search for finding the modeling parameters that best explain the horizontal velocity field and vertical velocity field separately. Figure S15 shows the velocity fields with a 2 km thick elastic layer on top of a  $1.2 \times 10^{19}$  Pa s viscoelastic half-space, which is one of the two regimes that make the least RMS residuals. Figure S16 shows the velocity fields using the model that best explains the horizontal velocity field (3 km elastic layer and  $1.5 \times 10^{19}$  Pa s). Figure S17 shows the velocity fields using the model that best explains the vertical velocity (24 km elastic layer and  $0.4 \times 10^{19}$  Pa s). Figure S18 shows the corrected near-up velocity field and an improved glacial isostatic adjustment model.



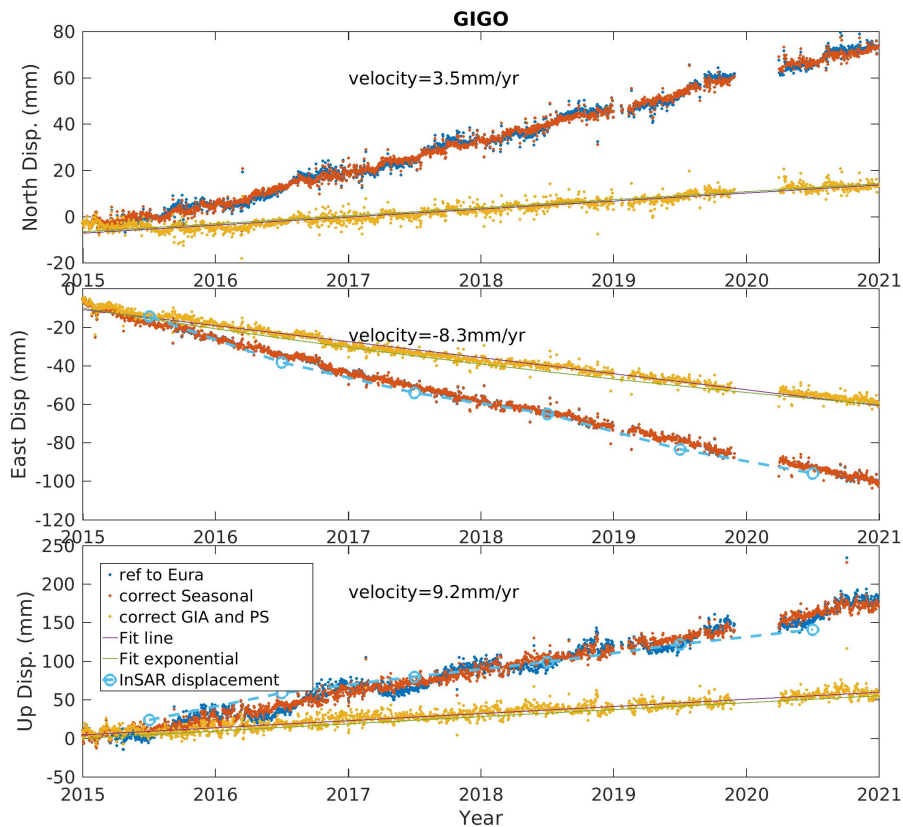


**Figure S1.** GNSS timeseries from GIGO station (see location in Figure 1). The blue dot curve is the timeseries from observation. The red dot curve is the observation corrected for seasonal variation. The yellow dot curve is corrected for seasonal variation, Glacial Isostatic Adjustment (GIA), and plate spreading (PS). The fitted red line is the average velocity estimated from the yellow dots, with the velocity labeled in the figure. We also fit an exponential line to our observation (green curve). Inferred InSAR displacement is shown in blue circles with a dashed line (see Figures S9 and S10).

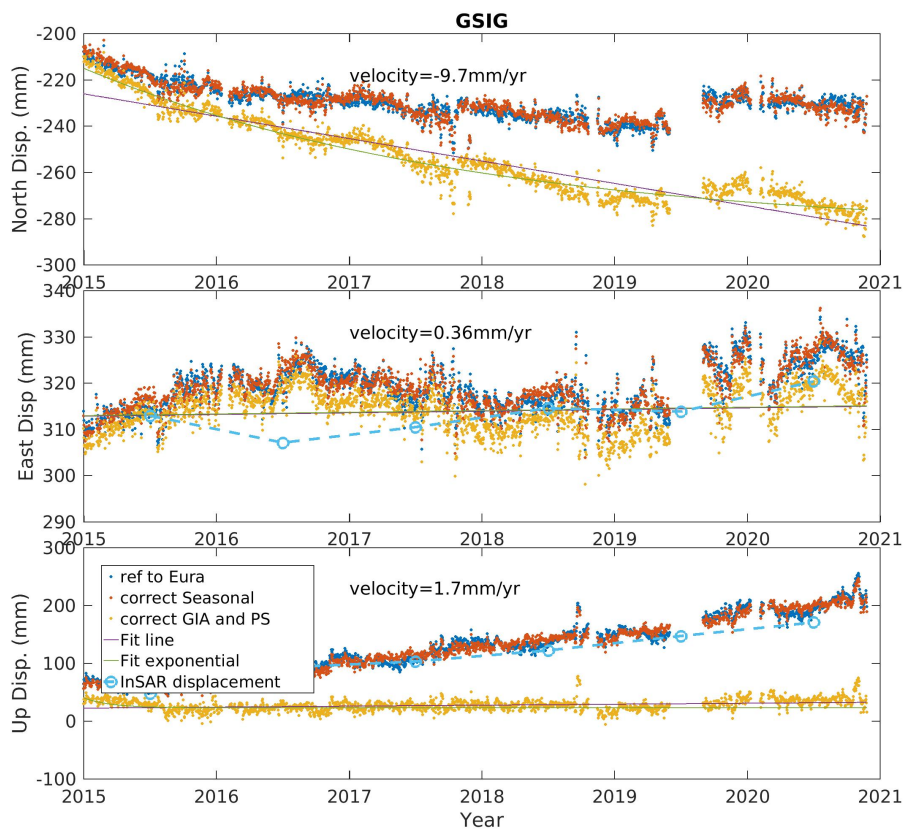


**Figure S2.** GNSS timeseries from GSIG station (see location in Figure 1). The blue dot curve is the timeseries from observation. The red dot curve is the observation corrected for seasonal variation. The yellow dot curve is corrected for seasonal variation, Glacial Isostatic Adjustment (GIA), and plate spreading (PS). The fitted red line is the average velocity estimated from the yellow dots, with the velocity labeled in the figure. We also fit an exponential line to our observation (green curve). Inferred InSAR displacement is shown in blue circles with a dashed line (see Figures S9 and S10).

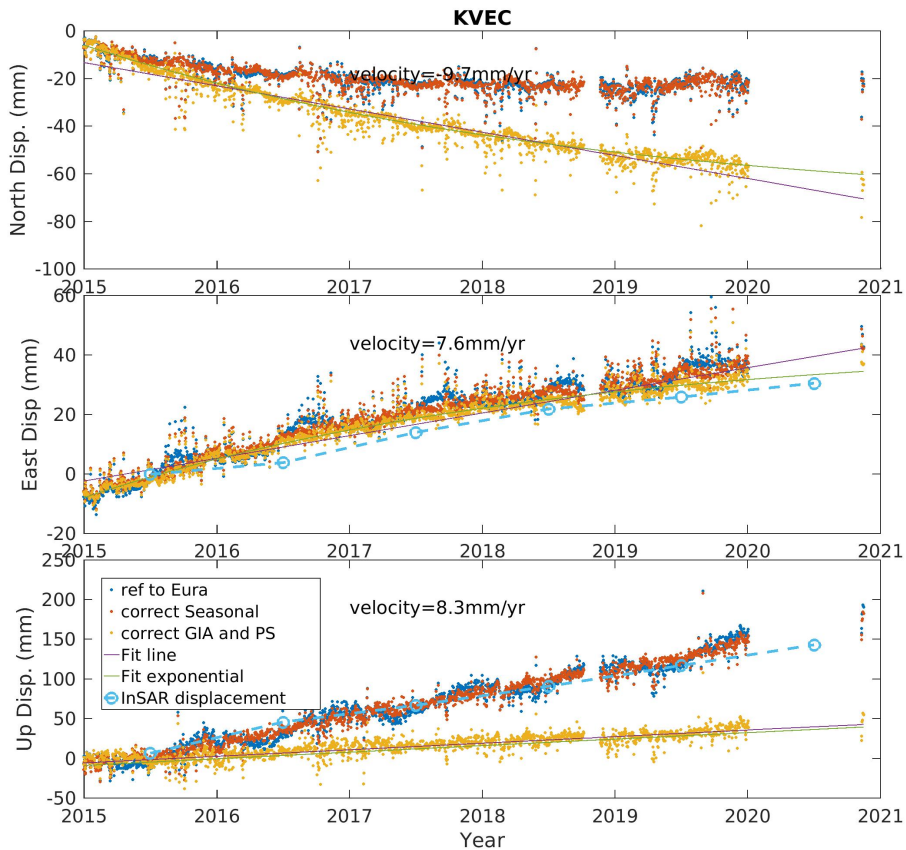


**Figure S3.** GNSS timeseries from KVEC station (see location in Figure 1). The blue dot curve is the timeseries from observation. The red dot curve is the observation corrected for seasonal variation. The yellow dot curve is corrected for seasonal variation, Glacial Isostatic Adjustment (GIA), and plate spreading (PS). The fitted red line is the average velocity estimated from the yellow dots, with the velocity labeled in the figure. We also fit an exponential line to our observation (green curve). Inferred InSAR displacement is shown in blue circles with a dashed line (see Figures S9 and S10).

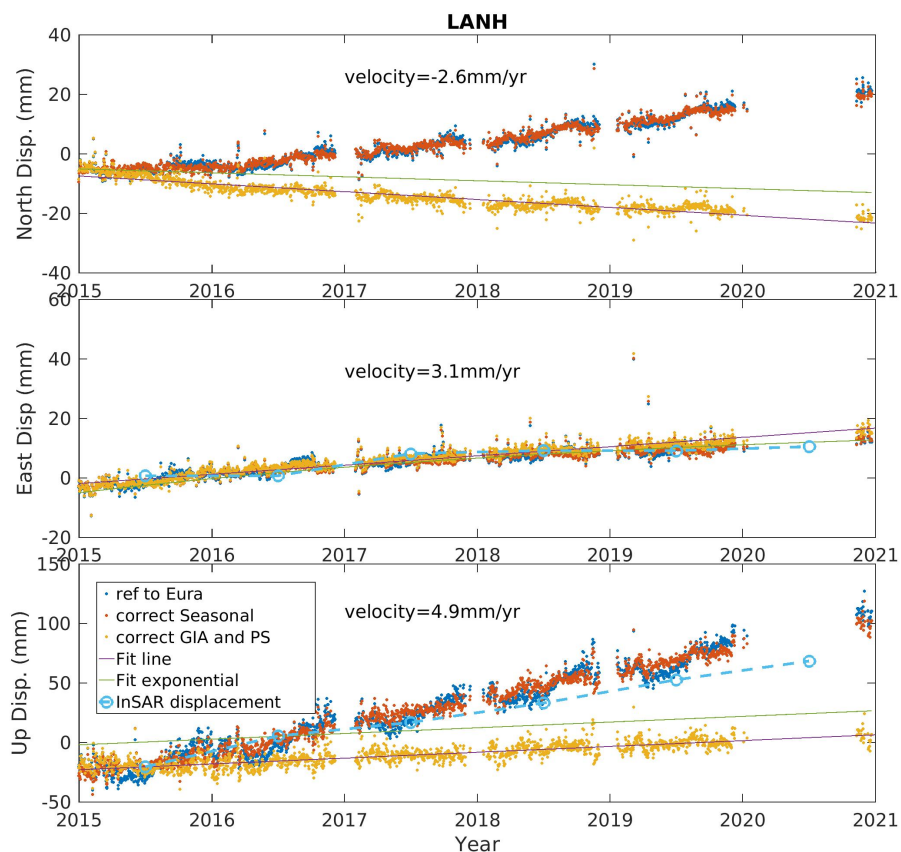


**Figure S4.** GNSS timeseries from LANH station (see location in Figure 1). The blue dot curve is the timeseries from observation. The red dot curve is the observation corrected for seasonal variation. The yellow dot curve is corrected for seasonal variation, Glacial Isostatic Adjustment (GIA), and plate spreading (PS). The fitted red line is the average velocity estimated from the yellow dots, with the velocity labeled in the figure. We also fit an exponential line to our observation (green curve). Inferred InSAR displacement is shown in blue circles with a dashed line (see Figures S9 and S10).

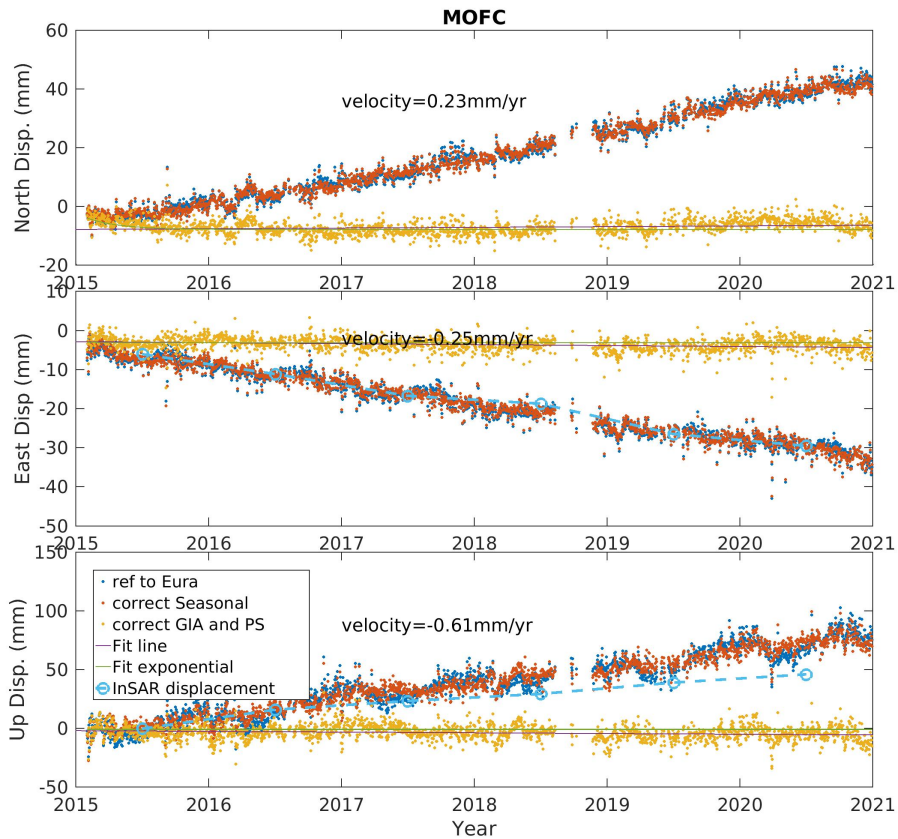


**Figure S5.** GNSS timeseries from MOFC station (see location in Figure 1). The blue dot curve is the timeseries from observation. The red dot curve is the observation corrected for seasonal variation. The yellow dot curve is corrected for seasonal variation, Glacial Isostatic Adjustment (GIA), and plate spreading (PS). The fitted red line is the average velocity estimated from the yellow dots, with the velocity labeled in the figure. We also fit an exponential line to our observation (green curve). Inferred InSAR displacement is shown in blue circles with a dashed line (see Figures S9 and S10).

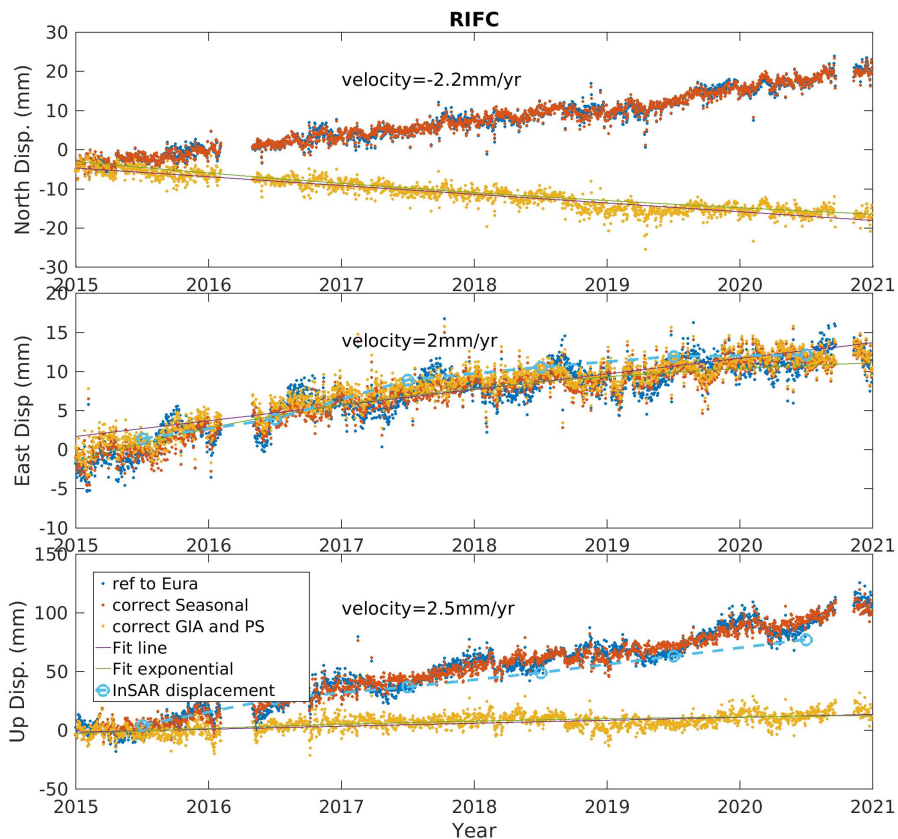


**Figure S6.** GNSS timeseries from RIFC station (see location in Figure 1). The blue dot curve is the timeseries from observation. The red dot curve is the observation corrected for seasonal variation. The yellow dot curve is corrected for seasonal variation, Glacial Isostatic Adjustment (GIA), and plate spreading (PS). The fitted red line is the average velocity estimated from the yellow dots, with the velocity labeled in the figure. We also fit an exponential line to our observation (green curve). Inferred InSAR displacement is shown in blue circles with a dashed line (see Figures S9 and S10).

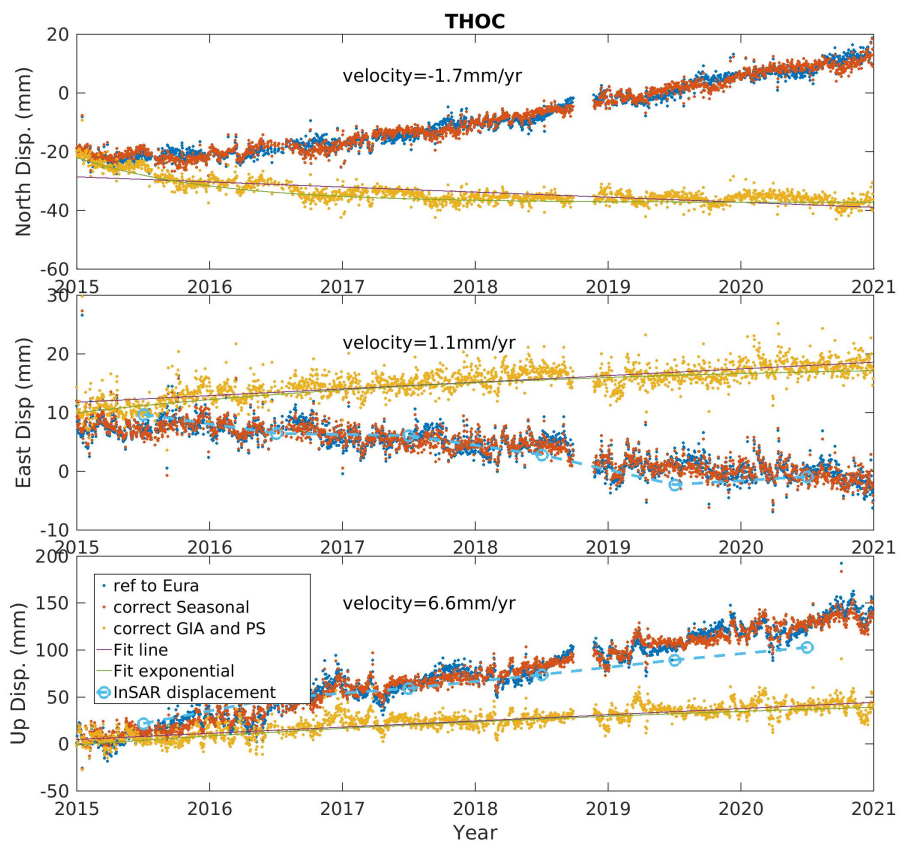


**Figure S7.** GNSS timeseries from THOC station (see location in Figure 1). The blue dot curve is the timeseries from observation. The red dot curve is the observation corrected for seasonal variation. The yellow dot curve is corrected for seasonal variation, Glacial Isostatic Adjustment (GIA), and plate spreading (PS). The fitted red line is the average velocity estimated from the yellow dots, with the velocity labeled in the figure. We also fit an exponential line to our observation (green curve). Inferred InSAR displacement is shown in blue circles with a dashed line (see Figures S9 and S10).

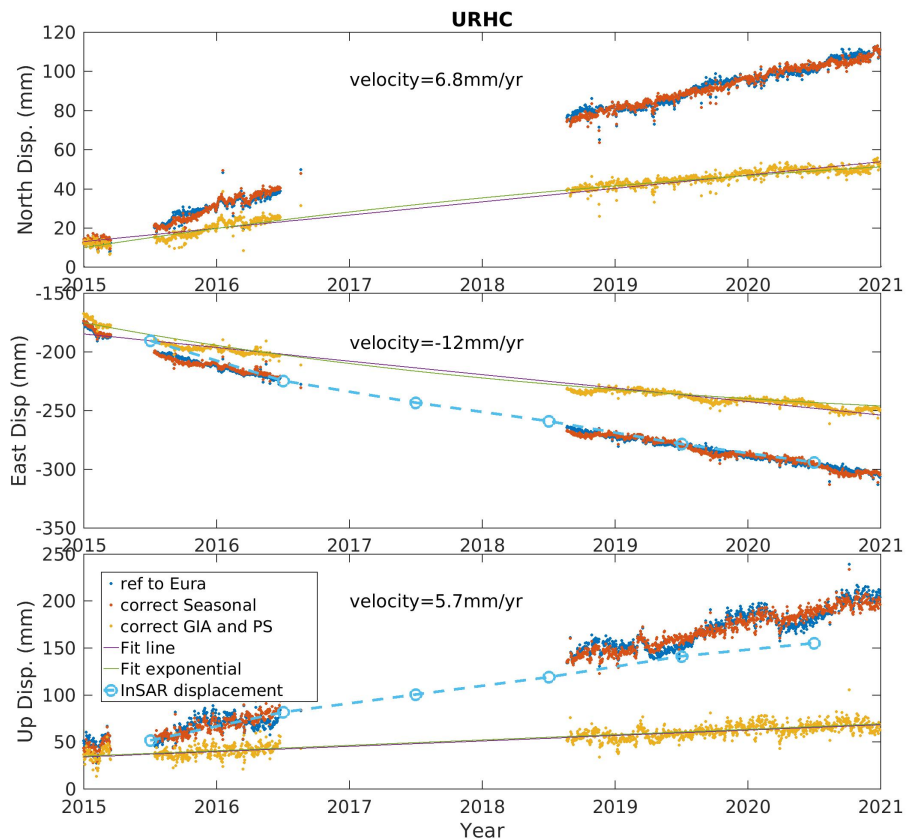


**Figure S8.** GNSS timeseries from URHC station (see location in Figure 1). The blue dot curve is the timeseries from observation. The red dot curve is the observation corrected for seasonal variation. The yellow dot curve is corrected for seasonal variation, Glacial Isostatic Adjustment (GIA), and plate spreading (PS). The fitted red line is the average velocity estimated from the yellow dots, with the velocity labeled in the figure. We also fit an exponential line to our observation (green curve). Inferred InSAR displacement is shown in blue circles with a dashed line (see Figures S9 and S10).



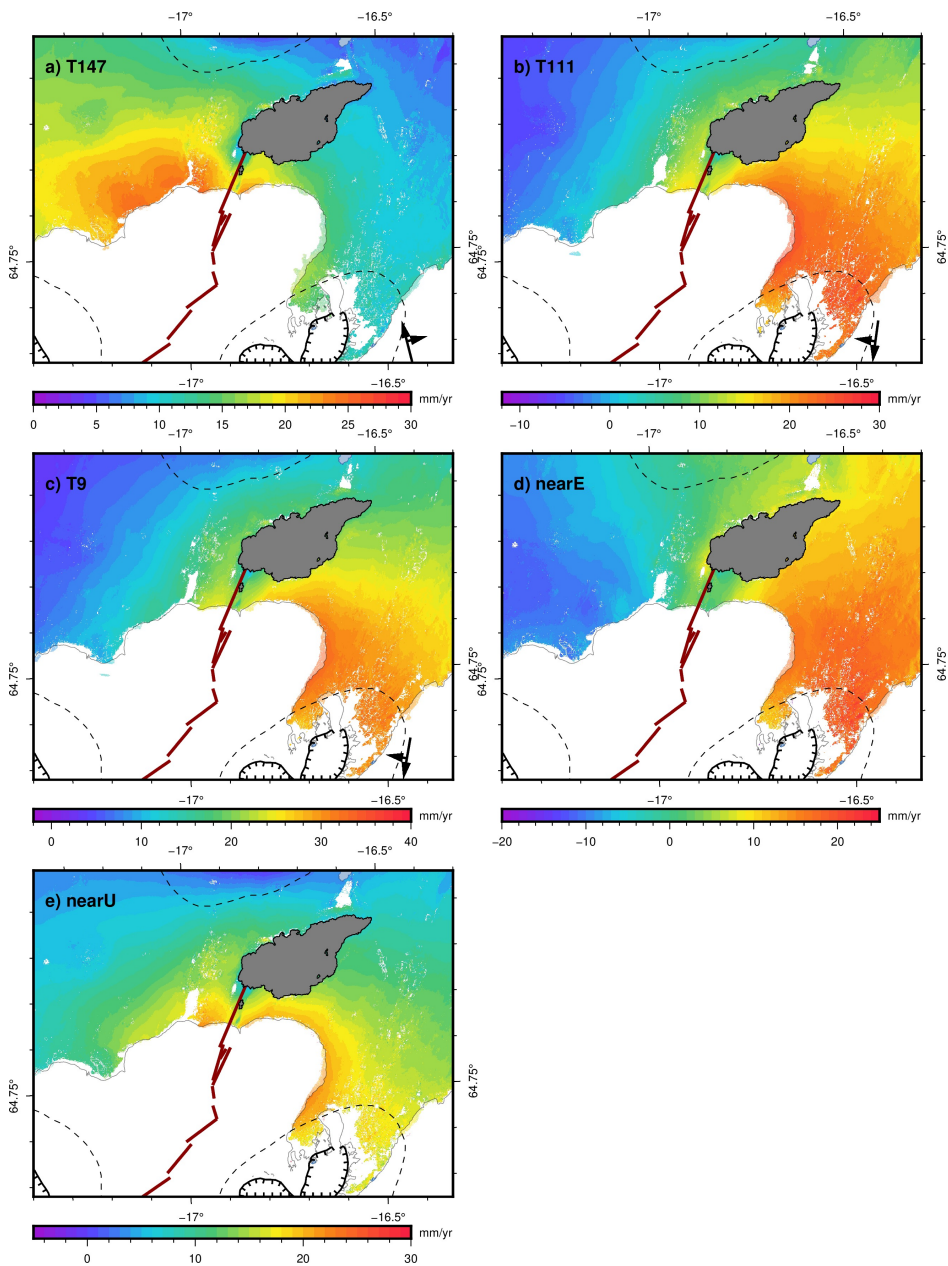


**Figure S9.** The observed average Line-of-Sight (LOS) InSAR velocity field during 2015-2020 from Sentinel (a) Track 147, (b) Track 111, and (c) Track 9. The LOS velocity fields are also decomposed into approximately-east (d) near-east and approximately-up e) near-up components.

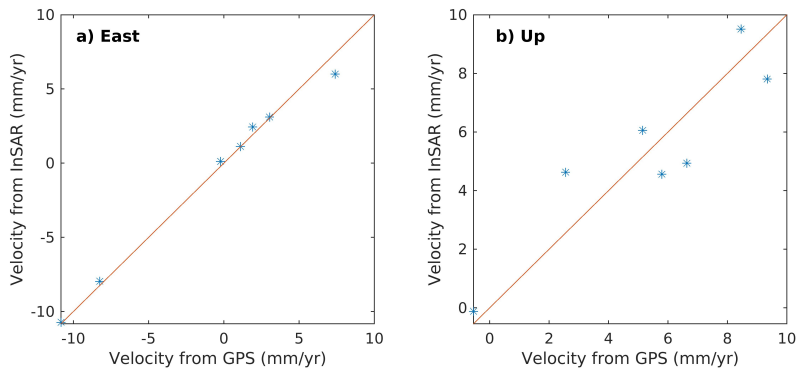


**Figure S10.** Comparison between the average GNSS (x-axis) and InSAR (y-axis) deformation rate in the east (a) and up (b) directions for the 2015-2020 period at continuous GNSS sites. The inferred InSAR velocities are from Figure S9. Temporal evolution of the InSAR displacement components is compared with GNSS in Figures S1-S8. There is a good agreement between the two data sets.

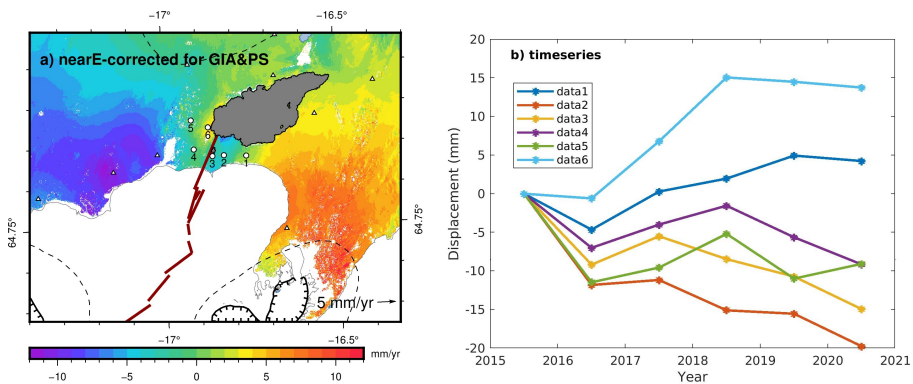


**Figure S11.** Six selected points close to the dike in our study area (a) and their near-east displacement measured by InSAR (b). The displacements (b) are corrected by subtracting the plate spreading and glacial isostatic adjustment model from our observations. Positive displacements are the movement towards the east. All the points show westward movement between 2015-2016, and eastward movement between 2016-2017. The fastest eastward average velocity is at point 6 and the fastest westward average velocity is at point 2.

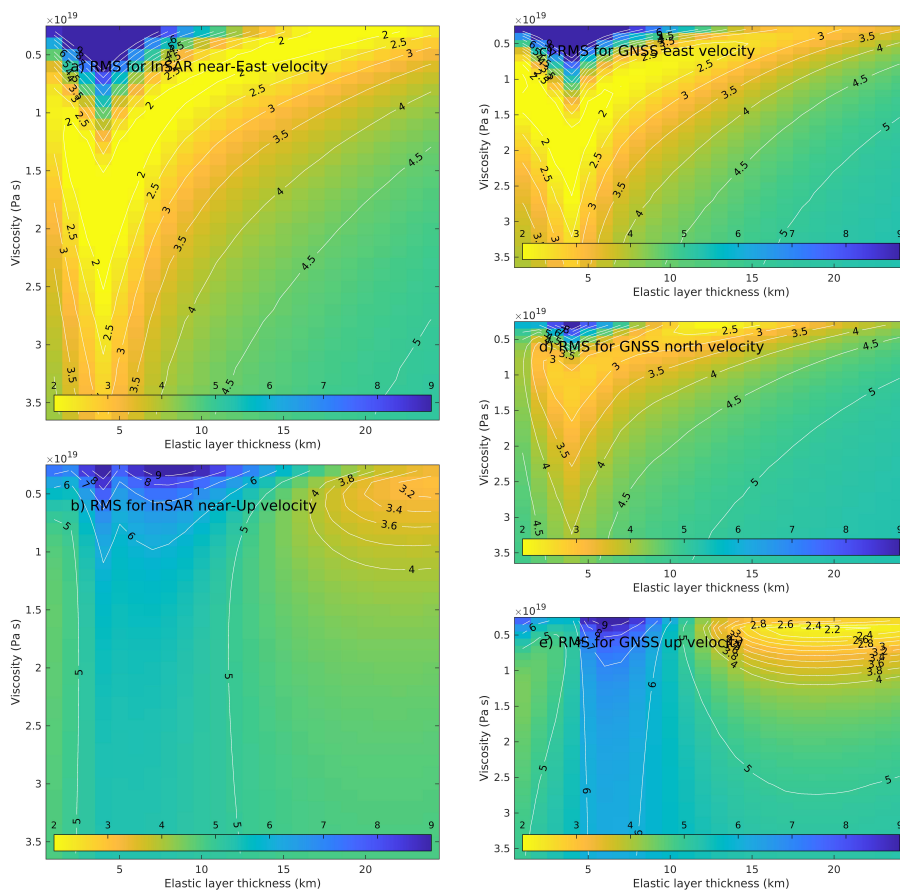


**Figure S12.** Root mean square (RMS) error between the corrected velocity fields and modeling results. The corrected velocity fields are from (a) InSAR near-east velocity, (b) InSAR near-up velocity, (c) GNSS east velocity, (d) GNSS north velocity, and (e) GNSS up velocity. The x-axis is the viscoelastic layer depth (1-24 km with 1 km step) and the y-axis is the viscosity ( $0.3$ - $3.6 \times 10^{19}$  Pa s with  $0.1 \times 10^{19}$  Pa s step). The horizontal components from both InSAR and GNSS prefer a model with a relatively thinner elastic layer, while the vertical components prefer a relatively thicker elastic layer.

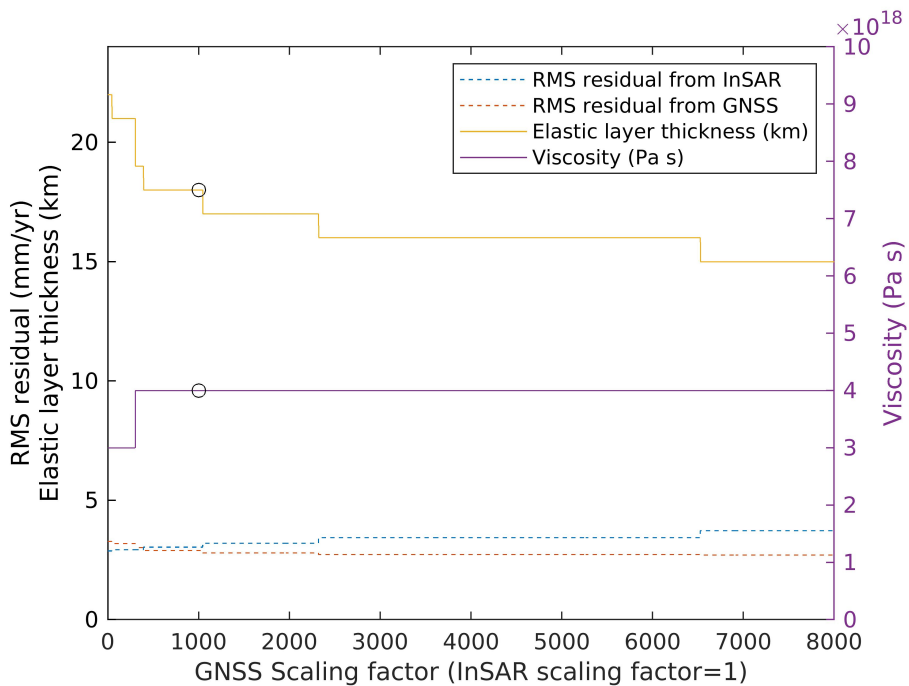


**Figure S13.** Selecting the scaling factor for GNSS. We set the scaling factor as 1 for InSAR, and vary the weight of GNSS from 1 to 8000. We consider near-east and near-up components for InSAR, and all 3 components for GNSS. We give twice the weight for horizontal components from both InSAR and GNSS. For each scaling factor, we find an optimal elastic layer thickness and viscosity, as done in Figure 3. We use 1000 (black circles) as the GNSS scaling factor.

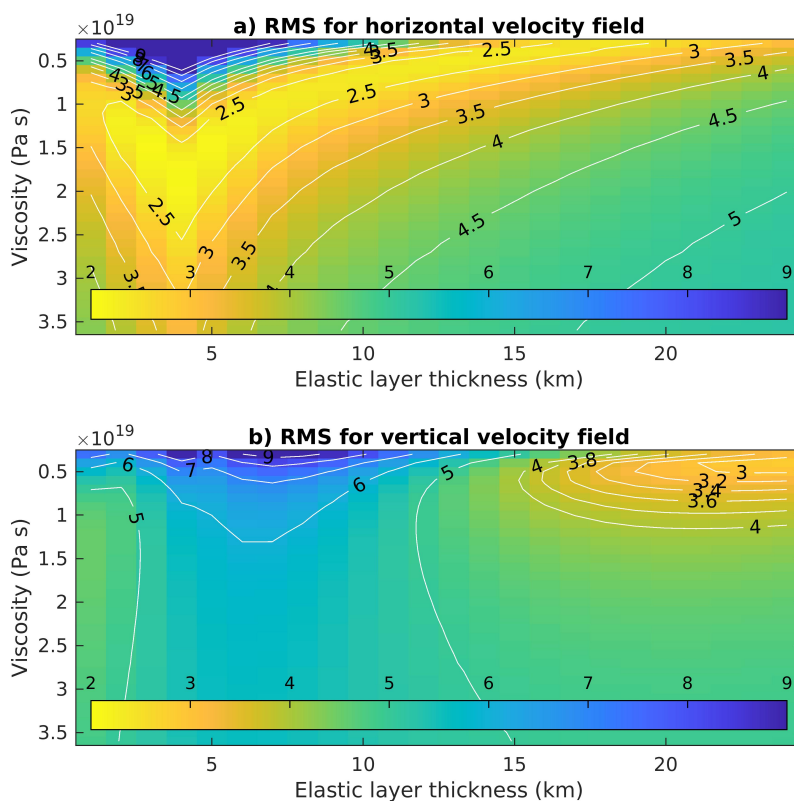


**Figure S14.** Root mean square (RMS) residual between the corrected velocity fields and modeling results. The horizontal velocity (a) includes the near-east component from InSAR, and the east and north components from GNSS. The vertical velocity (b) includes the near-up component from InSAR and up component from GNSS. The weight of GNSS vs InSAR is 1000:1. The x-axis is the elastic layer thickness (1-24 km with 1 km step) and the y-axis is the viscosity ( $0.3\text{-}3.6 \times 10^{19}$  Pa s with  $0.1 \times 10^{19}$  Pa s step). The optimal viscosity for the horizontal velocities is found at  $1.5 \times 10^{19}$  Pa s and the optimal elastic layer thickness is 3 km. For the vertical velocities, the model prefers the viscosity of  $0.4 \times 10^{19}$  Pa s and the deepest elastic layer.

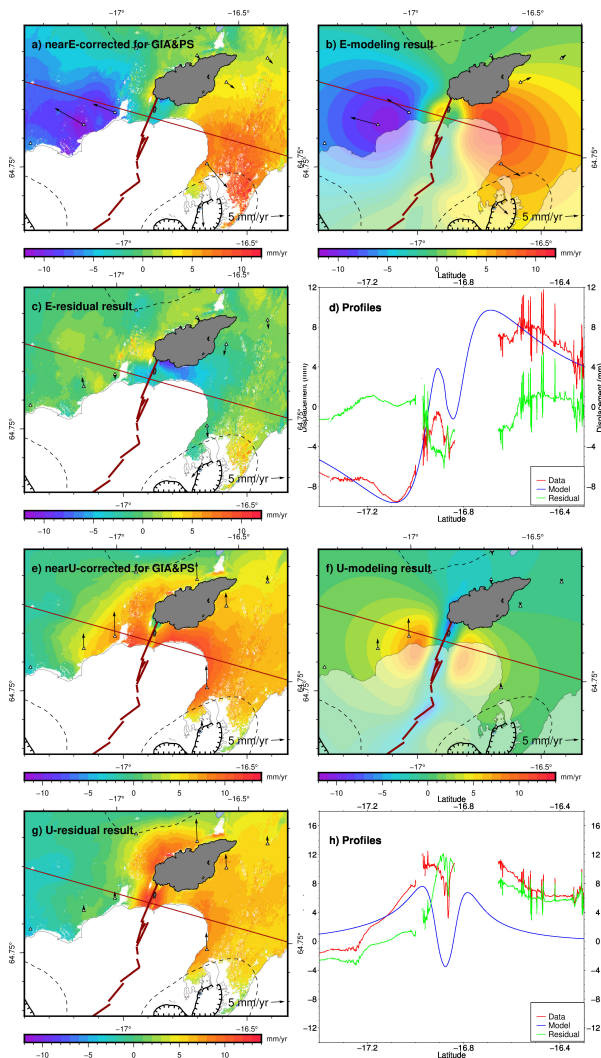


**Figure S15.** Corrected average velocity field in the horizontal (a-d) and vertical (e-h) directions during 2015-2020 from InSAR (color) and GNSS (black arrows). The decomposed near-east and near-up InSAR average velocities after correcting GIA and plate spreading signals are in a and e. The modeled east and up velocity from the viscoelastic model that best explains the horizontal velocity field is in b and f. The elastic layer thickness is 2 km and viscosity is  $1.2 \times 10^{19}$  Pa s. Panel c and g are the differences between corresponding observation (a and e) and model (b and f). Panel d and h are the near-east (red line in a, b, and c) and near-up (red line in e, f, and g) velocity profiles across the study area.

**Table S1.** The corrected velocity at GNSS stations used in this study. We use the Least Squares approach to estimate the corrected velocity from the GNSS timeseries (Figures S1-S8) after correcting for GIA and plate spreading.  $E$ ,  $N$ , and  $U$  stand for east, north, and up components. The locations of the stations are shown in Figure 1.

Station	$E$ (mm/yr)	$N$ (mm/yr)	$U$ (mm/yr)
URHC	-10.83	6.69	5.79
GIGO	-8.25	3.57	9.34
THOC	1.10	-1.47	6.63
KVEC	7.39	-9.36	8.46
LANH	3.04	-2.50	5.14
RIFC	1.91	-2.20	2.55
GSIG	0.20	-9.23	2.25
MOFC	-0.23	0.33	-0.55



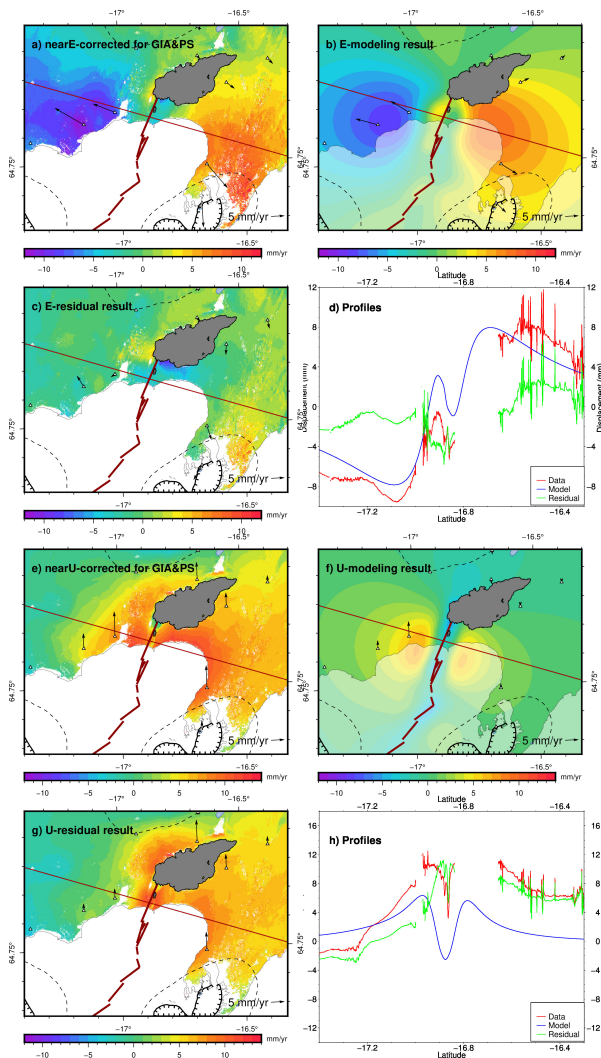


**Figure S16.** Corrected average velocity field in the horizontal (a-d) and vertical (e-h) directions during 2015-2020 from InSAR (color) and GNSS (black arrows). The decomposed near-east and near-up InSAR average velocities after correcting GIA and plate spreading signals are in a and e. The modeled east and up velocity from the viscoelastic model that best explains the vertical velocity field is in b and f. The elastic layer thickness is 3 km and viscosity is  $1.5 \times 10^{19}$  Pa s. Panel c and g are the differences between corresponding observation (a and e) and model (b and f). Panel d and h are the near-east (red line in a, b and c) and near-up (red line in e, f, and g) velocity profiles across the study area.

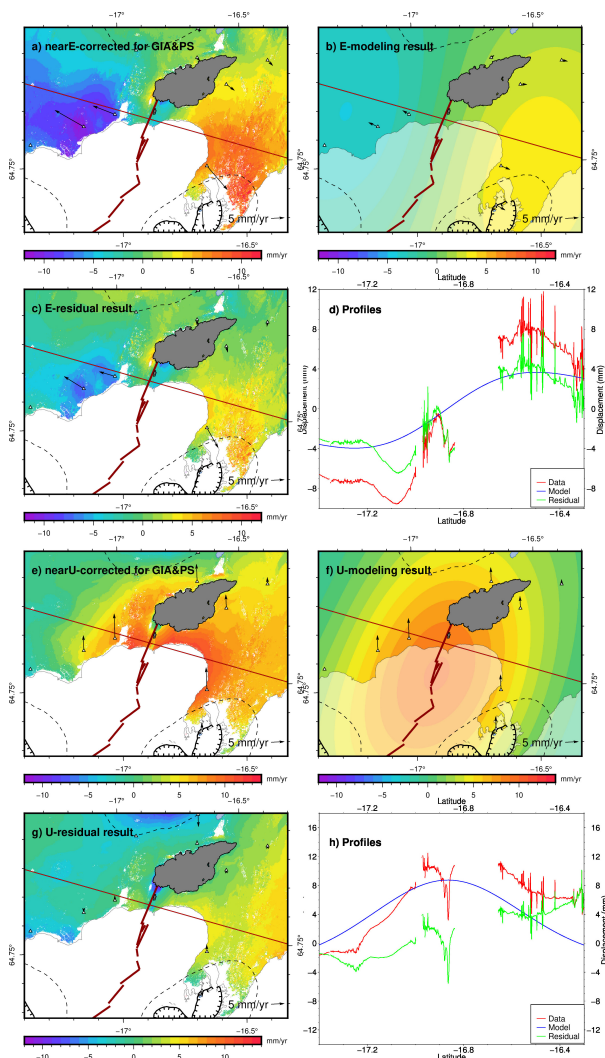


**Figure S17.** Corrected average velocity field in the horizontal (a-d) and vertical (e-h) directions during 2015-2020 from InSAR (color) and GNSS (black arrows). The decomposed near-east and near-up InSAR average velocities after correcting GIA and plate spreading signals are in a and e. The modeled east and up velocity from the viscoelastic model that best explains the horizontal velocity field is in b and f. The elastic layer thickness is 24 km and viscosity is  $0.4 \times 10^{19}$  Pa s. Panel c and g are the differences between corresponding observation (a and e) and model (b and f). Panel d and h are the near-east (red line in a, b, and c) and near-up (red line in e, f, and g) velocity profiles across the study area.

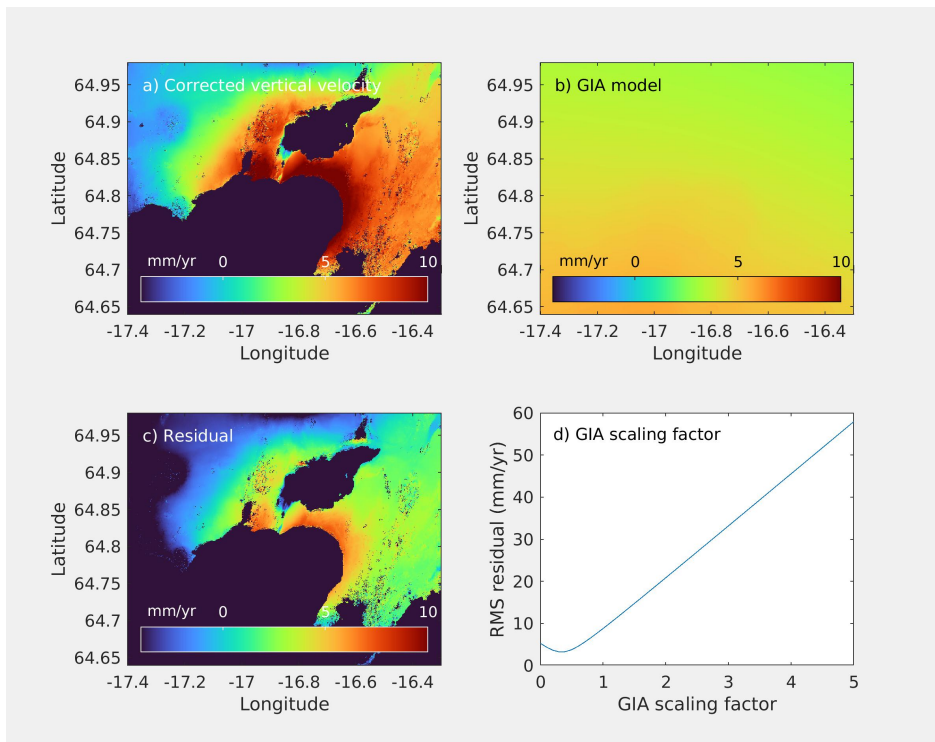


**Figure S18.** We test the hypothesis that an improved glacial isostatic adjustment (GIA) model can explain the corrected vertical displacement. We test if the corrected vertical velocity field (a) can be explained by applying a different scaling factor (d) to the model by Auriac (2014). The scaling factor we searched for ranges from 0 to 5 with the step of 0.1. The optimal value is found at 0.3, which is shown in panel b. The residual between panels a and b is in panel c.



## Paper III

### **Improving understanding of post-eruptive viscoelastic relaxation and magma inflow by studies of stress and surface displacement: A case study at Bárðarbunga volcano, Iceland**

Siqi Li, Freysteinn Sigmundsson, Tadashi Yamasaki, Páll Einarsson, Kristín Jónsdóttir, Halldór Geirsson and Andrew Hooper



---

manuscript to *Geophysical Journal International*

1       **Similarity of stress and ground displacement patterns**  
2       **caused by viscoelastic relaxation and magma inflow in a**  
3       **post-eruptive period: A case study at Bárðarbunga**  
4       **volcano, Iceland**

5       **Siqi Li<sup>1</sup>, Freysteinn Sigmundsson<sup>1</sup>, Tadashi Yamasaki<sup>2</sup>, Páll Einarsson<sup>1</sup>,**  
6       **Kristín Jónsdóttir<sup>3</sup>, Halldór Geirsson<sup>1</sup> and Andrew Hooper<sup>4</sup>**

7       <sup>1</sup>Nordic Volcanological Center, Institute of Earth Sciences, University of Iceland, Iceland

8       <sup>2</sup>Geological Survey of Japan, AIST, 1-1-1 Higashi, Tsukuba, Ibaraki 305-8567, Japan

9       <sup>3</sup>Icelandic Meteorological Office, Reykjavík, Iceland

10      <sup>4</sup>COMET, School of Earth and Environment, University of Leeds, UK

---

Corresponding author: Siqi Li, [sil10@hi.is](mailto:sil10@hi.is)

**Abstract**

Two common processes causing post-eruptive volcano deformation are renewed magma inflow into volcano roots and viscoelastic relaxation due to previous magma transfer. Earlier studies suggest that these two processes have similar spatial patterns of ground deformation. Here, we explore if associated stress changes or temporal variation of ground deformation signals can shed light on which process dominates during a post-eruptive period. We use a two-layered viscoelastic model with a point source to represent the viscoelastic response to previous large-scale magma drainage in volcano roots below the brittle-ductile boundary. The spatial patterns of stress fields induced by the viscoelastic model broadly resemble the stress due to magma inflow. Considering a point source model with volume contraction of  $0.4 \text{ km}^3$ , the stress field caused by viscoelastic relaxation with a viscosity of  $3 \times 10^{18} \text{ Pa s}$ , in the initial 6.3 years after magma drainage, is similar to that generated by a magma inflow model with the total inflow volume of  $0.36 \text{ km}^3$ . The temporal variation and spatial distribution of the stresses are similar for both models if the magma inflow rate decays with time. By comparing stresses, e.g., through seismicity studies, it is difficult to distinguish the two processes. In the viscoelastic model, the modeled ground displacement time series follows approximately an exponential decay, with a decay constant that varies with distance from the source. The magma inflow model has a spatially uniform decay constant if the source geometry does not evolve. We apply our findings to the Bárðarbunga volcano. The largest shear stress due to both processes occurs at a similar location, where faults move on a caldera boundary, driving upward motion within the caldera of the volcano in a post-eruptive period. The GNSS time-series show horizontal displacement rate decaying with time. The decay constant somewhat varies with distance from the caldera, between two to five years at all continuous stations. A viscoelastic relaxation model with the viscosity between  $1\text{-}6 \times 10^{18} \text{ Pa s}$ , however, has the decay constant longer than ten years at all the stations. The similarity of deformation due to magmatic inflation and post-eruptive viscoelastic relaxation means that rapid inflation of recently erupting volcanoes is not necessarily due to new magma inflow. However, detailed long-term studies of temporal response can help to discriminate between the different processes. To better explain the post-eruptive deformation and stress at the Bárðarbunga volcano, a different elastic layer thickness, source geometry, or type of viscoelastic model could be explored.



## 1 Introduction

Ground deformation measurements provide important constraints on volcano hazards, as surface uplift may relate to magma accumulation beneath a volcano, which can lead to an eruption (, e.g., Sturkell et al., 2006; Segall et al., 2019; Sigmundsson et al., 2010). However, magma accumulation is not the only cause of surface uplift. Other processes, such as viscoelastic relaxation, may also contribute (Del Negro et al., 2009; Novoa et al., 2019; Morales Rivera et al., 2019; Yamasaki et al., 2020). Understanding whether magma is involved and the amount of magma involved is important for volcano monitoring and hazard management (Donovan et al., 2012; Biggs et al., 2014).

For the same eruption or volcanic unrest, several studies have used either viscoelastic relaxation or magma inflow to explain ground deformation signals, such as at Etna (Bonaccorso et al., 2005; Del Negro et al., 2009), Laguna del Maule (Novoa et al., 2019; Feigl et al., 2013; Le Mével et al., 2015, 2016), Kilauea, Krafla, Kutcharo Caldera and Aira Caldera (Yamasaki et al., 2018; Fujiwara et al., 2017), and Bárðarbunga (Li et al., 2021).

We here address the similarity of geophysical signals of magma inflow and viscoelastic relaxation, by initially attempting to re-create a viscoelastic relaxation three-dimensional stress field using a magma inflow model. If a magma inflow model cannot create a stress field similar to a viscoelastic model, then seismicity or dike trajectories may help to distinguish between the two processes. We also compare the temporal variation of the stress and surface displacement fields using these models, to improve the understanding of the differences between temporal variation in the two types of signals. We apply our findings to the Bárðarbunga volcano, Iceland, as a test case.

## 2 Model setup

We calculate viscoelastic and magma inflow models separately, with a point pressure source at the same depth and location. This allows a comparison of the predictions of simple conceptual models of the two processes, but ignores some complications that may arise in reality. For example, caldera collapse in relation to major co-eruptive magma transfer will alter topography and may lead to additional influence on a viscoelastic model, magma may flow into a sill rather than a point source, and fault slip may occur. We vary the magma inflow volume for the magma inflow model, attempting to find model parameters that recreate the most comparable stress field as the viscoelastic model. Figure 1a

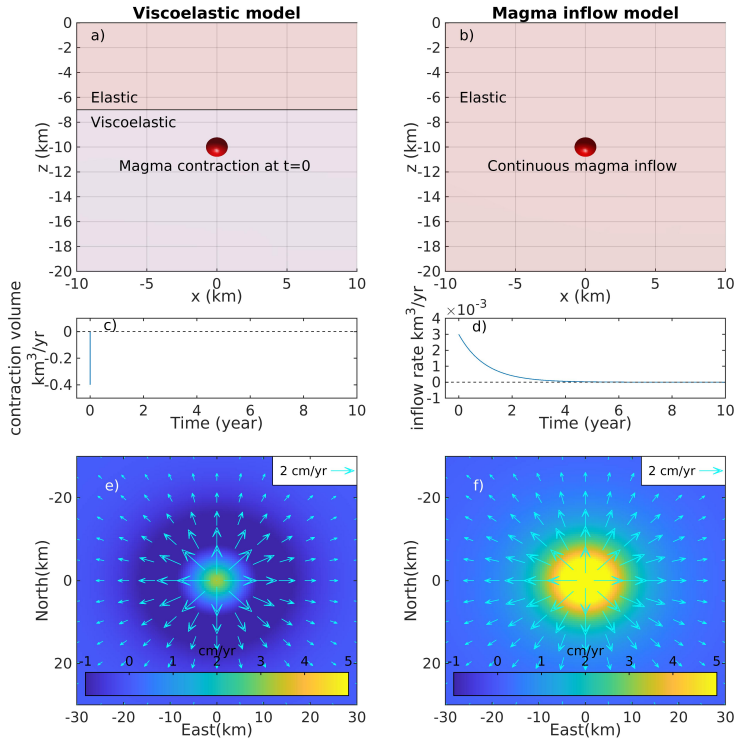


**Figure 1.** Viscoelastic relaxation model (left) and magma inflow model in elastic material (right). Cross-sections of the central part of the two models (top panels), modeled magma flow rate at the source (middle panels), and map view of the average velocity field in the initial 6.3 years in the post-eruptive period (bottom panels). In the displayed cross-section, the x-axis is north-south oriented, and the z-axis is the vertical direction. Both models have magma sources at 10 km below the surface. For the viscoelastic model (a), the magma source contracts by  $0.4 \text{ km}^3$  at  $t=0$ , and no magma movement after  $t=0$  (c). For the elastic model (b), magma inflow occurs continuously after  $t=0$  with a time-dependent inflow rate (d). The time step is 0.1 years from 0 to 10 years. The average surface velocities are in cm/yr (panel e and f), where the arrows show the horizontal velocity and the color shows the vertical velocity.

75 and b show the model setup for the viscoelastic and magma inflow model. For the vis-  
76 coelastic relaxation process, we use a two-horizontally-layered structure with a 7 km thick  
77 elastic layer on top of a  $3 \times 10^{18}$  Pa s viscoelastic half-space. For magma inflow model,  
78 we consider a uniform elastic half-space. Both models have homogeneous isotropic ma-  
79 terial within the layers, with the same shear modulus of 30 GPa and Poisson's ratio of  
80 0.25.

81 We use the semi-analytical software RELAX to run the models (Barbot, 2014; Bar-  
82 bot & Fialko, 2010a, 2010b). The models are three-dimensional,  $256 \times 256 \times 128$  km  
83 in x (north), y (east), and z (down) directions, with 250 m resolution. Stress is taken as  
84 positive for extensional stress and negative for contractional stress. The time step in the  
85 viscoelastic model is 0.1 years, from 0 to 10 years. The point source is in both models,  
86 placed at 10 km depth.

87 For the viscoelastic model, equilibrium conditions are assumed at the beginning  
88 time (all stresses relaxed). Magma withdrawal during an eruption is represented by the  
89 contraction of a point source at  $t=0$  in the model. No magma movement is involved af-  
90 terward (Figure 1c). This viscoelastic model for effects of co-eruptive pressure drop in  
91 volcano roots is the same as used by Li et al. (2021), although that study also consid-  
92 ered the additional effect of caldera collapse modeled as surface unloading (in relation  
93 to the creation of caldera subsidence changing the surface topography). For the elastic  
94 model, we consider magma inflow continuously during the post-eruptive period at the  
95 same depth, into a point source of pressure. Magma inflow volume decays exponentially  
96 with time to make the temporal variation of the surface displacement comparable to the  
97 viscoelastic relaxation, as a potential response to co-eruptive pressure drop (Figure 1d).  
98 The map view of the average velocity field in the initial 6.3 years for both models has  
99 surface uplift directly above the source and horizontal displacement away from the source  
100 in the surrounding area. With our model setting, the viscoelastic model predicts slight  
101 subsidence in area 6-33 km away from the center, while the elastic model causes an up-  
102 lift in the whole area (Figure 1e and f). Adding an effect of caldera collapse to the vis-  
103 coelastic model, approximated as surface unloading, may take the two vertical velocity  
104 fields more similar, as such a model will cause additional uplift in the viscoelastic model.

### 3 Spatial pattern of the stress changes

In this section, we consider the cumulative stress change caused by the two processes from  $t=0^+$  to  $t=6.3$  years, excluding the crustal volume in the immediate vicinity of the point source (because of modeling simplifications, stresses are unrealistically high there).

#### 3.1 Viscoelastic relaxation

With the viscoelastic relaxation setup, our demonstration model considers a contraction volume of  $0.4 \text{ km}^3$  for a 10 km deep source instantaneously at  $t=0$  (Figure 1c, Li et al., 2021). The region closest to the source is masked (white region), corresponding to a radius of 2 km (Figure 2). Magma withdrawal causes surface contraction instantaneously at  $t=0$ . After  $t=0$ , the subsurface relaxes (Figure 1), with stress change in the subsurface, as shown in Figure 2a, d, and g. The normal stresses  $\sigma_{11}$ ,  $\sigma_{22}$  and  $\sigma_{33}$  change by up to 160 MPa over the initial 6.3 years. Shear stress change  $\sigma_{13}$  has a different sign to the north and south of the source because of symmetry and the direction of the axes of the coordinate system (Figure 2j). If faults would exist in these areas, they would tend to slip in opposite directions in response to the stress changes. The boundary between the viscoelastic half-space and the elastic layer strongly affects the stress field, as the stress change caused by the viscoelastic relaxation decays significantly when passing the boundary, which can be seen in all four components at a depth of 7 km (Figure 2a, d, g, and j).

#### 3.2 Magma inflow

In order to test the hypothesis that magma inflow can create a similar stress field as viscoelastic relaxation, we search for the magma inflow volume that best replicates a similar stress field. First, we run forward modeling for a magma inflow model, with the magma inflow volume of  $4.0 \times 10^8 \text{ m}^3$  (Figure 1b) as a reference model. As the stress field scales linearly with the source volume, we can vary the stress field by multiplying a scaling factor to vary the magma inflow volume.

We compare the stresses created by viscoelastic relaxation over the initial 6.3 years (Figure 2) and magma inflow within a  $10 \times 10 \text{ km}^2$  cross-sectional ignoring a  $2 \text{ km} \times 2 \text{ km}$  squared central area (as we only consider the stress field outside of the source). By

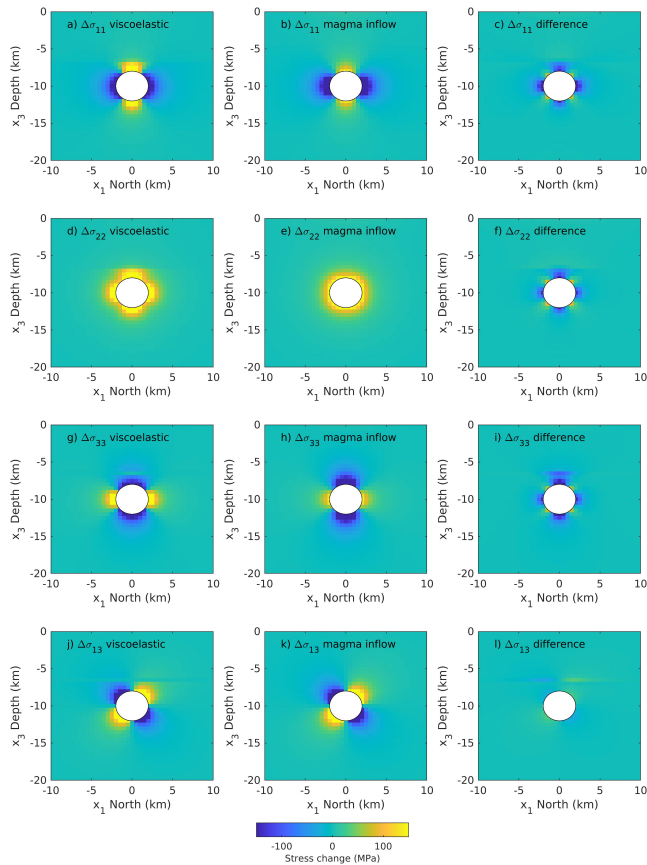


**Figure 2.** The spatial pattern of the stress change caused by viscoelastic relaxation (left) and magma inflow (middle) since  $t=0^+$ . Panels to the right show the corresponding stress difference between the two models. The panels show cross-sections of four components of stress change in a plane parallel to the north-south direction in the initial 6.3 years. The left panels show the stress change in the viscoelastic relaxation caused by magma withdrawal from a  $0.4 \text{ km}^3$  point source. The middle panels show stress change in a magma inflow model with a total inflow volume of  $0.36 \text{ km}^3$ . The four stress components are:  $\sigma_{11}$ ,  $\sigma_{22}$ ,  $\sigma_{33}$ ,  $\sigma_{13}$ . The x-axis is the north-south direction, and the z-axis is the vertical direction (depth). The crustal volume within a 2-km radius from the source center (white circle at the center of each panel) is masked to eliminate unrealistically high stress change predicted by the point source.

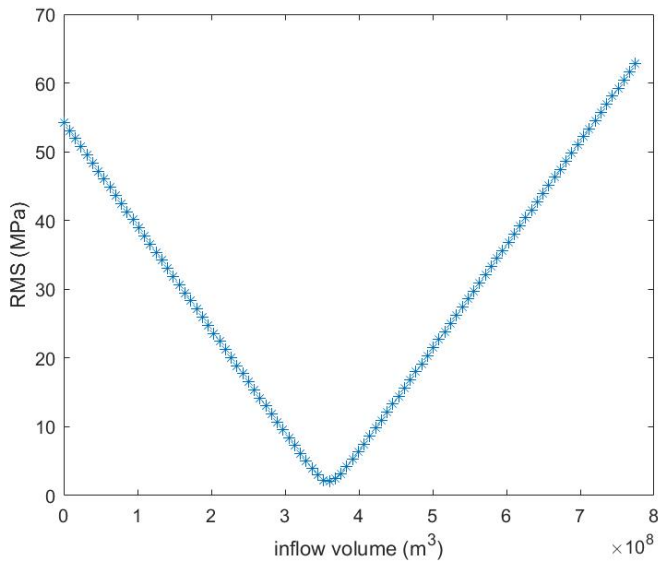


**Figure 3.** Derivation of the optimal magma inflow volume that produces a stress field similar to that produced by viscoelastic relaxation. The minimum RMS is 2 MPa when the total magma inflow volume is  $3.6 \times 10^8 \text{ m}^3$ .

135 varying the magma inflow volume from  $7.8 \times 10^6 \text{ m}^3$  to  $7.8 \times 10^{10} \text{ m}^3$  with a step of  
 136  $7.8 \times 10^6 \text{ m}^3$ , we find minimum residuals between the predicted viscoelastic relaxation  
 137 and magma inflow stresses when the magma inflow volume is  $3.6 \times 10^8 \text{ m}^3$  (Figure 3),  
 138 only 10% less than the volume change in the viscoelastic relaxation model.

139 Stresses created by the two models are similar (Figure 2). The minimum root-mean-  
 140 squared (RMS) residual between the magma inflow and viscoelastic models is 2 MPa in  
 141 the crustal volume considered, less than 5% of the maximum stress values. The main dif-  
 142 ference between the models is in the pattern of stresses above 7 km, where the stresses  
 143 from the viscoelastic model are much smaller than that in the magma inflow model (Fig-  
 144 ure 2). The material change from viscoelastic to elastic in the viscoelastic model is the  
 145 reason behind this. As the largest values of stresses in the viscoelastic model are within  
 146 the viscoelastic material, this difference does not significantly influence the RMS. We con-  
 147 clude that magma inflow can create a spatial pattern of stress change similar to that caused  
 148 by viscoelastic relaxation in a post-eruptive period.

## 149 4 Temporal variation of the stress changes

150 We next evaluate if the temporal variation of the stress field due to viscoelastic re-  
 151 laxation can be mimicked by magma inflow. For this purpose, we study the shear stress  
 152 component  $\sigma_{13}$ .

### 153 4.1 Viscoelastic relaxation

154 The shear stresses caused by viscoelastic relaxation decay with time. Figure 4a-  
 155 d show the cross-section of the shear stress change  $\sigma_{13}$  at  $0^+$ , 2, 4, and 6 years. The stress  
 156 change is calculated using the stress difference between time  $t$  and  $t+0.1$  year. When com-  
 157 paring the stress change rate at selected locations (6, 8, and 10 km depth below the sur-  
 158 face at 2.5 km horizontal distance away from the source shown in Figure 4a), the high-  
 159 est shear stress change is at 8 km below the surface. The shear stress at all depths de-  
 160 cays over time. The stress change rate at 8 km depth takes 5.8 years to decay 90%. The  
 161 sign of the shear stresses are opposite on the north and south side of the source, as well  
 162 as above and below the source.

### 163 4.2 Magma inflow

164 We aim to find a time-dependent magma inflow model that fits the temporal vari-  
 165 ation of the viscoelastic stress change. We start with extracting the stress field from vis-  
 166 coelastic relaxation model with time step of 0.1 year from 0 to 10 years. Using the same  
 167 strategy as in section 3, we can find the optimal magma inflow rate. These magma in-  
 168 flow models should produce similar stress field as viscoelastic relaxation model at each  
 169 time.

170 The results are shown in Figure 5, demonstrating it is possible to find magma in-  
 171 flow rate that reproduces the temporal variation of the stress field as in the viscoelas-  
 172 tic relaxation model. As the stress decays with time in the viscoelastic model, the stress  
 173 field in the magma inflow model also follows a decaying trend with time.

174 We fit the predicted magma inflow that best matches the viscoelastic relaxation  
 175 shown in Figure 5 with an exponential function

$$y(t) = ae^{-\frac{t}{\tau}}, \quad (1)$$

176 where  $y(t)$  is the magma inflow rate versus time. The best fit model has  $a=1.55 \times 10^8$   
 177  $\text{m}^3/\text{year}$  and a decay constant of  $\tau=2.48$  years.

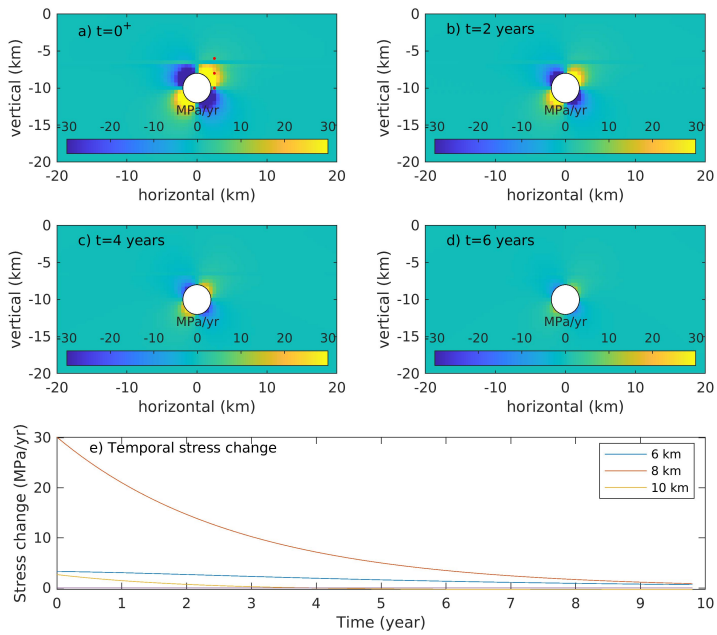


**Figure 4.** Cross-sections (panels a-d) of the spatial distribution of shear stress change rate. Panel e shows the stress change rate over the first ten years from the viscoelastic relaxation model. The red dots in panel a represent the observation locations shown in panel e.



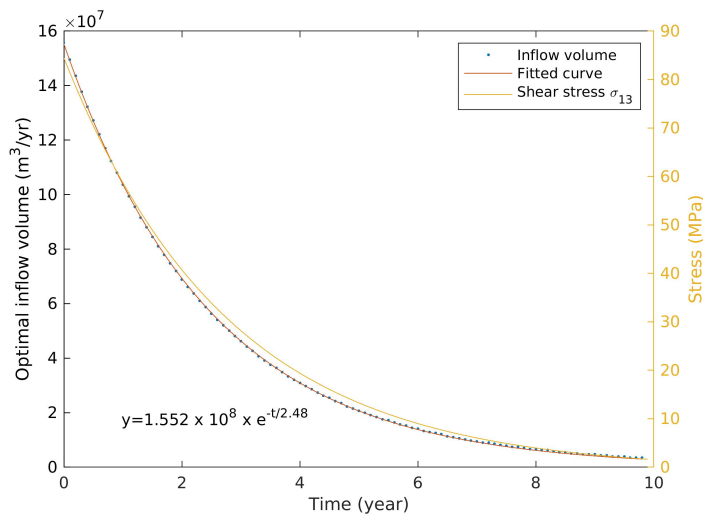


**Figure 5.** The optimal magma inflow rate that reproduces best the stress field created by the viscoelastic relaxation model. The x-axis is time. The y-axis on the left is the magma inflow rate ( $\text{m}^3/\text{yr}$ ) and on the right is the value of shear stress  $\sigma_{13}$  (MPa) in the viscoelastic model. The blue dots are the magma inflow rates from the inflow model that best explain the corresponding viscoelastic stress change, and the best-fitting curve is shown in red. The shear stress  $\sigma_{13}$  is for a point 2.5 km radially away from the source center at 10 km below the surface.

178 Magma inflow between two connected vertically stacked magma bodies is often mod-  
 179 eled with an equation similar to equation 1 (e.g., Segall, 2019), in particular if pressure  
 180 is initially lower in one of the bodies (upper one; after an eruption) and pressure remains  
 181 constant in the other (lower one; larger magma reservoir feeding the upper body). The  
 182  $a$  and  $\tau$  constants of the model depend on the pressure difference between the magma  
 183 bodies, their size and compressibility, and the nature of the conduit connecting them (Segall,  
 184 2019).

## 185 5 Temporal variation of the surface displacement

186 Temporal variation of surface displacement may help to distinguish the two pro-  
 187 cesses. For a point pressure source in an elastic deformation half-space, the vertical dis-

188 placement field,  $U_z$ , is given by

$$U_z = \Delta V \frac{1 - \nu}{\pi} \frac{d}{(r^2 + d^2)^{3/2}} \quad (2)$$

189 (Dzurisin, 2006). Here  $\nu$  is Poisson's ratio,  $d$  is the source depth, and  $r$  is the distance  
 190 from the surface projection of the source to the observation point. For the elastic mod-  
 191 eling, there is a linear relationship between the surface displacements and magma inflow  
 192 volume  $\Delta V$ . Therefore, with a time-dependent magma inflow rate, we would expect the  
 193 surface displacement at all geodetic stations in the area to show the same temporal pat-  
 194 tern as the magma inflow rate. All the geodetic stations then should share the same de-  
 195 cay constant if the magma inflow rate decays exponentially. This behavior can be com-  
 196 pared to the evolution of surface displacements in the viscoelastic model after  $t_0$ .

197 With the viscoelastic model structure in Figure 1a, we calculate the surface dis-  
 198 placement time series at stations 0, 5, 10, 15, and 20 km away from the center (Figure  
 199 6). Horizontal contraction and subsidence occur at  $t=0$ . After  $t=0$ , the horizontal dis-  
 200 placements are directed away from the center. The center of the source subsides slightly  
 201 at the very beginning, but then turns to uplift. Similar behavior occurs farther from the  
 202 source, but the farther from the center, the slower and more gradual the turn from sub-  
 203 sidence to uplift. We evaluate if an equation of the same form as equation 1 can describe  
 204 the temporal variation of horizontal displacement at each location in the initial 6.3 years:

$$disp(t) = Ae^{-\frac{t}{\tau}} \quad (3)$$

205 Here  $t$  is the observation time, and  $disp$  is the corresponding displacement at each  
 206 point. We fit equation 3 only to the horizontal displacements from both models, as the  
 207 vertical displacement from the viscoelastic model is not well described by an exponen-  
 208 tial decay pattern. We use the Fit function in the Matlab software (MATLAB, 2020) to  
 209 derive the decay constant and amplitude vs. distance from the center, and the associ-  
 210 ated uncertainties (95% confidence bounds; Figure 7).

211 With the model setup illustrated in Figure 1 and viscosity of  $3 \times 10^{18}$ , the decay  
 212 constant for the horizontal displacements varies with distance. The maximum amplitude  
 213 is at a distance of around 7 km away from the source center. The decay constant ver-  
 214 sus distance depends on the viscosity. Testing models with different viscosities shows that  
 215 higher viscosities cause larger decay constant (Figure 7b). The modeling result shows  
 216 that viscoelastic relaxation causes different decay constants at different distances from  
 217 the source.

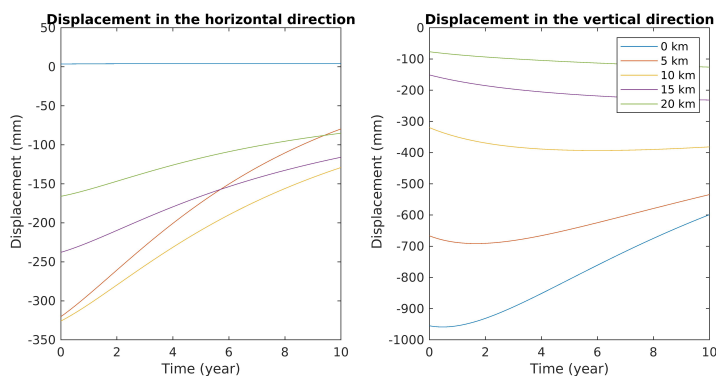


**Figure 6.** Surface displacement from 0 to 10 years at the points 0, 5, 10, 15, and 20 km away from the source center in the horizontal (left) and vertical (right) directions in the viscoelastic relaxation model.

218           The characteristics of the displacement field for the magma inflow and viscoelas-  
 219           tic relaxation model can be compared. Both models have the highest horizontal displace-  
 220           ment at a distance of a few kilometers away from the source center. The main difference  
 221           between the two models is in the decay constant, where the magma inflow model has the  
 222           same decay constant at all distances, while the viscoelastic relaxation model has decay  
 223           showing some variation with distance from the source (Figure 7). This is more pronounced  
 224           for lower viscosities. The offset in the results for  $6 \times 10^{18}$  Pa s is due to how the displace-  
 225           ment curve is fitted to equation 3, where there can be trade-off between the  $A$  and  $\tau$  pa-  
 226           rameters. Mapping the decay constant may be a tool to distinguish the two processes.  
 227

## 228   6 Post-eruptive stress and displacement at Bárðarbunga volcano

229           We use the 2014-2015 Bárðarbunga eruption as a case study to test our findings.  
 230           Bárðarbunga volcanic system includes a central volcano with a caldera and a fissure swarm  
 231           in central Iceland, partly under the Vatnajökull ice cap. The 2014-2015 Bárðarbunga erup-  
 232           tion lasted for six months, from August 2014 until February 2015 (Gudmundsson et al.,  
 233           2016; Pedersen et al., 2017). The volume involved in the eruption is  $1.9 \pm 0.3$  km<sup>3</sup>, in-  
 234           cluding  $\sim 1.4$  km<sup>3</sup> Holuhraun lava erupted to the northeast of the caldera and  $\sim 0.5$  km<sup>3</sup>  
 235           remaining in the 48 km long dike that formed, linking the Bárðarbunga caldera and the

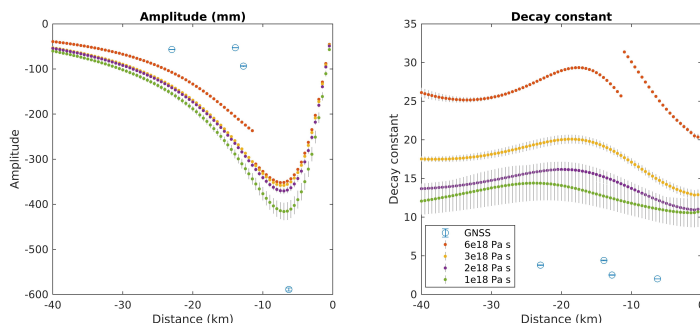


**Figure 7.** Amplitude (left) and decay constant (right) estimated from the horizontal surface displacement time series in a viscoelastic model, fit with an exponential function. The dots with error bars show the estimated amplitude and decay constant from viscoelastic models with different viscosities. The circles with error bars show the estimated amplitude and decay constant from the corrected GNSS time series in Figure 9. The x-axis is the distance from the source center in kilometers.

236 Holuhraun eruptive site (Sigmundsson et al., 2015; Gudmundsson et al., 2016; Pedersen  
 237 et al., 2017). During the eruption, the Bárðarbunga caldera floor collapsed 65 meters (Gudmundsson  
 238 et al., 2016). The glacial coverage and steep topography on the flanks of the central volcano  
 239 cause difficulty in fieldwork for ground deformation measurements.

240 Li et al. (2021) used the 2015-2018 average velocity fields calculated from both In-  
 241 SAR and GNSS to study the post-eruptive deformation field. Viscoelastic relaxation, magma  
 242 inflow with or without caldera fault movement, or a combination of these processes can  
 243 explain the observed average velocity field in the vicinity of the caldera. Their viscoelas-  
 244 tic relaxation model considers contraction volume of  $0.4 \text{ km}^3$  of a point source of pres-  
 245 sure below the caldera at 10 km depth in a viscoelastic model. The two-layer viscoelas-  
 246 tic model has a 7 km thick elastic layer on top of a  $3 \times 10^{18} \text{ Pa s}$  viscoelastic half-space  
 247 (same model as used here; Figure 1a).

248 The cumulative seismic moment in the caldera area of Bárðarbunga, and its vari-  
 249 ation with time, are taken as an indicator of the stress conditions (Figure 8, Li et al.,  
 250 2021; Jónsdóttir et al., 2019). We expect the evolution pattern of the cumulative seis-  
 251 mic moment and shear stress changes at depth to be comparable following some read-  
 252 justment period directly following the eruption, as earthquakes are driven by stresses.

253 In about nine months following the eruption, few earthquakes occurred, all of which had  
254 low magnitude. After that, seismic activity and magnitude increased, with the largest  
255 earthquake being  $M_w$  4.9 on January 2018,  $\sim 3.4$  years after the beginning of the erup-  
256 tion.

257 The rate of cumulative seismic moment release begins to decline at a similar time  
258 (signifying lower and lower energy release in earthquakes). Viscoelastic relaxation mod-  
259 eling suggests that stresses decay with time. This time-dependent stress change can also  
260 be reproduced using a magma inflow model with the inflow rate decaying with time, in  
261 such a manner that the pattern of stress decay at 8-9 km depth is similar to the cumu-  
262 lative seismic moment curve. As indicated by the model comparison in section 4, it is  
263 hard to tell the difference between the two stress fields.

264 Four continuous GNSS stations near the Bárðarbunga volcano measured the sur-  
265 face displacement and its temporal variation. We use time series of displacements at these  
266 GNSS sites to study the temporal variation of the post-eruptive surface displacements.  
267 We consider the observation period between 2015-2021, the initial six years following the  
268 2014-2015 eruption. The GNSS station closest to the caldera (KISA, 6 km away from  
269 the source) has the clearest decay in the horizontal component displacement (Figure 9).  
270 We find a decay constant of 2 years by fitting it with an exponential curve. We carry out  
271 such analysis for the continuous stations, and compare both the amplitude and decay  
272 constant with the modeled amplitude and decay constant (Figure 7). The decay constants  
273 from the four continuous stations are somewhat different, but in the range of 2-5 years.  
274 Compared with the modeling results, where the decay constants are longer than ten years  
275 for viscosities from  $1-6 \times 10^{18}$  Pa s (Figure 7), the GNSS decay constants are much smaller.  
276 Therefore, one should consider other processes, such as magma inflow, which might have  
277 a role in causing post-eruptive deformation. Different source geometries or viscoelastic  
278 models are also possible explanations.

## 279 7 Discussion

280 Our modeling results suggest that we can broadly reproduce a post-eruptive vis-  
281 coelastic stress field using an elastic time-dependent magma inflow model. The main stress  
282 difference between the models is at around 7 km depth, where the stress transfer from  
283 the viscoelastic material to elastic material is small, and causing smaller stress than in  
284 the magma inflow model at the same depth. In a cross section, the maximum change in  
285 shear stress above the source is in two lobes with different sign, offset with respect to

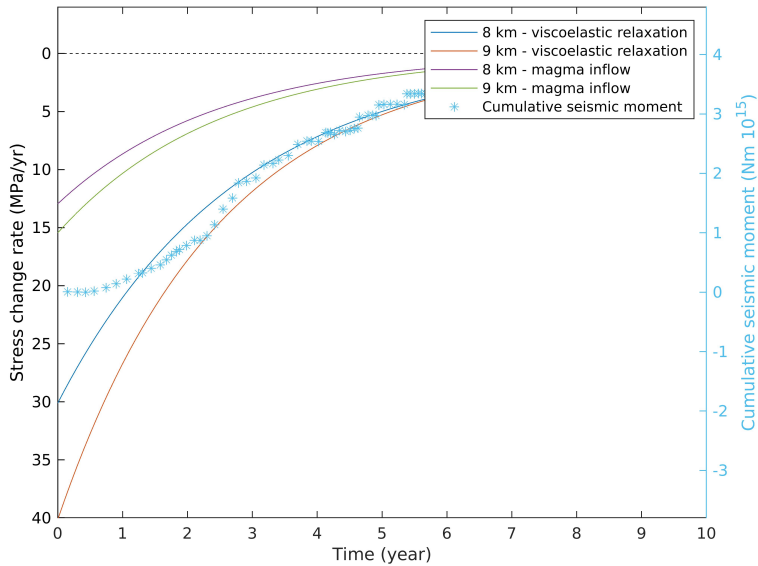


**Figure 8.** Cumulative seismic moment and the shear stress change over time from viscoelastic and magma inflow model. The lines are the stresses at different depths, 3 km horizontal distance away from the source. The viscoelastic model has  $0.4 \text{ km}^3$  contraction at  $t=0$ . The continuous magma inflow rate follows the equation  $y(t) = 1.552 \times 10^8 \times e^{-t/2.48} \text{ m}^3/\text{yr}$ . Stars show the cumulative seismic moment (Li et al., 2021). Both the stress change rate and the rate of cumulative seismic moment release (the slope of the cumulative seismic moment curve) show a decay after a period of two years.

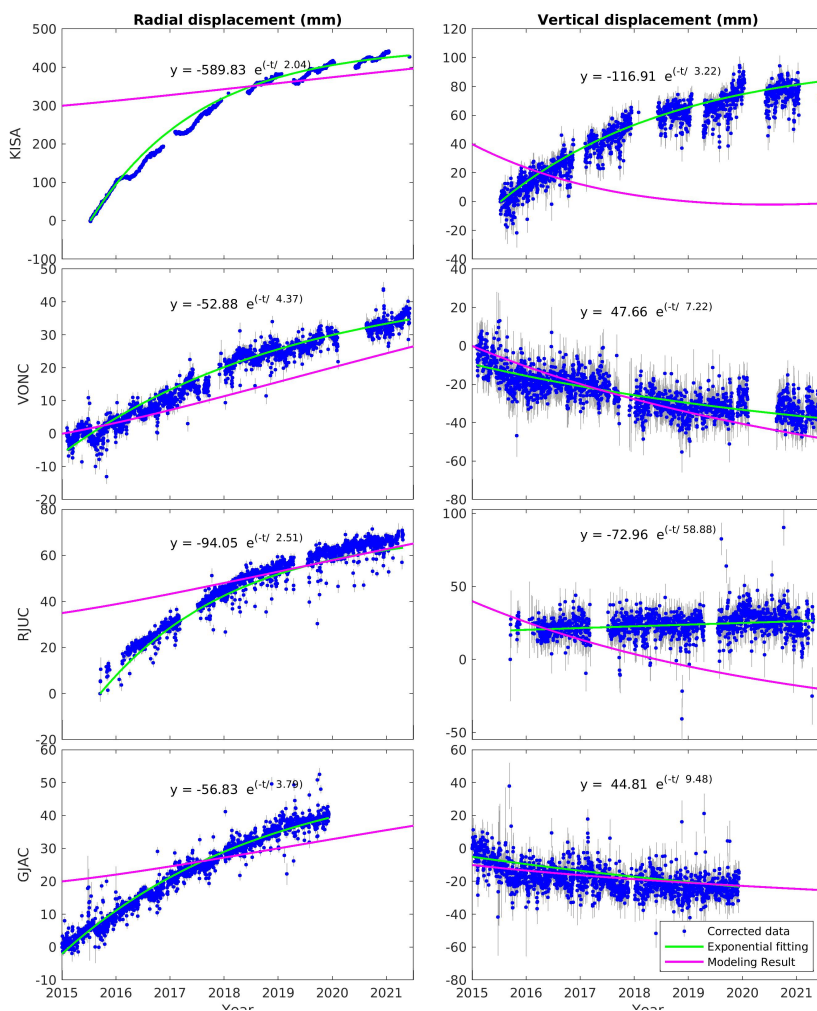


**Figure 9.** GNSS time series from four continuous stations, KISA, VONC, RJUC, and GJAC stations. The GNSS time series from radial (left panels) and up (right panels) directions are shown separately (blue dots). The radial direction is between the Bárðarbunga caldera center (64.63, -17.48) and the station location. We fit the GNSS time series with exponential decay (green curve, shown in each panel). The GNSS time series and the exponential fitting curves are shifted for displaying purposes so that the first observation point at each time series is at zero. The viscoelastic modeling results with viscosity of  $3 \times 10^{18}$  Pa s from the viscoelastic relaxation model in Figure 1a for these stations are shown in magenta.

286 the location of the surface projection of the modeled point source (Figures 2). At Bárðar-  
287 bunga volcano, seismicity along the caldera ring fault is observed in the post-eruptive  
288 period, consistent with either viscoelastic or magma inflow model, as the maximum shear  
289 stresses are not directly above its center. Earthquake activity in a post-eruptive period  
290 indirectly measures stress changes (that are the cause of earthquakes). Nevertheless, the  
291 eventual similarity of stress changes caused by magma inflow and viscoelastic relaxation  
292 make it difficult to use earthquake patterns to conclude which process dominates.

293 Considering temporal variation of ground displacements, the decay constant of the  
294 surface displacements measured by continuous GNSS stations could be used as an in-  
295 dicator for discriminating between the processes. We vary the viscosity from  $1\text{-}6 \times 10^{18}$   
296 Pa s and calculate the decay constant for horizontal displacement, and compare it with  
297 the decay constant estimated from GNSS stations at Bárðarbunga volcano (Figure 7).  
298 The modeled decay constant is higher than that from GNSS stations. Lowering the vis-  
299 cosity might better explain the observation, but viscosity lower than  $1 \times 10^{18}$  Pa s is not  
300 considered realistic for whole crustal sections (uniform horizontal layers) as modeled here,  
301 considering e.g. results from modeling of glacial isostatic adjustment. Different rheolog-  
302 ical structure in viscoelastic models could be considered, e.g., a temperature-dependent  
303 model or a viscoelastic shell around the magma body. An approach like that of Yamasaki  
304 and Kobayashi (2018) could also be considered, which model the effects of a localized  
305 low viscosity zone below a deformation source for producing rapid decay of surface dis-  
306 placements in volcanic regions following magma transfer.

307 For the Bárðarbunga volcano, an earlier study by Li et al. (2021) found that the  
308 average velocity field created by viscoelastic relaxation, deep magma inflow coupled with  
309 caldera fault slip, or shallow magma inflow are all similar in the far-field, outside the ice-  
310 cap. As we only have limited number of GNSS stations in the area (limited spatial res-  
311 olution) and the amplitude decays fast when going away from the source center, it is chal-  
312 lenging to infer the respective role of each process involved in the post-eruptive unrest  
313 at Bárðarbunga volcano. One of the reasons is that the Bárðarbunga caldera is covered  
314 by the Vatnajökull ice cap, which prevents accurate observations of surface displacements  
315 directly above the source. The largest difference in ground displacements due to the two  
316 processes is directly above the source. Furthermore, we do not have enough continuous  
317 GNSS stations to observe the temporal variation of the surface displacement at a suf-  
318 ficient distribution of distances from the source.



319 Our findings provide important guidance for future studies of viscoelastic relaxation.  
320 Ground deformation following volcanic eruptions that have large-scale magma withdrawal  
321 should be interpreted by taking into account viscoelastic relaxation, as the viscoelastic  
322 signal could be significant. Better temporal and spatial coverage of ground deformation  
323 observations than available at Bárðarbunga could be a solution for evaluating the rel-  
324 ative role of the magma inflow and viscoelastic relaxation in creating post-eruptive ground  
325 deformation.

## 326 8 Conclusion

327 Stress fields generated by viscoelastic relaxation following major magma drainage  
328 and magma inflow in a post-eruptive period are compared. Here the viscoelastic relax-  
329 ation model refers to a two-layer model, with a 7 km thick elastic layer on top of a vis-  
330 coelastic half-space. A magma inflow model can broadly reproduce both the spatial pat-  
331 tern and the temporal variation of the stress field of the viscoelastic model. Therefore,  
332 the stress field set up by the two processes cannot easily distinguish which of the two pro-  
333 cesses is more active in volcano roots in a post-eruptive period. Temporal variation of  
334 the stresses caused by viscoelastic relaxation can be recreated with a magma inflow model  
335 considering a magma inflow rate that decays exponentially with time.

336 Temporal variation of the observed surface displacement can be an indicator for  
337 discriminating between the two processes, as viscoelastic relaxation causes different de-  
338 cay constants at different locations. On the other hand, magma inflow model has the same  
339 decay constant at all distances from the deformation source. The horizontal surface dis-  
340 placement time series in the viscoelastic model presented here can be fitted with an ex-  
341 ponential function. In that case, the viscoelastic model has the maximum amplitude about  
342 7 km away from the source center, while the maximum decay constant (slowest relax-  
343 ation) is about 15 km away from the source.

344 At the Bárðarbunga volcano, we find that the stress change from viscoelastic re-  
345 laxation and time-dependent magma inflow models in the post-eruptive period are both  
346 consistent with the rate of cumulative seismic moment in the years following a readjust-  
347 ment period of about three years since the end of the eruption. The shear stresses gen-  
348 erated by both models suggest the preferred locations of the earthquake are shifted from  
349 the source center and could align on the caldera fault complex. With the temporal vari-  
350 ation of the stress field and the observed seismic variation, we can constrain the viscos-

ity of the subsurface or the magma inflow rate presented in our model. For the assumed  
crustal layering in a viscoelastic model, the viscosity of  $3 \times 10^{18}$  Pa s or a magma in-  
flow model with cumulative magma inflow volume following the equation  $1.55 \times 10^8 e^{-\frac{t}{2.48}}$   
fits the temporal variation of the cumulative seismic moment the best ( $t$  is the time in  
years). The surface displacement from different stations shows a somewhat different de-  
cay constant, which varies from 2 - 5 years. Our two-layer viscoelastic model alone can-  
not explain the GNSS horizontal displacement decay constants, so both further models  
of viscoelastic relaxation and magma inflow process should be considered for Bárðarbunga.

## References

- Barbot, S. (2014). *RELAX v1.0.7 [software]*, *Computational Infrastructure for Geo-*  
*dynamics*.
- Barbot, S., & Fialko, Y. (2010a). Fourier-domain Green's function for an elastic  
semi-infinite solid under gravity, with applications to earthquake and volcano  
deformation: Fourier-domain elastic solutions. *Geophysical Journal Interna-*  
*tional*, 182(2), 568-582. doi: 10.1111/j.1365-246X.2010.04655.x
- Barbot, S., & Fialko, Y. (2010b). A unified continuum representation of post-  
seismic relaxation mechanisms: semi-analytic models of afterslip, poroe-  
lastic rebound and viscoelastic flow: Semi-analytic models of postseismic  
transient. *Geophysical Journal International*, 182(3), 1124-1140. doi:  
10.1111/j.1365-246X.2010.04678.x
- Biggs, J., Ebmeier, S., Aspinall, W., Lu, Z., Pritchard, M., Sparks, R., & Mather, T.  
(2014). Global link between deformation and volcanic eruption quantified by  
satellite imagery. *Nature communications*, 5(1), 1-7.
- Bonaccorso, A., Cianetti, S., Giunchi, C., Trasatti, E., Bonafede, M., & Boschi,  
E. (2005, 11). Analytical and 3-D numerical modelling of Mt. Etna (Italy)  
volcano inflation. *Geophysical Journal International*, 163(2), 852-862. doi:  
10.1111/j.1365-246X.2005.02777.x
- Del Negro, C., Currenti, G., & Scandura, D. (2009, feb). Temperature-dependent  
viscoelastic modeling of ground deformation: Application to Etna volcano  
during the 1993-1997 inflation period. *Physics of the Earth and Planetary*  
*Interiors*, 172(3-4), 299-309. doi: 10.1016/j.pepi.2008.10.019
- Donovan, A., Oppenheimer, C., & Bravo, M. (2012). Science at the policy interface:

- 383 volcano-monitoring technologies and volcanic hazard management. *Bulletin of*  
384 *Volcanology*, 74(5), 1005–1022.
- 385 Dzurisin, D. (2006). *Volcano deformation: new geodetic monitoring techniques*.  
386 Springer Science & Business Media.
- 387 Feigl, K. L., Le Mével, H., Tabrez Ali, S., Córdova, L., Andersen, N. L., DeMets,  
388 C., & Singer, B. S. (2013). Rapid uplift in Laguna del Maule volcanic field of  
389 the Andean Southern Volcanic zone (Chile) 2007–2012. *Geophysical Journal*  
390 *International*, 196(2), 885–901. doi: 10.1093/gji/ggt438
- 391 Fujiwara, S., Murakami, M., Nishimura, T., Tobita, M., Yarai, H., & Kobayashi, T.  
392 (2017). Volcanic deformation of Atosanupuri volcanic complex in the Kussharo  
393 caldera, Japan, from 1993 to 2016 revealed by JERS-1, ALOS, and ALOS-2  
394 radar interferometry. *Earth, Planets and Space*, 69(1), 1–14.
- 395 Gudmundsson, M. T., Jónsdóttir, K., Hooper, A., Holohan, E. P., Halldórsson,  
396 S. A., Ófeigsson, B. G., ... Aiuppa, A. (2016). Gradual caldera collapse at  
397 Bárðarbunga volcano, Iceland, regulated by lateral magma outflow. *Science*,  
398 353(6296), aaf8988. doi: 10.1126/science.aaf8988
- 399 Jónsdóttir, K., Rodriguez, F. R., Hjørleifsdóttir, V., Jónsdóttir, K., Rodriguez,  
400 F. R., & Hjørleifsdóttir, V. (2019). Using repeating earthquakes to reveal  
401 temporal behavior of caldera faults. *Abstract EGU2019-2690 presented at 2019*  
402 *EGU General Assembly, Vienna, 7-12 April.*, 2690.
- 403 Le Mével, H., Feigl, K. L., Córdova, L., DeMets, C., & Lundgren, P. (2015). Evo-  
404 lution of unrest at Laguna del Maule volcanic field (Chile) from InSAR and  
405 GPS measurements, 2003 to 2014. *Geophysical Research Letters*, 42(16),  
406 6590–6598.
- 407 Le Mével, H., Gregg, P. M., & Feigl, K. L. (2016). Magma injection into a long-lived  
408 reservoir to explain geodetically measured uplift: Application to the 2007–2014  
409 unrest episode at laguna del maule volcanic field, chile. *Journal of Geophysical*  
410 *Research: Solid Earth*, 121(8), 6092–6108.
- 411 Li, S., Sigmundsson, F., Drouin, V., Parks, M. M., Ófeigsson, B. G., Jónsdóttir, K.,  
412 ... Hreinsdóttir, S. (2021). Ground Deformation After a Caldera Collapse:  
413 Contributions of Magma Inflow and Viscoelastic Response to the 2015–2018  
414 Deformation Field Around Bárðarbunga, Iceland. *Journal of Geophysical*  
415 *Research: Solid Earth*, 126(3), e2020JB020157.

- 416 MATLAB. (2020). *version 9.8.0.1323502 (r2020a)*. Natick, Massachusetts: The  
417 MathWorks Inc.
- 418 Morales Rivera, A. M., Amelung, F., Albino, F., & Gregg, P. M. (2019). Impact of  
419 Crustal Rheology on Temperature-Dependent Viscoelastic Models of Volcano  
420 Deformation: Application to Taal Volcano, Philippines. *Journal of Geophysical  
421 Research: Solid Earth*, *124*, 978–994. doi: 10.1029/2018JB016054
- 422 Novoa, C., Remy, D., Gerbault, M., Baez, J. C., Tassara, A., Cordova, L., ...  
423 Delgado, F. (2019). Viscoelastic relaxation: A mechanism to explain the  
424 decennial large surface displacements at the Laguna del Maule silicic vol-  
425 canic complex. *Earth and Planetary Science Letters*, *521*, 46–59. doi:  
426 10.1016/j.epsl.2019.06.005
- 427 Pedersen, G., Höskuldsson, A., Dürig, T., Thordarson, T., Jónsdóttir, I., Ri-  
428 ishuus, M., ... Schmith, J. (2017). Lava field evolution and emplacement  
429 dynamics of the 2014–2015 basaltic fissure eruption at Holuhraun, Ice-  
430 land. *Journal of Volcanology and Geothermal Research*, *340*, 155–169. doi:  
431 10.1016/j.jvolgeores.2017.02.027
- 432 Segall, P. (2019). Magma chambers: what we can, and cannot, learn from vol-  
433 cano geodesy. *Philosophical Transactions of the Royal Society A*, *377*(2139),  
434 20180158.
- 435 Segall, P., Anderson, K. R., Johanson, I., & Miklius, A. (2019). Mechanics of In-  
436 flationary Deformation During Caldera Collapse: Evidence From the 2018  
437 Kīlauea Eruption. *Geophysical Research Letters*, *46*(21), 11782–11789. doi:  
438 10.1029/2019GL084689
- 439 Sigmundsson, F., Hooper, A., Hreinsdóttir, S., Vogfjörð, K. S., Ófeigsson, B. G.,  
440 Heimisson, E. R., ... Eibl, E. P. (2015). Segmented lateral dyke growth in  
441 a rifting event at Bárðarbunga volcanic system, Iceland. *Nature*, *517*(7533),  
442 191–195. doi: 10.1038/nature14111
- 443 Sigmundsson, F., Hreinsdóttir, S., Hooper, A., Árnadóttir, T., Pedersen, R.,  
444 Roberts, M. J., ... Feigl, K. L. (2010). Intrusion triggering of the 2010  
445 Eyjafjallajökull explosive eruption. *Nature*, *468*(7322), 426–430. doi:  
446 10.1038/nature09558
- 447 Sturkell, E., Einarsson, P., Sigmundsson, F., Geirsson, H., Ólafsson, H., Pedersen,  
448 R., ... Stefánsson, R. (2006). Volcano geodesy and magma dynamics in Ice-

- 449 land. *Journal of Volcanology and Geothermal Research*, 150(1-3), 14–34. doi:  
450 10.1016/j.jvolgeores.2005.07.010
- 451 Yamasaki, T., & Kobayashi, T. (2018). Imaging a low viscosity zone beneath the  
452 Kutcharo caldera, eastern Hokkaido, Japan, using geodetic data. *Earth and*  
453 *Planetary Science Letters*, 504, 1–12.
- 454 Yamasaki, T., Kobayashi, T., Wright, T. J., & Fukahata, Y. (2018). Viscoelastic  
455 crustal deformation by magmatic intrusion: A case study in the Kutcharo  
456 caldera, eastern Hokkaido, Japan. *Journal of Volcanology and Geothermal*  
457 *Research*, 349, 128–145. doi: 10.1016/j.jvolgeores.2017.10.011
- 458 Yamasaki, T., Sigmondsson, F., & Iguchi, M. (2020). Viscoelastic crustal re-  
459 sponse to magma supply and discharge in the upper crust: Implications for  
460 the uplift of the Aira caldera before and after the 1914 eruption of the Saku-  
461 rajima volcano. *Earth and Planetary Science Letters*, 531, 115981. doi:  
462 10.1016/j.epsl.2019.115981